Measurement of π^0 and η mesons with photon conversions in ALICE in proton-proton collisions at $\sqrt{s} = 0.9,\ 2.76$ and $7\,\mathrm{TeV}$

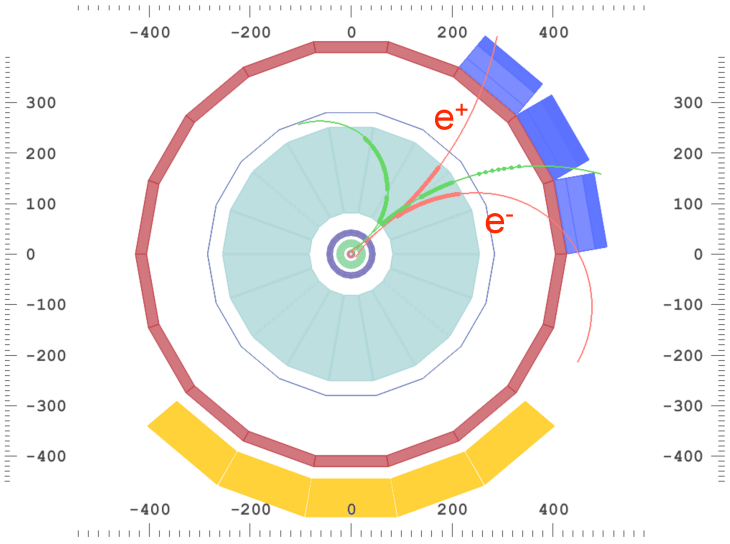

Kathrin Koch
Heidelberg 2011

Dissertation
submitted to the
Combined Faculties of the Natural Science and Mathematics
of the Ruperto-Carola-University of Heidelberg, Germany
for the degree of
Doctor of Natural Science

Put forward by
Kathrin Koch
born in Stralsund, Germany
Oral examination: 01 February 2012

Measurement of π^0 and η mesons with photon conversions in ALICE in proton-proton collisions at $\sqrt{s} = 0.9,\ 2.76$ and $7\,\mathrm{TeV}$

Referees: Prof. Dr. Johanna Stachel
Prof. Dr. Hans-Christian Schultz-Coulon

For Olaf and Marlene

Abstract

In this thesis the differential invariant cross sections of the inclusive π^0 and η meson production in proton-proton collisions at $\sqrt{s} = 0.9,\ 2.76$ and $7\,\mathrm{TeV}$ are presented. They have been obtained by the reconstruction of electrons and positrons from photon conversions in the Inner Tracking System and the Time Projection Chamber of the ALICE experiment. Therefore, the method is completely independent of calorimeters and allows the extraction of the π^0 (η) signal down to very low transverse momenta of $0.3\,\mathrm{GeV/c}$ ($0.4\,\mathrm{GeV/c}$) for $\sqrt{s} = 7\,\mathrm{TeV}$. The resulting differential invariant cross sections are compared to those of the PHOton Spectrometer and charged pions and found to be almost everywhere in good agreement. The combined spectra of the photon conversion method and PHOS cover a broad transverse momentum range. The π^0 and η spectra agree with NLO perturbative QCD predictions at $\sqrt{s} = 0.9\,\mathrm{TeV}$, however, the calculations overestimate the data at $\sqrt{s} = 7\,\mathrm{TeV}$. Also m_T scaling has been tested at $\sqrt{s} = 2.76$ and $7\,\mathrm{TeV}$. For $\sqrt{s} = 2.76\,\mathrm{TeV}$ no clear statement can be made while for $\sqrt{s} = 7\,\mathrm{TeV}$ an indication of violation is observed at low m_T. The measured η/π^0 ratios at the different energies are in agreement with world data. Furthermore, the production of π^0 mesons as a function of charged-particle multiplicity has been investigated for $\sqrt{s} = 7\,\mathrm{TeV}$. A strong dependence is observed. With increasing charged-particle multiplicity an increase of the neutral pion yield and of the average transverse momentum is seen.

Zusammenfassung

In der vorliegenden Arbeit werden die differentiellen invarianten Wirkungsquerschnitte der inklusiven π^0- und η-Produktion in Proton-Proton Kollisionen bei den Schwerpunktsenergien von $\sqrt{s} = 0.9,\ 2.76$ und $7\,\mathrm{TeV}$ vorgestellt. Diese wurden aus der Rekonstruktion von Photonen gewonnen, die im Detektormaterial des Inner Tracking System und der Time Projection Chamber des ALICE-Experimentes konvertieren. Die vorgestellte Methode ist daher vollständig unabhängig von Messungen mit Kalorimetern und erlaubt die Extrahierung des π^0 (η) Signals hin zu sehr kleinen Transversalimpulsen wie $0.3\,\mathrm{GeV/c}$ ($0.4\,\mathrm{GeV/c}$) für $\sqrt{s} = 7\,\mathrm{TeV}$. Die erhaltenen differentiellen invarianten Wirkungsquerschnitte wurden mit denen des PHOton Spektrometers und dem Spektrum geladener Pionen verglichen. Alle Spektren stimmen weitestgehend überein. Die kombinierten Spektren der Photonkonversionsmethode und PHOS erweitern den gemessenen Transversalimpulsbereich. Der Vergleich zu störungstheoretischen QCD-NLO-Rechnungen zeigt Übereinstimmung für $\sqrt{s} = 0.9\,\mathrm{TeV}$, aber eine deutliche Überschätzung der Spektren bei $\sqrt{s} = 7\,\mathrm{TeV}$. Auch m_T scaling wurde im Rahmen der vorliegenden Arbeit getestet. Für $\sqrt{s} = 2.76\,\mathrm{TeV}$ kann keine eindeutige Aussage getroffen werden, bei einer Schwerpunktsenergie von $\sqrt{s} = 7\,\mathrm{TeV}$ ist m_T scaling im Bereich von kleinen transversalen Massen verletzt. Das ebenfalls gemessene Verhältnis von η Mesonen zu neutralen Pionen stimmt mit bisher gemessenen Weltdaten überein. Überdies wurde die Produktion von neutralen Pionen in Abhängigkeit von der Multiplizität geladener Teilchen untersucht. Eine starke Korrelation zwischen beiden wurde beobachtet. Mit ansteigender Multiplizität der geladenen Teilchen ist auch ein Anstieg der π^0-Produktion und des mittleren Transversalimpulses der Pionen zu verzeichnen.

Contents

List of Figures

List of Tables

Authors contribution

A big experiment such as the ALICE experiment can only be run successfully within a collaboration of many scientists. Every member focuses on his/her task but typically there is an overlap with the activities of other members. The results presented in this thesis are obtained by the *Photon Conversion Group* within ALICE, which is organized by Dr. Ana Marin. The results are the outcome of fruitful discussions between all members of this group. The author is involved in this working group since its very beginning in 2008.

The fundamental functionality of the entire analysis chain to reconstruct photons and π^0 (η) mesons has been developed by the author within the first years of her doctorate studies. It has been later ported by several group members (including the author) to the analysis framework of the ALICE experiment. Furthermore, different procedures have been developed to estimate the material budget and the resolution of the determined transverse momentum and geometrical variables. The investigation of the material budget within ALICE has then been the topic of the bachelor thesis of Friederike Bock. The different methods to calculate the combinatorial background have been developed and implemented by Kenneth Aamodt.

In the time before the first collisions at the LHC the main efforts have been put into understanding the reconstruction and the applied cuts to extract photons and π^0 and η mesons. With the first collisions the outcome of simulation and data has been checked by several group members including the author to ensure that the applied cuts have the same effect on both. Moreover, the consistency within the used Monte Carlo generators PYTHIA and PhoJet in terms of geometrical acceptance, reconstruction efficiencies etc. has been checked for the π^0 meson by the author, for the η meson by Ana Marin and Friederike Bock. The decision for the used background calculation is based on the authors study of their different shapes with respect to the reconstructed signal. The shape of the reconstructed meson peak turned out to be non-Gaussian, thus different kinds of fits have been investigated by the author. The presently used cuts in the analysis are based on the analysis of $\sqrt{s} = 7\,\text{TeV}$ data. They are the result of very intensive cut studies by several group members including the author. The presented results base on the analysis of events with a specific trigger signal. In addition, the author has investigated the influence of a stricter trigger as well as the influence of pile-up events on the results.

The data analysis includes the three collision energies $\sqrt{s} = 0.9, 2.76$ and $\sqrt{s} = 7\,\text{TeV}$. In the analysis of the data from $\sqrt{s} = 2.76\,\text{TeV}$ the author has not been involved directly, but indirectly through the development of the software, which is the same for all energies. The estimation of the systematic uncertainties for the three collision energies has been done by Friederike Bock.

The achieved analysis results have been compared to results from other inputs as there are the measurement of π^0 and η mesons by ALICE PHOS, the measurement of charged pions within ALICE and theoretical predictions from NLO pQCD calculations. The latter two have been checked by the author. Furthermore, the question of m_T-scaling and, last but not least, the production of π^0 as a function of charged-particle multiplicity has been investigated by the author.

1. Motivation

In 1927 Abbe Georges Lemaitre was the first to bring up the theory of what was later called the „Big Bang" [Lem1927]. He concluded from Einstein's theory of relativity and the observed red-shift in the spectra of distant galaxies that the universe must be expanding and, if so, would have started its expansion from „a unique quantum" [Lem1931]. At that time, this was a revolutionary idea that got little attention until Edwin Hubble found a linear relation between the red-shift of the galaxies and their distance to Earth, which clearly indicated an expansion of the universe [Hub1931]. Today, the Big Bang theory is commonly accepted and we have gained great knowledge in the fields of astronomy, nuclear physics and particle physics which allows us to get more and more insights in the evolution of the universe.

After a period of rapid expansion, called inflation, which ended at around 10^{-30} seconds after the Big Bang quarks, leptons, $W^{\pm}$, Z, photons and gluons started to evolve forming a state called quark-gluon plasma (QGP). This state was created some 10 picoseconds after the Big Bang and only lasted 10 microseconds [Bra2007]. With the further expansion of the universe it cooled down. Quarks could not exist anymore as free particle and started to form hadrons. With the expansion and cooling of the universe heavier hadrons decayed into protons, neutrons and their corresponding anti-particles. The first nuclear fusions of protons and neutrons started around 10 seconds after the Big Bang. After a hundred thousand years stable atoms started to form from nuclei and electrons. Now photons were able to travel long distances without absorption and the universe got transparent. The decoupling of photons from matter lasted about 100 thousand years. Today these photons are observed as cosmic microwave background, discovered in 1964 by Arno Penzias and Robert W. Wilson [Pen1965]. Going further in time, about a 100 million years later, the first stars and galaxies were formed.

We now live in a world with a rather low temperature of about $0.23\,\mathrm{meV}$ ($\approx 2.7\,\mathrm{K} \cdot k_B$); in the early phase of our universe, the quark-gluon plasma, the temperature was much higher. Calculations within the framework of Lattice Quantum Chromodynamics (section 2.2) find a critical temperature of $T_c = 175\,\mathrm{MeV}$ and energy density ε_c of $700\,\mathrm{MeV/fm^3}$ for the transition from the plasma into the hadronic phase [Kar2002]. The phase diagram of Quantum Chromodynamics is given in figure 1.1 in the plane of temperature T and net baryon density (baryons minus anti-baryons). The phase transition takes place at high temperatures and/or high net baryon densities. It is believed that in neutron stars a cold QGP exists.

To study this phase of evolution an environment with similar temperature and energy density must be created. Moreover, to extract thermodynamical information from the created system it must contain a large number of particles (of the order of thousands or more [Bra2007]), so that a local equilibrium can be assumed. Collisions of protons or electrons are not able to produce such conditions since too few particles are created. In contrast, collisions of heavy ions provide this environment. Additionally, the number of produced quarks and gluons is directly related to the duration of the fireball. The system created in laboratory experiments is much smaller than during the Big Bang. It quickly expands and cools down much faster, so it only exists for about $10^{-22}\,\mathrm{s}$ [Bra2007].

Programs in this new field of research began in 1986. At the accelerators Alternating Gra-

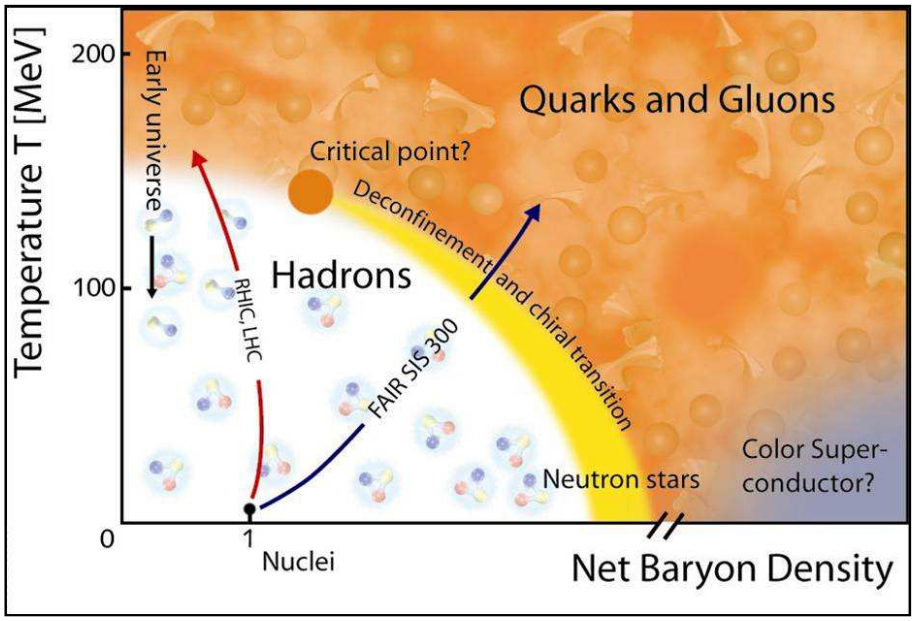

Figure 1.1.: QCD phase diagram [GSI2011].

dient Synchrotron (AGS) at Brookhaven National Laboratory (BNL) and the Super Proton Synchrotron (SPS) at the European Organization for Nuclear Research (CERN) fixed target collisions started with lighter ions, namely oxygen, silicon and sulfur. At the AGS oxygen and silicon ions were accelerated up to an energy of 14.6 GeV per nucleon [Bar1987] while at the SPS $60 - 200$ GeV per nucleon were achieved for oxygen and sulfur ions [Hei2008]. In the beginning of the 1990's both programs continued with heavier ions. At AGS gold ions were accelerated to a center-of-mass energy per nucleon pair of $\sqrt{s_{NN}} = 4.6$ GeV while at SPS $\sqrt{s_{NN}} = 17.2$ GeV for lead ions were reached. At the same time, the Relativistic Heavy-Ion Collider (RHIC) at BNL was built, dedicated to heavy-ion physics, and serving pp and $A + A$ collisions to four experiments, called BRAHMS, PHENIX, PHOBOS and STAR. At these colliding experiments center-of-mass energies of $\sqrt{s_{NN}} = 200$ GeV are reached [Bra2007]. With the Large Hadron Collider (LHC) at CERN a huge step towards even higher energies has been taken. Collisions with lead ions up to $\sqrt{s_{NN}} = 5.5$ TeV are possible, at present $\sqrt{s_{NN}} = 2.76$ TeV has been achieved. This opened a new energy regime in the hunt for the quark-gluon plasma. The dedicated experiment at the LHC for this research is the ALICE (A Large Ion Collider Experiment) experiment.

One characteristic of heavy-ion collisions is the suppression of highly energetic particles. Partons with high transverse momentum are produced in hard scattering processes in the early stage of the collision. Thus, the produced number in heavy-ion collisions scales with the number of binary nucleon-nucleon collisions. The partons interact with the created hot and dense medium and hereby lose energy. In figure 1.2 the measured ratio of the yields in heavy-ion collisions (normalized by the number of binary collisions) and proton-proton collisions, R_{AA}, is shown. In central gold-gold collisions a suppression of neutral pions by a factor of 5 is observed.

This observable requires a measurement of the neutral-pion production in proton-proton (pp) collisions. But also other observables have to be measured in pp collisions to provide a baseline for measurements in nuclear reactions. However, proton-proton collisions themselves are very important and do not only serve as a baseline for heavy-ion collisions. While the latter provide access to properties and the evolution of strongly interacting matter, proton-proton collisions allow to study the structure of particles.

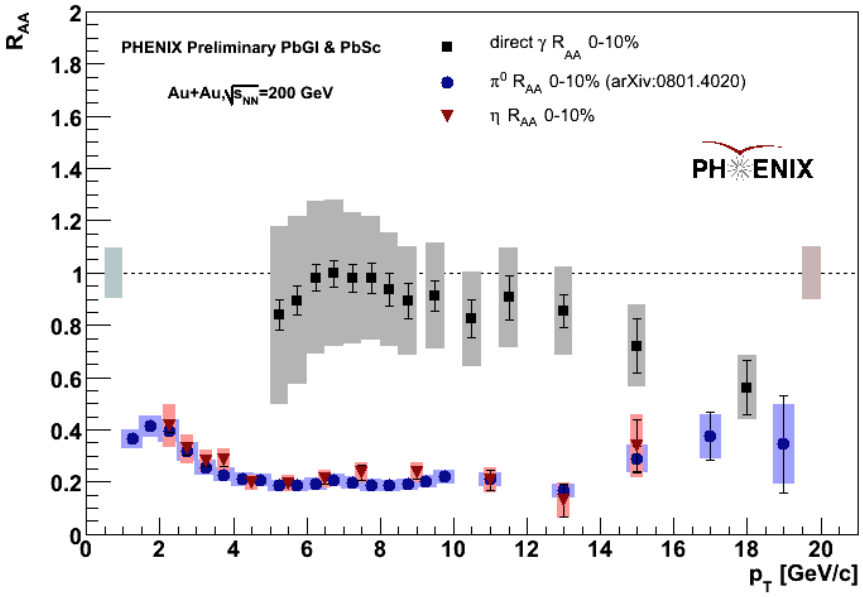

Figure 1.2.: Nuclear modification factor R_{AA} for neutral pions, η mesons and direct photons in gold-gold collisions with $0-10\%$ centrality at $\sqrt{s_{NN}} = 200\,\text{GeV}$ measured by the PHENIX collaboration [PHE2011].

The measurements of particle fragmentation functions at hadron colliders give the possibility to check the universality of hadronisation models. Fragmentation functions are mainly derived from e^+e^- collisions at low energies and may not fit anymore at LHC collision energies [DSS2007]. Especially gluon fragmentation functions are not well constrained in electron-positron collisions since gluon production is only observed as a sub-leading process in three-jet events. By contrast, π^0 and η meson production at the LHC is dominated by gluon fragmentation. Fragmentation functions are assumed to be independent of the colliding system. The ALICE experiment with its good particle identification capabilities has the opportunity to test this assumption. In particular, neutral pions and η mesons provide a very good cross check since they can be identified over a very large momentum range. In figure 1.3 the differential cross sections for neutral pions and η mesons in pp collisions measured by the PHENIX collaboration are shown as a function of transverse momentum p_T at the center-of-mass energy $\sqrt{s} = 200\,\text{GeV}$ at RHIC [Ada2007] [Ada2011].

Both spectra are compared to Next-to-Leading Order perturbative QCD calculations (NLO pQCD) at the scales $\mu = 0.5\,,\ 1$ and $2\,\text{p}_\text{T}$ for renormalization, factorization and fragmentation, see section 2.2. For π^0 (left) theoretical predictions and data points agree in the transverse momentum range of $2 - 20\,\text{GeV/c}$. The inset shows the lower p_T region of the π^0 differential cross section and the charged-pion differential cross section ($\frac{\pi^+ + \pi^-}{2}$) (black circles). Both spectra are in agreement, too. The line results from a fit of the charged pion data with an exponential function in the range of $p_T = 0.3 - 0.8\,\text{GeV/c}$. An exponentially falling spectrum corresponds to a non-perturbative component of a spectrum while a power law behavior describes perturbative contributions. For the given charged-pion spectrum the transition from soft to hard processes occurs in the p_T range of $1 - 2\,\text{GeV/c}$. For the η meson the comparison of measured data points and theoretical predictions at the scales $\mu = 0.5\,,\ 1$ and $2\,\text{p}_\text{T}$ is shown in the right figure. The measured differential cross sections were used in a global fit to extract fragmentation functions [Ada2011].

The data in proton-proton collisions at $\sqrt{s} = 200\,\text{GeV}$ are described very well by theoretical predictions, but the particle production rate changes with increasing collision energy. In figure 1.4 three important variables for π^0 production versus π^0 transverse momentum are shown: the

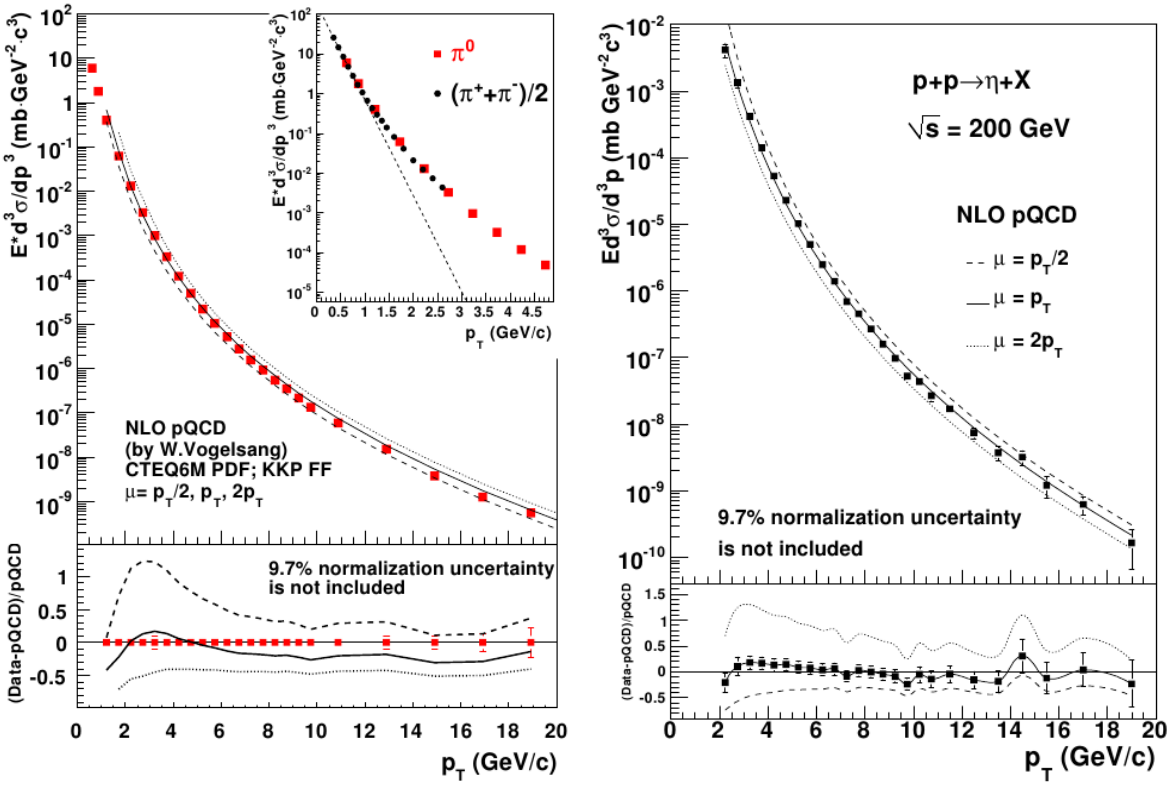

Figure 1.3.: Cross sections for inclusive π^0 (left) and η (right) production measured in pp collisions by the PHENIX collaboration at $\sqrt{s} = 200\,\text{GeV}$ as a function of transverse momentum. The figures also show the comparison to NLO pQCD calculations at three different scales. Measured data and theoretical predictions agree. For the η meson the used fragmentation functions are partially constrained by these data. The inset in the left plot compares the production of neutral pions and charged pions. In the bottom of both plots the deviation of measured data from the theoretical predictions with respect to the predictions are shown. Data and prediction agree for π^0 as well as for η for $\mu = 1\,\text{p}_\text{T}$ [Ada2007] [Ada2011].

parton fractional momentum x with respect to the scattered hadron, the fraction of the formed hadron momentum with respect to the momentum of the scattered partons z and the fraction of π^0 from gluon fragmentation [Vog2011]. Due to the much higher energy and momentum of the proton beam at the LHC energy a smaller x is sufficient to produce a neutral pion with a given transverse momentum. This is shown in figure 1.4 (top). The middle plot gives a comparison of the fraction of the produced π^0 momentum with respect to the parton momentum. It can be seen that at the LHC the fragmentation function is probed at slightly smaller z ($<z> \approx 0.4$, compared to $0.5 - 0.7$ at RHIC). For LHC energies more partons with high transverse momentum exist, therefore the necessary fraction to create neutral pions is smaller. The bottom plot compares the fraction of neutral pions coming from gluon fragmentation at RHIC and LHC energies. For $\sqrt{s} = 200\,\text{GeV}$ this fraction falls steeply with increasing transverse momentum. At $p_T^{\pi^0} = 30\,\text{GeV/c}$ only 10 % of π^0's come from gluons. For $\sqrt{s} = 7\,\text{TeV}$ the behavior is completely different. The fraction of π^0 from gluon fragmentation dominates in the full given transverse momentum range. Even at $p_T^{\pi^0} = 100\,\text{GeV/c}$ gluon fragmentation gives the major contribution to the neutral pion spectrum [SZS2010]. Therefore, gluon fragmentation gets much more important at the LHC energies.

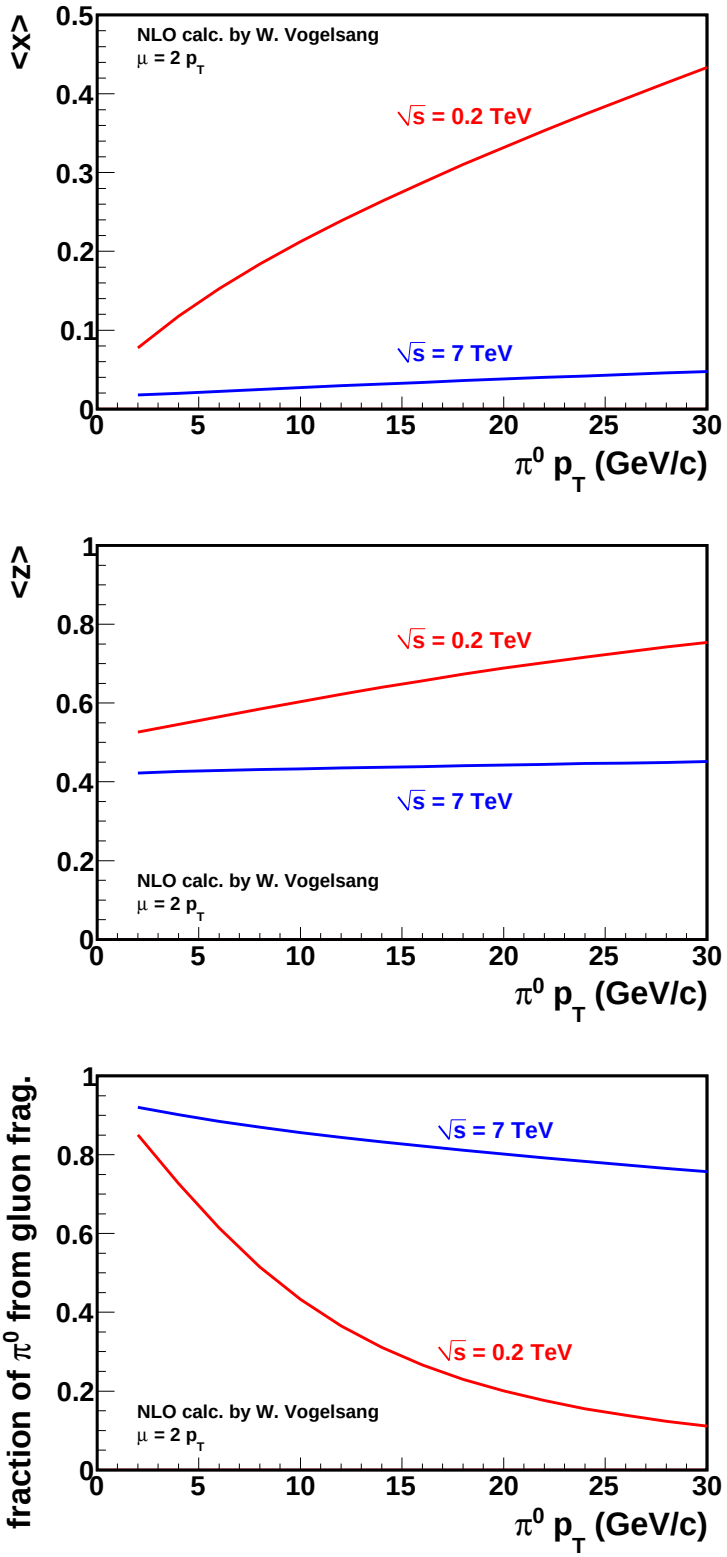

Figure 1.4.: Theoretical predictions for the fraction of the parton momentum relative to the momentum of the incident proton x (top) in parton-parton scatterings that lead to the production of a π^0, the fraction of the momentum of the outgoing hadron relative to the parton momentum z (middle) and the fraction of neutral pions from gluon fragmentation (bottom), all distributions are shown as functions of the π^0 transverse momentum. Red lines correspond to RHIC energy while blue presents LHC predictions [Vog2011].

In this thesis the measurement of neutral pions and η mesons in proton-proton collisions at the center-of-mass energies $\sqrt{s} = 0.9, 2.76$ and $7\,\text{TeV}$ at the LHC is presented. Both mesons are reconstructed in their decay channel $\pi^0 \to \gamma\gamma$ and $\eta \to \gamma\gamma$. Within the ALICE experiment the detection of photons is not only possible with calorimeters but also via the reconstruction of electron-positron pairs from photon conversions in the central tracking detectors, which is the method used in this analysis. The obtained invariant-mass distributions from these photon pairs show peaks at the rest masses of both mesons. The presented analysis method has two advantages. Firstly, π^0 and η mesons can be reconstructed down to very low transverse momentum of $0.3\,\text{GeV/c}$ ($0.4\,\text{GeV/c}$). Secondly, due to the tracking momentum resolution, especially at low p_T, the achieved mass resolution is very good in this regime, which allows a precise measurement. Moreover, since the method is independent of those from calorimeters it allows a cross check of the π^0 and η measurements.

The structure in this thesis is as follows: after this motivation, a theoretical overview is given in chapter 2 followed by an introduction to photon and electron interactions with matter. Chapter 4 provides an overview of the experimental setup. Chapter 5 is dedicated to the data analysis, acceptance and efficiency corrections are discussed in chapter 6. The results are presented in chapter 7. The thesis concludes with a summary and an outlook.

2. Theoretical background

2.1. The Standard Model

At present, the Standard Model of particle physics is the most present answer to the old human question: What is the basis of everything? With the construction of gigantic particle accelerators the hunting of the primary constituents started. The very high number of new discovered particles in the middle of last century supported the idea of even more fundamental particles: quarks. These have been postulated by Gell-Mann and Zweig [Gel1964] [Zwe1964]. The quark model evolved into Quantum Chromodynamics. The unified theory of electromagnetic and weak interactions, Quantum Chromodynamics and the Higgs mechanism build the Standard Model of particle physics [Gla1962] [Sal1969] [Sal1970] [Wei1967] [Hig1964].

The fundamental particles in the Standard Model are fermions, which form all matter, and bosons which mediate the forces between them. The elementary fermions are particles of spin 1/2, divided into quarks and leptons. They are grouped into three families. Each lepton family contains a charged lepton (*electron*, *muon*, *tau*) and the corresponding neutral neutrino ν. The three quark families each contain one quark of charge 2/3 (*up*, *charm* and *top*) and one of the charge $-1/3$ (*down*, *strange* and *bottom*). The different types of quarks are also called flavor. Quarks are bound into hadrons which consist either of a quark-anti-quark pair, called *mesons*, or a combination of three quarks, called *baryons*. Due to the Pauli principle the baryon constituents need to be distinguishable in at least one property. This led to the introduction of a new quantum number, *color charge*. Quarks carry either *red*, *blue* or *green* charge and anti-quarks *anti-red*, *anti-blue* or *anti-green* charge. All fermions are associated with antiparticles of the same mass and spin but opposite charge. Masses, charges and spin of the fermions are summarized in figure 2.1.

The forces incorporated to the Standard Model are of electromagnetic, weak and strong nature. The force carriers are gauge bosons with spin 1. In electromagnetic interactions the photon

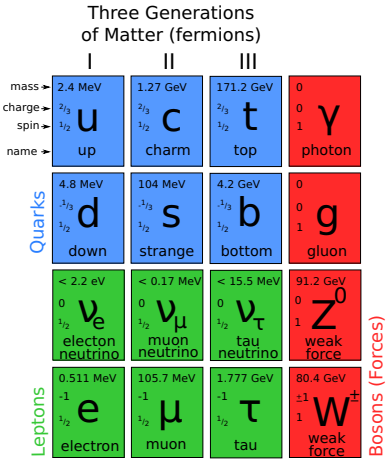

Figure 2.1.: Basic constituents and gauge bosons of the Standard Model [Wik2011].

acts as mediating gauge particle. In weak interactions $W^{\pm}$ and Z^0 gauge bosons mediate between quarks and leptons. Electromagnetic and weak interactions are unified at high energies, described in the electroweak theory. The strong force is mediated by eight color charged gluons. Due to their charge gluons also interact among themselves. The strong interactions between quarks and gluons are described by the theory of Quantum Chromodynamics (QCD).

The only undiscovered particle of the Standard Model is the Higgs particle. It has no spin and is thus classified as a boson. The Higgs boson plays a unique role in the Standard Model since it provides an explanation of the $W^{\pm}$ and Z^0 masses. The Higgs mechanism is responsible for the spontaneous electroweak symmetry breaking resulting in the non-zero mass of the gauge bosons. The hunt for the Higgs boson at the LHC is ongoing. Recent measurements by ATLAS and CMS, section 4.1, excluded the Higgs over most of the mass range $145 - 466\,\mathrm{GeV/c^2}$ [LHC2011].

2.2. Quantum Chromodynamics

The strong interaction between quarks and gluons is described by the theory of Quantum Chromodynamics (QCD). The Lagrange density of QCD is given by

$$\mathcal{L} = \sum_q \overline{\psi_q}\gamma^\mu(i\partial^\mu - g_s A_q^\mu \frac{\lambda_a}{2})\psi_q - \sum_q m_q \overline{\psi_q}\psi_q - \frac{1}{4}\sum_a F_a^{\mu\nu}F_{\mu\nu,a} \qquad \text{[Bar1996]}, \tag{2.1}$$

where ψ_q corresponds to the quark field, g_s represents the effective strong charge and A_q^μ the gluon field. The λ_a are the Gell-Mann-matrices. The factor $F_a^{\mu\nu} = \partial^\mu A_a^\nu - \partial^\nu A_a^\mu + i g_s f_{abc} A_\mu^b A_\nu^c$ describes the gluon field strength tensor, the last term in this equation corresponds to the gluon self-interaction.

The invariance of the QCD Lagrangian under the exchange of left- and right-handed components of the quark spinor is called *chiral symmetry*. For each moving particle with spin $\overrightarrow{s}$ and momentum $\overrightarrow{p}$ the helicity is defined as the projection of the spin onto its propagation direction

$$h = \frac{\overrightarrow{s}\cdot\overrightarrow{p}}{|\overrightarrow{p}|}. \tag{2.2}$$

The exchange of a gluon between two quarks does not influence the quark helicity, therefore the baryon number B_L for left-handed and B_R for right-handed quarks should be conserved separately. Due to the quark masses, although very small, the chiral symmetry is explicitly broken. Massive particles have a velocity smaller than the speed of light, thus one can find a reference frame that moves faster. In this case the momentum of the moving particle changes its sign and value with respect to the reference frame. Thus, the quark helicity is transformed from left-handed into right-handed or vice versa and only the sum $B = B_L + B_R$ is conserved. Moreover, even for massless quarks, the strong force between quarks and anti-quarks leads to fluctuations giving rise to the so-called *quark* or *chiral condensate*:

$$\langle\overline{q}q\rangle \equiv \langle 0|\overline{q}_L q_R + \overline{q}_R q_L|0\rangle \neq 0 \qquad \text{[Kha2002]}. \tag{2.3}$$

The condensate is not invariant under the exchange of left- and right-handed fermions. Thus, the chiral symmetry of the QCD Lagrangian is spontaneously broken. One consequence of this is the existence of massless bosons with spin 0, so called *Goldstone bosons*. Those can be identified with the lightest hadrons $\pi^0, \pi^{\pm}, K^{\pm}, K^0, \bar{K}^0$ and η. Due the explicite breaking of chiral symmetry also the Goldstone bosons acquire a small mass.

The strength of the strong coupling g_s, typically expressed as $\alpha_s = g_s^2/4\pi$, depends on the momentum transfer Q in the interaction at which it is examined. The actual value of α_s is not

predicted by QCD but can be determined from experiments, e.g. at the mass of the Z boson $m_Z = 91.2\,\mathrm{GeV/c^2}$, $\alpha_s = 0.1184 \pm 0.0007$ [Bet2009].

In one-loop approximation (see below) α_s can be written as

$$\alpha_s(Q^2) \approx \frac{12\pi}{(33 - 2N_f)\ln\frac{Q^2}{\Lambda^2}} \qquad \text{[Sch1995]}, \tag{2.4}$$

where N_f is the number of quark flavors and Λ the QCD scaling parameter. The experimentally found value for Λ is about 200 MeV [Cas1998]. Eq. 2.4 is only valid for $Q^2 \gg \Lambda^2$, but it describes the strength of the coupling very well. For increasing momentum transfer Q the coupling decreases as shown in figure 2.2. In the limit $Q \longrightarrow \infty$ quarks behave like free particles. This is called *asymptotic freedom* [Col1975]. For its discovery the physicists David Gross, David Politzer and Frank Wilczek received the Nobel prize for physics in 2004. Towards low momentum transfer the coupling strength increases and finally reaches unity. At this energy scales, quarks and gluons are bound in colorless hadrons, this phenomenon is known as *confinement*.

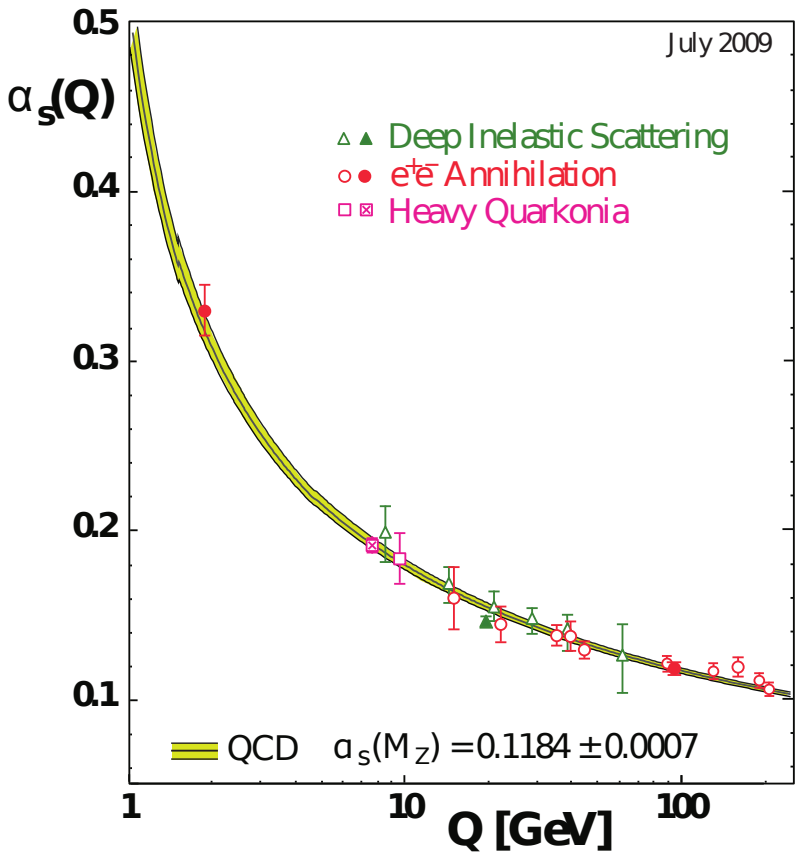

Figure 2.2.: Strong coupling constant α_s as function of momentum transfer Q [Bet2009].

In the regime of high momentum transfer perturbation theory can be applied to calculate interactions with the help of Feynman diagrams. Perturbation theory is an expansion in order of couplings (around the non-interacting theory). As an example the process $e^+e^- \longrightarrow q\bar{q}$ is shown in figure 2.3. For a given process the Feynman diagrams with the smallest number of couplings (vertices) are the dominant contribution, called *Leading Order* (LO), drawn on top. Adding another coupling, e.g. the emission of a gluon by a parton, results in corrections to the dominant diagram, called *Next-to-Leading Order* (NLO), drawn in the middle and in the

bottom. More complicated diagrams lead to further corrections in higher order (NNLO etc.).

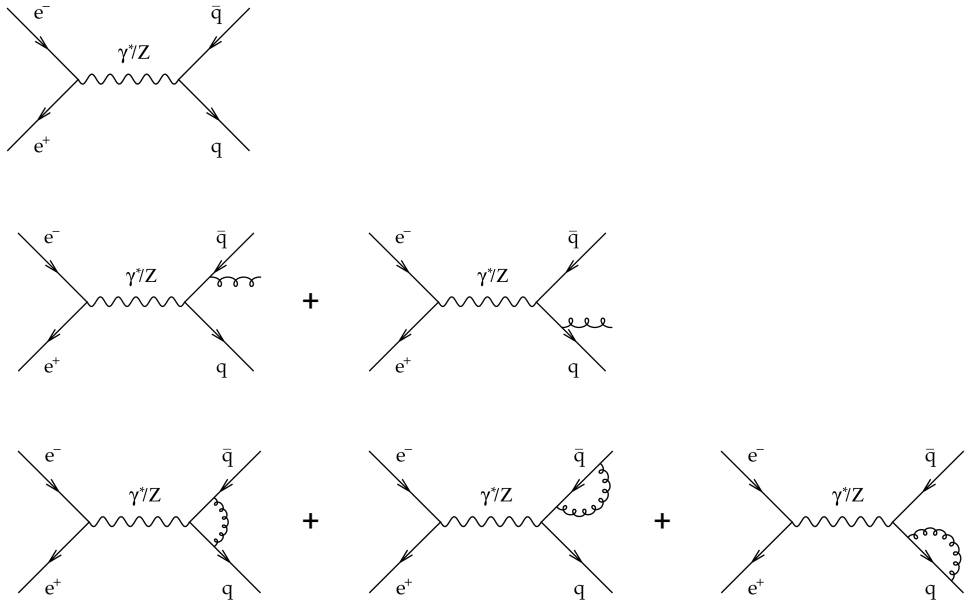

Figure 2.3.: Feynman diagrams contributing to the interaction amplitude of $e^+e^- \longrightarrow q\bar{q}$. The dominant contribution comes from the Leading Order diagram (top). The amplitude needs to be corrected for real (middle) and virtual (bottom) processes.

There are two kinds of corrections: *real* and *virtual*. In the first case the emitted parton fragments and thus leads to measurable particles (figure 2.3 middle). In virtual corrections the emitted parton is re-absorbed (figure 2.3 bottom). Generally, virtual diagrams are ultra-violet (UV) divergent due to the integration over the unbounded momentum in the loop. These divergences can be absorbed in a redefinition of the parameters (coupling etc.) using a procedure called *renormalization*. The subtraction of the divergent terms is performed at an arbitrary renormalization scale μ_R. Often μ_R is chosen as the transferred momentum $\mu_R = Q$ of the process.

The emissions of partons in real as well as in virtual corrections lead to two other divergences: infrared and collinear. Infra-red divergences occur when the momentum of the radiated gluon is close to zero, collinear divergences in case of a very small emission angle. The Kinoshita-Lee-Nauenberg theorem states, that for suitably defined observables every complete order in theory is finite, i.e. the infra-red and collinear divergences cancel between real and virtual corrections [Ell1996].

Cross sections are generally a combination of short-distance (perturbative) and long-distance (non-perturbative) effects. They are calculated based on a very important property of QCD, namely *factorization*. It allows to separate the short-distance from the long-distance physics since they do not influence each other. The latter is encoded in the parton distributions functions (PDF's), describing the partonic structure of the proton, and in the fragmentation functions (FF's), describing how quarks and gluons transform into hadrons. The separation scale between the two regimes is called factorization scale μ_F. Very often the scales for factorization and renormalization are set equal to $\mu = \mu_F = \mu_R$. Partons emitted with a small momentum, less than μ_F, are considered to be part of the hadron and thus included in the PDF's while partons with high momentum can be treated perturbatively. PDF's describe the probability to find a

parton that carries a fraction x of the momentum of the hadron in which it is bound:

$$x = \frac{p_{parton}}{p_{hadron}}. \tag{2.5}$$

As mentioned, PDF's are of non-perturbative nature and therefore they need to be extracted from data using global fits. Although they can not be determined perturbatively, their dependence on the factorization scale μ_F can be calculated in perturbative QCD (pQCD). The change in the quark distribution due to gluon emissions is described by the Altarelli-Parisi equation, the evolution of the gluon distribution is described by the Doksitzer-Gribov-Lipatov-Altarelli-Parisi (DGLAP) equations, see [Ell1996].

Another important effect that cannot be described perturbatively is *hadronization*, i.e. when partons turn into colorless hadrons. Hadronization is a long-distance process with only small momentum transfers, described by fragmentation functions. FF's give the probability of a parton to convert into a hadron taking a fraction z of the parton momentum:

$$z = \frac{p_{particle}}{p_{parton}}. \tag{2.6}$$

As well as PDF's, fragmentation functions are derived from global fits to measured data. This relies on a very important property of both functions: *universality*. PDF's and FF's are the same regardless of the scattering process. As an example and already shown in the introduction, chapter 1, e.g. gluon fragmentation functions are mainly derived from e^+e^- collisions but are as well valid in proton-proton collisions.

The factorization of the particle production cross section $\sigma(P1, P2)$ is sketched in figure 2.4 and given in eq. 2.7 [Ell1996]:

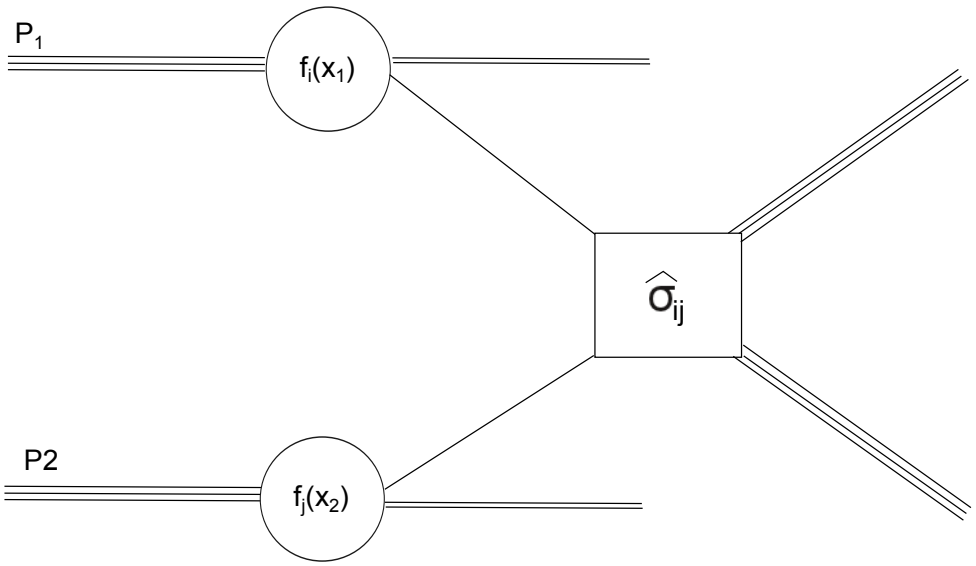

Figure 2.4.: Parton model description of a hard scattering process.

$$\sigma(P_1, P_1) = \sum_{i,j} \int \mathrm{d}x_1 \mathrm{d}x_2 f_i(x_i, \mu^2) f_j(x_j, \mu^2) \hat{\sigma}_{ij}(p_1, p_2, \alpha_s(\mu^2), Q^2/\mu^2) \tag{2.7}$$

The incoming particles P_1 and P_2 are presented by their PDF's (f), the interaction cross section $\hat{\sigma}_{ij}$ describes the probability of the interaction at the partonic level.

As mentioned, in the regime of strong coupling pQCD is not applicable. One method to determine thermodynamical information from such a particle system is provided by Lattice QCD (LQCD) [Wil1974]. In LQCD the system is discretized on a space-time coordinate grid. Quarks and anti-quarks are defined as lattice sites, gluons as links to neighboring sites. To move on the lattice from point A with time t_a and position a to point B with time t_b and position b different paths are possible. The partition function is given by the integral over all paths. The lattice spacing is related to a minimum distance and, thus, a maximum momentum transfer. Therefore, the results for any calculated quantity depend on the spacing. To overcome this dependence the calculations are repeated several times with decreasing spacing. Afterwards the results are extrapolated to zero-spacing. LQCD calculations predict a cross-over from a confined to a deconfined phase at high temperature and low net-baryon potential as it is realized in the Big Bang scenario. Figure 2.5 shows the dependence of the scaled energy density ε/T^4 as a function of the scaled temperature T/T_c for different quark numbers. At $T/T_c = 1$ a sudden rise in the energy density is visible which is interpreted as a phase transition.

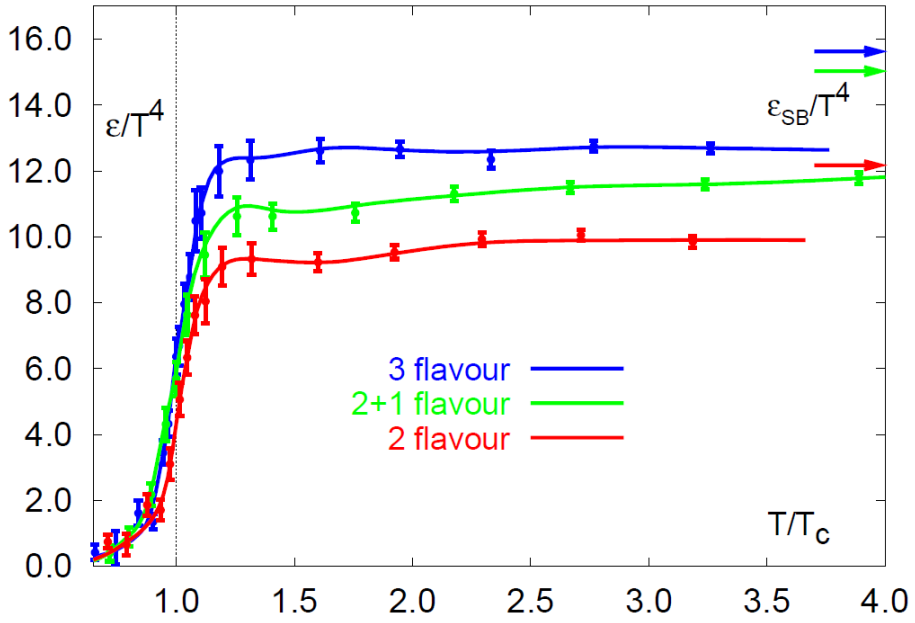

Figure 2.5.: Scaled energy density ε/T^4 as a function of the temperature T calculated with lattice Quantum Chromodynamic [Kar2002]. Three conditions have been calculated: two light quarks (up and down – red), three light quarks (up, down and strange – blue) and two light and one heavier quark (up and down as light, strange as heavy quark – green). The critical temperature T_c is indicated by the vertical line. The colored arrows show the expected ε/T^4 in the Stefan-Boltzmann limit. For an ideal gas holds $\varepsilon \sim C \cdot T^4$. The constant C reflects the number of degrees of freedoms in the system. The sudden rise of ε/T^4 can be interpreted as a rise in this number and thus as a phase transition of the system.

The treatment of the low momentum transfer regime is not only possible with Lattice QCD. Different phenomenological models exist, e.g. bag models [Cho1974]. Inside a bag of finite temperature quarks have very small masses, outside the masses are infinite. The confinement of quarks is a consequence of the balance of the pressure of the moving quarks on the bag and the inwards directed pressure excited by the QCD vacuum. A disturbance of the equilibrium may lead to deconfined matter.

2.3. Event generators

Monte Carlo event generators provide simulations of events as close to reality as possible. The simulations can be used in different ways. They might be used to achieve knowledge in the underlying theory of observed phenomena, to understand production mechanism and the interplay of hard and soft processes. In experiments the generators are necessary to prepare analysis strategies, to estimate experimental efficiencies and acceptance, corrections, backgrounds or unfolding. Additionally, event generators are a tool for detector design studies, where no data exist.

A full event simulation in hadronic collisions as shown in figure 2.6 contains typically the following aspects [Sjo2006]:

- Two beam particles approaching each other. The initial state composition is described in PDFs.
- One parton of each beam particle branches and starts an initial state parton shower.
- From both initial state parton showers one incoming parton enters the hard process. The kind of the scattering process determines the main characteristic to the event. Short-lived resonances like Z^0 or $W^{\pm}$ might be produced and decay to partons.
- Outgoing partons may produce final state parton shower.
- Hadronisation.
- The remaining beam partons (remnants) still may interact and semihard processes may happen between the other partons of the beam particles (*underlying event*).
- The produced hadrons are not stable and decay further.

A difficulty in the event description is given by the underlying event. For a sufficient collision energy the possibility of more than one independent partonic scattering exist. This is beyond the factorization theorem. Models typically involve a perturbatively motivated and soft part [Sjo1987].

In the ALICE experiment two Monte Carlo models are used to simulate proton-proton collisions: PYTHIA 6.4 [Sjo2006] and PhoJet [Eng1995].

PYTHIA PYTHIA is a general purpose event generator which contains theory and models for various physics aspects. The event simulation starts with a hard scattering process. Only Leading Order $2 \longrightarrow 2$ processes are taken into account. For the description of the initial states the CTEQ5L PDF's [CTE2011] are presently used as default. Final state parton showers have a significant influence on jet structures. Hadronization simulations are based on the *LUND String Model* [And2002]. It might well be that the formed hadrons are not stable. Here PYTHIA contains lists of decay properties as there are branching ratio, decay products, life time. In order to reproduce the measured data also diffractive processes based on Regge Field Theory [Col1977] are considered. In PYTHIA many tunable parameters with significant influence on the generated distributions exist, especially for low momentum transfer processes. The connection between low and high momentum transfer regions is given by a minimum momentum transfer $p_{T,cut-off}$. This cut-off is set to 2 GeV/c.

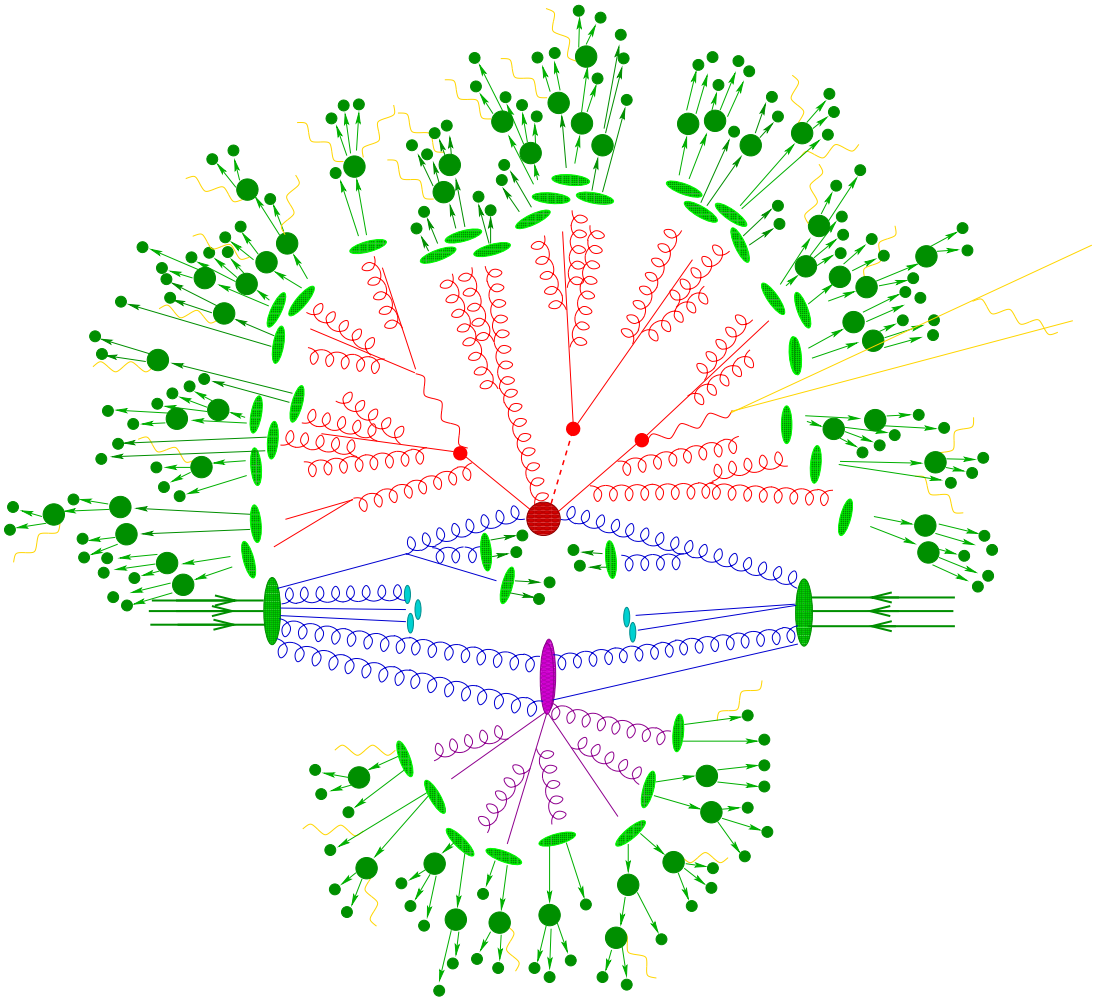

Figure 2.6.: Sketch of a proton-proton collision [Kra2011].

PhoJet PHOJET is based on a combination of perturbative QCD in the hard scattering regime and the Dual Parton Model [Cap1994] in the soft scattering regime together with the extension to photons. Within the Dual Parton Model it is possible to calculate both elastic and inelastic processes within a single event. Initial state parton showers are initiated according to the DGLAP evolution equations, the hadronization is based on the LUND model as in PYTHIA. Hard and soft scattering regimes are separated by a minimum momentum transfer of $p_{T,cut-off} = 3\,\mathrm{GeV/c}$. In contrast to PYTHIA the tune parameters are connected to each other. Thus, the change in one parameter leads to changes of the others. The parameters are connected in a way that the sum of hard and soft cross sections is nearly independent from $p_{T,cut-off}$.

3. Photon and electron interaction with matter

The measurement of neutral pions and η mesons in the branching $\pi^0(\eta) \longrightarrow \gamma\gamma$ presented in this analysis bases on the detection of photons in the Inner Tracking System and the Time Projection Chamber, sections 4.2.2 and 4.2.3. Therefore, a short introduction is given into photon and electron (positron) interactions with matter.

3.1. Photon interaction with matter

Photons are the massless electromagnetic field quanta, electrically neutral and with a constant velocity in vacuum. While passing through material, photons interact mainly in three ways, namely *photoelectric effect*, *Compton scattering* and *pair creation*. The cross sections depend on the energy of the traversing photon and the characteristics of the traversed material. In these mechanisms the photon transfers a fraction or its total energy to an electron (positron). The photon cross sections are shown in figure 3.1 for two different materials, carbon (^6C) as a light material (left) and lead (^{82}Pb) as a heavy material (right).

The photoelectric effect $\sigma_{p.e.}$ (blue dashed-dotted line) is the dominant process at low energies up to $\sim 100\,\text{keV}$. A bound electron absorbs a photon and is ejected from the atom. The electron receives the entire photon energy $E_\gamma = h\nu$ of the electron in the atom. Its kinetic energy is:

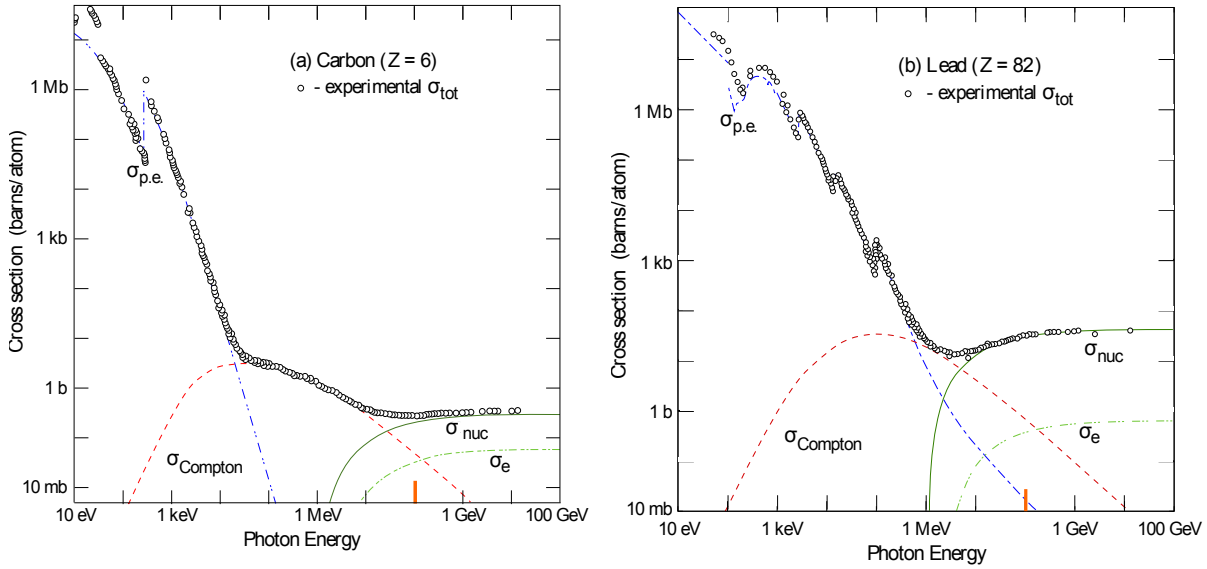

Figure 3.1.: Photon cross sections as a function of energy in carbon (left) and lead (right). Shown are the measured total cross section and the contributions of

$\sigma_{p.e.}$	=	Photoelectric effect (blue dashed-dotted line)
$\sigma_{Compton}$	=	Compton scattering of an electron (red dashed line)
σ_{nuc}	=	Pair production in nuclear field (green solid line)
σ_e	=	Pair production in electron field (green dashed-dotted line)

The photon reconstruction in the analysis presented in this thesis starts at about 100 MeV (marked as vertical line in orange). Taken and modified from [Nak2010].

$$E_{\text{electron, kin.}} = E_\gamma - E_b. \tag{3.1}$$

where E_b is the binding energy of the electron in its shell in the atom. The cross section $\sigma_{p.e.}$ exhibits absorption edges. These discontinuities appear at photon energies that match an electron shell. They are clearly visible in both materials in figure 3.1. For each K-shell electron the cross section is given by:

$$\sigma_{p.e.} \sim Z^5 \left[\frac{m_e c^2}{E_\gamma}\right]^n \qquad n = \frac{7}{2} \qquad \text{[Wil1997]} \tag{3.2}$$

where Z is the atomic number, m_e the electron mass and c the speed of light. For very high photon energies $E_\gamma \gg m_e c^2$ the cross section can be approximated by

$$\sigma_{p.e.} \sim \frac{1}{E_\gamma} \qquad \text{[Wil1997].} \tag{3.3}$$

The Feynman diagram for the photoelectric effect is shown in figure 3.2 (left).

In the intermediate photon energy range from several 100 keV to few MeV Compton scattering becomes dominant, presented by the red dashed line in figure 3.1. The incident photon scatters off a quasi-free electron of the detector material and is deflected by an angle θ with respect to its original direction. Part of its energy is transferred to the electron. The energy of the scattered photon $E_\gamma^\star$ varies with the deflecting angle:

$$\frac{1}{E_\gamma^\star} = \frac{E_\gamma}{1 + \frac{E_\gamma}{m_e c^2}}(1 - \cos\theta) \qquad \text{[Sch1995].} \tag{3.4}$$

For a photon with an energy $E_\gamma \gg m_e c^2$ the cross section for Compton scattering $\sigma_{Compton}$ follows:

$$\sigma_{Compton} \sim \frac{\ln E_\gamma}{E_\gamma} \qquad \text{[Wil1997].} \tag{3.5}$$

The Feynman diagram for Compton scattering is given in figure 3.2 (right).

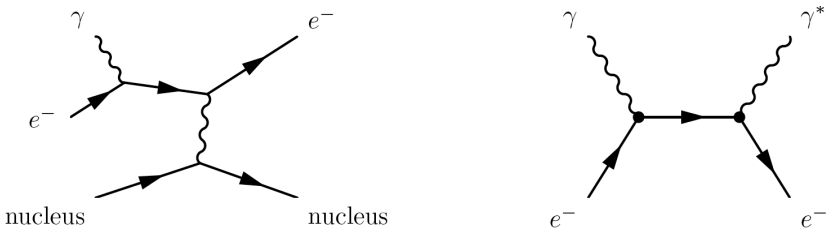

Figure 3.2.: Leading order Feynman diagrams for Photoelectric effect (left) and Compton scattering (right).

The most important process for the analysis presented in this thesis is pair creation. The corresponding Feynman diagrams are given in figure 3.3. When a photon with an energy $E > 2m_e c^2 \approx 1.02\,\text{MeV}$ (m_e is electron mass) enters the Coulomb field of a nucleus, it can convert into an electron-positron pair. Energy and momentum conservation require the nucleus to participate in the interaction. The momentum transfer to the nucleus decreases with increasing photon energy. With increasing photon energy the screening of the nucleus by the surrounding

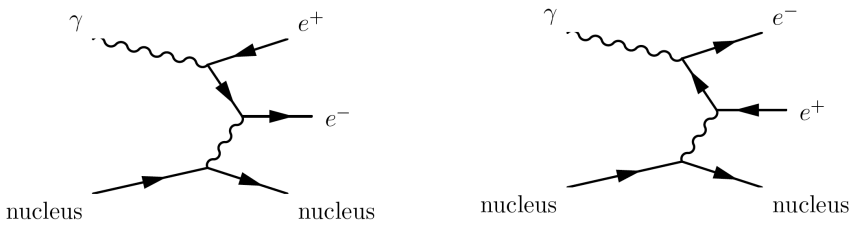

Figure 3.3.: Feynman diagrams for pair creation.

electrons has to be taken into account. Therefore, the cross section σ_{nuc} rises and then reaches a plateau at about 1 GeV. In the plateau σ_{nuc} only depends on the material and is given by:

$$\sigma_{nuc} = \frac{28}{9}\frac{Z^2\alpha^3(\hbar c)^2}{(m_e c^2)^2}\left(\ln\frac{183}{Z^{1/3}} - \frac{2}{7}\right) \qquad \text{[Wil1997]} \tag{3.6}$$

where α is the fine structure constant and $\hbar$ the reduced Planck constant. The mean free path X_{nuc} is given by:

$$X_{nuc} = \frac{1}{n\sigma_{nuc}} = \frac{28}{9}\frac{nZ^2\alpha^3(\hbar c)^2}{(m_e c^2)^2}\left(\ln\frac{183}{Z^{1/3}} - \frac{2}{7}\right)^{-1} \qquad \text{[Wil1997]} \tag{3.7}$$

with n as electron density. Using

$$X_0 = \frac{4nZ^2\alpha^3(\hbar c)^2}{(m_e c^2)^2}\left[\ln\frac{183}{Z^{1/3}}\right]^{-1} \qquad \text{[Wil1997]} \tag{3.8}$$

the mean free path X_{nuc} can be expressed as a function of the radiation length X_0:

$$X_{nuc} \simeq \frac{9}{7}X_0 \qquad \text{[Wil1997]}. \tag{3.9}$$

The radiation length is a characteristic of the material and is related to the energy loss of highly energetic, charged or ionizing particles in the material. In a mixture of materials X_0 is given by

$$\frac{1}{X_0} = \sum_{i=1}^{n}\omega_i\frac{1}{X_{0i}} \qquad \text{[Nak2010]} \tag{3.10}$$

where ω_i and X_{0i} correspond to proportion of the weight and radiation length of the i^{th} material in the material mixture. In the high-energy limit the probability that an electron-positron pair is created within a distance X, also called *conversion probability*, is given by

$$P = 1 - \exp\left(-\frac{7}{9}\frac{X}{X_0}\right) \qquad \text{[Nak2010]}. \tag{3.11}$$

This is shown for different materials in figure 3.4. The strong rise of the conversion probability at low photon energies and the plateau above 1 GeV reflect the behavior of the cross section σ_{nuc} (figure 3.1). Also the dependence on the atomic number Z can be seen. For lead with $Z = 82$ the rise in the photon conversion probability starts already at the energy of about $2 - 5$ MeV and the plateau is reached for $E_\gamma \approx 100$ MeV while for a light material, e.g. carbon ($Z = 6$) the rise starts later, between $5 - 10$ MeV, and it is weaker as for lead. Moreover, the plateau is reached at higher photon energies of the order of 1 GeV.

The dependence of the photon conversion probability on the atomic number is used in experimental setups. Electromagnetic calorimeter deal with electromagnetic showers. Photons convert

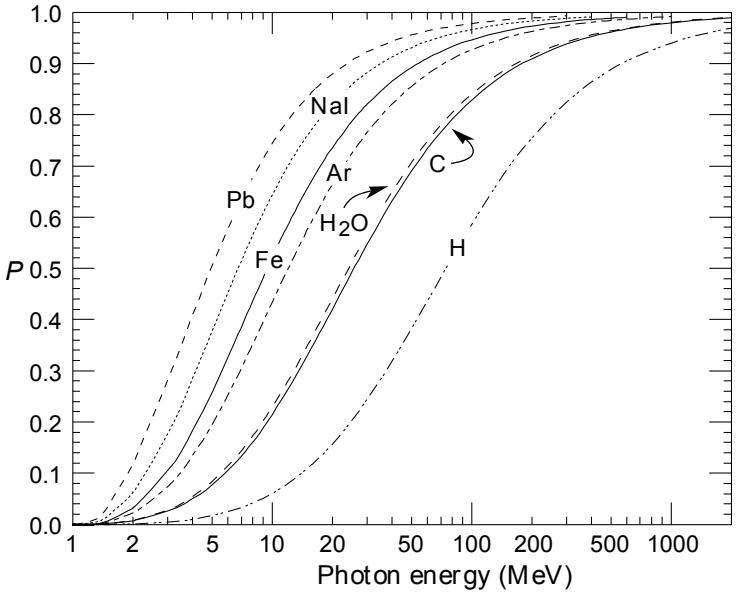

Figure 3.4.: Photon conversion probability after traveling a distance about the attenuation length X_{nuc}, shown for different materials as a function of the photon energy [Nak2010].

Material	A	X_0 (g/cm^2)	ρ (g/cm^3)
Ne	20.2	28.94	0.0008073
CO_2		36.2	0.001977
N_2	14	37.99	0.001203
TPC gas			0.0009374151

Table 3.1.: Atomic mass, radiation length and density of the TPC gas components [Nak2010].

in the material. The created electron-positron pairs produce subsequently new photons due to bremsstrahlung processes, see section 3.2. This results in an electromagnetic shower. Therefore, such calorimeters are made of materials with a high atomic numbers and, thus, short radiation lengths. As an example, the Photon Spectrometer in the ALICE experiment, section 4.2.5, is made of lead-tungstate ($PbWO_4$) crystals with a radiation length $X_0 = 0.89\,\text{cm}$ [Ale2005]. On the other hand, for the Inner Tracking System and the Time Projection Chamber materials with a small atomic number are used to keep photon conversions and electron-positron bremsstrahlung at a minimum. The Inner Tracking System mainly consists of silicon detectors ^{14}Si with $X_0 = 9.36\,\text{cm}$. The gas in the Time Projection Chamber is composed of neon ^{10}Ne, carbondioxid $C0_2$ and nitrogen $^7N_2$ (85.7 : 9.5 : 4.8), see section 4.2. Using eq. 3.10 and the characteristics of the different gas components, table 3.1, the radiation length of the gas mixture amounts to 32522.03 cm.

In detector simulations such as GEANT the conversion probability is simply given by the ratio of converted photons to generated photons:

$$P = \frac{\text{converted photons}}{\text{all generated photons}}. \tag{3.12}$$

In the analysis presented in this thesis neutral pions and η mesons are measured in their decay channel $\pi^0(\eta) \longrightarrow \gamma\gamma$ via the reconstruction of the electron-positron pairs created in photon

conversions $\gamma + X \longrightarrow e^+e^- + X$. It is of key importance that the implementation of the detector material in simulations in terms of geometry and chemical composition is as close as possible to reality since otherwise the results of simulations may not correspond to real data. This analysis method allows a direct and precise measurement of the detector material, which can be used to tune and to cross check the detector simulation.

3.2. Electron (positron) interaction with matter

When an electron (positron) traverses material, it looses energy mainly due to *ionization* and *bremsstrahlung*, depending on its energy. At low energies the main mechanism is ionization, although *Møller scattering* (electron-electron scattering), *Bhabba scattering* (electron-positron scattering) and *electron-positron annihilation* (for positrons) contribute. The fractional energy loss per radiation length, normalized to the energy of the electron (positron), is shown in figure 3.5. The normalized energy loss due to ionization decreases logarithmically while it is increasing linearly for bremsstrahlung. Above few tenths of MeV bremsstrahlung gives the main contribution.

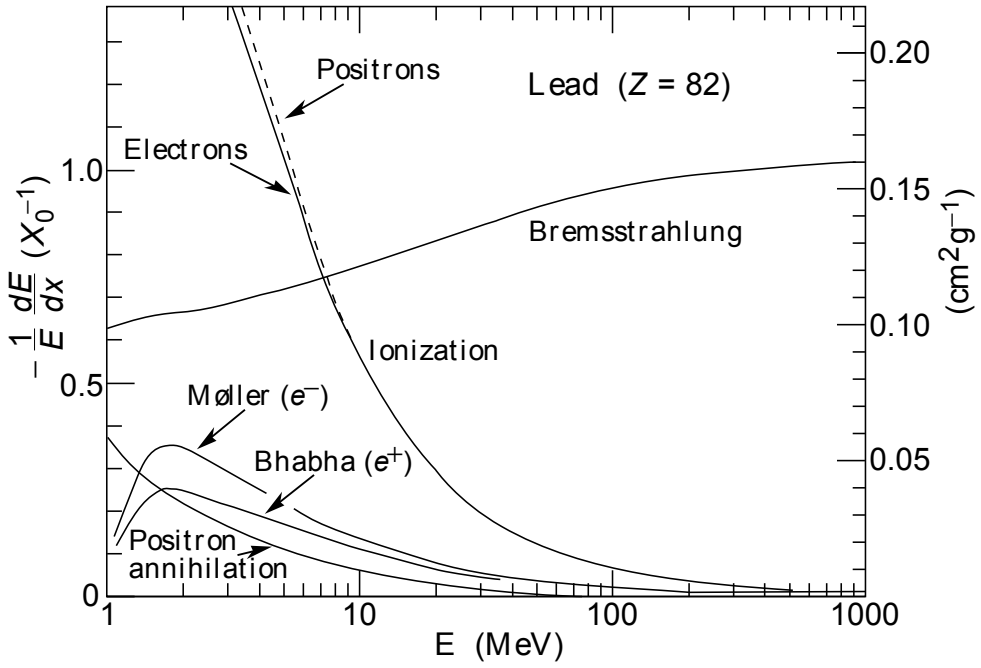

Figure 3.5.: Normalized fractional energy loss per radiation length in lead as a function of electron-positron energy [Nak2010].

The specific energy loss of electrons due to ionization differs from heavy charged particles due to kinematics and spin. Moreover, the incident electrons are indistinguishable from electrons in the material. The specific energy loss of electrons is described by the modified Bethe-Bloch formula:

$$-\frac{\mathrm{d}E}{\mathrm{d}x} = 4\pi N_A r_e^2 m_e c^2 \frac{Z}{A}\frac{1}{\beta^2}\left[\ln\frac{2\gamma m_e c^2}{2I} - \beta^2 - \frac{\delta^\star}{2}\right] \qquad \text{[Gru1996]} \tag{3.13}$$

where N_A is the Avogadro constant, A the number of protons in the nucleus, $\beta = v/c$ the velocity of the electron and I the mean ionization potential of the medium ($I \approx 16Z^{0.9}\,\mathrm{eV}$ for $Z > 1$ [Gru1996]), $\delta^\star$ describes how much the electric field of the incident electron is screened by the charge density of the atom electrons. Besides the dependence on Z the energy loss

only depends on the velocity of the electron. For small β it is proportional to $1/\beta$. After a minimum the energy loss rises logarithmically. This is shown for electrons and muons in figure 3.6, both measured in water. The position of the minimum is around 1 MeV for electrons and around 100 MeV for muons. Additionally, the energy loss due to bremsstrahlung is shown for the electron. The dropping energy loss in the beginning is caused by the increasing particle momentum, where the particle has less and less time to interact, while for higher momentum the rise originates from the contraction of the electric field of the incident electron in the transverse direction. This affects atoms in the medium that are further away from the incident electron.

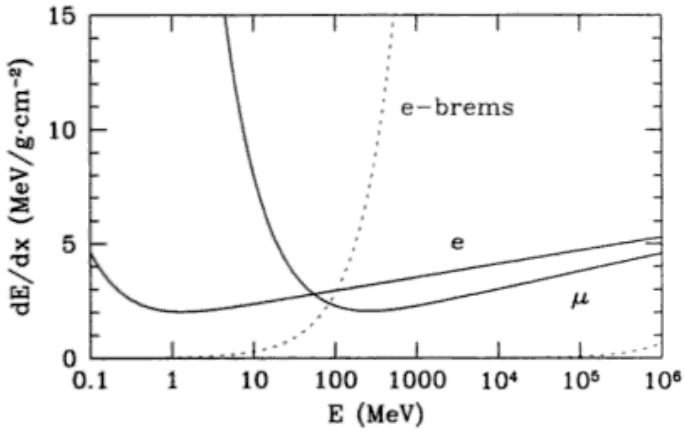

Figure 3.6.: Energy loss due to ionization as a function of their energy for electrons and muons in water [Fuk2003].

As mentioned, for energies above a few tenths of MeV electrons (positrons) loose their energy mainly due to bremsstrahlung. Due to their small mass they get decelerated in the field of the nuclei and radiate. This energy loss is given by

$$-\frac{\mathrm{d}E}{\mathrm{d}x} = 4\alpha N_A \frac{Z^2}{A} r_e^2 E \ln\frac{183}{Z^{1/3}} = \frac{E}{X_0} \qquad \text{[Gru1996].} \tag{3.14}$$

The energy loss rises linearly with the energy. For electrons the radiation length X_0 describes the mean distance over which the energy is reduced by a factor $1/e$.

The critical energy for the transition from ionization to bremsstrahlung is

$$E_c = \frac{610\,\mathrm{MeV}}{Z \cdot 1.24}\ \text{(solids and liquids)},\ E_c = \frac{710\,\mathrm{MeV}}{Z \cdot 0.92}\ \text{(gases)} \qquad \text{[Nak2010].} \tag{3.15}$$

Besides specific energy loss due to ionization and bremsstrahlung charged particles undergo two other processes can be used for the identification of the species. The first one is transition radiation, emitted by charged particles crossing the boundary surface of two media with different dielectric constants. The combination of an energy measurement with the measurement of the transition radiation therefore allows to determine the mass and thus the identity of the particle. This is used by the ALICE TRD. Another technique for particle identification is Cherenkov radiation. It is emitted when a charged particle traverses a medium with a velocity higher than the speed of light in that medium. Cherenkov radiation is emitted under an angle of $\cos(\theta) = 1/n\beta$, which depends on the particle velocity. Combined with a measurement of the momentum this yields the particle mass. This process is used in the ALICE HMPID.

4. Experimental setup

4.1. The Large Hadron Collider

The Large Hadron Collider [Eva2008] at CERN (European Organization for Nuclear Research) near Geneva, Switzerland, is at present the world's largest and most powerful man-made particle accelerator. The research at the LHC is expected to provide new insights into the structure of matter. In particular, it will help to extend the knowledge about the generation of mass through spontaneous symmetry breaking in electroweak and strong interaction. Assuming a mass range of $115-145\,\mathrm{GeV/c^2}$ for the Higgs boson the LHC is predestined to prove or disprove the existence of this last undiscovered particle of the Standard Model of particle physics. Furthermore, there are well-founded reasons, both conceptual and phenomenological, to believe that new physics beyond the Standard Model exist. Conceptual reasons include the wish for the unification of all fundamental forces and the question why there are three quark- and lepton families. A strong phenomenological reason is the existence of dark matter in the universe which can not be explained by Standard Model particles [Gar2011]. The research at the LHC might answer these questions with the investigation of fundamental theories beyond the Standard Model, e.g. Supersymmetry (SUSY) or extra dimensions. Another important goal for the LHC is to study the hot and dense medium created in heavy-ion collisions and to extract signatures of the quark-gluon plasma.

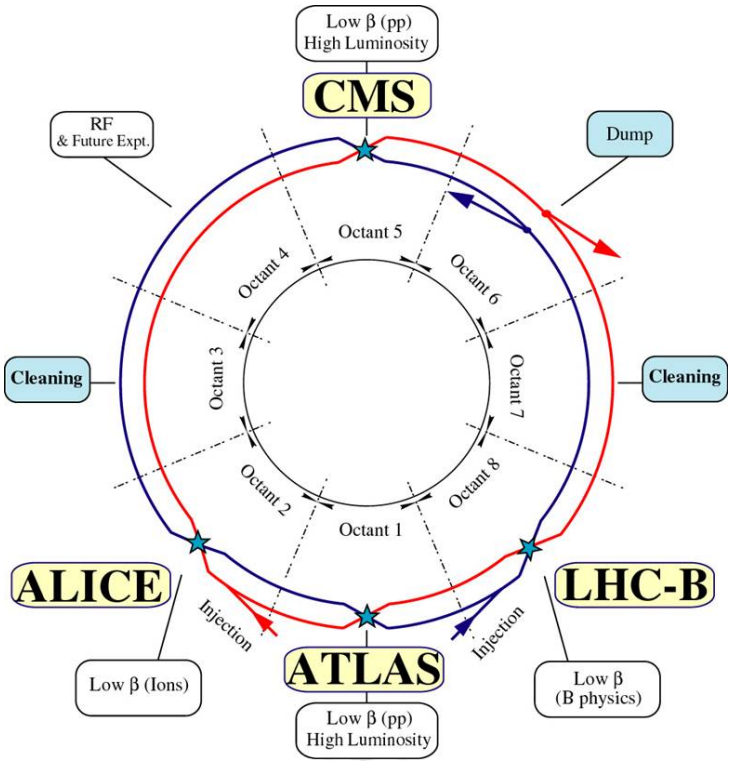

Figure 4.1.: Schematic overview of the LHC accelerator complex [Eva2008].

There are four major experiments at the LHC. ATLAS, A Toroidal LHC ApparatuS, is one of the two general purpose detectors at the LHC. It consists of an inner silicon detector system for tracking and momentum measurements surrounded by electromagnetic and hadronic calorimeters and a muon spectrometer. The main research goals for the ATLAS experiment are the discovery of the Higgs boson, extra dimensions and new insights to dark matter. The second general purpose detector at the LHC accelerator is CMS, the Compact Muon Solenoid. Like ATLAS it hunts for the Higgs boson and looks for clues of the nature of dark matter, but with complementary techniques. This provides the possibility to cross-check the research results. Both collaborations also have heavy-ion research programs. The next big experiment is the LHCb, the LHC beauty experiment. In the Big Bang equal amounts of matter and antimatter were created, while today matter largely prevails. This as well as flavour physics are investigated by LHCb. The fourth big experiment is ALICE, A Large Hadron Collider Experiment. ALICE is the dedicated experiment at LHC to investigate heavy-ion collisions. It is designed to identify and characterize the quark-gluon plasma. Of course, also proton-proton collisions are investigated since they provide reference for heavy-ion data and are interesting in their own right. A description of ALICE is given in the next section.

The LHC is installed in the tunnel of the former Large Electron Positron Collider (LEP) measuring 26.7 km in circumference. An overview is shown in figure 4.1. It is divided into eight parts. Both high luminosity experiments are located diametrically to each other in octant 1 (ATLAS) and octant 5 (CMS). In octant 2 and 8 the ALICE experiment and the LHCb experiment are located. In both sectors also the beam injection points are located. The beams only cross at the locations for these four experiments.

The LHC is designed to collide protons at a center-of-mass energy upto $\sqrt{s} = 14\,\text{TeV}$ or heavy ions up to $\sqrt{s_{NN}} = 5.5\,\text{TeV}$. The design luminosity is $\mathcal{L} = 10^{34}\,\text{cm}^{-2}\text{s}^{-1}$ for protons and $\mathcal{L} = 10^{27}\,\text{cm}^{-2}\text{s}^{-1}$ for heavy ions. Since at the LHC equally charged beams collide, both beams need to be separated in two rings. At the four experiments both beams share approximately 130 m of common beam pipe. While the particle acceleration is achieved by high frequency electrical fields the bending of the beams in the ring is provided by a magnetic field of 8.33 T. This field is created by a total of 1232 superconducting dipole magnets. Additionally, 392 quadrupole magnets keep the beams focused. The number of bunches per beam is upto 2808, each with nominal 1.15×10^{11} protons and a minimal bunch spacing of 25 ns [Eva2008]. The high luminosity leads to pile-up, e.g. there is on average more than one (namely 134 in total) proton-proton collision per bunch crossing.

To reach the LHC energies the particles are accelerated in steps with several pre-accelerators as shown in figure 4.2. In the Linear Particle Accelerator LINAC2 protons with an average energy of 50 MeV are generated. Next, the Proton Synchrotron Booster (PBS) boost them to 1.4 GeV. Afterwards the protons are fed to the Proton Synchrotron (PS) and further accelerated to 26 GeV. In the next step the nucleons are accelerated in the Super Proton Synchrotron (SPS) to an the energy of 450 GeV. The final beam energy of 7 TeV is achieved in the LHC ring itself. The pre-acceleration for lead ions is slightly different in the first two steps from the procedure for protons. The lead ions are accelerated to an energy of 4.2 MeV per nucleon by the Linear Accelerator LINAC3 and next injected into an ion accumulator, which stores and cools the ions. Then they are fed into the Proton Synchrotron, from this point on the handling is the same as for protons.

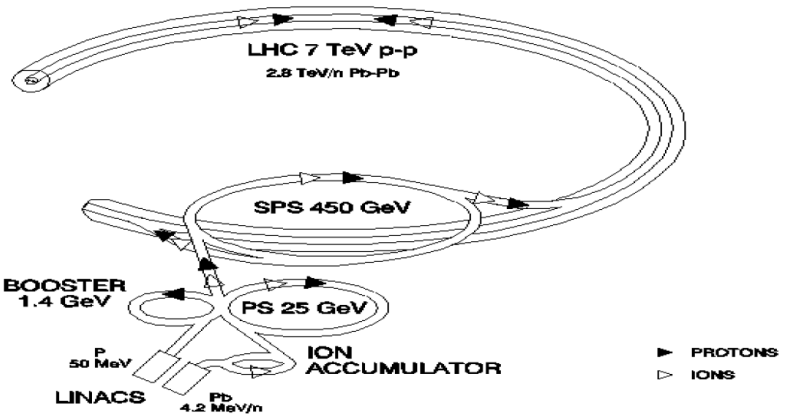

Figure 4.2.: LHC injector complex [Eva2008].

4.2. A Large Ion Collider Experiment

The ALICE experiment [Aam2008] has been designed to investigate strongly interacting matter and the quark-gluon plasma in nucleus-nucleus collisions at the CERN LHC. The physics program covers a broad range of observables. Parton kinematics and energy in the plasma phase can be studied via heavy flavor production and jet fragmentation while elliptic flow probes properties like shear viscosity and the equation of state. Information about the temperature in the quark-gluon plasma can be derived from prompt photons. Quarkonia allow to study deconfinement and parton recombination. Using resonances chiral symmetry restoration in the plasma can be investigated. Thermodynamical properties and the hydrodynamical evolution of the matter can be investigated by looking at particle ratios and transverse momentum spectra. The space-time evolution of the collision can be observed by particle interferometry. Of course, not only nucleus-nucleus collisions are investigated. Also proton-proton and proton-nucleus collisions at different center-of-mass energies are important since they provide reference data for heavy ion collisions.

An important design constraint has been the expected particle multiplicity density $\mathrm{d}N/\mathrm{d}\eta$ (where η is the pseudo-rapidity $\eta = -\ln[\tan(\theta/2)]$) in heavy-collisions. This can be three orders of magnitude larger than in proton-proton collisions at the same energy and up to a factor of 2-5 more than measured at the RHIC. Early estimates varied in a range of $\mathrm{d}N/\mathrm{d}\eta = 2000 - 8000$ for central Pb-Pb collisions. More recent estimations from RHIC results led to a much lower particle multiplicity estimate of $\mathrm{d}N/\mathrm{d}\eta = 1500 - 4000$. These values have been used for the optimization of the detector. The actual measurement of the particle multiplicity in most central Pb-Pb collisions reaches about 1600 at mid-rapidity ($\eta = 0$) for a center-of-mass energy of $\sqrt{s_{NN}} = 2.76\,\mathrm{TeV}$ [Aam2011] and is thus much lower than the first expectations.

The broad range of physics observables also requires a broad coverage in the momentum measurement, from tens of MeV/c up to about 100 GeV/c. To ensure good momentum resolution the detector material is minimized to reduced multiple scattering at low transverse momentum (momentum in the xy-plane $p_T = \sqrt{p_x^2 + p_y^2}$). A large tracking lever arm of about 3.5 m ensures a good resolution at high p_T. Particle identification over the full momentum range is of key importance since many of the physics observables require particle masses or flavors. Within the ALICE experiment various quantities are used for particle identification, e.g. specific energy loss $\mathrm{d}E/\mathrm{d}x$, time-of-flight, transition and Cherenkov radiation, electromagnetic calorimetry and topological decay reconstruction.

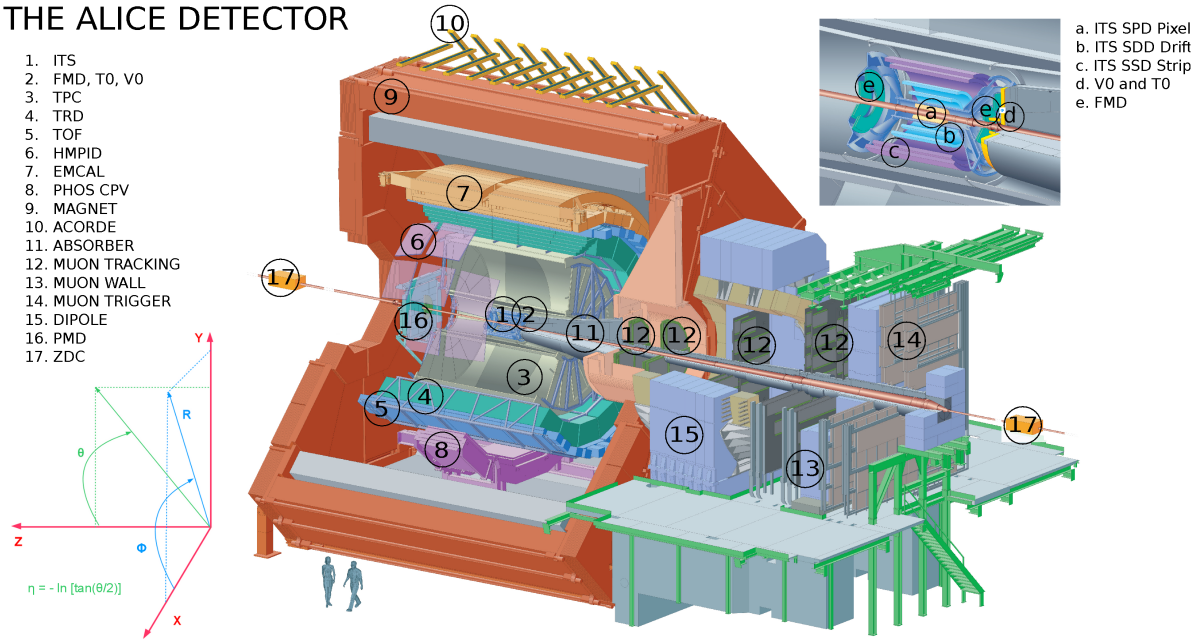

Figure 4.3.: Layout and coordinate system of the ALICE experiment [Aam2008].

4.2.1. Detector layout

In order to fulfill the physics program the ALICE detector is built as a complex system of sub-detectors. A schematic overview including the coordinate system is shown in figure 4.3. The coordinate system is defined as follows: The X-axis is perpendicular to the beam direction and pointing to the center of the accelerator ring. The Y-axis is perpendicular to the X-axis and perpendicular to the beam direction, pointing upwards. The Z-axis corresponds to the beam direction, the negative side points to the muon spectrometer. The positive Z-direction is also called A-side, the negative C-side. The azimuthal angle ϕ is defined in the XY-plane with the positive X-direction defining $\phi = 0$ and the positive Y-direction at $\phi = \pi/2$. The polar angle θ increases from the Z-axis ($\theta = 0$) towards the XY-plane ($\theta = \pi/2$).

The sub-detectors are mainly arranged in concentric layers around the beam pipe. The central part covers the pseudo-rapidity range of $|\eta| < 0.9$. It consists of various detectors to measure hadrons, electrons and photons. These detectors are (following the numbering in figure 4.3) the Inner Tracking System (ITS) (1), built as a six-layer silicon detector, the large-volume Time Projection Chamber (TPC) (3), the Transition Radiation Detector (TRD) (4), the Time-Of-Flight detector (TOF) (5), a Ring Imaging Cherenkov detector (High Momentum Particle Identification – HMPID) (6) and two electromagnetic calorimeters (ElectroMagnetic CALorimeter – EMCAL and PHOton Spectrometer (PHOS)) (7 and 8). The central systems are embedded in a large solenoid magnet L3 (9). On top of the magnet the ALICE Cosmic Ray Detector (ACORDE) (10) is installed. In negative Z direction, at large negative pseudo-rapidity ($-2.5 < \eta < -4.0$) the forward muon arm is located, an arrangement of hadron absorbers, a dipole magnet, tracking and triggering chambers (11-15). The ALICE detector system is completed by several smaller sub-detectors at large pseudo-rapidity, namely the Forward Multiplicity Detector (FMD), V0, T0 (both (2)), the Zero-Degree Calorimeter (ZDC) (17) and the Photon Multiplicity Detector (PMD) (16). These detectors are designed for triggering and global event characterization. Most of the detectors, except for HMPID, PHOS, EMCAL, ACORDE and ZDC, cover the full

azimuthal range of 2π.

The inset on the top right of figure 4.3 shows a zoom into the innermost detector part. Here (a)-(c) point to the different components of the ITS, the Silicon Pixel Detector (SPD) (a), the Silicon Drift Detectors (SDD) and the Silicon Strip Detectors (c). Additionally, the positions of the V0, T0 (both (d)) and FMD (e) are shown in more detail.

The Inner Tracking System, the Time Projection Chamber and the V0 detector are particularly important for the presented analysis. Therefore they are described in more detail in the following sections. Additionally, a short overview of the electromagnetic calorimeters PHOS and EMCAL is given.

4.2.2. The Inner Tracking System

The main tasks of the ITS are the reconstruction of collision (=primary) vertices with a resolution better than $100\,\mu$m [Car2004] as well as secondary vertices from heavy-flavor and strange particle decays. It is also used for tracking and particle identification in the transverse momentum regime below $200\,\mathrm{MeV/c}$ [Car2004]. Furthermore, it improves the momentum and angular resolution for high-p_T-particles that traverse the Time Projection Chamber.

The ITS has a cylindrical shape and consists of six layers of silicon detectors at radii of $3.9\,, 7.6\,, 15.0\,, 23.9\,, 38.0$ and $43.0\,$cm. The coverage in pseudo-rapidity depends on the layer. It is $|\eta| \leq 2$ for the innermost and $|\eta| \leq 1.4$ for the second layer. Both following layer cover $|\eta| \leq 0.9$ while the last two reach $|\eta| \leq 0.97$. Number, position and segmentation of the layers are optimized for efficient track finding and high resolution. The innermost radius is as small as allowed by the radius of the beam pipe ($r_{BP} = 2.94\,$cm) while the radius of the outermost layer was determined to match tracks with those from the TPC. In central heavy-ion collisions the innermost layer has to face a very high particle density of 50 particles per cm^2 whereas the track density for the outer two layers is below one particle per cm^2. Therefore the two innermost layers are Silicon Pixel Detectors (SPD) with a high spacial resolution, followed by two layers of Silicon Drift Detectors (SDD). The outermost layers are equipped with Silicon Strip Detectors (SSD). The four outer layers have an analogue readout and can be used for particle identification via specific energy loss in the non-relativistic region. This makes it possible to use the ITS as a stand-alone low transverse momentum spectrometer. The main characteristics of the ALICE Inner Tracking System are summarized in table 4.1.

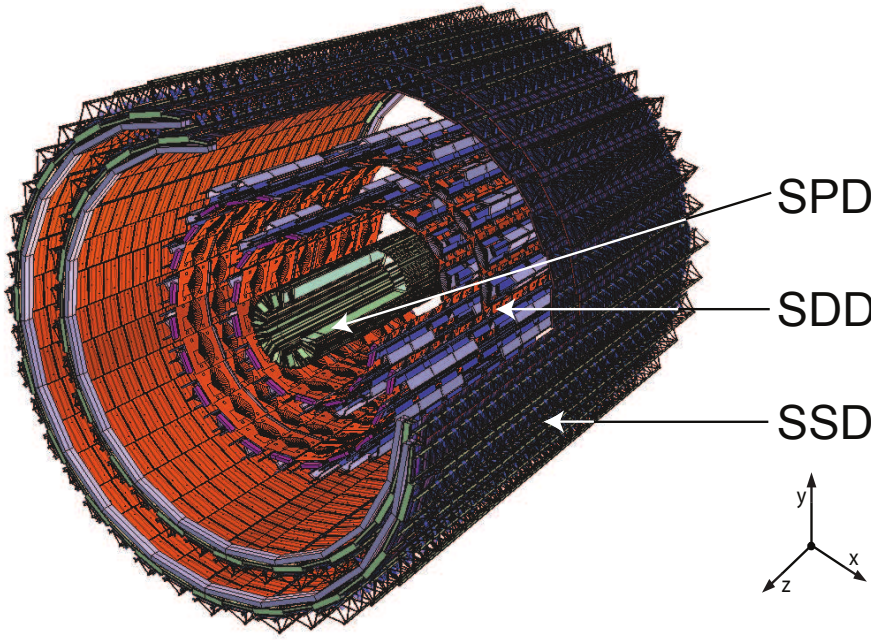

Figure 4.4.: Illustration of Inner Tracking System. Its single layers as well as the support structure are visible. Detailed numbers to all sub-detectors are summarized in table 4.1 [Aam2010].

Detector	SPD	SDD	SSD
Spatial precision $r\phi$ (μm)	12	35	20
Spatial precision Z (μm)	100	25	830
Two track resolution $r\phi$ (μm)	100	200	300
Two track resolution Z (μm)	850	600	2400
Radial position inner layer (cm)	3.9	15.0	38.0
Radial position outer layer (cm)	7.6	23.9	43.0
Length inner layer (cm)	28.2	44.4	86.2
Length outer layer (cm)	28.2	59.4	97.6
Coverage in η inner layer	± 2.0	± 0.9	± 0.97
Coverage in η outer layer	± 1.4	± 0.9	± 0.97
Coverage in ϕ both layer	$0° - 360°$	$0° - 360°$	$0° - 360°$
Total area (m^2)	0.2	1.31	4.77
Modules	240	260	1698
Readout channels per module	40960	2×256	2×768
Cell size (μm^2)	50×425	202×294	95×40000
Active area (mm^2)	12.8×69.6	72.5×75.3	73×40
Max. occupancy for central Pb–Pb inner layer (%)	2.1	2.5	4.0
Max. occupancy for central Pb–Pb outer layer (%)	0.6	1.0	3.3

Table 4.1.: Main characteristics for the ITS sub-detectors [Aam2008].

The resolution of momentum and impact parameter at low transverse momentum is dominated by multiple scattering effects. Therefore the active detector material (so-called *material budget*) has been kept to a minimum. It amounts to 7.16 % of a radiation length X_0 excluding air. The

specifications for each layer in the ITS are summarized in table 4.2.

The relative momentum resolution achieved with the Inner Tracking System is better than 2 % for charged pions within the transverse-momentum range of 100 MeV/c and 3 GeV/c [Aam2008]. In stand-alone performances the resolution in the specific energy loss reaches $\sigma_{\mathrm{d}E/\mathrm{d}x} \approx 10-15\,\%$ [Kal2011].

Detector	SPD	SDD	SSD
Inner layer	1.14	1.13	0.83
Outer layer	1.14	1.26	0.86
Thermal shield / support	0.52	0.25	0.53

Table 4.2.: Material budget of the ITS sub-detectors at $\eta = 0$, given in percentage of radiation length X_0 [Aam2008].

4.2.3. Time Projection Chamber

The Time Projection Chamber is the main device for charged-particle tracking and particle identification in the central part of the ALICE detector. Its coverage in pseudo-rapidity is $|\eta| \leq 0.9$ for full radial track length and $|\eta| \leq 1.5$ for 1/3 radial track length, both with full azimuthal angle except from dead zones in-between the readout chambers. A schematic overview of the TPC is shown in figure 4.5.

The TPC is a cylindrical gaseous detector with a gas mixture of Ne, CO_2 and N_2 (85.7 : 9.5 : 4.8) [Alm2010]. The gas mixture is optimized for low radiation length and thus low multiple scattering, low electron diffusion and high drift speed. The active volume of the TPC is about $90\,\mathrm{m}^3$, given by a radial size of $84.8\,\mathrm{cm} < r < 246.6\,\mathrm{cm}$ and a length of 5 m. The inner radius is determined by the maximum acceptable hit density while the outer one is given by the required track length to achieve a resolution in the specific energy loss of better than $5-7\,\%$.

The field cage of the TPC provides a uniform electrostatic field in the gas volume in order to transport ionization electrons from their origin to the readout chambers at the endplates. The high-voltage electrode is installed in the center of the field cage at $z = 0$. A high voltage of 100 kV is applied resulting in an electron drift time of about 90 μs. A total of 72 rods supports the field cage strips for the inner and outer vessels.

For the signal readout multi-wire proportional chambers at the endplates of the field cage are used. The TPC readout is divided into 18 sections on each side, each section covering 20 ° in azimuthal angle. Due to the radial dependence of the track density the sections are again divided into two readout chambers (ROC). Those are once more split into small pads with different sizes: $4 \times 7.5\,\mathrm{mm}^2$ for the inner chambers and $6 \times 10\,\mathrm{mm}^2$ and $6 \times 15\,\mathrm{mm}^2$ for the outer chambers. This ensures a low occupancy and the necessary resolution for position and specific energy loss. With the use of the drift time a 3-dimensional track reconstruction is possible.

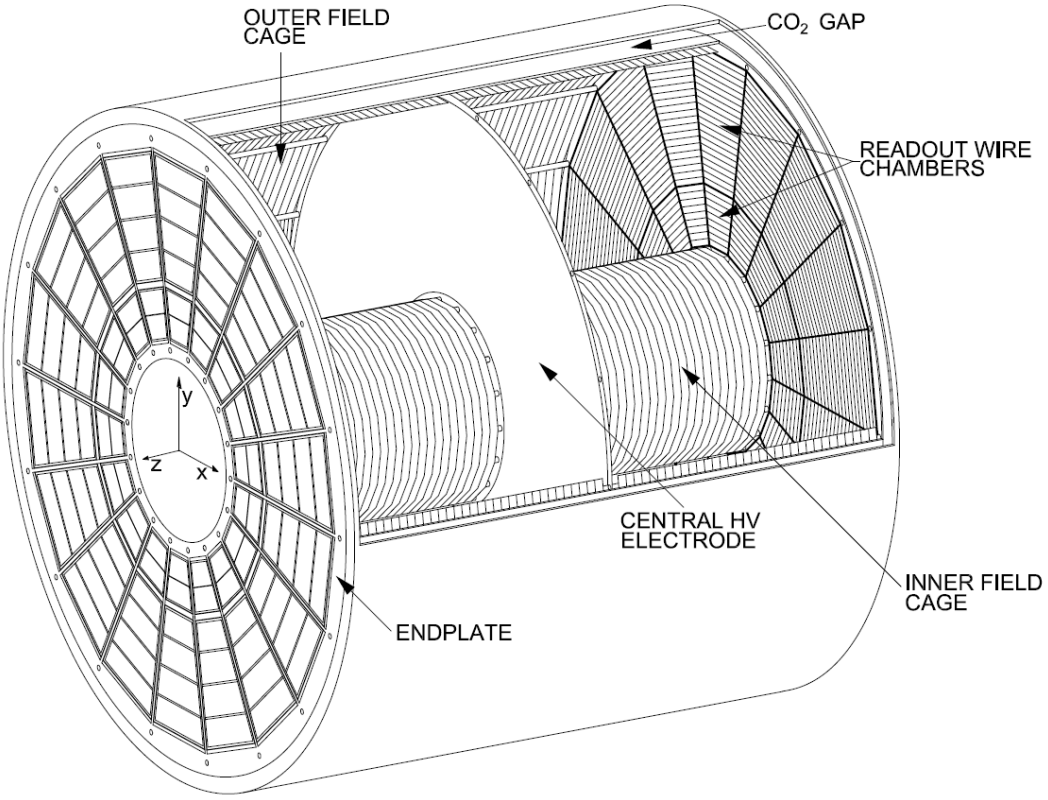

Figure 4.5.: Illustration of the ALICE Time Projection Chamber. The high voltage electrode is located at the center while the readout chambers are installed at the endplates of the field cage. Inner and outer field cage guarantee a uniform electrostatic field in the gas volume [Alm2010].

The left plot in figure 4.6 shows the momentum resolution as a function of transverse momentum measured for cosmic tracks. The transverse momentum resolution is about 1 % for $p_T < 2\,\mathrm{GeV/c}$. It shows the typical linear dependence $\sigma_p/p \propto p$ for tracking detectors [Boc1998]. Nevertheless, at the transverse momentum of 10 GeV/c a momentum resolution of 7 % is achieved. To study particle-correlations one needs to separate tracks with similar momenta. Therefore a good two-track resolution is necessary. To distinguish tracks with a momentum difference of 5 MeV/c, a magnetic field of $B = 0.5\,\mathrm{T}$ is required [Car2004].

The right plot in figure 4.6 shows the particle-identification capability of the TPC via specific energy loss for various charged particles as a function of momentum measured in *pp* collisions at $\sqrt{s} = 7\,\mathrm{TeV}$. Electrons, pions, kaons protons and deuterons are well separated. The black lines correspond to parametrizations of the Bethe-Bloch formula. At transverse momentum $p_T = 10\,\mathrm{GeV/c}$ a resolution in the specific energy loss of $\sigma_{\mathrm{d}E/\mathrm{d}x} \approx 5\,\%$ has been achieved [Kal2011]. This high performance enables strong cuts on the particle type for physics analyses.

The main specifications of the Time Projection Chamber are summarized in table 4.3.

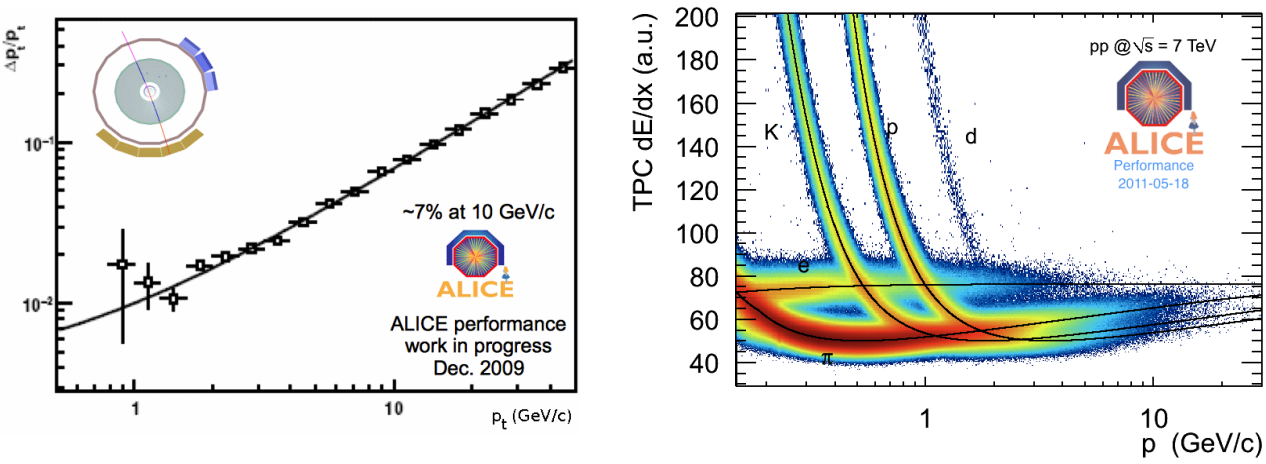

Figure 4.6.: Left: Momentum resolution as a function of transverse momentum achieved for cosmics tracks in the ALICE TPC. Right: Specific energy loss $\mathrm{d}E/\mathrm{d}x$ for different particle species as a function of transverse momentum in pp collisions at $\sqrt{s} = 7\,\mathrm{TeV}$, measured with the ALICE TPC. The lines correspond to a parametrization of the Bethe-Bloch curve [ALI2011].

Parameter	Value
Coverage in η	± 0.9 for full track length
	± 1.5 for 1/3 track length
Coverage in ϕ	360°
Radial position active volume (mm)	$848 < r < 2466$
Length (mm)	2×2497
Segmentation in ϕ	20 °
Segmentation in R	2 chambers per sector
Total number of readout chambers	$2 \times 2 \times 18 = 72$
Inner readout geometry	trapezoidal, $846 < r < 1321$ mm
pad size	4×7.5 mm^2 $(r\phi \times z)$
pad rows	60
total pads	5504
Outer readout geometry	trapezoidal, $1346 < r < 2466$ mm
pad size	6×10 mm^2, 6×15 mm^2 $(r\phi \times z)$
pad rows	$64 + 32 = 96$ (small and large pads)
total pads	$5952 + 4032 = 9984$ (small and large pads)
Detector gas	Ne, CO_2 and N_2 (87.5 : 9.5 : 4.8)
Gas volume	90 m^3
Drift voltage	100 kV
Drift field	400 V/cm
Drift velocity	2.65 cm/μs
Drift time	90 μs
Diffusion (longitudinal and transversal)	220 $\mu\mathrm{m}/\sqrt{cm}$
Material budget including counting gas	$\frac{X}{X_0} = 3.5\,\%$ near $\eta = 0$

Table 4.3.: Main characteristics for the TPC [Alm2010].

4.2.4. V0 detector

The V0 detector consists of two arrays of scintillation counters, called V0A and V0C. The first one is installed at $z = 340\,\text{cm}$ in a pseudo-rapidity range of $2.8 < \eta < 5.1$ while the latter is located at $z = -90\,\text{cm}$ in a pseudo-rapidity range of $-3.7 < \eta < -1.7$. The scintillator arrays are segmented in four rings. 32 elementary counters are distributed at the A-side in sectors of $45\,^\circ$ while on the C side 48 counters are arranged with 8 counters on the two inner rings and 16 on the two outer rings. The counters on the outer rings are connected in pairs to give the same scheme on both sides. The single elements consist of scintillating material with 2.5 cm and 2.0 cm thickness for V0A and V0C, respectively. The light is collected by 1 mm diameter wave length shifting fibers and send to photo multiplier tubes.

The V0 detector has several tasks. On the one hand, it provides the minimum-bias (MB) trigger to the central barrel detectors in proton-proton as well as in heavy-ion collisions. On the other hand, the registered particles in the detector arrays show a monotonic dependence on the total number of produced primary particles. Therefore, the V0 detector can also be used for multiplicity estimation. Cuts on fired counters and total charge are used to achieve rought centrality trigger, namely multiplicity, semi-central and central.

The trigger can be operated either in AND mode, if a signal in both arrays is required, or in OR mode, where only one array is needed. The latter is used in the measurement of the luminosity, see section 4.3. In this mode the trigger efficiency for at least one charged particle in each array is about 75 %, excluding secondary particles from interactions with the environment. If those are included, the trigger efficiency rises up to 84 %. Additionally, interactions of protons with the residual gas in the vacuum chamber at the collision point can be identified and rejected. Due to the location of the V0C right before the muon spectrometer, the absence of V0C signals in an event can be used to reduce the background for muon analysis.

4.2.5. Electromagnetic calorimetry

The PHOton Spectrometer (PHOS) is a high-resolution electromagnetic spectrometer covering a limited rapidity and azimuthal range of $|\eta| \leq 0.12$ and $220\,^\circ \leq \phi \leq 320\,^\circ$, presently three modules that cover the acceptance of $260\,^\circ \leq \phi \leq 320\,^\circ$ are installed. Since it is dedicated to photon physics the detector is predestined to study thermal and dynamical properties of the initial phase of the collision. This includes the measurement of low-p_T direct photons as well as jet quenching through the measurement of high-p_T π^0 and γ-jet correlations. The identification of photons, electrons and positrons requires fast response and very good position and energy resolution. This is provided by lead-tungstate ($PbWO_4$) crystals with a granularity of the order of the $PbWO_4$ Molière radius which is about 20 mm. The length of the crystals is about 180 mm, corresponding to $20\,X_0$. The scintillation photons are measured by a photo diode attached on each crystal. To increase the light yield and to reduce thermal noise, PHOS operates at a temperature $T = -25\,^\circ\text{C}$.

The ElectroMagnetic CALorimeter (EMCAL) is a Pb-scintillator sampling calorimeter. It is designed to explore in detail the physics of jet quenching over a large kinematic range. The detector provides a fast and efficient trigger for hard jets, photons and electrons. The EMCAL also measures the neutral energy component of jets which allows full jet reconstruction. It is installed opposite to PHOS at $|\eta| \leq 0.7$ and $80\,^\circ \leq \phi \leq 187\,^\circ$ to allow γ-jet reconstruction. Presently 10 of 12 modules are installed. Due to the emphasis on high transverse momentum the intrinsic energy resolution of the EMCal is worse than the one of PHOS. The main parameters for both detectors are summarized in table 4.4.

Detector	PHOS	EMCAL
Distance to the interaction point R (cm)	460	450
Coverage in η	± 0.12	± 0.7
Coverage in ϕ	220° – 320°	$80^\circ < \phi < 187^\circ$
Granularity	$22 \times 22 \times 180\ mm^3$	$60 \times 60 \times 246\ mm^3$
Spatial resolution xy (mm)	$\sigma_{xy} = \sqrt{\left(\frac{3.26}{\sqrt{E}}\right)^2 + 0.44^2}$	$\sigma_{xy} = \sqrt{\left(\frac{5.3}{\sqrt{E}}\right)^2 + 1.5^2}$
Energy resolution	$\frac{\sigma_E}{E} = 1.12\% \oplus \frac{3.6\%}{\sqrt{E}}$	$\frac{\sigma_E}{E} = 1.7\% \oplus \frac{12\%}{\sqrt{E}}$
Radiation length X_0 (cm)	0.89	1.23

Table 4.4.: Main characteristics of the electromagnetic calorimeters [Aam2008] [Ale2005] [Bel2010].

4.2.6. Triggering in ALICE

The interaction rate in proton-proton and heavy-ion collisions at LHC luminosities is much higher than the maximum feasible rate of Data Acquisition (DAQ). Therefore a trigger system is installed which selects online the events to measure and to store. In ALICE, the trigger is organized into three different levels, Level-0 (L0), Level-1 (L1) and Level-2 (L2), which have different latencies. The reason for this separation is the different arrival times of the trigger inputs and the stringent timing requirements of the detectors.

The Level-0 (L0) trigger effects the initial activation of the detectors. This trigger is issued by the Central Trigger Processor (CTP) and based on the fulfillment of its L0 input conditions. The detectors contributing to the L0 input are fast detectors which do not need a start-up signal and which are continuously sensitive to new physics events. The L0 signal reached the involved sub-detectors within $1.2\,\mu$s after the collision takes place and initiates the local data recording on the affected detectors. The next stage is the Level-1 trigger which can follow any L0. If it is not issued the event is aborted and the electronics have to become ready for the next L0. The time interval between L0 and L1 should be short to reduce the dead time, in which no other L0 can be issued. The L1 trigger inputs have to be contributed about $6.5\,\mu$s after the L0. The decision is based on the information acquired after the L0 trigger. The third step, the L2 decision, comes after the end of the drift time in the TPC, i.e. at about $88\,\mu$s. The main purpose of this third step is to wait for the end of the past–future pile-up protection. The read-out of the detector electronics into the optical data link is initiated only upon receipt of a positive L2 decision.

At this stage data are shipped to DAQ and High-Level trigger (HLT) in parallel. In the HLT the full information from all major detectors is combined and processed in a large cluster of 1000 multi-processor computers. The task of the HLT is to select the most relevant data from the large input data stream and to reduce the data volume by well over an order of magnitude in order to fit the available average storage bandwidth of 1.25 GB/s while preserving the physics information of interest. In addition ALICE uses a very fast interaction 'pretrigger', which is derived from the multiplicity arrays (V0, T0 and TOF) and fed directly to the TRD within 800 ns in order to activate the TRD electronics.

4.2.7. AliRoot Framework

In the ALICE experiment the AliRoot software framework offers the functionality to reconstruct and analyze physics data either from simulation or from real collisions [Aam2008]. It is based on ROOT [Bru1997], a C++ based object-oriented programming tool for high energy physics analysis developed at CERN. Both frameworks are in continuous development. Their modularity allows partial replacements without affecting the rest of the software. AliRoot provides the necessary tools for simulation, reconstruction and analysis. A sketch of the analysis flow is shown in figure 4.7.

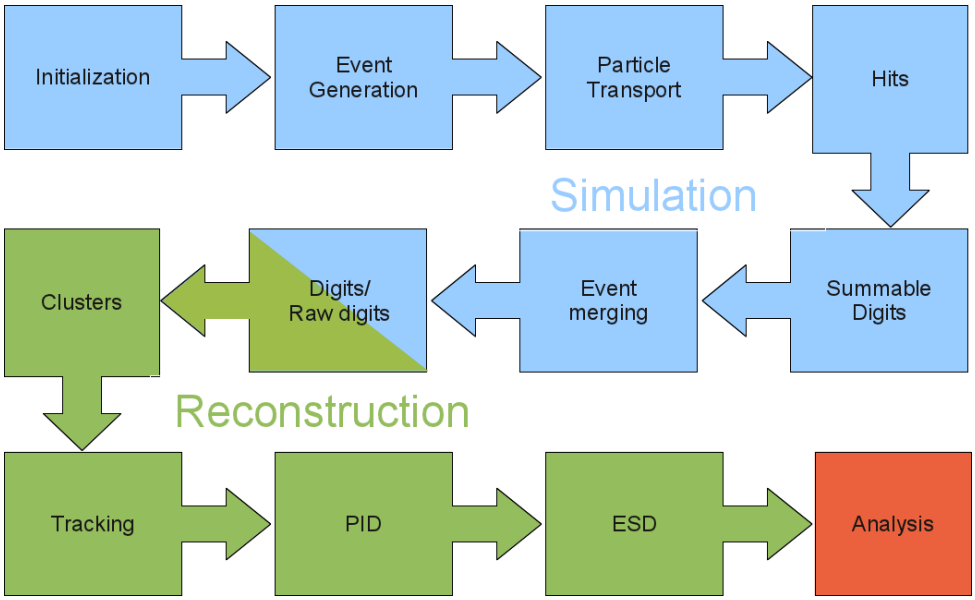

Figure 4.7.: Sketch of the analysis flow in ALICE. Adapted and modified from [ALI2011doc].

Using Monte Carlo event generators like PYTHIA and PHOJET physics processes at the partonic level and the particles resulting from fragmentation, so-called *primary particles*, are generated. At this stage the full information of the particle like momentum, charged or mother-daughter relationship is available. The particles are propagated through the detector and their interactions with the material are simulated using GEANT3 [Bru1985], GEANT4 [Ago2003] and FLUKA [Fas1993]. The energy deposition and its particular time and position are stored for each interaction point (so-called *hits*). Afterwards the hits are processed into *digits*. These are produced for each sub detector and correspond to the detector response. The detector response is implemented as close to reality as possible. The resulting signal is stored in two different formats. The first one is given by a ROOT structure. The second format corresponds to the electronic output of the detector *Front End Electronic*, so-called *raw data* as it is given in case of real collisions. The raw data only contain local response, no global event information.

In the reconstruction raw data either from simulations or real data are converted into readable objects for physics analysis. As a first step, clusters are reconstructed from neighboring digits in space and/or time, assuming that they have been generated by the same particle crossing the detector. The tracking then combines clusters according to their probability to belong to the same particle, see section 4.2.8. The output of the reconstruction is collected in the Event Summary Data (ESD). Those are used for further analysis.

4.2.8. Primary vertex and track reconstruction

The reconstruction of the primary vertex starts in the Silicon Pixel Detector (SPD), the two innermost layers of the ITS. It is sketched in figure 4.8. Reconstructed points of each layer are combined to pairs, so-called *tracklets*. From the tracklets those are selected which are very close to each other in the xy-plane. The variables $x1, y1, Z1$ and $R1 = \sqrt{(x1)^2 + (y1)^2}$ correspond to the first reconstructed point and $x2, y2, Z2$ and $R2 = \sqrt{(x2)^2 + (y2)^2}$ to the second, respectively. A linear extrapolation of their Z-coordinates gives an estimation of the Z-position of the primary vertex. A similar procedure is used to calculate the X- and Y-coordinate of the primary vertex. Although the particle trajectory is bent in the magnetic field, the distance between the points is very small and therefore a linear extrapolation can be used as approximation. The distribution of all lines connecting the coordinates $(x1, y1)$ and $(x2, y2)$ of the pairs has its maximum very close to the true vertex coordinates. The position of the primary vertex is recalculated after the foll track reconstruction using the measured track parameters.

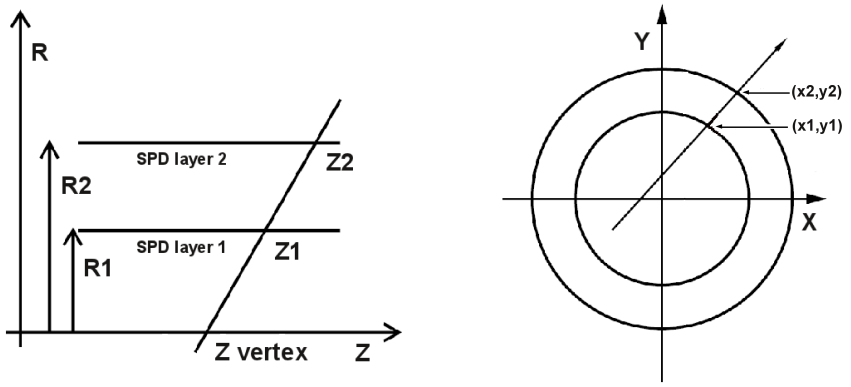

Figure 4.8.: Sketch of the primary vertex reconstruction. The left figure illustrates the estimation of the Z-coordinate while in the right one the estimation of the X- and Y-coordinates is shown. Figure adapted and modified from [Ale2006].

The spread in the X- and Y-coordinates of the primary vertex as a function of tracklet multiplicity is shown in figure 4.9. The open symbols correspond to the multiplicity measured with SPD tracklets and the full symbols measured with full track reconstruction. Two aspects are visible. Firstly, the spread in the coordinates using full track reconstruction is much more narrow than only using SPD tracklets. The full reconstructed track defines the particle trajectory and therefore its origin is much more precise. Secondly, the quality of the measurement of the primary vertex is highly dependent on the multiplicity. At the average proton-proton event with a charged-particle multiplicity of $\mathrm{d}N_{ch}/\mathrm{d}\eta = 6-7$ [Aam2008] the vertex spread is of the order of $400\,\mu$m for SPD tracklets and $150\,\mu$m for fully reconstructed tracks. With increasing multiplicity the spread reaches an asymptotic limit of the order of $(34 \pm 2)\,\mu$m for the X-coordinate and $(33 \pm 3)\,\mu$m for the Y-coordinate. These limits are simply given by the size of the beam.

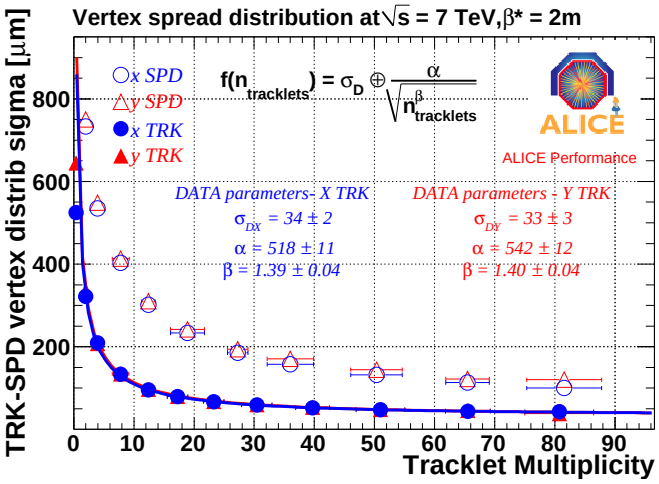

Figure 4.9.: Vertex spread distribution in X and Y as a function of tracklet multiplicity at $\sqrt{s}$ = 7 TeV, measured with tracklets within the Silicon Pixel Detector (open symbols) as well as from fully reconstructed tracks (full symbols). The solid lines are the results of a fit following the given equation. The asymptotic limits at high multiplicity (σ_{Dx} and σ_{Dy}) are given by the beam size [ALI2011].

The track reconstruction itself is based on Kalman filtering [Bil1984]. The determination of initial seed values for the track parameter and their covariance matrix is of key importance for this method. It uses clusters (reconstructed energy depositions) in pad row and 'time' direction in the TPC. As starting point two clusters from the outermost pad rows of the TPC are combined and a helix going through both points is calculated. This is done twice, once assuming the track comes from a primary vertex and once without this restriction.

The Kalman filtering follows three steps: The state vector of the track parameters and their covariance matrix is propagated to the next pad row following the calculated helix. The covariance matrix represents the information about the track parameter at a given point. Some noise is added to the matrix to take multiple-scattering effects in the material or energy loss fluctuations into account. It is checked whether a cluster exists in the pad row corresponding to the calculated track prolongation. If a cluster is found, this point is added to the track and the track parameters and covariance matrix are updated. This procedure is repeated until the outermost layer of ITS is reached. Now both samples of tracks (with and without vertex constraints) are propagated through the ITS, starting with the highest momentum track. Whenever more than one cluster is found around the prolongation all possible assignments are used independently and followed to the innermost ITS layer. The decision for the best track is made only at the end based on the χ^2. Afterwards the Kalman filtering is reversed, following the track from the ITS inner layer outwards. This leads to much higher precision in the track parameter and improperly assigned points can be taken out. This procedure is called *refit*. When the end of the TPC is reached, the track is extrapolated and matching clusters in TRD, TOF or HMPID are assigned. Now a last reverse of the Kalman filtering is applied and all tracks are refitted starting from outside and directed inwards.

Optionally an additional track finding can be performed in the ITS after the removal of all already assigned ITS clusters. This is very useful if a track went through non-sensitive areas in the TPC, e.g. between readout chambers. The track parameters for the sample with and without vertex constraints are stored in order to allow subsequent analysis of short-lived particles.

4.2.9. Secondary vertex reconstruction

Tracks without primary vertex assumption, so-called *secondary tracks*, are used to find particles from strange decays that this way originate from a secondary vertex. The procedure is sketched in figure 4.10. It starts with the selection of two oppositely charged secondary tracks. The impact parameters of the tracks (b, b^+) with respect to the primary vertex are calculated. Tracks with a too small impact parameter are discarded. Afterwards the distance of closest approach (DCA) in space between both tracks is calculated. The track pair is rejected if the DCA is above a given value, depending on the radial distance to the primary vertex. The highest allowed DCA is 1 cm. Once the secondary vertex is defined, it is only kept if it belongs to a given fiducial zone (displayed as dashed lines). The inner limit is of the order of 0.5 cm, given by the expected particle density and tracking precision. The outer limit is 220 cm to ensure the quality of reconstructed tracks. Afterwards it is checked, whether the momentum vector of the reconstructed V^0 points back to the primary vertex. The momenta of both tracks are extrapolated to the DCA and their sum is calculated as the particle momentum at the secondary vertex. A cut of 0.85 on the cosine of the angle between V^0 momentum (P) and the vector between primary vertex and V^0 position (R) is applied.

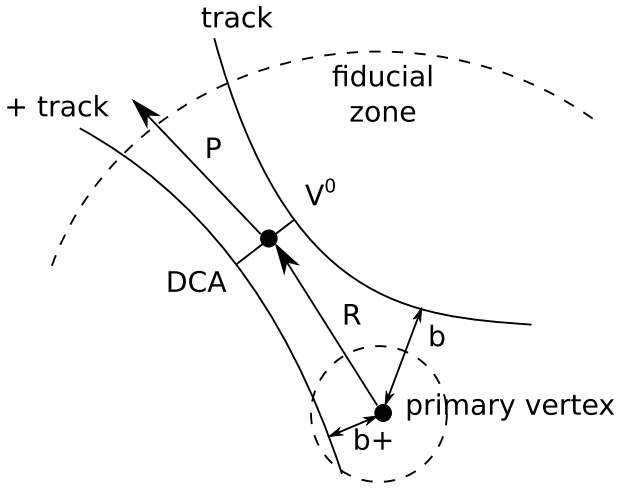

Figure 4.10.: Sketch of secondary vertex reconstruction [Ale2006].

Within the ALICE experiment two different secondary vertex finding procedures are available. These are the *on-the-flight* and *offline* V^0 finder. The former is applied during data reconstruction. The tracks are refitted and the track parameter are recalculated assuming a secondary vertex. This is only possible at this stage since the information about clusters in the Inner Tracking System and the Time Projection Chamber is still available. This improves the position and momentum resolution of the secondary vertex. The offline secondary vertex finder on the other hand, is applied after the full tracking procedure. Therefore, the information about hits and clusters in the ITS and the TPC is no longer available. Nevertheless, this V^0 finder gives the opportunity to reprocess the secondary vertex finding without reprocessing the full data.

4.3. Data sample

The data samples at $\sqrt{s} = 0.9\,\text{TeV}$ and $\sqrt{s} = 7\,\text{TeV}$ used for this analysis were collected by the ALICE experiment in 2010 while the data sample for $\sqrt{s} = 2.76\,\text{TeV}$ was taken in 2011. To this events an offline event selection has been applied. The selection rejects events where the trigger conditions for the central barrel were not fulfilled or which are not of physics type, e.g.

calibration events, or assigned to noise or beam-gas interactions. This selection is called *Physics Selection* (PS). The data used in this analysis have been assigned to minimum bias ($\mathrm{MB_{OR}}$). This trigger requires a hit in the SPD or in either one of the two V0 detectors.

To calculate the interaction cross section for $\mathrm{MB_{OR}}$ events, several steps have been done. Only events with signals in both V0 detectors at the same time ($\mathrm{MB_{AND}}$) have been used. The luminosity $\mathcal{L}$ is measured using a Van-der-Meer scan (VdM). With the trigger rate R_{trigg} the interaction cross section $\sigma_{\mathrm{MB_{AND}}} = R_{trigg}/\mathcal{L}$ is calculated. These cross sections have been calculated for the energies $\sqrt{s} = 2.76$ and 7 TeV [Oya2011]. To calculate the interaction cross section $\sigma_{\mathrm{MB_{OR}}}$ the ratio of both trigger efficiencies has been calculated and applied to $\sigma_{\mathrm{MB_{AND}}}$. For $\sqrt{s} = 0.9$ TeV the cross section is calculated using the inelastic cross section $\sigma_{INEL} = 50.3 \pm 0.4_{\mathrm{stat.}} \pm 1_{\mathrm{sys.}}$ mb measured by the UA5 collaboration in $p\bar{p}$ collisions at the same energy [Ans1986]. The cross section is scaled by the $\mathrm{MB_{OR}}$ trigger efficiency of 0.916 ± 0.013 at $\sqrt{s} = 0.9$ TeV for the ALICE experiment. The measured $\sigma_{\mathrm{MB_{AND}}}$ at $\sqrt{s} = 2.76$ and 7 TeV in conjunction with Monte Carlo simulations have been used to obtain the inelastic cross section σ_{INEL} [Gag2011]. All resulting cross sections are summarized in table 4.5.

$\sqrt{s}$ (TeV)	$\sigma_{\mathrm{MB_{AND}}}$ (mb)	$\frac{trigg.eff.\mathrm{MB_{OR}}}{trigg.eff.\mathrm{MB_{AND}}}$	$\sigma_{\mathrm{MB_{OR}}}$ (mb)	σ_{INEL} (mb)
0.9			46.1±1.1	
2.76	47.2±3.3	0.86±0.01	55.1±3.9	$62.1 \pm 1.6_{sim} \pm 4.3_{VdM}$
7	54.2±2.2	0.87±0.01	62.1±2.5	$72.7 \pm 1.1_{sim} \pm 5.1_{VdM}$

Table 4.5.: Reaction cross sections $\sigma_{\mathrm{MB_{AND}}}$, $\sigma_{\mathrm{MB_{OR}}}$, σ_{INEL} and the ratio of both trigger efficiencies including systematic uncertainties for the measured data sample at the center-of-mass energies $\sqrt{s} = 0.9, 2.76$ and 7 TeV.

In the analysis presented in this thesis additional requirements are applied on the events. Only events with a reconstructed collision vertex within $|z_{Vtx}| < 10$ cm of the nominal value reconstructed from tracks traversing ITS and TPC (*global tracks*) or SPD tracklets are included.

In figure 4.11 the fraction of events that have

- a reconstructed collision vertex within $|z_{Vtx}| < 10$ cm (red),
- no reconstructed collision vertex from global track or SPD tracklets (blue),
- a reconstructed collision vertex above $|z_{Vtx}| = 10$ cm (green)

are shown. The amount of events passing all conditions is $75 - 90$ %, depending on the run period. From period *d* onwards a higher luminosity for all experiments is delivered. In the ALICE experiment this leads to an overlapping of events. Therefore, both beams were displaced to stay at lower interaction rate. This is reflected in the jump of the green points, that represents events with vertices outside of $|z_{vtx}| < 10$ cm. At the same time the amount of events without any vertex drops (blue).

The number of events passing the Physics Selection, but without events with $|z_{Vtx}| \geq 10$ cm, is used for the normalization of the neutral meson spectra. The total number of events according to their run period is given in table 4.6. The complete list of all runs can be found in appendix A.

Energy	Data Set	Events	(PS+Vtx+$\lvert z_{vtx}\rvert$ <10) /PS	(PS+noVtx) /PS	(PS+Vtx+$\lvert z_{vtx}\rvert$ >10) /PS
0.9TeV	Data (Pass3)	6.90e+06	0.77	0.130	0.105
	LHC10e12 Phojet	3.01e+06	0.82	0.093	0.090
	LHC10e13 Pythia	5.87e+06	0.76	0.149	0.095
2.76TeV	Data (Pass2,11a)	6.53e+07	0.79	0.119	0.093
7TeV	Data (Pass2, period b)	2.97e+07	0.90	0.093	0.004
	Data (Pass2, period c)	7.39e+07	0.90	0.093	0.007
	Data (Pass2, period d)	1.57e+08	0.80	0.098	0.101
	Data (Pass2, period e)	1.22e+08	0.80	0.096	0.105
	LHC10d1 (b) Pythia	2.38e+07	0.92	0.080	0.004
	LHC10d4 (c) Pythia	4.29e+07	0.95	0.037	0.010
	LHC10f6a (d) Pythia	1.14e+08	0.80	0.104	0.092
	LHC10e20 (e) Pythia	9.91e+06	0.81	0.100	0.086
	LHC10d2 (b) Phojet	1.82e+07	0.95	0.047	0.003
	LHC10d4a (c) Phojet	5.34e+07	0.97	0.018	0.010
	LHC10f6 (d) Phojet	7.37e+07	0.85	0.057	0.095
	LHC10e21 (e) Phojet	1.15e+07	0.86	0.056	0.089

Table 4.6.: Number of events passing the Physics selection and fraction of events passing additional constraints on the collision vertex for data and Monte Carlo simulations at $\sqrt{s} = 0.9,\ 2.76$ and 7 TeV for each run period. PS corresponds to Physics Selection. For $\sqrt{s} = 2.76$ TeV the statistics of Monte Carlo simulations is not sufficient. Therefore, the simulations at $\sqrt{s} = 7$ TeV have been used for corrections.

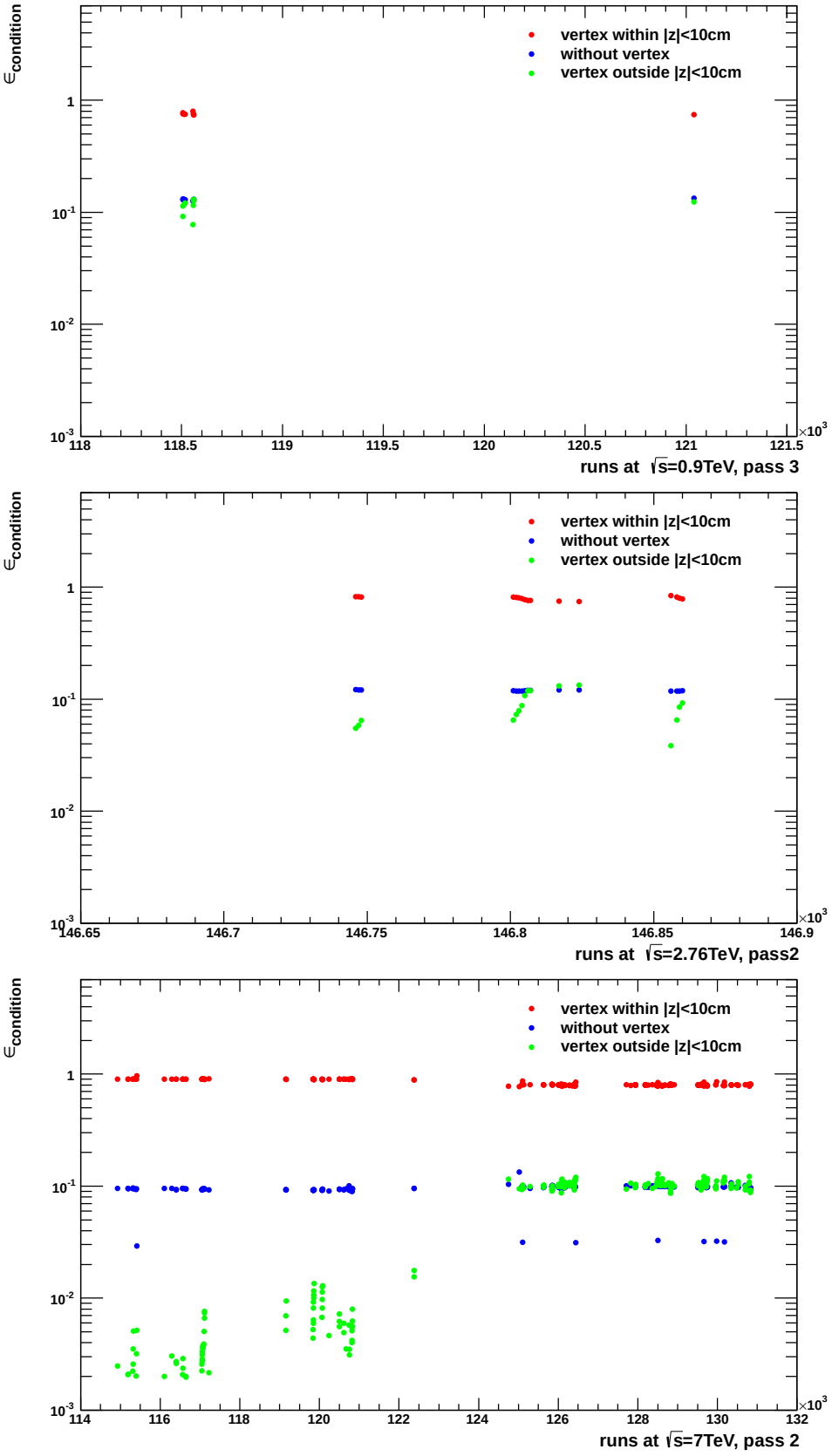

Figure 4.11.: Fraction of events compared to Physics Selection that pass all conditions (red), have no vertex (blue) or a vertex outside of $|z_{Vtx}| = 10\,\text{cm}$ (green). The fractions are given for the different collision energies $\sqrt{s} = 0.9\,\text{TeV}$ (top), $\sqrt{s} = 2.76\,\text{TeV}$ (middle) and $\sqrt{s} = 7\,\text{TeV}$ (bottom). The drop of events without reconstructed collision vertex in conjunction with the jump of reconstructed collision vertices above 10 cm is caused by a beam displacement staring in run period *d*. The displacement has been necessary due to a higher luminosity.

5. Data analysis

Neutral pions and η mesons decay into two photons with a branching ratio of 98.8 % and 39.3 %, respectively [Nak2010]. Photons themselves undergo conversion with a probability of $P = 1-\exp(-\frac{7}{9}\frac{X}{X_0})$ and create electron-positron pairs. These leave tracks which can be reconstructed by the tracking detectors. Figure 5.1 shows an event display for a π^0 candidate from a proton-proton collision at a center-of-mass energy $\sqrt{s} = 0.9\,\text{TeV}$. Four tracks are reconstructed in the TPC and combined into two mother particles that roughly point back to the collision vertex.

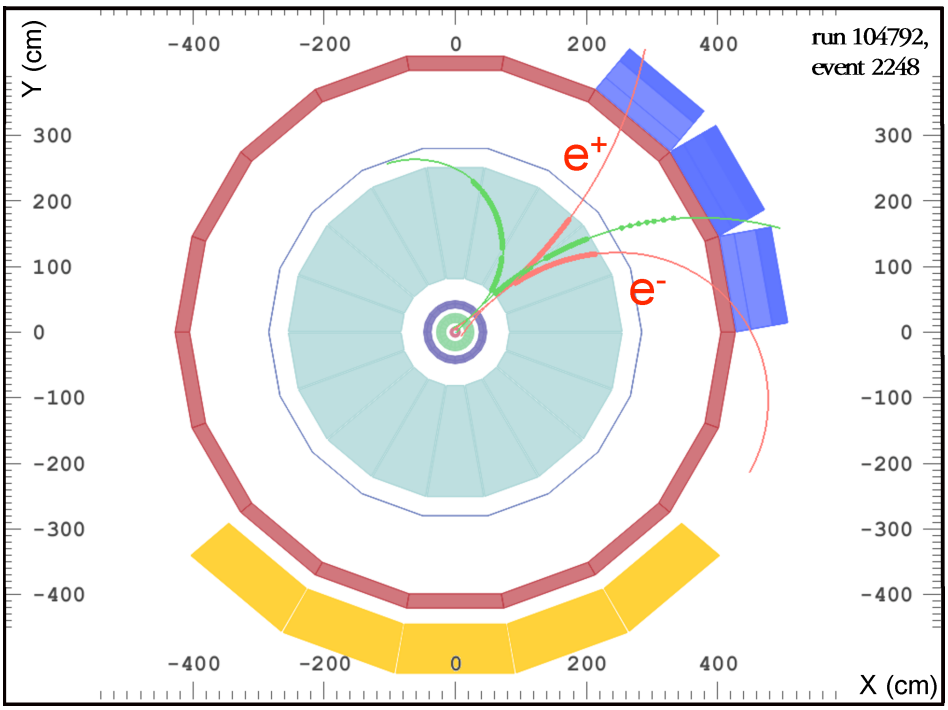

Figure 5.1.: Event display of a π^0 candidate. The figure has been taken from run 104792, event 2248, at the energy $\sqrt{s} = 0.9\,\text{TeV}$ in 2009.

5.1. Reconstruction of photon candidates

For the reconstruction of the photons a secondary-vertex finder is used which combines two oppositely-charged tracks, see section 4.2.9. In this analysis the on-the-fly V^0 finder is used instead of the offline V^0 finder. One reason is its higher efficiency. Figure 5.2 gives a comparison of both V^0 finders for reconstructable conversions as functions of $1/\sqrt{p_T}$, η and R of the negative tracks for simulations at $\sqrt{s} = 7\,\text{TeV}$. The plotting in units of $1/\sqrt{p_T}$ compensates the broadening of the transverse momentum bins toward very high transverse momentum and provides a concentrated distribution of the data points. On the left the on-the-fly method is displayed, on the right the offline method. The efficiency of the V^0 finder ϵ_{V0} is calculated if both tracks are reconstructed.

Figure 5.2 (top) shows the efficiency of the V^0 finding as a function of $1/\sqrt{p_T}$. Above $1/\sqrt{p_T} \approx 2.6\,\sqrt{\mathrm{c/GeV}}$ a drop develops with a minimum at about $1/\sqrt{p_T} \approx 2.9\,\sqrt{\mathrm{c/GeV}}$. The dip is a consequence of the selection criteria in the definition of findable tracks (tracks with more than 50 cluster). This effects tracks which are created close to the TPC. For both reconstruction methods the shape is similar above $1/\sqrt{p_T} \approx 2.9\,\sqrt{\mathrm{c/GeV}}$ but differs below. In case of the on-the-fly V^0 finder the efficiency increases towards low $1/\sqrt{p_T}$ from 0.8 to 1. For the offline method the reconstruction efficiency stays rather constant at about 0.8.

The efficiency of both methods with respect to η is shown in the middle of figure 5.2. In this analysis a range $|\eta| < 0.9$ is used. Within this range the efficiency is nearly flat for both methods except for a dip at $\eta \approx 0$ where the TPC central electrode is located. The achieved efficiencies are about 0.9 for the on-the-fly and 0.8 for the offline algorithm.

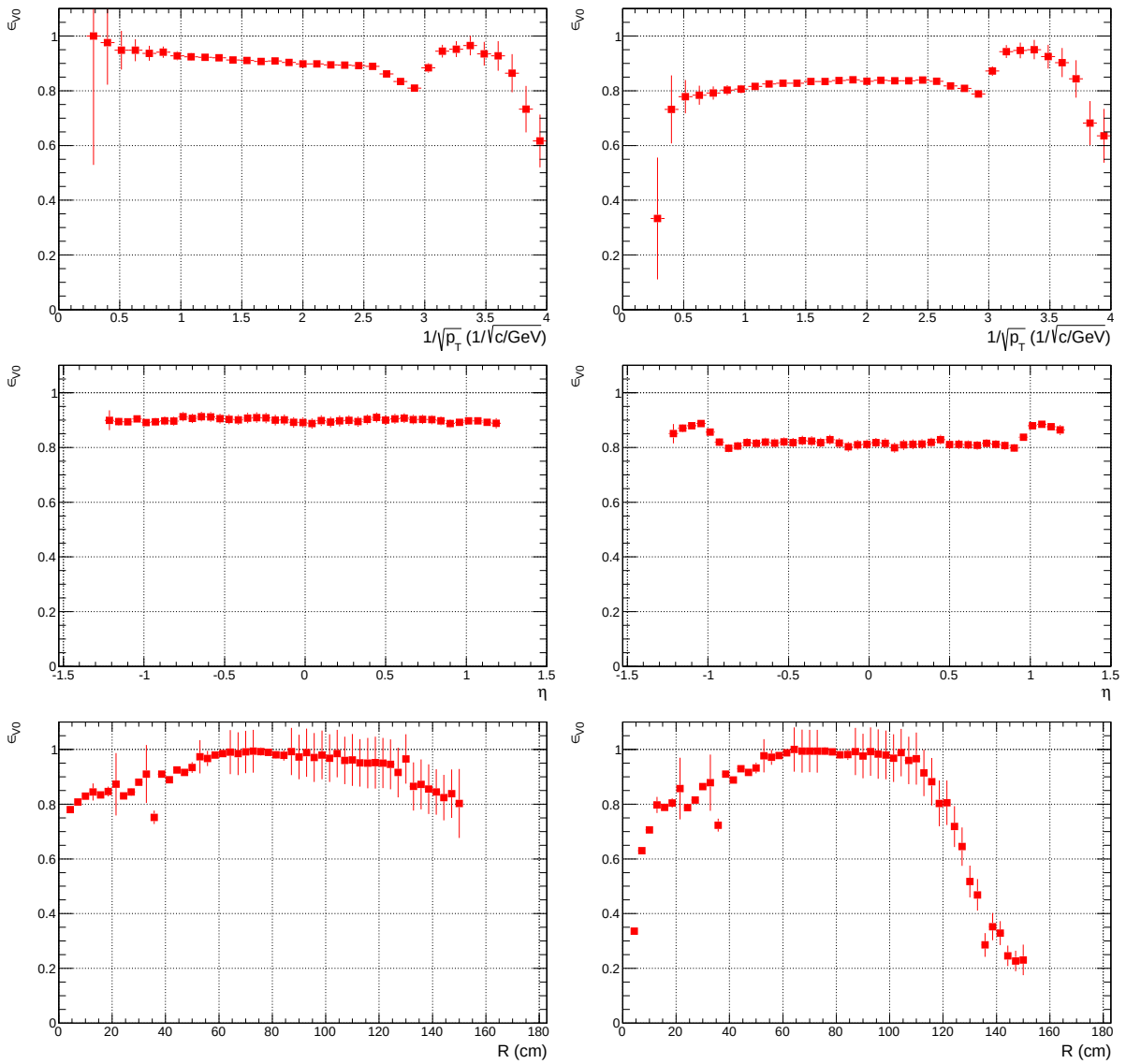

Figure 5.2.: Efficiency of the on-the-fly (left) and the offline (right) secondary-vertex finders for reconstructable conversions. The efficiencies are extracted as functions of $1/\sqrt{\mathrm{p_T}}$ (top), η (middle) and R (bottom) for the negative track from the simulations LHC10d1, LHC10d2, LHC10d4 and LHC10d4a.

Finally the radial dependence of both performances is given in the bottom. Within the ITS and above a radial distance of 110 cm the performance of the offline V^0 finder is rather low, the efficiency is going down to $0.2 - 0.3$. This is in contrast to the on-the-fly V^0 finder. Here the efficiency reaches at least 0.8. In the range of about $50 - 110$ cm both methods reach nearly full efficiency. The dips at $r = 20$ and 40 cm are caused by gaps between the two SDD layers and between SDD and SSD, respectively.

In addition to its higher efficiency for reconstructable photons, the achieved π^0 peak position of the on-the-fly secondary-vertex finder is closer to the literature value and the meson mass peaks are narrower.

For the estimation of the uncertainties in the material budget the exact calculation of the conversion position is of key importance. Due to momentum conservation the tracks for electrons and positrons need to be almost parallel at their origin. The V^0 finders are not optimized for this condition. Therefore, the conversion point is recalculated. The method is described in detail in [Aam2011a] and [Boc2010]. Figure 5.3 sketches the procedure. The recalculation of the conversion point starts with its X and Y coordinates. This is shown on the top. Both tracks have a helix shape due to the bending in the magnetic field. After a projection into the XY plane the helix centers are calculated and connected with a straight line. Then a new center of gravity is calculated which takes the radii of both helices into account. This way the new X and Y coordinates are calculated. Still in the XY plane the propagation of the first track points along the helices is calculated up to the point where the straight line crosses the helices. Afterwards the tracks are projected onto the Z axis. The calculated propagation of the first track points in XY is used to determine their new Z coordinates. This is shown on the bottom. As a last step the Z coordinate of the conversion point is calculated, again taking the radii of the helices into account.

With this recalculation resolutions better than 3 cm in R, 1.5 cm in Z and 6.5 mrad in ϕ are achieved. Figure 5.4 (top) shows the distributions of the reconstructed photon conversion points in XY (left) and ZR plane (right). These plots illustrate the resolution of the conversion method. Even smallest structures are well separated. In both plots the beam pipe and the six layers of the ITS including segmentation and support structures are clearly visible. For the TPC the inner vessel and the rods are resolved as well as the segmentation into 18 readout chambers. In the ZR plot also the central electrode at $Z \approx 0$ cm can be seen. The colors correspond to the amount of conversions and thus to the density of the material.

In the lower part of figure 5.4 the distributions of the conversion points are given in R (left) and in Z (right). Both plots provide a comparison of the conversion densities from data to simulations, shown in black and red, respectively. This allows to check the implementation of the detector material in simulations. To this end, the detector is divided into parts (*bins*) according to the location of the material. The number of conversions is scaled by the number of events and charged multiplicity. The latter factor is necessary since the charged-particle multiplicity distributions in data and Monte Carlo differ. A good agreement between data and simulation is achieved. Only in a few parts of the ITS and the TPC the implementation is not consistent with data. These are the SPD, the second SDD layer including support structure and the TPC inner field cage vessel. While in case of the ITS sub-detectors the material is underestimated in the simulations, it is overestimated in the latter case. The projection onto the Z axis shows an asymmetry in the implementation. In the negative Z direction more material is implemented in the simulation than actually exist. In contrast, at $Z \approx 0$ cm the material is underestimated. At present the systematic uncertainties for a material budget of a radiation length $11.4\,\%X_0$ upto the middle of the TPC (180 cm) amount to $^{+3.4}_{-6.2}\%$ [Boc2010]. Checks are ongoing for further

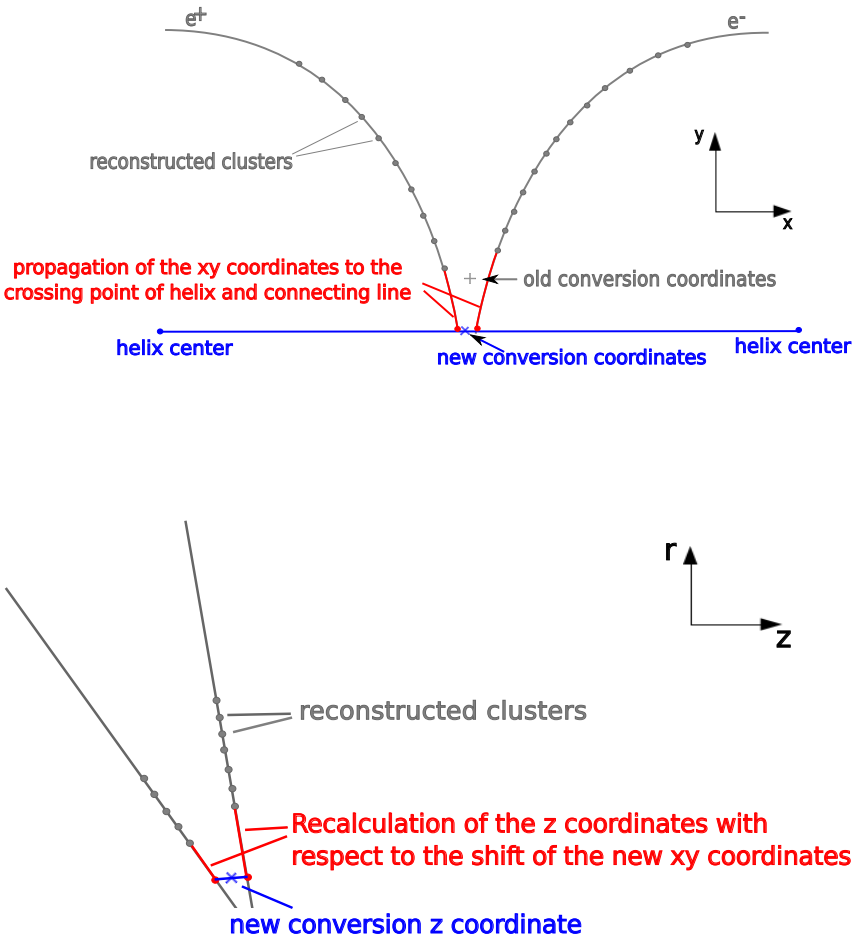

Figure 5.3.: Sketch of the recalculation of the conversion point. Top: Recalculation of the XY coordinates, bottom: Recalculation of the Z coordinate.

improvement.

Additionally to the check of the material implementation the bottom plots of figure 5.4 also provide information about the physics origin of the converted photons. The information has been obtained in simulation. True conversions are presented in yellow, contributions from π^0 and η Dalitz decays are marked in light and dark blue hatched. In Dalitz decays the meson directly decays into a photon and an electron-positron pair. Within the given statistics, photons coming from Dalitz decays are located at up to a radial distance of $3 - 5\,\text{cm}$ for η mesons and of $10\,\text{cm}$ for π^0. Combinatorial background, shown in brown are reconstructed V^0, where the daughter particles belong to different mother particles. These are mainly located in the ITS and the TPC inner field cage vessel in a range of $|z| < 30\,\text{cm}$. Contamination from hadronic background (black) results in combinations with charged pions, kaons and protons. The background has been found to be negligible in the range $|\eta| < 0.9$.

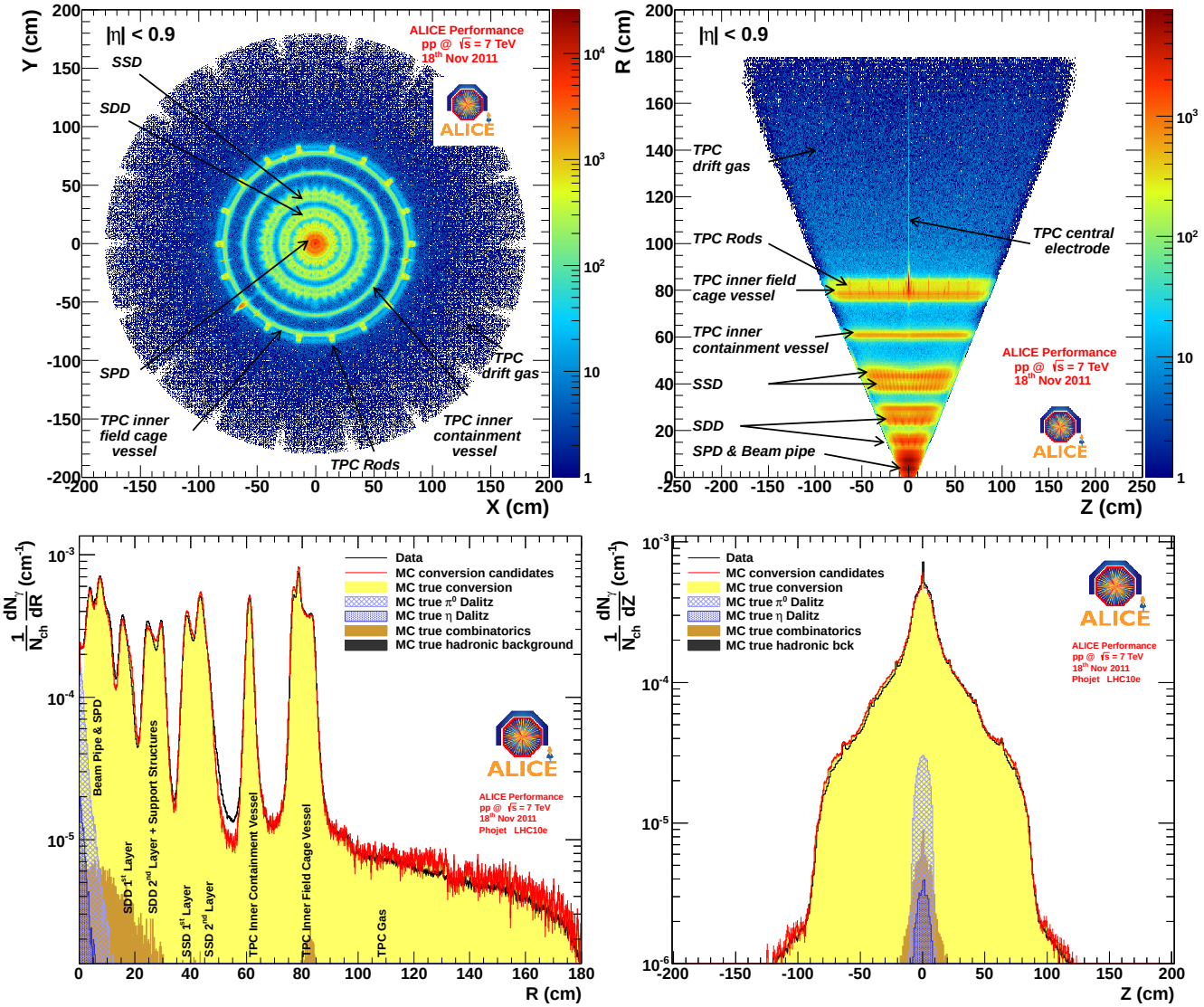

Figure 5.4.: Spatial distribution of the conversion points. On top the distribution in XY and ZR plane are given. These plots show the resolution of the used reconstruction method. Smallest structures in the ITS as well as in the TPC are separated. Even the beam pipe is clearly visible. The plots in the bottom give an overview about the agreement of the implemented material budget in simulation (red) to data (black) as a function of R (left) and Z (right). Furthermore, these plots show the physics origin of the converted photon [Aam2011c].

5.2. Cut selection for photon candidates

There are two main sources of background for neutral pions and η mesons, that can be reconstructed via photon conversions. The first source are V^0 wrongly identified as photons. The second one is the combinatorial background from photon pairs which is independent of the purity of the photon sample.

Intensive cut studies have been performed in order to optimize raw yield and significance of the neutral mesons. Moreover, the applied cuts need to have the same effect in simulation and data. Otherwise a proper calculation of the efficiency would not be possible. In the presented analysis the invariant-mass distributions of photon pairs around the expected π^0 and η mass range have been used to extract the raw yield of both mesons. Therefore, it was not necessary to have a very clean photon sample. This allows to loosen the requirements on the reconstructed photon candidates.

The reconstruction of π^0 and η mesons starts with the reconstruction of photon candidates and thus, with the identification of electrons and positrons that are combined to a V^0. In order to separate photons from the other contributions such as K^0_S, Λ or $\overline{\Lambda}$ in the V^0 sample, different cuts are applied.

As a first step, various checks on the track quality are performed. Like-sign pairs (e^-e^- and e^+e^+) are excluded. Only tracks that pass the refit in the TPC, see section 4.2.8, are taken into account for this analysis. Also kink topologies, like from a decay $K^+ \longrightarrow \mu^+ + \nu_\mu$, where the daughter particle is deflected by a small angle, are rejected. Afterwards a cut at low $R = 5\,\mathrm{cm}$ is applied to avoid contamination from π^0 and η Dalitz decays. This is discussed in detail in section 5.4.3. A maximum in the radial distance $R = 180\,\mathrm{cm}$ needs to be applied to ensure the track reconstruction for electrons and positrons. Additionally, a cut on the ratio of found clusters to findable track clusters within the TPC of 0.35 was applied to avoid tracks that are not reconstructed properly. For tracks that do not come from the collision vertex like tracks from a converted photon from secondary pions, a cut in pseudo-rapidity is not sufficient. Therefore an additional cut in the ZR plane is applied. This so-called *line cut* rejects reconstructed V^0s with $R < |Z| * slope - Z_0$, where $Z_0 = 7\,\mathrm{cm}$ and $slope = \tan(2 \cdot \arctan(e^{|\eta|}))$. Figure 5.5 illustrates the line cut for $|\eta| = 0.9$. The last geometrical constraints are applied for $Z \leq 240\,\mathrm{cm}$ and pseudo-rapidity $|\eta| < 0.9$. The minimum required transverse momentum for both tracks is set to 50 MeV. Furthermore, the number of contributors to the primary vertex has been checked to be at least one.

Figure 5.6 (left) shows the specific energy loss distribution in the TPC as a function of the particle momentum for the complete V^0 sample. The distribution for electrons and the crossing lines for pions, kaons and protons are clearly visible. In order to select electrons and positrons a cut of $^{+5}_{-4}\sigma_{\mathrm{d}E/\mathrm{d}x}$ around the expected electron energy loss hypothesis is applied. The electron selection is further refined by an additional constraint on the pion energy loss hypothesis: particles in the momentum range of $0.25\,\mathrm{GeV/c} < p < 3.5\,\mathrm{GeV/c}$, between $-\infty$ and $+2\sigma_{\mathrm{d}E/\mathrm{d}x}$ to the pion hypothesis, and particles with $p > 3.5\,\mathrm{GeV/c}$ and between $-\infty$ and $+0.5\sigma_{\mathrm{d}E/\mathrm{d}x}$, are rejected. The distribution at $\mathrm{d}E/\mathrm{d}x = 0$ results from tracks where no specific energy loss could be assigned, setting it to 0.

In figure 5.6 (right) a so-called *Armenteros-Podolanski* plot [Pod1954] is shown for the complete V^0 sample. On the X axis the longitudinal momentum asymmetry $\alpha = (p_L^+ - p_L^-)/(p_L^+ + p_L^-)$ is given. On the Y axis the projection of the momentum of the daughter particle (electron) with respect to the mother particle (V^0) in transverse direction $q_T = p \times \sin(\theta_{mother-daughter})$ is

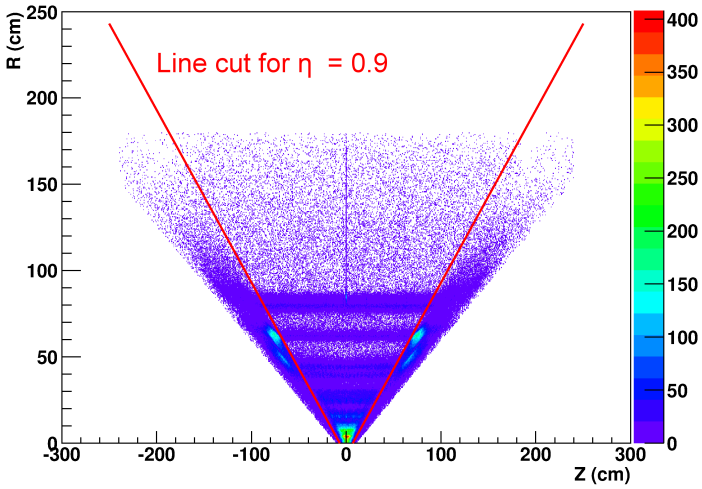

Figure 5.5.: Illustration of the line cut for $|\eta| = 0.9$ (red). The line cut is performed in the ZR plane. Reconstructed V^0s below the calculated line are rejected. To give a better picture, the illustration is based on a distribution for $|\eta| < 1.2$.

displayed. In case of photon conversions, electrons and positrons fly in the laboratory frame in the same direction as the photon with a very small opening angle. Therefore q_T is close to zero. The position of the photon candidates at low q_T is clearly visible, they are well separated from the other contributors to the V^0 sample. Since electrons and positrons have the same mass, the distribution is symmetric in α. This can also be seen for K^0_s, which decays into $\pi^+\pi^-$, but not for $\Lambda \longrightarrow \pi^- p$ and $\bar{\Lambda} \longrightarrow \pi^+ \bar{p}$, respectively, where the proton (antiproton) takes on average a larger part of the momentum. It has been found that the V^0 has been sufficiently pure, see figure 5.10, therefore the q_t cut is let open to 1 GeV/c.

For further selection of photons in the reconstructed V^0 sample a reconstruction package for fitting decay particles (*AliKFParticle*) [Gor2007] has been used. The reconstructed tracks are treated as electron and positron with mass $m_{e^\pm} = 0.511\,\mathrm{MeV/c^2}$ [Nak2010]. Furthermore, the V^0 mass is forced to be zero. This condition leads to the asymmetric band in the left of the Armenteros-Podolanski plot. The last constraint is applied on the momentum vector of the V^0. It is required to point back to the primary vertex. Under those conditions a fit is performed. Only V^0s with a $\chi^2/NDF < 30$ are taken into account for the meson reconstruction. As a last step the transverse momentum of the photon must be at least 0.1 GeV/c.

In summary, the applied steps to clean the V^0 sample are:

1. Like-sign check for the track pair to avoid e^-e^- and e^+e^+ pairs.
2. Refit in the TPC.
3. Rejection of kink topologies.
4. Cut on radial distance $r \leq 180\,\mathrm{cm}$.
5. Cut on lower radial distance $r \geq 5\,\mathrm{cm}$.
6. Cut on $r < |z| * slope - z_0$, where $z_0 = 7\,\mathrm{cm}$ and $slope = \tan(2 \cdot \arctan(e^{|\eta|}))$ (Line cut).
7. Cut on $|z| \leq 240\,\mathrm{cm}$.
8. Cut on $|\eta| < 0.9$.

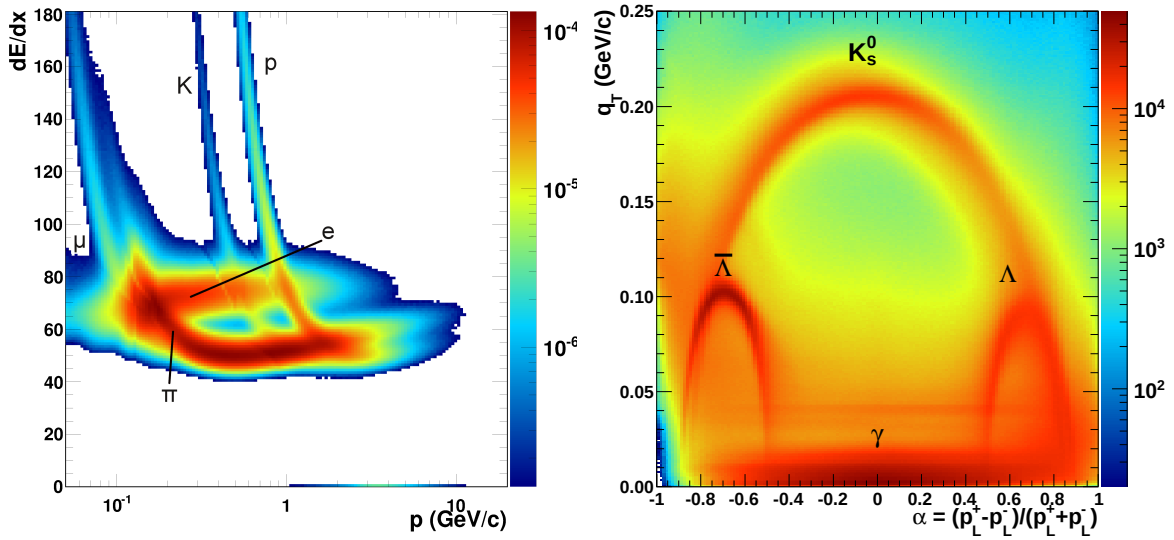

Figure 5.6.: Left: $\mathrm{d}E/\mathrm{d}x$ distribution in the TPC as a function of particle momentum for the complete V^0 sample, measured at $\sqrt{s} = 7\,\mathrm{TeV}$. Besides the electron distribution the distributions for pions, kaons and protons can be seen. Right: Armenteros-Podolanski plot for the complete V^0 sample measured at $\sqrt{s} = 7\,\mathrm{TeV}$. The single contributors K^0_s, Λ, $\bar{\Lambda}$ and photons are clearly visible in their characteristic distribution.

9. Cut on specific energy loss hypothesis for electrons $]-4\,\sigma_{\mathrm{dEdx}}, +5\,\sigma_{\mathrm{dEdx}}[$.

10. Cut on specific energy loss hypothesis for pions $]-\infty\,\sigma_{\mathrm{dEdx}}, +2\,\sigma_{\mathrm{dEdx}}[$ within a momentum range of $0.25\,\mathrm{GeV/c} < p < 3.5\,\mathrm{GeV/c}$ and $]-\infty\,\sigma_{\mathrm{dEdx}}, +0.5\,\sigma_{\mathrm{dEdx}}[$ above a momentum $p = 3.5\,\mathrm{GeV/c}$.

11. Cut on $q_T \leq 1\,\mathrm{GeV/c}$.

12. Cut on the number contributors to the primary vertex $N \geq 1$.

13. Cut on the ratio of found to findable clusters in the track reconstruction ≥ 0.35.

14. Cut on transverse momentum for reconstructed tracks $p_T \geq 50\,\mathrm{MeV/c}$.

15. Cut on number of degrees of freedom on the reconstructed V^0 NDF ≥ 0 in the fitting routing.

16. Cut on maximum $\chi^2/NDF \leq 30$.

17. Cut on transverse momentum for reconstructed V^0s $p_T \geq 100\,\mathrm{MeV/c}$.

Figure 5.7 summarizes the effect of the cuts ϵ_{Cut} applied to the V^0 sample and provides a comparison of data and simulation. The number of reconstructed V^0 corresponds to 100 %.

The geometrical cuts reduce the V^0 sample by $\approx 65\,\%$. These cuts do not only decrease the amount of material and thus the number of conversions, they also reduce the number of K^0_s, Λ, $\bar{\Lambda}$ in the V^0 sample. The difference between data and simulation after these cuts mainly results from the imperfect implementation of the material budget in the simulations for $|\eta| < 0.9$, see figure 5.4. The next major influence on the V^0 sample comes from the cut on the specific energy loss hypothesis of the particles. It reduces the sample by another 25 %. The effect on data and simulation is similar, both differ by about 3 %. The constraints on mass and momentum vector

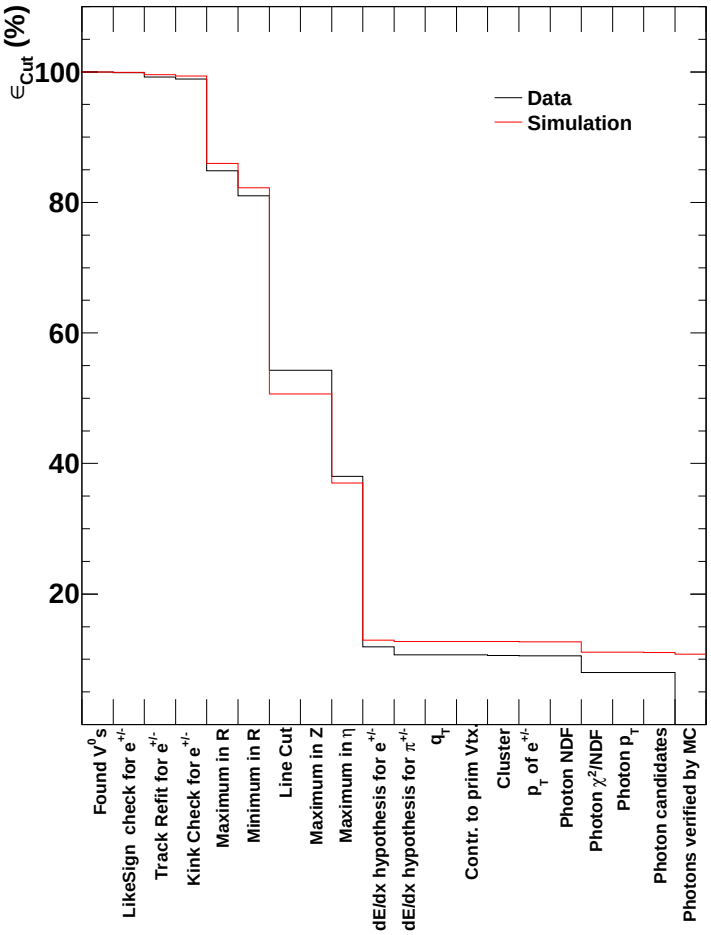

Figure 5.7.: Influence of the cuts ϵ_{Cut} on the V^0 sample, here black represents the data and red simulations.

of the V^0 have an influence of $2-3\,\%$, data and simulation differ by about $1\,\%$. At last, the remaining V^0 are verified to be photons by their Monte Carlo information. This can only be done in simulation, thus no entry for data is given. The verification reduces the V^0 sample by less than $1\,\%$. Therefore, the remaining V^0s are assumed to be real photons in data, too.

The purity of the photon candidates ($\epsilon_{Pur.}$) is given by the fraction of reconstructed true photons (verified with the Monte Carlo information) to all reconstructed photons candidates $\epsilon_{Pur.} = \gamma_{reco.,true}/\gamma_{rec.}$. The ratio is shown in figure 5.8 for simulations at $\sqrt{s} = 7\,\text{TeV}$. It is above $96\,\%$ for $p_T < 3\,\text{GeV/c}$. For a larger transverse momenta the purity decreases steeply down to $\approx 55\,\%$ at $10\,\text{GeV/c}$. Here the charged-pion rejection enters. In the momentum range $0.25 - 3.5\,\text{GeV/c}$ a strong pion rejection can be applied, for higher p_T only a weak rejection is possible, since the specific energy loss hypotheses for electrons and pions come very close.

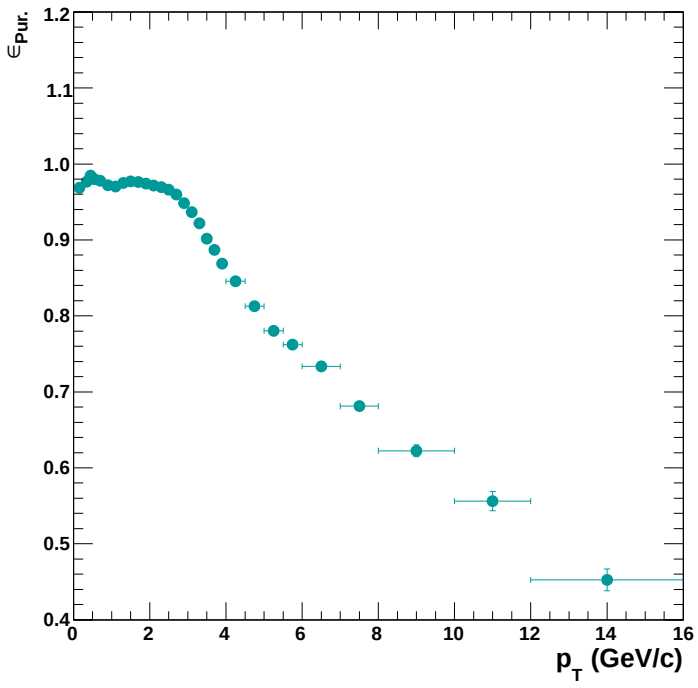

Figure 5.8.: Purity of the photon candidates after all cuts as a function of transverse momentum at $\sqrt{s} = 7\,\text{TeV}$.

5.3. Characteristics of the remaining photon candidates

The ALICE detector is designed with a minimal amount of detector material to avoid multiple scattering effects. This leads to a low conversion probability P, which is defined as the fraction of converted to all generated photons $P = \gamma_{conv.}/\gamma_{all}$, presented in figure 5.9 (left). Within the pseudo-rapidity range of $|\eta| < 0.9$ and $5\,\text{cm} \leq R \leq 180\,\text{cm}$, P is about 8.7 %. The drop in the conversion probability towards low transverse momentum results from the dependence of the cross section on the traversed material, as explained in section 3.1 and shown in figure 3.4. Figure 5.9 (right) shows the reconstruction efficiency $\epsilon_{reco.}$ for the remaining photon candidates in three cases:

Reconstructed true photons before cuts:	$\epsilon_{reco.} = \frac{\gamma_{reco.,w/ocut}}{\gamma_{all}}$	(green)
Reconstructed true photons after cuts:	$\epsilon_{reco.} = \frac{\gamma_{reco.,true}}{\gamma_{all}}$	(dark blue)
Reconstructed photons without verification:	$\epsilon_{reco.} = \frac{\gamma_{reco.}}{\gamma_{all}}$	(light blue)

The green curve shows the highest possible reconstruction efficiency for photons. It is calculated for all V^0 verified as photons in simulations but before cuts, with an average of about $\approx 80\,\%$. The dark blue points correspond to the efficiency for remaining photon candidates after all cuts. It reaches $\approx 65-70\,\%$ in the transverse momentum range of $2-4\,\text{GeV/c}$ and saturates at $\approx 65\,\%$ at high transverse momentum. The difference between both curves gives an estimate of the loss of photons due to the applied cuts. Depending on the transverse momentum range it varies from about 10 % (low p_T) to 20 % (high p_T). At very low transverse momentum of less than $1\,\text{GeV/c}$ the loss is rather negligible. The light blue curve shows the reconstruction efficiency for all photon candidates after cuts and without MC verification. Since it includes fake photons the reconstruction efficiency $\epsilon_{reco.}$ can reach values higher than 100 % as one can see for high transverse momenta.

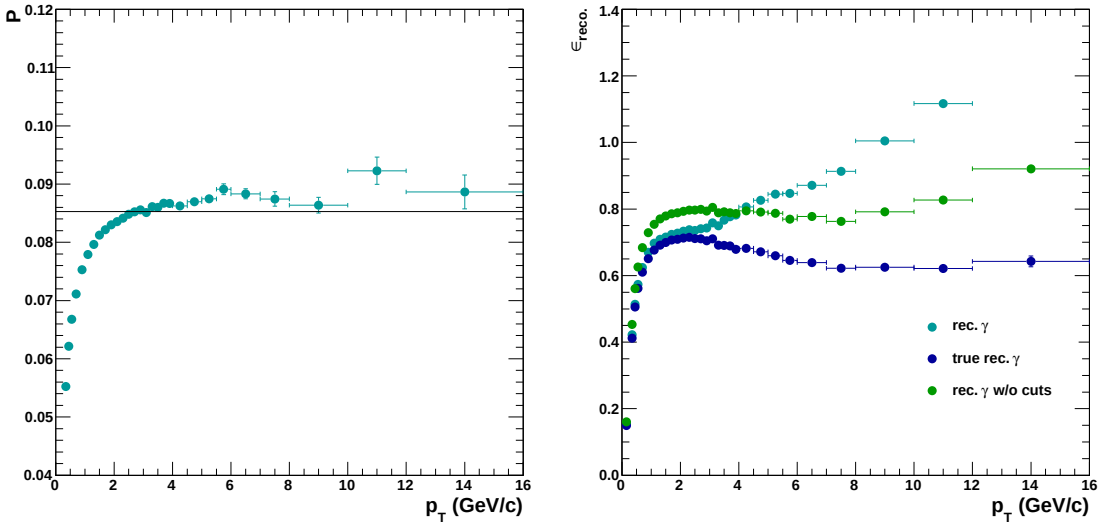

Figure 5.9.: Conversion probability (left) and reconstruction efficiency (right) for photons as functions of transverse momentum within $|\eta| < 0.9$ and $5\,\text{cm} \leq R \leq 180\,\text{cm}$ at $\sqrt{s} = 7\,\text{TeV}$. The reconstruction efficiency is shown for true photons before cuts (green), reconstructed true photons after cuts (dark blue), and all remaining photon candidates after cuts. (light blue).

Figure 5.10 shows the specific energy loss (left) and the Armenteros-Podolanski plot (right) after all cuts. The influence of the cuts is clearly visible compared to figure 5.6. The main fraction of pions, kaons and protons above the electron hypothesis disappeared, as well as the band from pions below. Further constraints on the energy loss hypothesis for kaons and protons were not applied, the bands are still visible, but with much reduced intensity. In the Armenteros-Podolanski plot the remaining contributions are mainly located at $q_T < 0.07\,\text{GeV/c}$ and come predominantly from photons. Therefore, it was not necessary to use the power of a q_T cut.

The distribution of the photon candidates in pseudo-rapidity as well as the comparison of data and simulation is shown in figure 5.11 (left). It reflects the increasing amount of detector material with increasing η. The peak at $\eta \approx 0$ is caused by the frame of the TPC central electrode. A difference between data and simulation can be seen at positive η. Checks on the implementation of the detector material in simulations are ongoing. The photon candidates reach for the given statistic a transverse momentum up to $50\,\text{GeV/c}$, shown in figure 5.11 (right). Nevertheless, the main fraction has a p_T of the order of $0.1 - 2\,\text{GeV/c}$. Up to $p_T \approx 10\,\text{GeV/c}$ data and simulation agree, above the simulated spectrum decreases faster than the real spectrum.

The comparison of the χ^2 distribution of the photon candidates between data and simulation is given in figure 5.12 (left). Both stop at 120 which corresponds to the applied cut of $\chi^2/NDF \leq 30$. Below $\chi^2 = 20$ data and simulation agree, above the photon candidates from data show a lower decrease and differ by a factor 2 at $\chi^2 = 120$. The resulting difference in the efficiency for the χ^2 is about 1 %, as shown in figure 5.7. Figure 5.12 (right) shows the invariant mass distribution $M_{e^+e^-}$ for the photon candidates. Almost all remaining particles have an invariant mass less than $150\,\text{MeV/c}^2$, they are mostly distributed below $50\,\text{MeV/c}^2$. Above this invariant mass, data and simulation start to differ. The simulated mass distribution falls off more steeply and thus it is narrower.

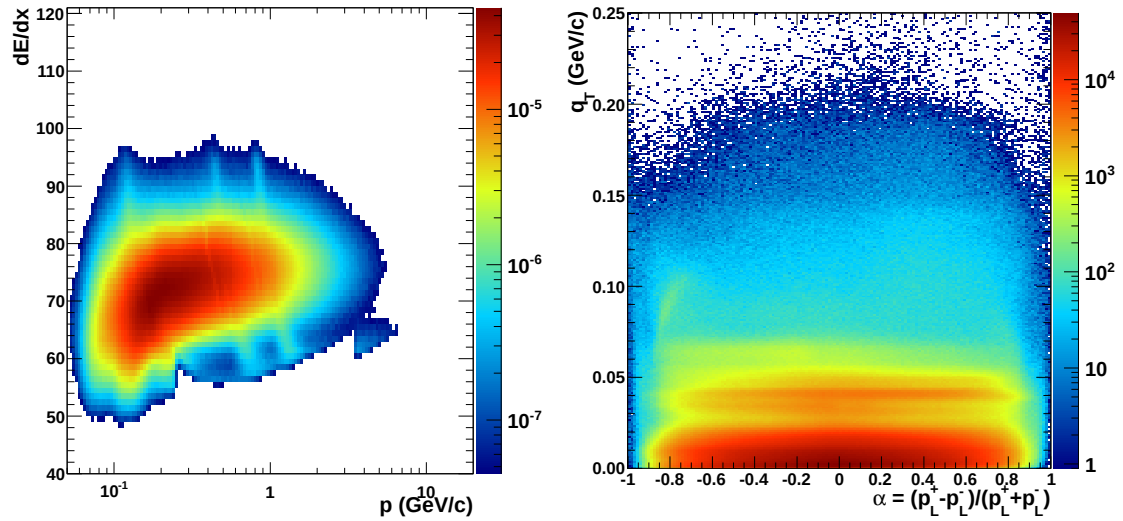

Figure 5.10.: Left: $\mathrm{d}E/\mathrm{d}x$ distribution as a function of particle momentum after all cuts. Tracks outside of ${}^{+5}_{-4}\sigma_{\mathrm{d}E\mathrm{d}x}$ of the electron hypothesis and within ${}^{+2}_{-\infty}\sigma_{\mathrm{d}E\mathrm{d}x}$ for a momentum range of $0.25\,\mathrm{GeV/c} < p < 3.5\,\mathrm{GeV/c}$ and within ${}^{+0.5}_{-\infty}\sigma_{\mathrm{d}E\mathrm{d}x}$ above a momentum $p = 3.5\,\mathrm{GeV/c}$ of the pion hypothesis are rejected. Right: Armenteros-Podolanski plot for the remaining V^0 sample. The contributions from K^0_s, Λ and $\bar{\Lambda}$ mainly disappeared. Both figures for measured data at $\sqrt{s} = 7\,\mathrm{TeV}$.

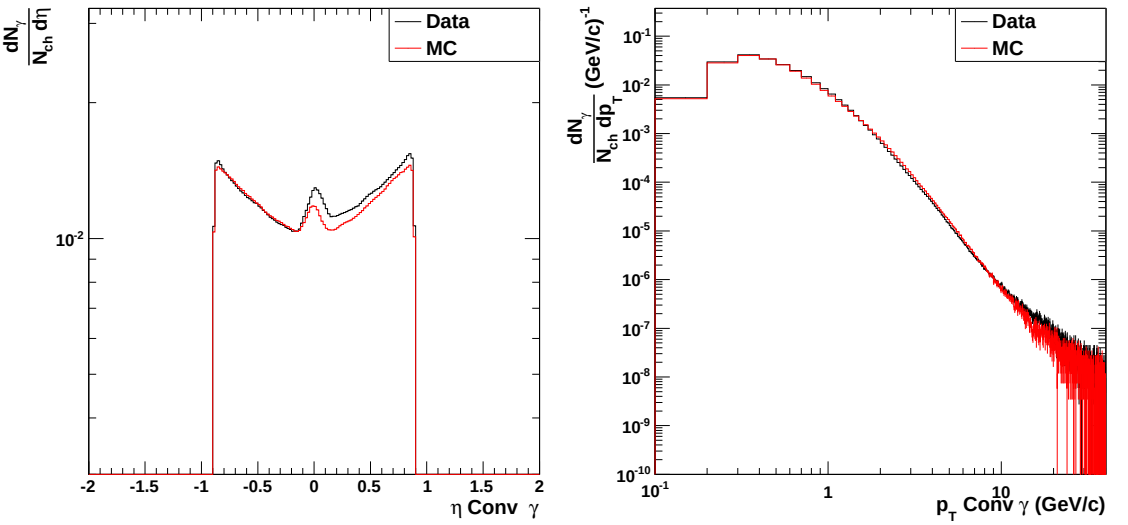

Figure 5.11.: η (left) and transverse momentum distribution (right) of the photon candidates at $\sqrt{s} = 7\,\mathrm{TeV}$, both normalized to charged multiplicity and bin width. Data are drawn in black, simulation in red.

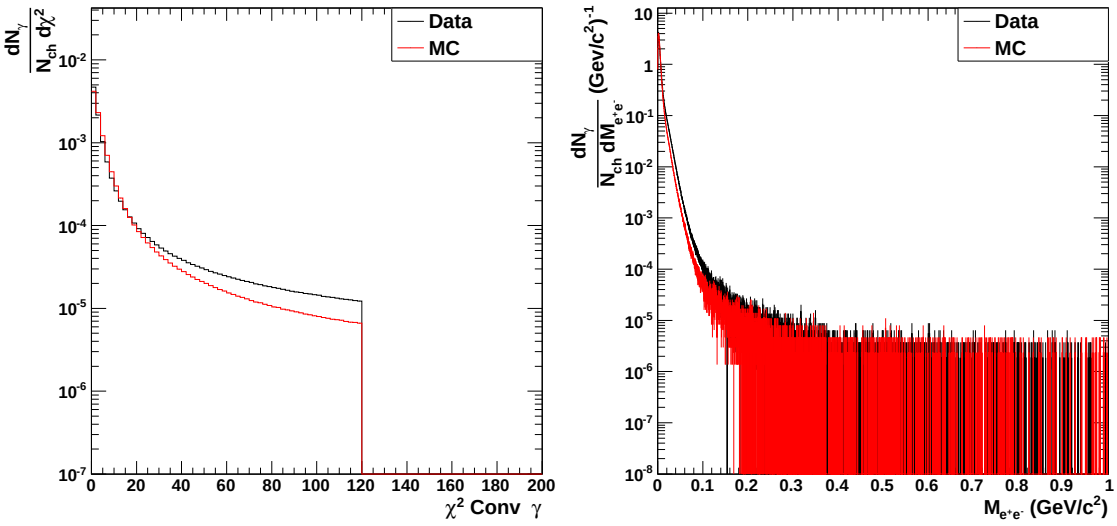

Figure 5.12.: χ^2 (left) and invariant mass $M_{e^+e^-}$ distribution (right) of the photon candidates at $\sqrt{s} = 7\,\text{TeV}$, both normalized to charged multiplicity and bin width. Data are drawn in black, simulation in red.

5.4. Neutral meson reconstruction in the $\gamma\gamma$ channel

5.4.1. Meson reconstruction

Once the photon candidates are extracted from the V^0 sample, they are combined into pairs. During the pairing photon pairs with a common track are excluded. Additionally the opening angle between both photons is required to be larger than 5 mrad.

The invariant-mass spectrum of the photon pairs is used to identify neutral pions and η mesons. It is given by

$$M_{\gamma\gamma} = \sqrt{2E_{\gamma 1}E_{\gamma 2}(1-\cos\theta_{12})}. \tag{5.1}$$

$E_{\gamma 1,2}$ represents the energy of the decay photons and θ_{12} their opening angle in the laboratory frame. For photon pairs coming from π^0 or η decay the invariant mass has to be equal within resolution to their rest mass, $0.135\,\mathrm{GeV/c^2}$ for π^0 and $0.548\,\mathrm{GeV/c^2}$ for the η meson.

Figure 5.13 shows the invariant mass distribution of the reconstructed photon pairs versus their transverse momenta measured at the center-of-mass energy $\sqrt{s} = 7\,\mathrm{TeV}$. Both mesons can clearly be seen. To extract the meson raw yields this distribution is divided into small ranges of transverse momentum, so-called *bins*, and projected onto the mass axis. In figure 5.14 a projection is given for photon pairs with a transverse momentum $p_T^{\gamma\gamma} > 0.4\,\mathrm{GeV/c}$. Clear peaks at the π^0 and η rest masses appear on top of a combinatorial background. Moreover, it can be seen that the distribution around the peaks is not purely Gaussian. A tail on the left side appears, resulting from electron (positron) bremsstrahlung. The corresponding figures for the center-of-mass energies $\sqrt{s} = 0.9$ and 2.76 TeV are given in appendix D.

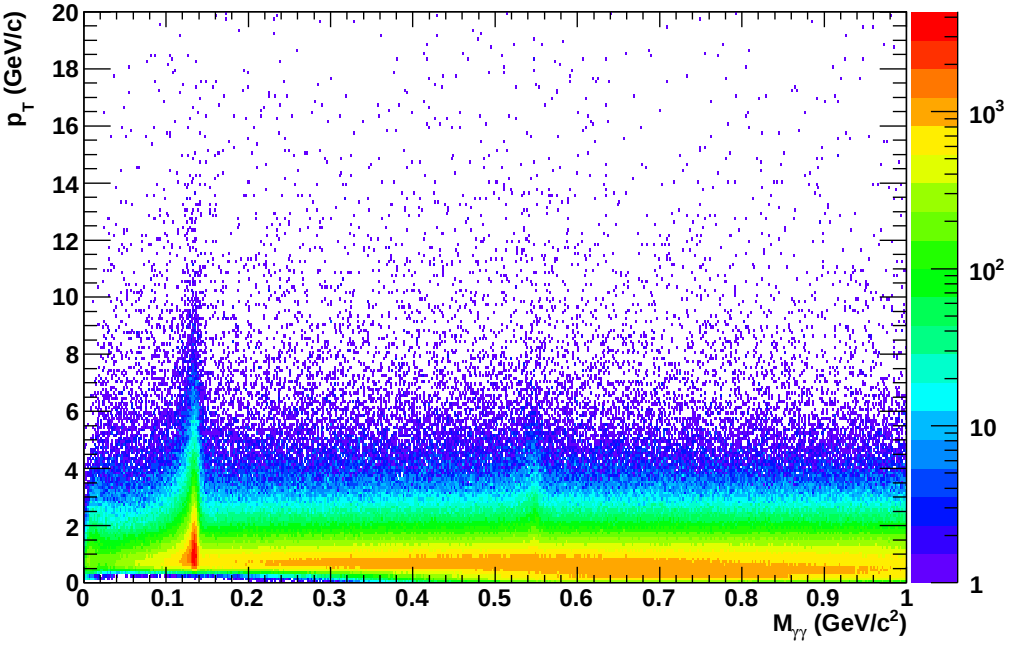

Figure 5.13.: Invariant-mass distribution of reconstructed photon pairs $M_{\gamma\gamma}$ versus their transverse momentum for $\sqrt{s} = 7\,\mathrm{TeV}$. Neutral pions and η mesons can be seen at their rest masses of $0.135\,\mathrm{GeV/c^2}$ and $0.548\,\mathrm{GeV/c^2}$, respectively.

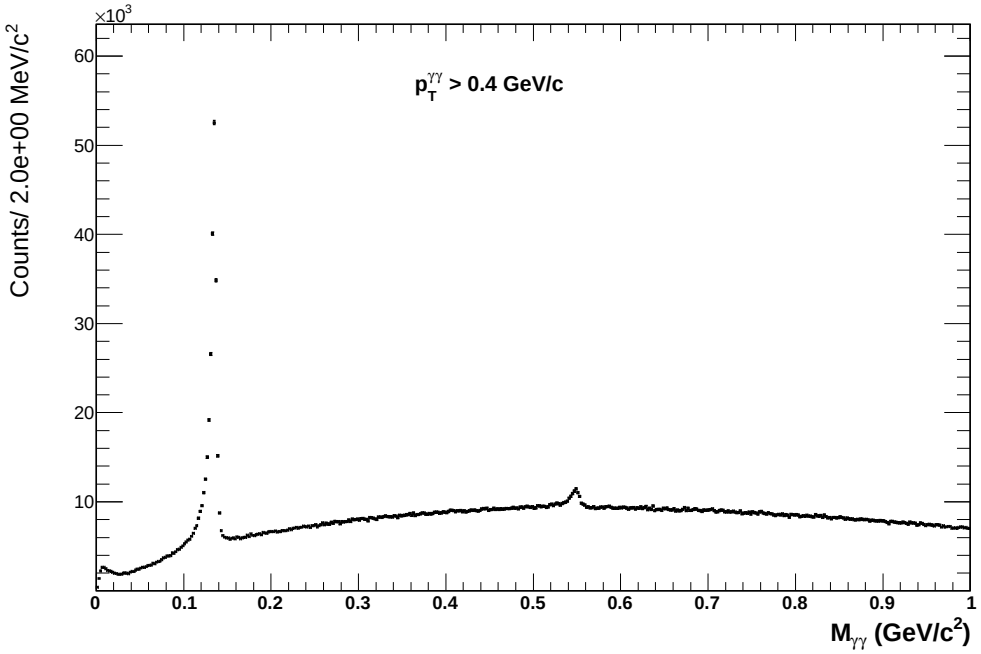

Figure 5.14.: Invariant-mass distribution of reconstructed photon pairs $M_{\gamma\gamma}$ with $p_T > 0.4\,\mathrm{GeV/c}$ at $\sqrt{s} = 7\,\mathrm{TeV}$. Peaks at the rest masses of π^0 and η mesons are clearly visible. Moreover, a tail on the left peak side can be seen, resulting from $e^{\pm}$ bremsstrahlung.

For the determination of the combinatorial background several algorithms were studied. A detailed description of the methods is given in section 5.4.2. At present a mixed-event technique within the same photon multiplicity and Z vertex position range (so-called *classes*) describes the background shape best.

The resulting invariant-mass distributions after subtraction of the calculated combinatorial background are fitted with a Gaussian function combined with an exponential low-energy tail on the left side to account for electron bremsstrahlung. A linear part is added, in case the calculated combinatorial background does not fully describe the background shape of the signal:

$$y = A \cdot \left[G + \exp\left(\frac{M_{\gamma\gamma} - M_{\pi^0(\eta)}}{\lambda} \right) \Big(1 - G \Big) \theta\Big(M_{\pi^0(\eta)} - M_{\gamma\gamma} \Big) \right] + B + C \cdot M_{\gamma\gamma} \tag{5.2}$$

$$\text{with} \quad G = \exp\left[-\frac{1}{2} \left(\frac{M_{\gamma\gamma} - M_{\pi^0(\eta)}}{\sigma} \right)^2 \right] \tag{5.3}$$

where G is a Gaussian function with width σ, amplitude A and measured value $M_{\pi^0(\eta)}$. λ is the inverse slope of the exponential function. This part is switched off by the Heavyside function $\theta(M_{\pi^0(\eta)} - M_{\gamma\gamma})$ above $M_{\pi^0(\eta)}$. B and C are the parameters of the linear function.

Figure 5.15 shows examples of the invariant-mass distributions before (left) and after (right) subtraction of the calculated combinatorial background. For π^0 (top) it is given in the transverse momentum bin $3.0 - 3.2\,\mathrm{GeV/c}$, for η (bottom) in $2.2 - 2.6\,\mathrm{GeV/c}$. The black points correspond to data, the dark blue line to the calculated combinatorial background. The cyan line presents the shape of the fit function, eq. 5.3 with 5.3. In case of the neutral pions the calculated combinatorial background agrees with the background shape of the reconstructed signal (top left), after subtraction the distribution outside of the peaks is zero (top right). The shape of the peak is well described by the fit function. In the bottom of figure 5.15 both distributions are shown for the η meson. Here the calculated combinatorial background does not

agree with the distribution of the reconstructed signal (bottom left). After its subtraction the distribution still shows remaining background (bottom right). This contribution is subtracted in the determination of the yield using the linear function in the fit. The corresponding figures for the meson spectra at the collision energies $\sqrt{s} = 0.9\,,\ 2.76$ and $7\,\text{TeV}$ are given in appendix F.

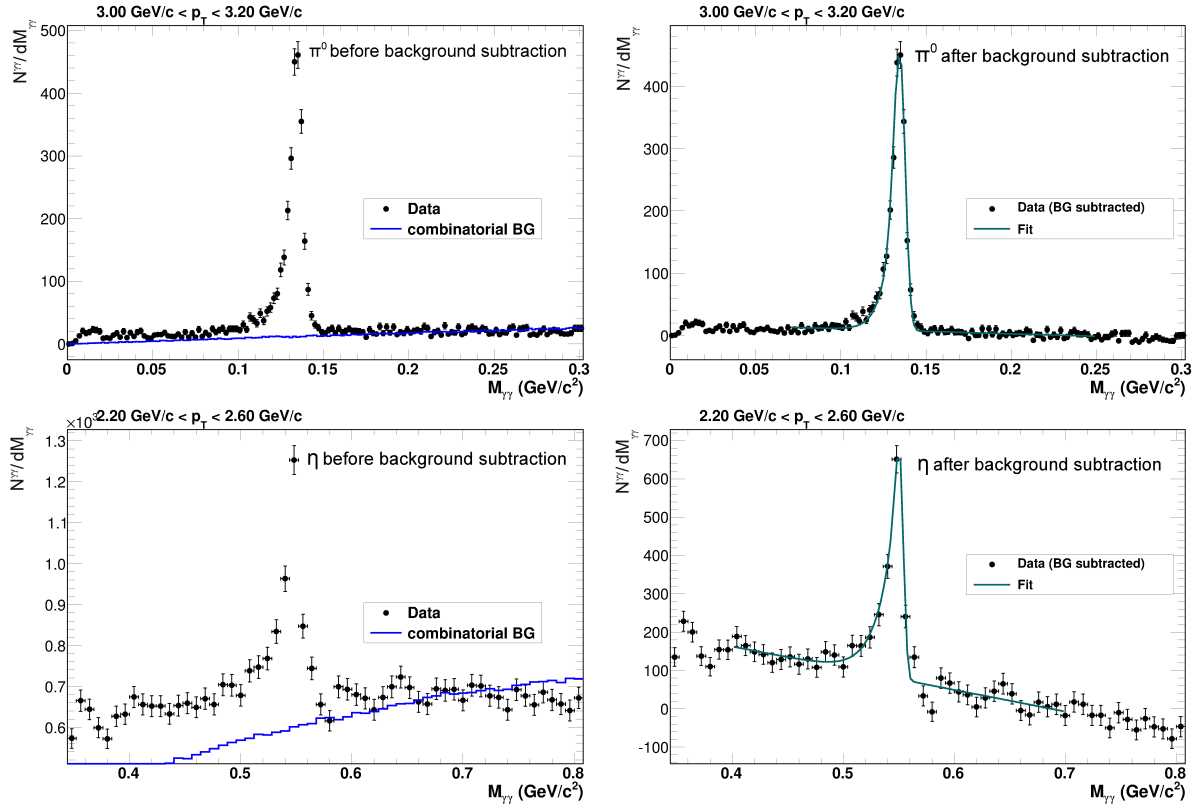

Figure 5.15.: Invariant-mass distribution in single transverse momentum bins. On top the distributions for π^0 before (left) and after (right) background subtraction are shown, in the bottom for the η meson. The blue lines in the distributions before background subtraction correspond to the calculated combinatorial background, the blue-green lines in the distributions after background subtraction correspond to the fit result.

To extract the meson yields the invariant mass spectra are integrated in a mass range around the fitted peak position. The remaining linear background is subtracted, as given in equation 5.4 for neutral pions. For π^0 the mass range covers $(m_{\pi^0} - 0.035\,\text{GeV/c}^2,\ m_{\pi^0} + 0.010\,\text{GeV/c}^2)$, for η $(m_\eta - 0.047\,\text{GeV/c}^2,\ m_\eta + 0.023\,\text{GeV/c}^2)$.

$$N^{\pi^0}_{raw} = \int_{m_{\pi^0}-0.035\,\text{GeV/c}^2}^{m_{\pi^0}+0.010\,\text{GeV/c}^2} (N^{\gamma\gamma} - N^{comb.BG})\mathrm{d}M_{\gamma\gamma} - \int_{m_{\pi^0}-0.035\,\text{GeV/c}^2}^{m_{\pi^0}+0.010\,\text{GeV/c}^2} (B + C \cdot M_{\gamma\gamma})\mathrm{d}M_{\gamma\gamma} \qquad (5.4)$$

The resulting raw yields for π^0 and η mesons at the different energies are shown in figure 5.16. The yields are normalized by the bin width and the number of analyzed events. Two aspects can be seen. Firstly, the reach in transverse momentum is determined by the given statistics. Secondly, the number of particles per bin grows with center-of-mass energy. The measured transverse-momentum ranges for each collision energy and the analyzed number of events are given in table 5.1.

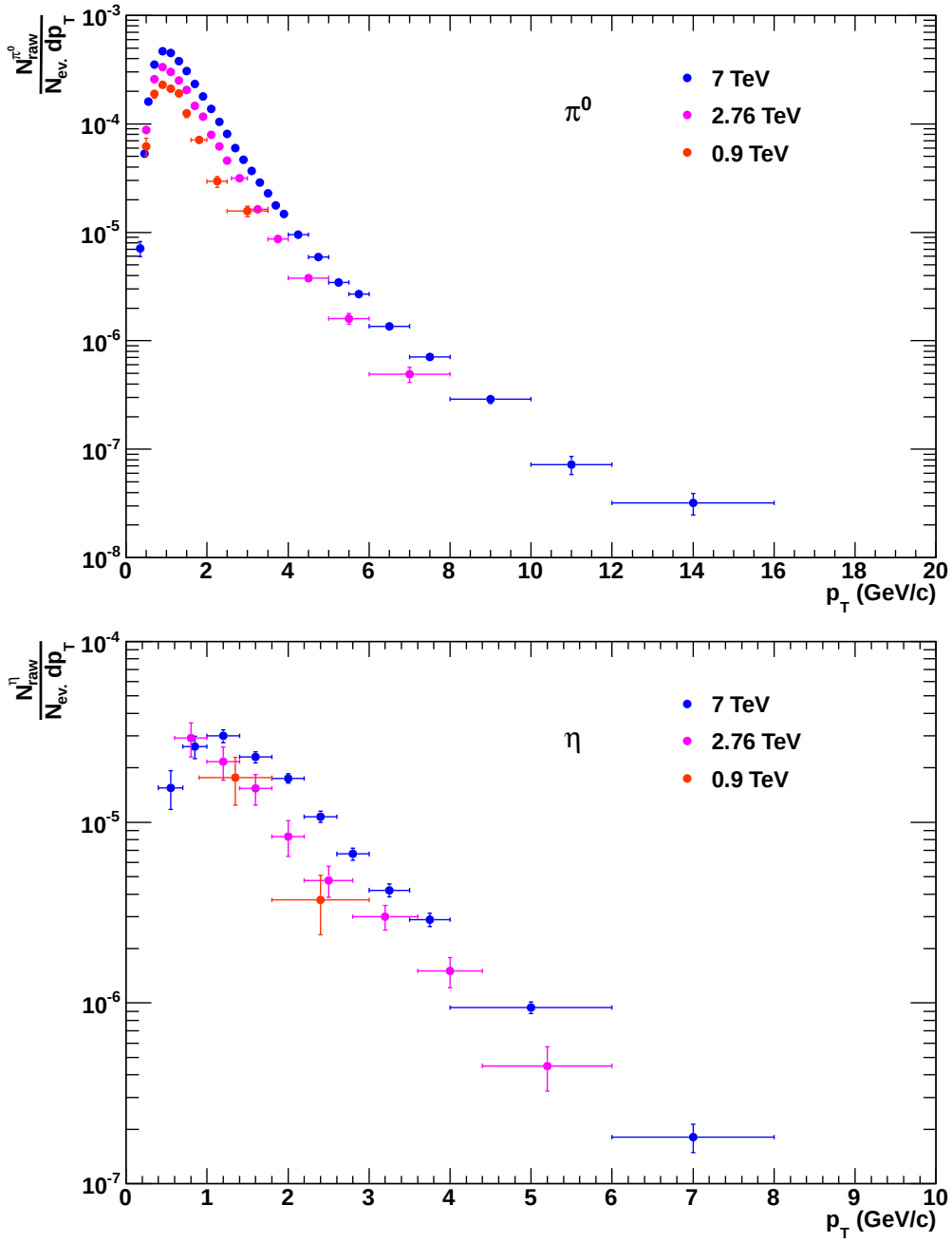

Figure 5.16.: Raw yields for π^0 (top) and η mesons (bottom) at $\sqrt{s} = 0.9$,(red) 2.76 (magenta) and $\sqrt{s} = 7$ TeV (blue) as functions of transverse momentum. A dependence of the extracted raw yield on the collision energy is visible. The p_T reach is limited by statistics.

$\sqrt{s}$ (TeV)	π^0 p_T (GeV/c)	η p_T (GeV/c)	Events
0.9	0.4 - 3.5	0.9 - 3.0	6.9×10^6
2.76	0.4 - 8.0	0.6 - 6.0	6.5×10^7
7	0.3 -16.0	0.4 - 8.0	3.8×10^8

Table 5.1.: Transverse-momentum range for π^0 and η meson reconstruction at different pp collision energies presented here.

The significance S^{π^0} (S^{η}) is defined as $Signal/\sqrt{Signal + Background}$ and is extracted in the range ($M^{\pi^0(\eta)}$−FWHM$^{\pi^0(\eta)}$/2.36, $M^{\pi^0(\eta)} + 1\sigma$). It is shown in figure 5.17 for the center-of-mass energy $\sqrt{s} = 7\,\text{TeV}$. For neutral pions it reaches about 33 and for η mesons about 13. For both mesons the maximum lies at the transverse momentum of about 1 GeV/c.

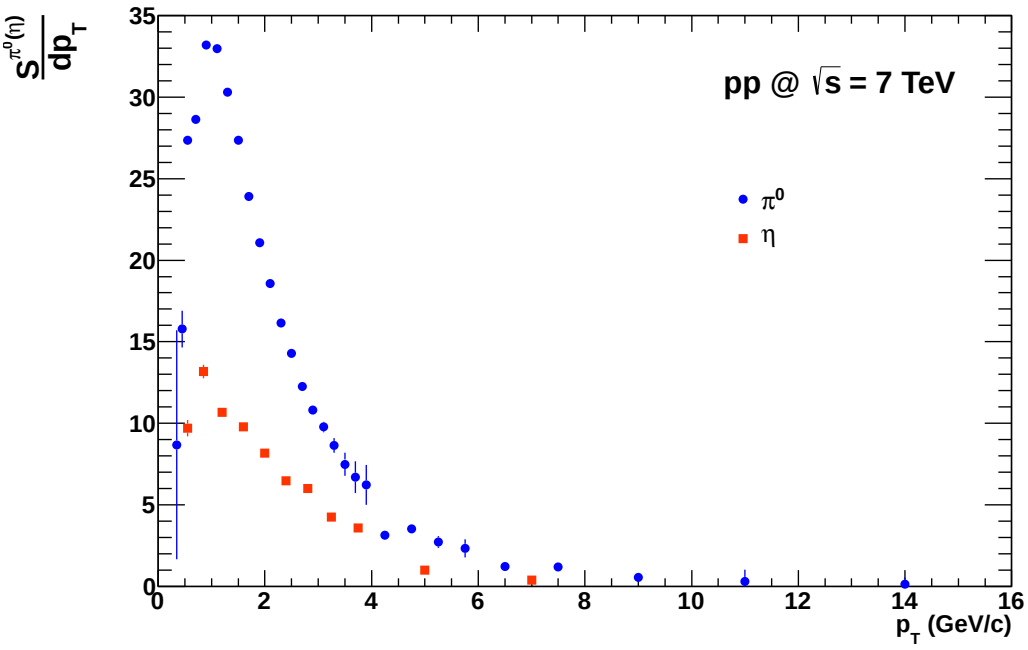

Figure 5.17.: Significance $S = Signal/\sqrt{Signal + Background}$ for π^0 (blue dots) and η mesons (red squares) at $\sqrt{s} = 7\,\text{TeV}$ as functions of transverse momentum.

Figure 5.18 shows the energy asymmetry $\alpha = (|E_{\gamma_1} - E_{\gamma_2}|)(E_{\gamma_1} + E_{\gamma_2})$ for all photon pairs at the center-of-mass energy $\sqrt{s} = 7\,\text{TeV}$. On top the distributions are shown for neutral pions, in the bottom for η mesons. Simulated π^0 (η) decay photons are given by the red squares, measured photon pairs by the black triangles and photon pairs from combinatorial background calculations by blue circles. The distributions of reconstruction signal and background agree between simulation and data. Thus only the distributions for data are shown in figure 5.18. The background has been normalized in the same mass window as done in the raw yield extraction. For simulations the spectra for both mesons are flat up to $\alpha \approx 0.75$. There a slow decrease starts, switching to a rapid drop at 0.95. All energy transfers from the meson to its decay photons are homogeneously distributed, only very asymmetric decays are suppressed. These are characterized by a wide opening angle. Thus one photon may miss the required acceptance range. The uniform distribution results from the fact, that both daughter particles have the same mass, in the present case the mass of photons is zero. In case of the reconstructed signal the energy asymmetry for both mesons decreases slowly until $\alpha \approx 0.7$. Above this value the asymmetry drops steeply due to acceptance and reconstruction efficiency effects. The same behavior has been seen for the normalized combinatorial background. Therefore, a cut using the energy asymmetry distribution within the photon pair would not help to reduce the background and improve the significance.

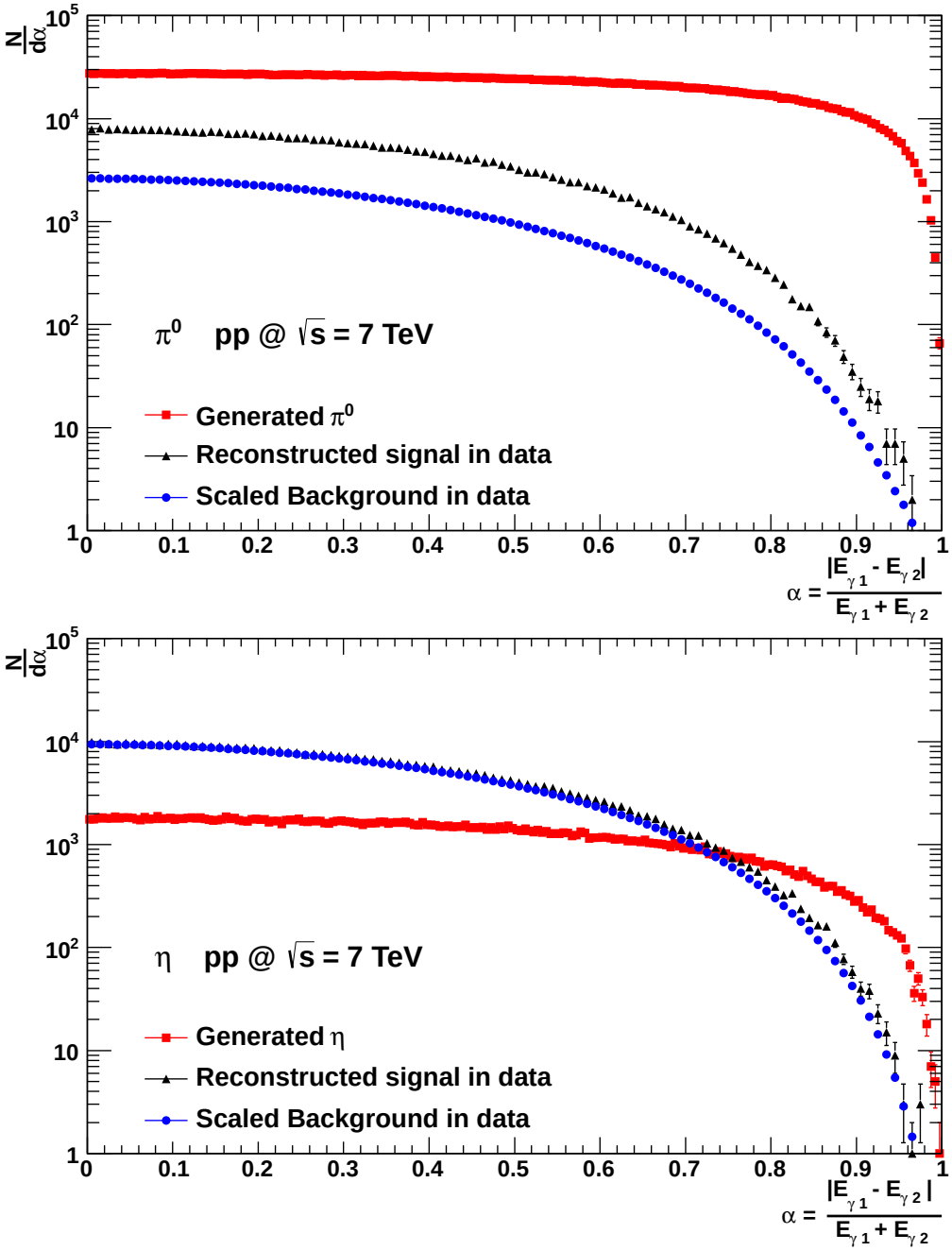

Figure 5.18.: Energy asymmetry distribution $\alpha = (|E_{\gamma_1} - E_{\gamma_2}|)(E_{\gamma_1} + E_{\gamma_2})$ between the decay photons for π^0 (top) and η meson (bottom) at $\sqrt{s} = 7\,\text{TeV}$. The red squares correspond to simulated decay photons, the black triangles to reconstructed signal and the blue circle to the normalized calculated combinatorial background. The shape for reconstructed signal and calculated background agree, thus a cut in the asymmetry would not influence the significance.

In the simulations better mass resolutions were obtained than in data. This translates into a small error on the yield extraction, especially at higher transverse momentum. Therefore a smearing was applied. Each of the momentum components $p_{x,y,z}$ in the simulation is multiplied by $(1 + \sqrt{\sigma_0^2 + \sigma_1^2 \cdot p^2})$, with $\sigma_0 = 0.011$ and $\sigma_1 = 0.007\,\mathrm{c/GeV}$. The extracted meson peak positions and the resolution as a function of transverse momentum for both mesons for $\sqrt{s} = 7\,\mathrm{TeV}$ are shown in figure 5.19. The obtained mass for π^0 (top left) is very close to the reference, for the η meson it is slightly above (bottom left). A very good mass resolution (FWHM/2.36) of less than $4\,\mathrm{MeV/c^2}$ for a transverse momentum below $3\,\mathrm{GeV/c}$ is achieved for the π^0 (top right), increasing linearly up to $10\,\mathrm{MeV/c^2}$ at $16\,\mathrm{GeV/c}$. The increase results from the tracking resolution $\sigma_p/p \propto p$. For the η meson the reached mass resolution is about $7\,\mathrm{MeV/c^2}$ for data and about $10\,\mathrm{MeV/c^2}$ for simulations (bottom right). The same behavior for both mesons has been obtained at $\sqrt{s} = 0.9$ and $\sqrt{s} = 2.76\,\mathrm{TeV}$, shown in appendix D.

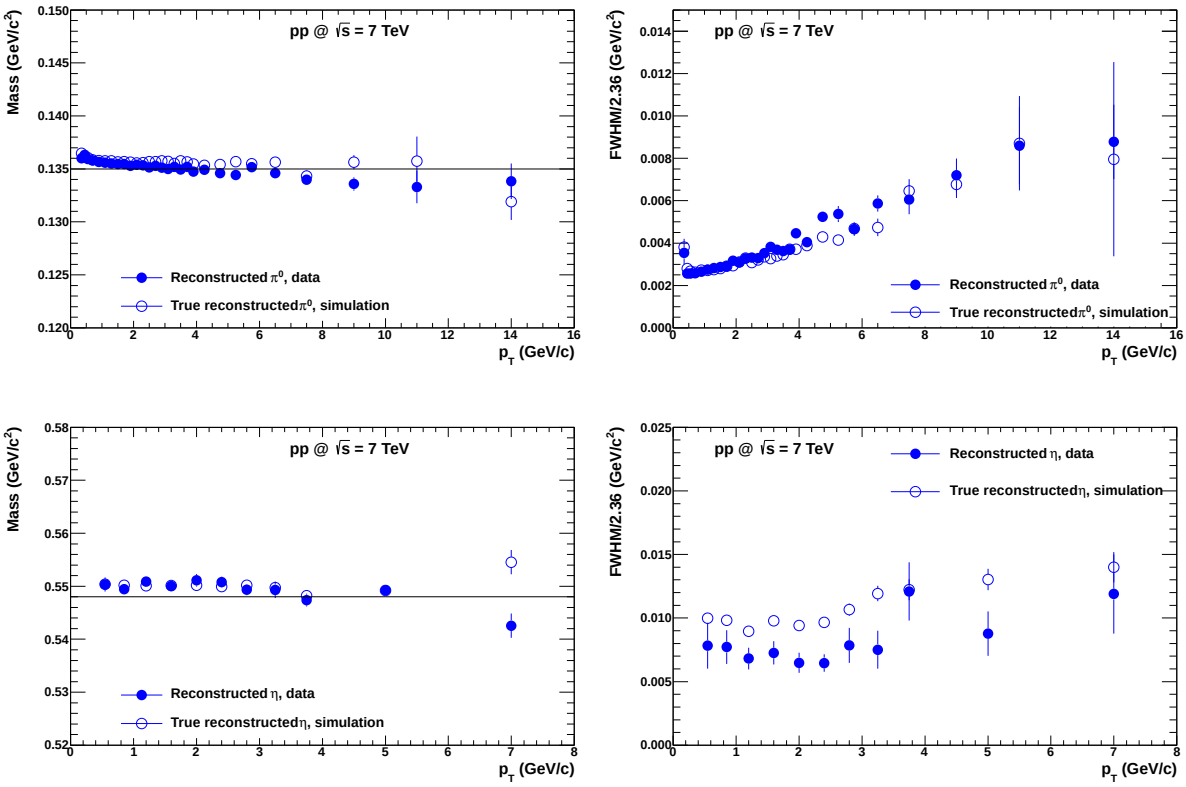

Figure 5.19.: Reconstructed mass (left) and resolution (right) for π^0 (top) and η meson (bottom) as functions for transverse momentum at $\sqrt{s} = 7\,\mathrm{TeV}$. The full symbols correspond to the measured data and open symbols to simulations.

5.4.2. Background evaluation

In order to extract the correct particle yield, the calculated combinatorial background has to describe the shape of the reconstructed signal. In this analysis two main methods have been investigated, a mixed-event technique and a rotation method, see [Aam2011b]. Both methods are described below. It has been found that the combinatorial background in the reconstructed signal changes significantly with looser cuts. The more open the cuts are set the more fake photon candidates will be accepted and used in the analysis. Moreover, the calculated combinatorial background does not match the shape of the reconstructed signal in the full invariant-mass

range $0-1\,\mathrm{GeV/c^2}$. Therefore, the calculated background has been normalized for neutral pions and η mesons in different mass ranges, $[0.17-0.30\,\mathrm{GeV/c^2}]$ for π^0 and $[0.58-0.8\,\mathrm{GeV/c^2}]$ for η, respectively.

For low-transverse momentum photon pairs an unexpected shoulder has been found at $M_{\gamma\gamma}$ near $0\,\mathrm{GeV/c^2}$, getting more pronounced with increasing photon multiplicity in the event. It is believed that this distribution results from jet-like events. In these events many particles are produced in cone-like distributions. A higher amount of reconstructed tracks in a cone may lead to a higher number of fake photons. Combinations of photons, that originate in the jet cone, have a small opening angle and thus low invariant masses. This is taken into account by the rotation method. It is assumed that the jet like events have a dijet topology. However, at present this method fails to describe the invariant-mass distribution at $M_{\gamma\gamma} \approx 0\,\mathrm{GeV/c^2}$.

Mixed event technique

In mixed events any correlations are removed since particles from different events are combined. The calculated combinatorial background turned out to be different for different particle multiplicities. Additionally, a dependence on the primary vertex location in Z and the transverse momentum was found. Two different approaches were tested, in one case the multiplicity has been given by the number of photon candidates, in the other case the charged-particle multiplicity was used. For both approaches the same classes in Z vertex coordinate were used. The events are stored in classes according to

V^0 multiplicity (photon candidates)
2, 3, 4, 5, $\geq$5

Charge particle multiplicity
0-8.5, 8.5-16.5, 16.5-27.5, 27.5-41.5, 41.5-100

Z vertex coordinate
-50.0 - -3.375, -3.375 - -1.605, -1.605 - -0.225, -0.225 - 1.065, 1.065 - 2.245, 2.245 - 50.0

The limits in Z and charged multiplicity are set to have similar statistics in each class. In figure 5.20 the distributions in multiplicity and Z vertex coordinate are shown for reconstructed data at $\sqrt{s} = 7\,\mathrm{TeV}$.

In the event mixing the interaction point for both photon candidates was recalculated. The method uses a buffer of 80 events for each class. In case of a full buffer, the first stored event is removed and the current one is added. All photon candidates from the current event are combined with all candidates from the other stored events. The calculated invariant masses and transverse momenta are filled in a histogram, according to the multiplicity and Z bin.

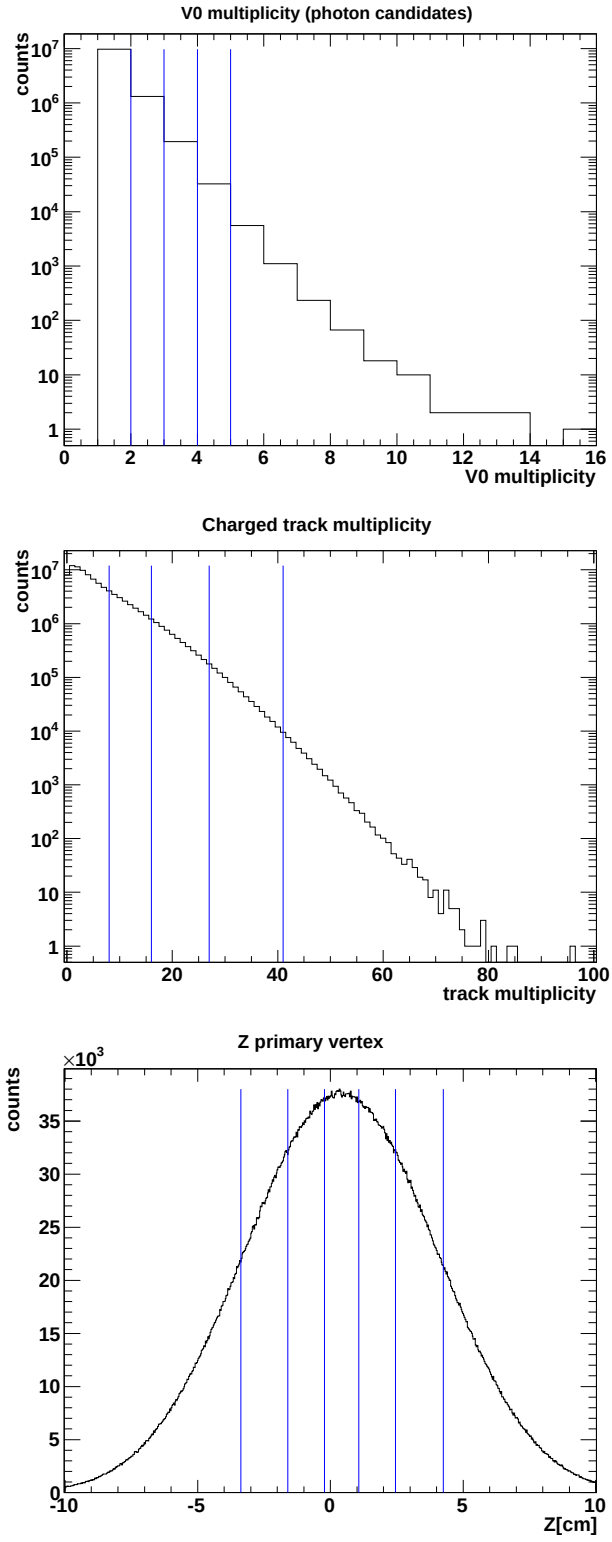

Figure 5.20.: Distributions of number of photon candidates (top), charged particles (center) and Z collision vertices (bottom) that are used for the background evaluation. Vertical lines indicate the bin limits of the classes.

Rotation method

Another possibility to calculate combinatorial background is the Rotation Method. The advantage of this method is that the event topology is kept, although the correlation between the particles is removed. One photon candidate is rotated in ϕ by a random value in a range of $]\pi - \frac{\pi}{9}, \pi + \frac{\pi}{9}[$. The rotation is repeated 20 times per photon candidate. After the rotation the photon candidate is now located in the opposite direction as shown in figure 5.21.

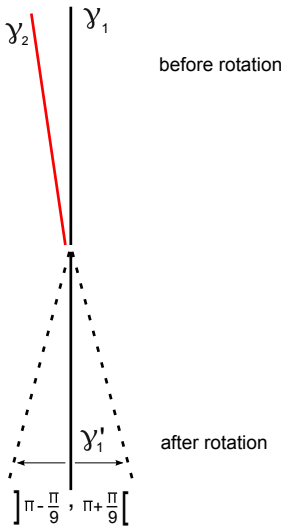

Figure 5.21.: Sketch of the rotation method. One photon from the reconstructed pair is kept in its space coordinates (red), while the other one is rotated by an angle within $]\pi - \frac{\pi}{9}, \pi + \frac{\pi}{9}[$ (black).

Figure 5.22 shows the reconstructed signals and corresponding calculated combinatorial background distributions for the different assumptions. Blue corresponds to background calculated with the rotation method, green to mixed event technique based on charged-particle multiplicity and red to mixed-event technique based on photon candidate multiplicity. In the top the distributions are shown for neutral pions in the lowest transverse-momentum bin at $0.3 - 0.4\,\mathrm{GeV/c}$ (left) and in the highest one, $12.0 - 16.0\,\mathrm{GeV/c}$ (right). The peak near $M_{\gamma\gamma} \approx 0\,\mathrm{GeV/c^2}$ is clearly visible at low p_T, but disappears at high p_T. The calculated background from the rotation method fails to describe the shape of the signal in this range as well as both background spectra from the mixed-event technique. For an invariant mass above $0.07\,\mathrm{GeV/c^2}$ the calculated background spectra are similar and describe the background shape in data. In the high-transverse momentum range the mixed-event technique using the photon candidate multiplicity reflects the shape of the reconstructed signal best. The same method also describes the distribution for the η meson at low transverse momentum, bottom panel. At high transverse momentum the spectra for calculated combinatorial background do not differ much. For the presented final data the mixed-event technique based on photon candidate multiplicity is used.

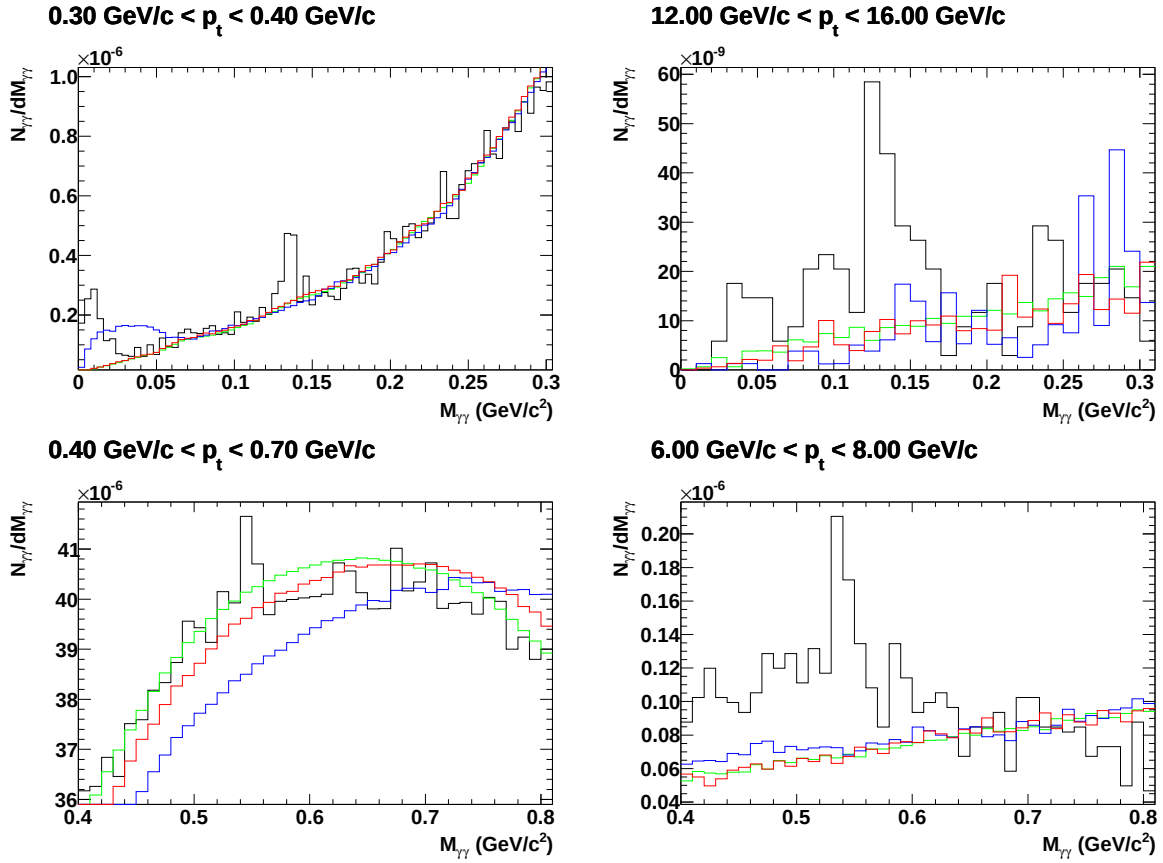

Figure 5.22.: Reconstructed signals and calculated combinatorial background distributions for the different methods. Blue corresponds to the rotation method, green to mixed events within the same track multiplicity and red to mixed events within the same photon candidate multiplicity. On top the distributions are shown for neutral pions, in the bottom for η mesons. For both mesons the spectra are given for the lowest (left) and the highest (right) transverse momentum bin.

5.4.3. Contamination from Dalitz decays and secondary π^0

The single contributions to the invariant-mass distribution $M_{\gamma\gamma}$ have been checked in simulations for $\sqrt{s} = 7\,\text{TeV}$. This is shown in figure 5.23. On top the distributions are shown without a minimum cut in R, in the bottom a cut of $R = 5\,\text{cm}$ has been applied. The black line corresponds to all photon pairs. The green line describes the background from photon pairs where both photons are verified by their MC information. The red line shows combinations where one photon candidate results from a misidentified Dalitz decay $\pi^0(\eta) \longrightarrow e^+e^-\gamma$. The non-photonic electron-positron pair passed all applied cuts. The pink line shows the contribution from secondary π^0. The distributions given in blue correspond to photon pairs coming from the same mother particle (true π^0 and η). With a cut of $R = 5\,\text{cm}$ the contamination from Dalitz decays is largely removed while most of the real photon conversions are kept.

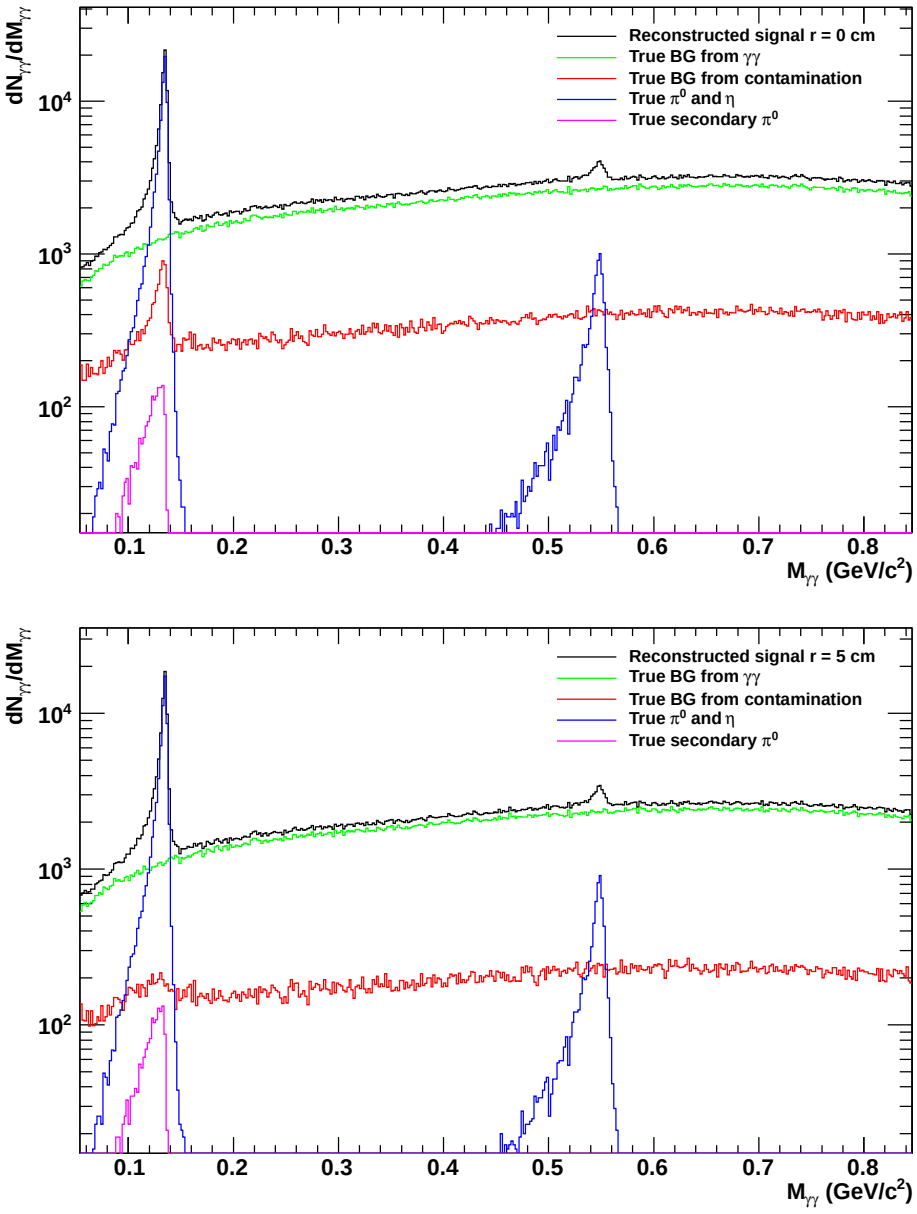

Figure 5.23.: Invariant mass for all photon pairs (black), combinatorial background from true $\gamma\gamma$ pairs (green), combinatorial background where one photon candidate results from a misidentified electron-positron pair of a Dalitz decay (red), for true photon candidate combinations where both photons come from the same mother (blue) and secondary π^0 (pink). In the top the contributions without cut at low R are shown, in the bottom a cut of $R = 5.0\,\mathrm{cm}$ is applied.

5.4.4. Estimation of the systematic uncertainties

This section gives an overview on the estimation of the systematic uncertainties, a full review can be found in [Aam2011a] and [Aam2011c]. The selection of the cut used in the presented analysis, in the following called *standard cut*, was made on the one hand by studying yield and significance of neutral pions for various cuts and on the other hand by optimizing the agreement between Monte Carlo simulations and data. As standard secondary-vertex finder the *on-the-fly* V^0 was chosen due its higher efficiency and the fact that the determined peak position is closer to the known π^0 and η masses and its better mass resolution, see section 4.2.9.

The estimation of the systematic uncertainties has several contributions:

Yield extraction

The systematic uncertainties on the yield extraction have been calculated using different windows for the normalization of the calculated combinatorial background as well as different integration windows around the peak position. In the latter variation differences in background shape and width of the meson peak are taken into account. The variations are listed in table 5.2.

Normalization window	π^0	η
Right side (standard)	(0.17,0.3) GeV/c^2	(0.58,0.8) GeV/c^2
Left side	(0.05,0.08) GeV/c^2	(0.35,0.48) GeV/c^2
Integration range	**π^0**	**η**
standard	(m_{π^0}-0.035,m_{π^0}+0.010) GeV/c^2	(m_η-0.047,m_η+0.023) GeV/c^2
narrow	(m_{π^0}-0.015,m_{π^0}+0.005) GeV/c^2	(m_η-0.032,m_η+0.013) GeV/c^2
wide	(m_{π^0}-0.055,m_{π^0}+0.025) GeV/c^2	(m_η-0.067,m_η+0.033) GeV/c^2

Table 5.2.: Variation of the normalization and integration windows in the invariant mass spectrum for both mesons used for the estimation of the systematic uncertainties in the yield extraction.

PID cuts based on the specific energy loss

The standard cut only accepts electrons (positrons) within $]-4\sigma, +5\sigma[$ around the specific energy loss hypothesis for electrons (positrons). Additionally, a pion rejection within $]-\infty, +2\sigma[$ of the theoretical specific energy loss for pions has been applied in the momentum range of $0.25 - 3.5\,\mathrm{GeV/c}$. Above $p = 3.5\,\mathrm{GeV/c}$ a weak pion rejection within $]-\infty, +0.5\sigma[$ of the pion hypothesis is used. The variations to the standard cut are given in table 5.3.

	Cut B	Cut C	Cut D	Cut E
$\sigma_{\mathrm{d}E/\mathrm{d}x}$ $e^\pm$	]-4,+5[	]-5,+5[	]-5,+5[	]-4,+5[
π p_{min} GeV/c	0.25	0.5	0.4	0.3
π p_{max} GeV/c	3.5	100	3	3.5
$\sigma_{\mathrm{d}E/\mathrm{d}x}$ π within $[p_{min}, p_{max}]$	2	0	2	2
$\sigma_{\mathrm{d}E/\mathrm{d}x}$ π above p_{max}	1	1	-10	-10

Table 5.3.: Variation of the cuts on the specific energy loss hypothesis for electrons (positrons) and pions used for the estimation of the systematic uncertainties in the PID.

Minimal transverse momentum for electron and positrons
For the minimum transverse momentum of electrons and positrons variations of 50 , 75 , 100 and 125 MeV/c have been evaluated where 50 MeV/c has been set as default. Using a minimum p_T of 100 MeV/c or more causes a significant loss in the signal in the first transverse momentum bins for neutral pions. Therefore, these bins have been taken out from the calculation of the systematic uncertainties.

Ratio of found to findable clusters in the TPC
This cut has been introduced to avoid very low momentum tracks, which have either a bad resolution or are not properly reconstructed. This might be caused by crossing the TPC central membrane or other reconstruction difficulties. The ratio has been chosen to be 35 % for the standard cut. For the estimation of the uncertainty it is has been varied to 0 and to 60 %.

χ^2/NDF of photon candidates
The photon candidates used for the meson extraction are required to have a mass close to zero and to point to the primary vertex. With this cut only photon candidates are selected that fulfill the constraints. For the standard cut the value has been set to 30, variations to 15, 20 and 100 have been considered for the calculation of the systematic error.

Asymmetry α for meson
In the presented analysis the full range on the energy asymmetry $\alpha = 0 - 1$ has been used. A cut $\alpha = 0 - 0.7$ has been considered for the systematic error calculation.

Background calculation
For the background calculation three different methods are used (see section 5.4.2):

- Rotation method,
- Mixed event technique with charged track multiplicity and Z classes;
- Mixed event technique with photon multiplicity and Z classes.

The uncertainties due to the choice of the secondary-vertex finder, Monte Carlo event generator, run periods and radial distance to the collision vertex have already been taken into account in the estimation of the systematic uncertainty in the material budget [Boc2010]. These uncertainties amount to $-6.21\%, +3.44\%$.

For the rest of the components the variations have been compared to the standard cut. The difference has been calculated via

$$\Delta = \text{Yield}_{\text{corrected,modified}} - \text{Yield}_{\text{corrected,standard}} \tag{5.5}$$

The error of Δ has been calcuated using eq. 5.6:

$$\sigma_\Delta = \sqrt{|\sigma^2_{\text{Yield}_{\text{corrected,modified}}} - \sigma^2_{\text{Yield}_{\text{corrected,standard}}}|} \tag{5.6}$$

Only in the comparison of the run periods eq. 5.7 has been used since the data set are uncorrelated:

$$\sigma_\Delta = \sqrt{\sigma^2_{\text{Yield}_{\text{corrected,modified}}} + \sigma^2_{\text{Yield}_{\text{corrected,standard}}}} \tag{5.7}$$

For the evaluation of the systematic uncertainties it was checked whether the deviation is significant ($\Delta/\sigma_\Delta > 0.9$). Then the errors were summed quadratically. All errors are calculated as positive and negative deviation from the standard cut. Since only significant deviations count, unphysical fluctuations might appear. In this case the estimated systematic uncertainty of the

component is smoothed with respect to to the neighboring bins. For transverse-momentum bins in the center of the measured spectrum the average of the surrounding bins has been calculated. For transverse-momentum bins at the low or high limit it has been checked for a possible trend. In this case the error has been extrapolated. In case of $\sqrt{s} = 2.76\,\text{TeV}$ the uncertainties of $\sqrt{s} = 7\,\text{TeV}$ except of yield extraction and PID on specific energy loss of the tracks have been used.

In the following the contributions to the uncertainties for each extracted spectrum are briefly discussed. As an example figures 5.24 and 5.25 provide a graphical overview to the positive and negative contributions of the different components at $\sqrt{s} = 7\,\text{TeV}$ for both mesons. The corresponding figures for $\sqrt{s} = 2.76\,\text{TeV}$ and $\sqrt{s} = 0.9\,\text{TeV}$ can be found in the appendix C as well as detailed tables for all measured spectra.

Systematic uncertainties at $\sqrt{s} = 7$ TeV

π^0 Within the full transverse momentum range the main contributions to the systematic uncertainties results from the required transverse momentum of electrons and positrons as well as their specific energy loss and from the χ^2/NDF for the photon candidates. At high transverse momenta also the contributions of yield extraction, required fraction of found to findable clusters in the TPC and the calculation of the combinatorial background are significant.

η Also for the η meson the required transverse momentum of electrons and positrons, the yield extraction as well as the cut on χ^2/NDF for photon candidates are important in the full measured range. At high transverse momenta the main uncertainties come from cuts on the cluster ratio and background calculation. A cut on the asymmetry would slightly lower the spectrum.

Systematic uncertainties at $\sqrt{s} = 2.76$ TeV

For both mesons the systematic uncertainties have been taken from the uncertainties at $\sqrt{s} = 7\,\text{TeV}$, except yield extraction and PID cut on the specific energy loss of the tracks. Thus, the contributions to the systematics come from the same components as before mentioned.

Systematic uncertainties at $\sqrt{s} = 0.9$ TeV

π^0 At $\sqrt{s} = 0.9\,\text{TeV}$ the yield extraction has a high influence on the meson yield as well as the calculation of the combinatorial background and the χ^2/NDF for photon candidates. Furthermore the cut on the minimum transverse momentum of the track has an impact at low transverse momentum while in the high range the specific energy loss is important, too.

η For the η meson, since it could only be extracted in two bins, nearly all variables enter. The largest contributions come from p_T cut on electrons and positrons, their specific energy loss PID cuts, the variation in the χ^2/NDF of the photon candidate and the estimation of the combinatorial background.

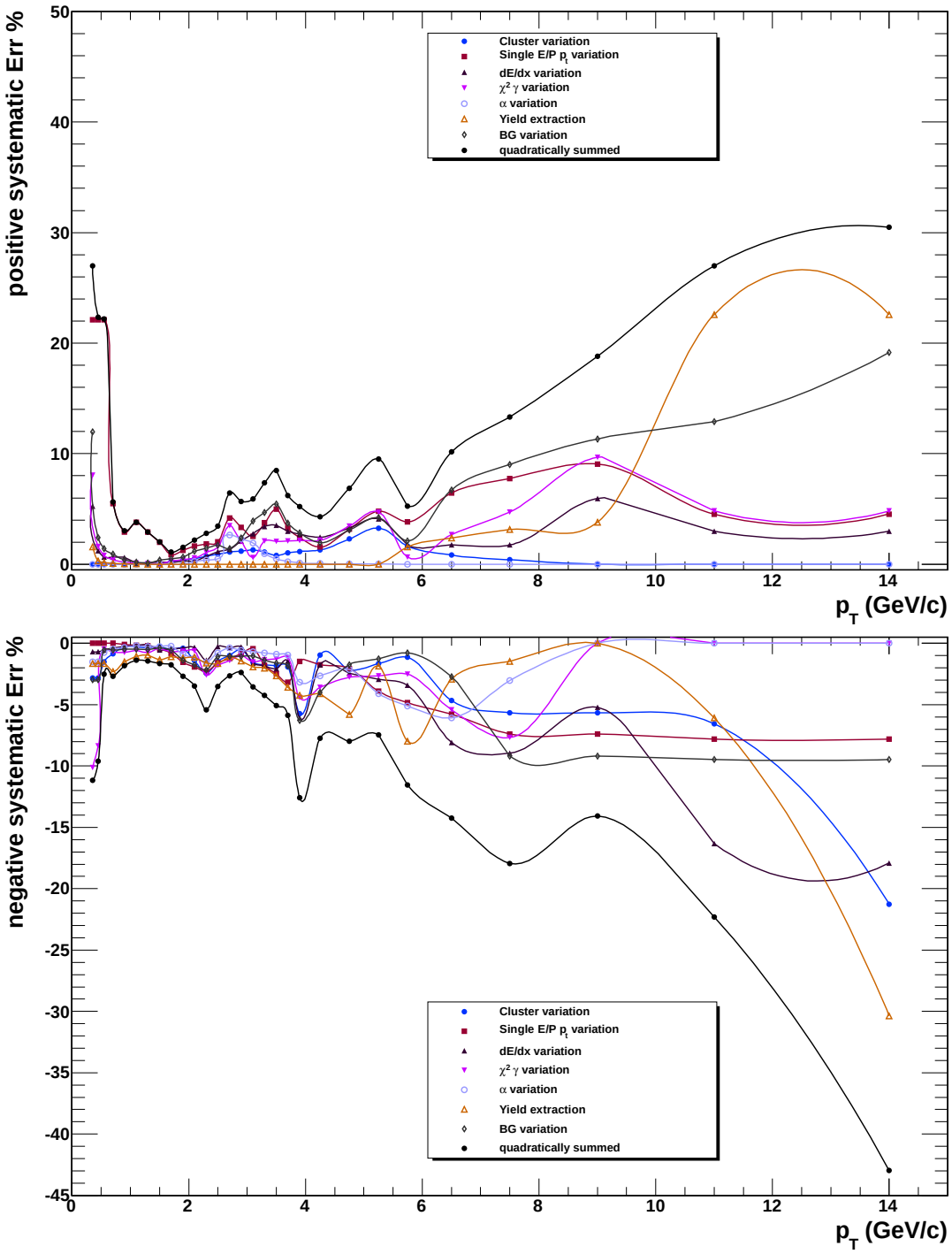

Figure 5.24.: Positive (top) and negative (bottom) systematic uncertainties as a function of transverse momentum for neutral pions at $\sqrt{s} = 7\,\text{TeV}$.

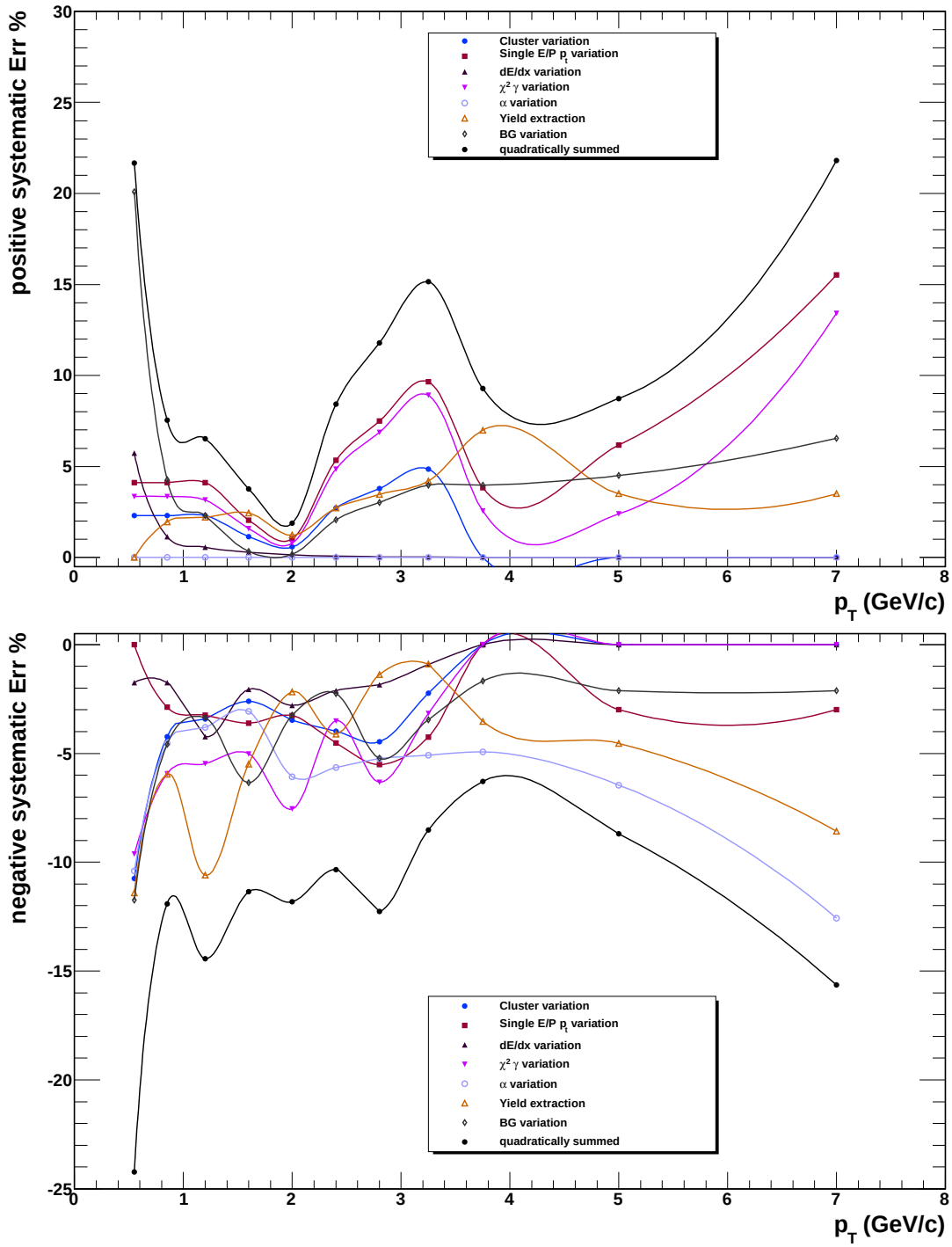

Figure 5.25.: Positive (top) and negative (bottom) systematic uncertainties as a function of transverse momentum for η mesons at $\sqrt{s} = 7\,\text{TeV}$.

6. Meson spectra corrections

6.1. Acceptance and efficiency calculation

Once the raw yields of the mesons are extracted they need to be corrected for detector acceptance and reconstruction efficiency. Both are calculated using the event generators PYTHIA and PHOJET. The generated particles are propagated through the detector. Their interactions with the detector material are simulated in GEANT 3.21. The detector responses to the interactions are simulated with AliRoot in so-called *anchor runs*. Anchor runs are characterized by the same detector setup and calibration as used in data taking, to be as close as possible to the real detector signal.

The geometrical acceptance A is calculated as the ratio of π^0 (η) within $|y| < 0.8$ whose daughter particles are within $|\eta| < 0.9$ over all generated π^0 (η) mesons within $|y| < 0.8$. In both cases only neutral pions and η mesons with two photon daughters are selected. The resulting geometrical acceptance for both mesons is shown in figure 6.1. The rise for the π^0 is much faster with increasing transverse momentum than for the η meson as expected. The plateau of the acceptance for π^0 is reached at a transverse momentum of about 3 GeV/c. The mass of the η meson causes a wider average opening angle for the decay photons. This results in a slower increase of the acceptance. For the η meson the acceptance is about 97 % at 8 GeV/c, whereas the presented analysis starts to be limited by statistics.

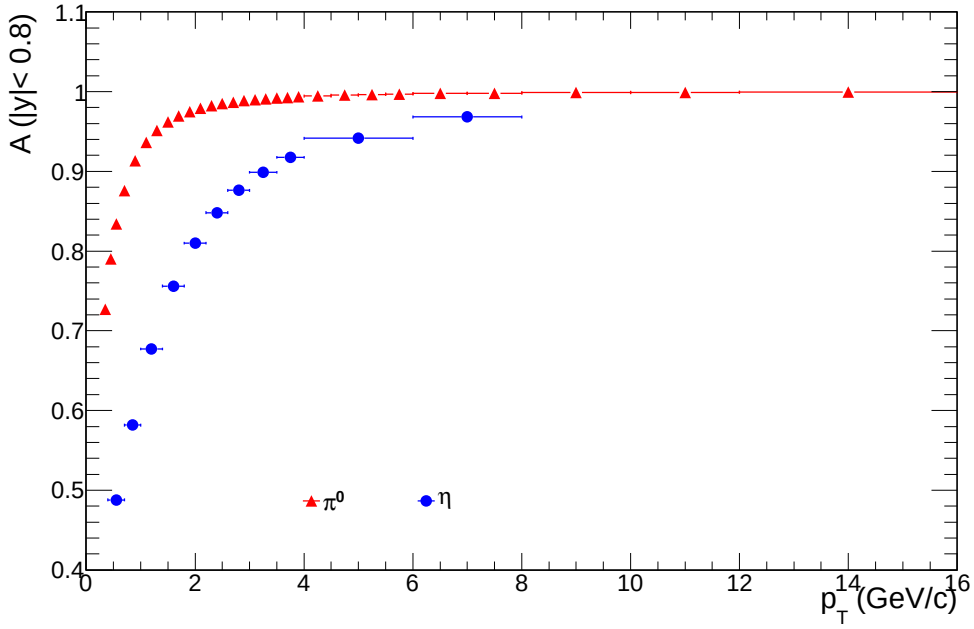

Figure 6.1.: Geometrical acceptance of π^0 (black) and η mesons (blue) within $|y| < 0.8$ as a function of transverse momentum at $\sqrt{s} = 7$ TeV.

To estimate the reconstruction efficiency the same analysis method has been used in simulation as for real data. Both reconstructed photons have been verified by their Monte Carlo information. It also had been checked that they have the same mother particle. Thus, contributions

from Dalitz decays or combinatorial background are excluded, only primary π^0 have been taken into account. The reconstruction efficiency $\epsilon_{\pi^0,\eta}$ is shown in figure 6.2. The shape of the reconstruction efficiency depends on the photon conversion probability and the photon reconstruction efficiency, see section 5.1. Both photons must convert in the detector material within the given acceptance. The momentum of the created electron and positron must be high enough to reach the TPC for reconstruction. This causes the rapid decrease of the π^0 and η meson reconstruction efficiency towards the low transverse momentum region. The photon conversion probability and the photon reconstruction efficiency enter quadratically in the meson reconstruction efficiency. With the maximum values of about 8.7 % for the conversion probability and about 67 % for the photon reconstruction efficiency, see figure 5.9, the maximum reconstruction efficiency for π^0 and η mesons is limited to 0.34 %. The asymptotic value of the π^0 and η reconstruction efficiency is about 0.8 %, this is slightly below the limit. This is most likely caused by asymmetric energy distributions between the decay photons.

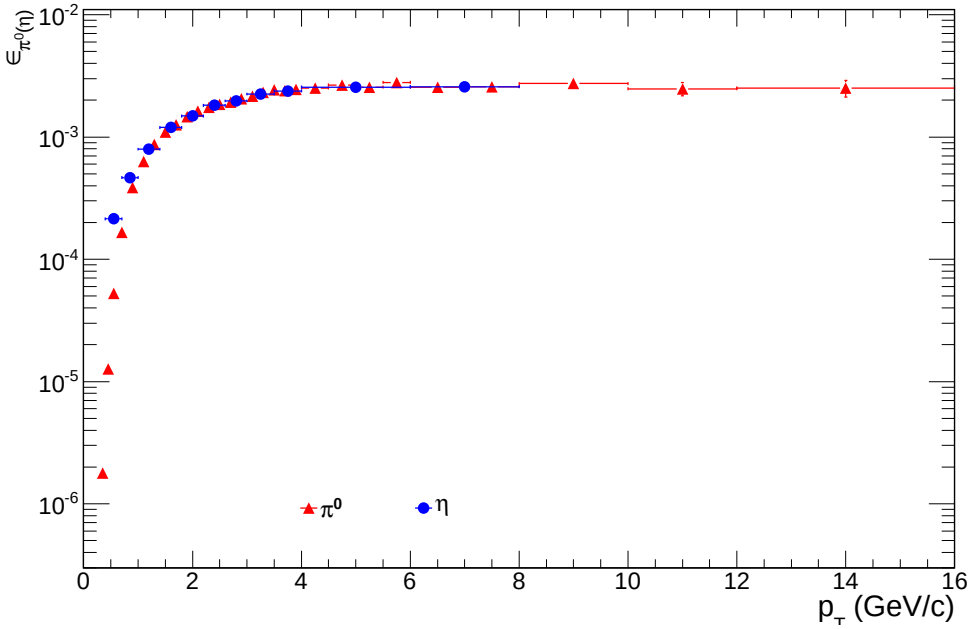

Figure 6.2.: Reconstruction efficiency of π^0 (black) and η mesons (blue) as a function of transverse momentum at $\sqrt{s} = 7\,\text{TeV}$.

The reconstruction of the η meson in simulations is limited by the available statistics. This would result in a higher statistical error of the corrected η meson yield. The obtained reconstruction efficiencies for π^0 (red) and η mesons (blue) are shown in figure 6.3 (top). Above a transverse momentum $p_T = 1.5\,\text{GeV/c}$ both distributions agree. Assuming that both reconstruction efficiencies are uncorrelated, the η reconstruction efficiency for $p_T > 2.6\,\text{GeV/c}$ (black) has been recalculated as average of the original π^0 and η reconstruction efficiencies according to [JoP2006]:

$$\overline{x} \pm \delta\overline{x} = \frac{\sum_i \omega_i x_i}{\sum_i \omega_i} \pm \left(\sum_i \omega_i\right)^{-1/2}, \text{ where } \omega_i = \frac{1}{(\delta x_i)^2} \tag{6.1}$$

where x_i and δx_i are the value and the error of the i^{th} distribution, respectively. Here x_i corresponds π^0 and η reconstruction efficiencies and δx_i to their statistical error.

Furthermore, the reconstruction software for raw data changed between the run periods *bc* and *de*. In the latter also one pad clusters have been included in the tracking and thus, in the calculation of the specific energy loss in the TPC. This results in a different reconstruction

efficiency for electrons (positrons) mainly in the transverse momentum range below 1 GeV/c as shown in figure 6.3 (bottom). To use the full statistics an average reconstruction efficiency has been calculated with the use of eq. 6.1. Here x_i correspond to the reconstruction efficiencies of the run periods *bc* and *de* while δx_i is given by the number of collisions in each period.

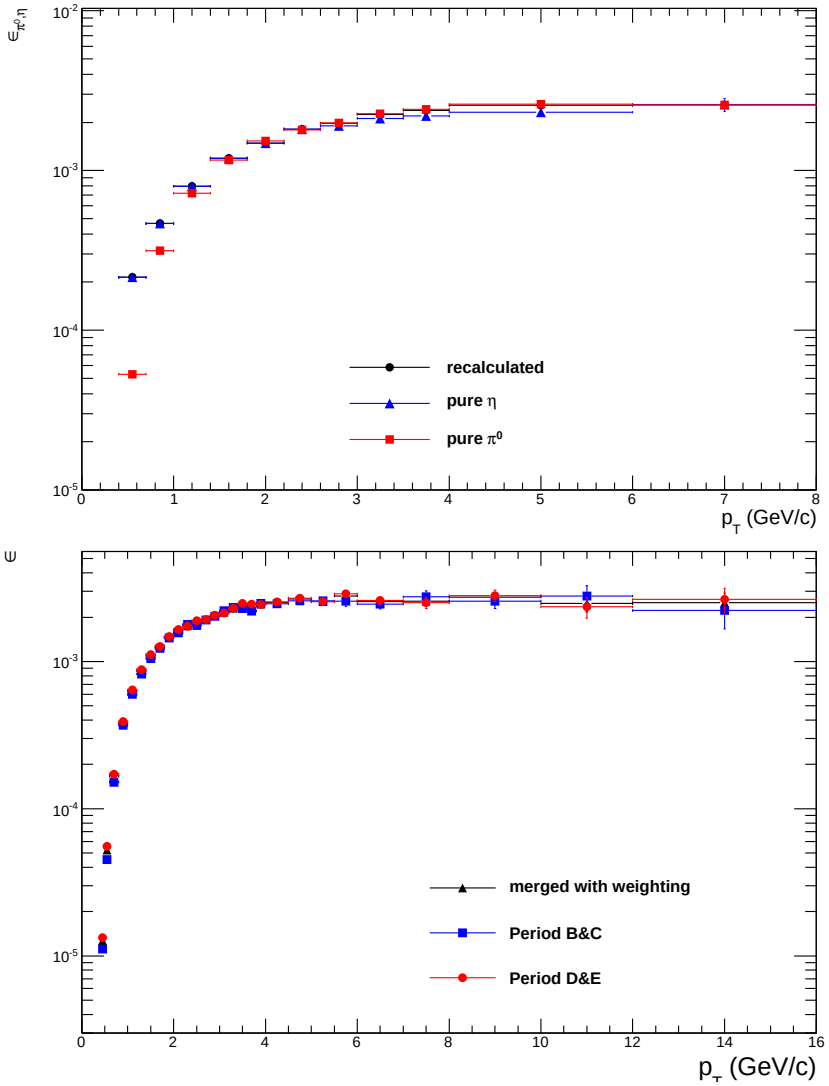

Figure 6.3.: Top: Comparison of π^0 and η reconstruction efficiencies at $\sqrt{s} = 7\,\text{TeV}$. Red squares correspond to π^0 and blue triangles to η before recalculation. Above $p_T = 1.5\,\text{GeV/c}$ both distributions agree and the reconstruction efficiency for η has been recalculated above $p_T = 2.6\,\text{GeV/c}$ (black points). Bottom: Comparison of the π^0 reconstruction efficiencies as functions of transverse momentum in the run periods *bc* and *de* at $\sqrt{s} = 7\,\text{TeV}$ as functions of transverse momentum. Blue triangles correspond to period *bc*, red squares to period *de*. Both differ due to changes in the track reconstruction software. The averaged π^0 reconstruction efficiency is shown as black points.

For $\sqrt{s} = 2.76\,\text{TeV}$ the available statistics in simulations was very limited. Therefore, the simulations at $\sqrt{s} = 7\,\text{TeV}$ have been used to correct the raw yield spectra. This is verified in figure 6.4 where the π^0 acceptance (top) and reconstruction efficiencies (bottom) at $\sqrt{s} = 0.9$ and 7 TeV are shown. In both cases the distributions agree within the statistical uncertainties. Thus, the obtained geometrical acceptance and reconstruction efficiencies for π^0 and η mesons at $\sqrt{s} = 7\,\text{TeV}$ have been used to correct the meson spectra at $\sqrt{s} = 2.76\,\text{TeV}$.

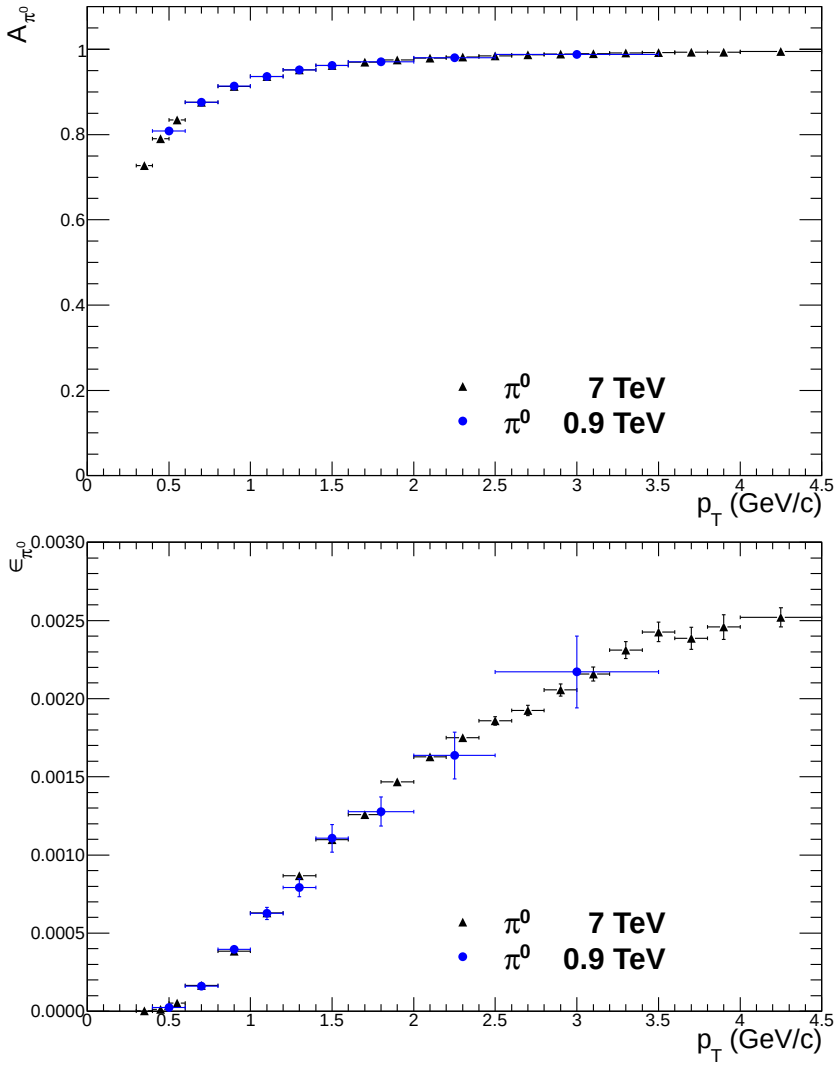

Figure 6.4.: Comparison of π^0 acceptances (top) and reconstruction efficiencies (bottom) at $\sqrt{s}$=0.9 and 7 TeV as a function of transverse momentum. Blue points correspond to $\sqrt{s} = 0.9\,\text{TeV}$, black triangles to $\sqrt{s} = 7\,\text{TeV}$. In both cases the distributions agree within the statistical errors. Therefore, the same geometrical acceptance and reconstruction efficiency has been assumed for π^0 and η mesons at $\sqrt{s} = 2.76\,\text{TeV}$ as at $\sqrt{s} = 7\,\text{TeV}$.

6.2. Correction for secondary neutral pions in the π^0 raw yields

To specify an invariant cross section, which consists exclusively of primary neutral pions contributions of weak decays or hadronic interactions in the detector material must be subtracted. The reconstructed π^0 raw yields still contain contributions from secondary neutral pions and thus needs to be corrected. The correction has been evaluated using the same Monte Carlo simulations as for acceptance and efficiency calculations.

The main contribution to secondary π^0 results from the decay $K^0_s \to \pi^0\pi^0$ with a branching ratio $BR = 30.7\,\%$. Figure 6.5 shows the ratios of reconstructed secondary π^0 to reconstructed π^0 (eq. 6.2) (red) and of reconstructed secondary π^0 from K^0_s to reconstructed π^0 (eq. 6.3) (black). All neutral pions have been verified by their Monte Carlo information. The contribution of secondary pions to the yield raw spectrum is about 7 % for p_T smaller than 1 GeV/c and about 1 % for p_T larger than 3 GeV/c. Neutral pions from K^0_s decays are responsible for about 75 % of all secondary π^0.

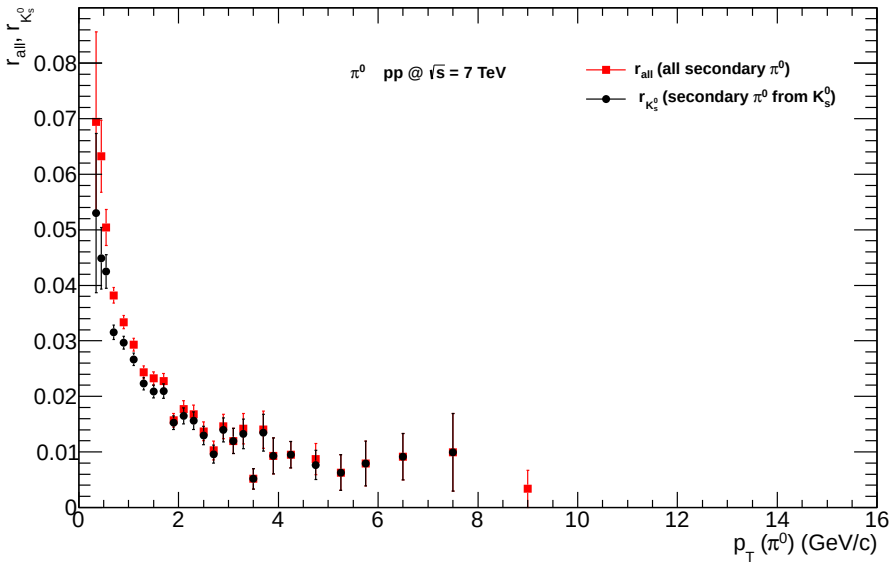

Figure 6.5.: Ratios r_{all} of reconstructed secondary π^0 to reconstructed π^0 (red squares) and $r_{K^0_s}$ of reconstructed secondary π^0 from K^0_s decays to reconstructed π^0 (black dots) at $\sqrt{s} = 7\,\text{TeV}$. The main contribution to secondary neutral pions comes from K^0_s decay.

$$r_{all} = \frac{\text{all secondary } \pi^0}{\text{all } \pi^0} \tag{6.2}$$

$$r_{K^0_s} = \frac{\text{secondary } \pi^0 \text{ from } K^0_s}{\text{all } \pi^0} \tag{6.3}$$

It has been found that the measured differential yields for K^0_s at $\sqrt{s} = 0.9\,\text{TeV}$ [Aam2011d] and for K^+ at $\sqrt{s} = 7\,\text{TeV}$ [ALI2011] are not reproduced in Monte Carlo simulations as shown in figure 6.6. Moreover, both event generators (PYTHIA and PHOJET) differ in the shape of the spectra. For both energies the distributions are underestimated by the simulations. Therefore, it is not sufficient for the calculation of the raw yield for primary pions only to deduct the raw yield of all secondary neutral pions. The raw yield spectra for secondary π^0 from K^0_s decays need to be corrected, too.

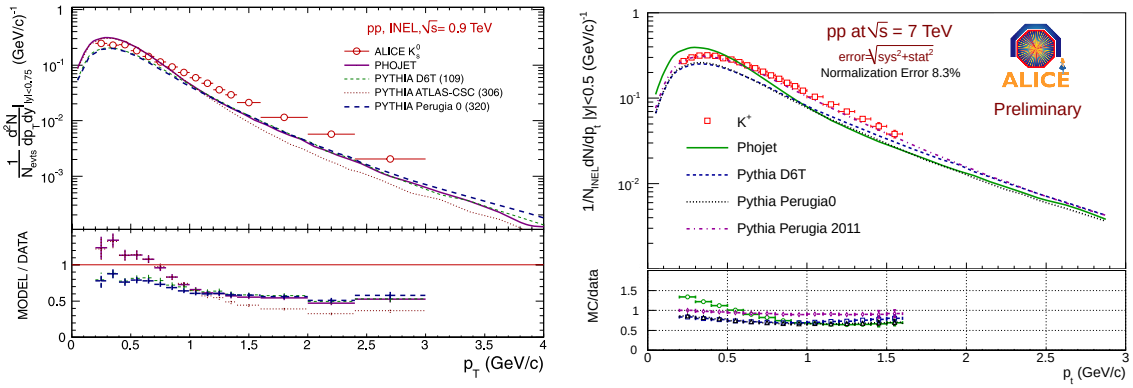

Figure 6.6.: Differential invariant yields of K^0_s at $\sqrt{s} = 0.9\text{TeV}$ (left) and K^+ at $\sqrt{s} = 7\text{TeV}$ (right), both compared to Monte Carlo simulations. In both cases the yield is underestimated in simulations [Aam2011d] [ALI2011].

Above a transverse momentum of 1 GeV/c the ratio of simulated to measured kaons is constant, below it shows a strong p_T dependence. Thus, the transverse momentum of contributing K_s^0 has been checked, shown in figure 6.7. The main part of K_s^0 is located above $p_T \approx 1\,\mathrm{GeV/c}$. At $\sqrt{s} = 0.9\,\mathrm{TeV}$ 40 % of K_s^0 are missing in simulations, about 25 % at $\sqrt{s} = 7\,\mathrm{TeV}$. For the energy $\sqrt{s} = 2.76\,\mathrm{TeV}$ no measured K_s^0 (K^+) spectrum is available yet. Assuming a linear dependence, the missing part of K_s^0 amounts to 31 %.

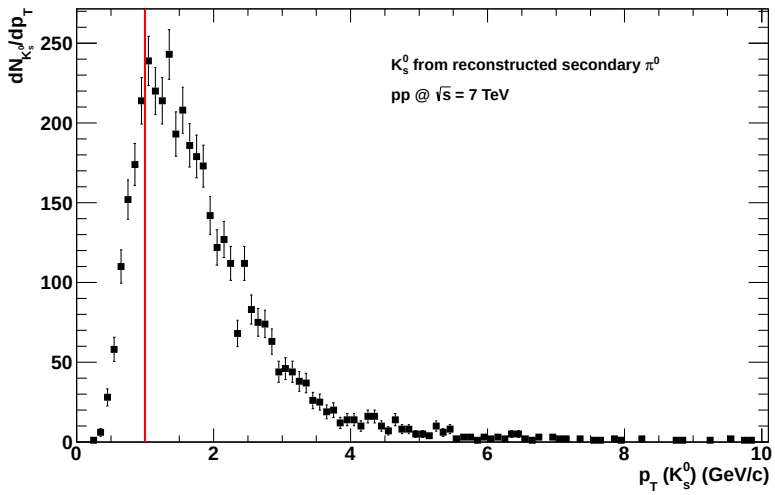

Figure 6.7.: Transverse momentum range of K_s^0 from simulations at $\sqrt{s} = 7\,\mathrm{TeV}$. The red line at $p_T = 1\,\mathrm{GeV/c}$ indicates the beginning of the constant deviation in the comparison of measured and simulated K_s^0 (K^+), see figure 6.6.

To correct for the missing part of secondary π^0 from K_s^0 decays, at first their raw yield spectrum has been calculated by applying the ratio $r_{K_s^0}$ to the neutral pion yield. Secondly, the resulting raw yield of secondary π^0 from K_s^0 decays is scaled by the fraction of missing K_s^0. In this way a raw yield of missing π^0 from K_s^0 decays has been obtained. Applying the ratio r_{all} to the neutral pions raw yield leads to a separate raw yield for all secondary pions. As a last step, the obtained raw yields for secondary pions and missing pions from K_s^0 are subtracted from the neutral pions raw yield. The resulting π^0 raw yield are supposed to contain only primary neutral pions.

6.3. Correction for finite bin width

Due to the steeply falling transverse momentum spectra the p_T value at the bin center does not correspond to the true p_T value for the yield in the interval [Laf1995]. One possibility to solve this problem is by shifting the data point horizontally in p_T such that it corresponds to the true p_T for the given yield. The other option is shifting the data point vertically in the yield such, that it corresponds to the true yield at the bin center. For comparison of spectra with different shapes like in the nuclear modification factor R_{AA}, it is more convenient to correct the yield. Then the spectra can be divided at the bin center, if they have been measured in the same binning.

Therefore, an additional correction of the meson yield [Laf1995] is applied using a Tsallis function $\mathcal{T}$ [Tsa1988] as an approximation of the real spectrum:

$$\frac{\mathrm{d}^2N}{\mathrm{d}y\mathrm{d}p_T} = \frac{(n-1)(n-2)}{nT[nT+m(n-2)]} \times \frac{\mathrm{d}N}{\mathrm{d}y} \times p_T \times \left(1 + \frac{m_T - m}{nT}\right)^{-n} \tag{6.4}$$

where m and $m_T = \sqrt{m^2 + p_T^2}$ correspond to particle mass and transverse mass, $\frac{\mathrm{d}N}{\mathrm{d}y}$, T and n are the free parameters of the fit function. The average yield in an interval with bin center p_T^c and width Δp_T is compared to the value given by the function $\mathcal{T}(p_T)$:

$$r = \frac{1}{\Delta p_T} \cdot \frac{\int_{p_T^c - 0.5\Delta p_T}^{p_T^c + 0.5\Delta p_T} \mathcal{T}(p_T)\mathrm{d}p_T}{\mathcal{T}(p_T^c)} \tag{6.5}$$

The corrected yield is then given by:

$$\left.\frac{\mathrm{d}N}{\mathrm{d}p_T}\right|_{corrected} = \frac{1}{r} \left.\frac{\mathrm{d}N}{\mathrm{d}p_T}\right|_{uncorrected} \tag{6.6}$$

The shifting of the data points leads to a different fit result. Therefore, it has to be repeated until the deviations are negligible. Usually, agreement is found within less than five iterations. An example for the order of magnitude in the correction is shown in figure 6.8. The comparison is given for π^0 at $\sqrt{s} = 7\,\mathrm{TeV}$. For small bin width at low p_T the correction is rather small of the order of $1 - 2\,\%$. For each change in the bin width a jump is observed because of a higher correction. After each jump the correction decreases with increasing transverse momentum since the spectrum becomes flatter with p_T. The largest correction of the order of $18\,\%$ is given in the last bin which covers $2\,\mathrm{GeV/c}$ in p_T.

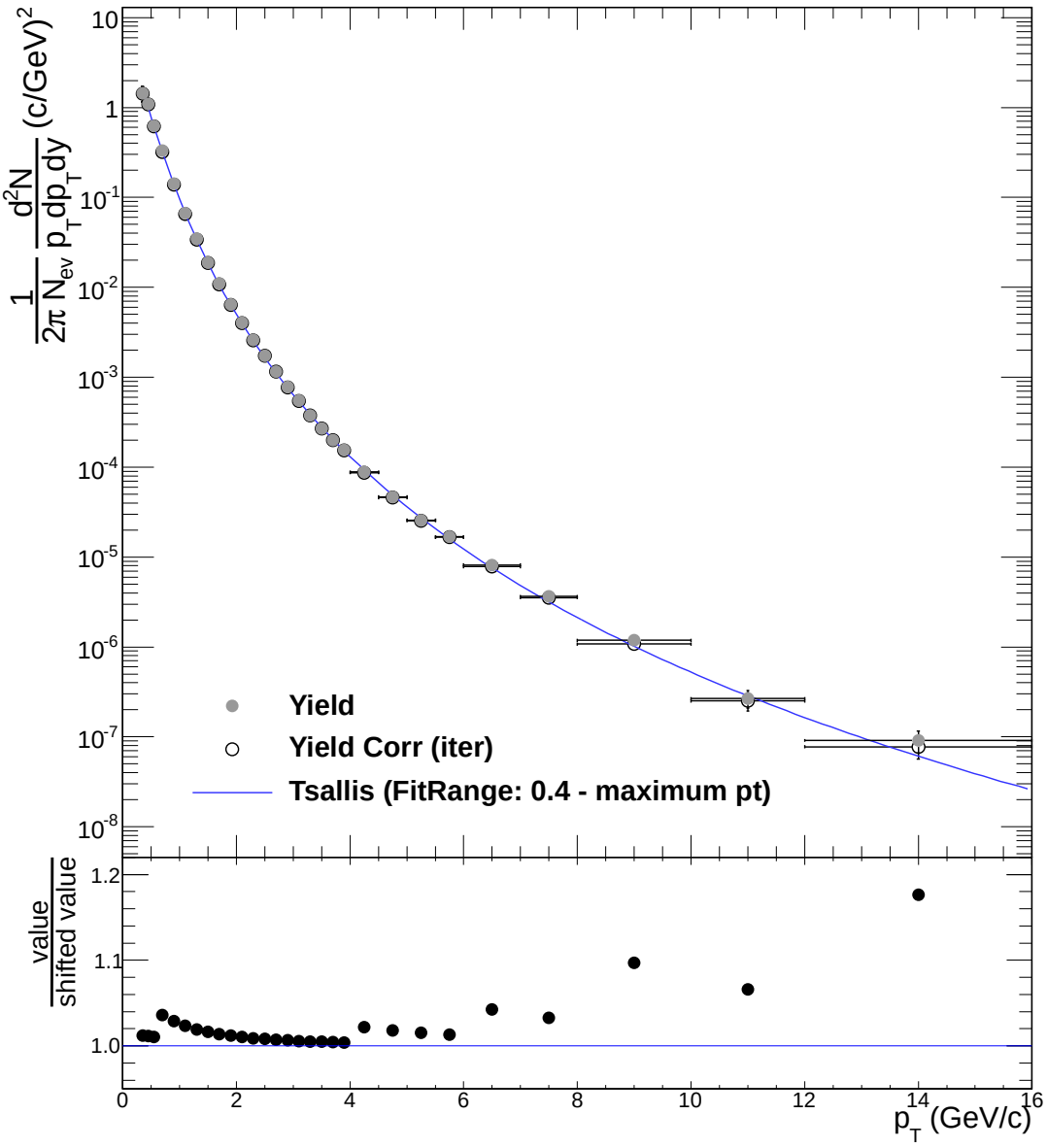

Figure 6.8.: Comparison of the spectrum corrected for finite bin width to the non-corrected π^0 transverse momentum spectrum at $\sqrt{s} = 7\,\text{TeV}$. For the correction a Tsallis function (eq. 6.4) has been used, following [Laf1995].

7. Results

7.1. Differential invariant cross sections

After correcting the π^0 raw yields for secondary π^0 contamination, see section 6.2, and using the geometrical acceptance A and reconstruction efficiency ϵ for π^0 and η mesons, section 6.1, the differential invariant yields of π^0 and η mesons have been calculated according to:

$$E\frac{d^3N^{\pi^0(\eta)}}{dp^3} = \frac{c}{N_{ev.}}\frac{d^3N^{\pi^0(\eta)}}{p_T^c dp_T dy d\phi} = \frac{c}{N_{ev.}}\frac{1}{2\pi}\frac{1}{p_T^c}\frac{d^2N^{\pi^0(\eta)}}{dy dp_T} = \frac{c}{N_{ev.}}\frac{1}{2\pi}\frac{1}{p_T^c}\frac{1}{\epsilon}\frac{1}{A}\frac{1}{BR}\frac{N^{\pi^0(\eta)}}{\Delta y \Delta p_T} \tag{7.1}$$

where $N_{ev.}$ is the number of triggered events, BR the branching ratio of the decay $\pi^0(\eta) \longrightarrow \gamma\gamma$ and $N^{\pi^0(\eta)}$ the number of reconstructed π^0 (η) mesons within the rapidity range $[-0.8, 0.8]$ and transverse momentum bin Δp_T, where p_T^c corresponds to the bin center. Furthermore, an additional correction for the finite bin width, described in section 6.3, has been applied.

With the measured interaction cross sections σ_{pp}, which corresponds to $\sigma_{MB_{OR}}$ see section 4.3, the differential invariant cross sections have been calculated following

$$E\frac{d^3\sigma}{dp^3} = \frac{c}{2\pi}\frac{\sigma_{pp}}{N_{ev.}}\frac{1}{p_T^c}\frac{1}{\epsilon}\frac{1}{A}\frac{1}{BR}\frac{N^{\pi^0(\eta)}}{\Delta y \Delta p_T}. \tag{7.2}$$

In figures 7.1 and 7.2 the differential invariant π^0 and η meson cross sections[1] measured in proton-proton collisions at the center-of-mass energies $\sqrt{s} = 0.9, 2.76$ and $7\,\text{TeV}$ are presented as a function of the transverse momentum. All spectra have been measured for the first time at these energies. At $\sqrt{s} = 7\,\text{TeV}$ the π^0 is detected in a transverse-momentum range from $0.3\,\text{GeV/c}$ to $16.0\,\text{GeV/c}$, at $\sqrt{s} = 2.76\,\text{TeV}$ from $0.4\,\text{GeV/c}$ to $8.0\,\text{GeV/c}$ and at $\sqrt{s} = 0.9\,\text{TeV}$ from $0.4\,\text{GeV/c}$ to $3.5\,\text{GeV/c}$. The η meson has been measured in the range from $0.4\,\text{GeV/c}$ to $8.0\,\text{GeV/c}$ at $\sqrt{s} = 7\,\text{TeV}$, $0.6\,\text{GeV/c}$ to $6.0\,\text{GeV/c}$ at $\sqrt{s} = 2.76\,\text{TeV}$ and $0.9\,\text{GeV/c}$ to $3.0\,\text{GeV/c}$ at $\sqrt{s} = 0.9\,\text{TeV}$, albeit only in two transverse momentum bins. For clarity the spectra at $\sqrt{s} = 0.9$ and $2.76\,\text{TeV}$ are scaled by a factor 10^{-1} and 10^{-2}, respectively. The statistical errors of the measurements are given by the error bars, the systematic uncertainties are shown as boxes around the data points. The width of the error box corresponds to the width of the transverse momentum bin. The given uncertainties of the differential invariant cross sections do not include the systematic uncertainties of the interaction cross section σ_{pp}. This uncertainty is $4\,\%$ at $\sqrt{s} = 7\,\text{TeV}$, $7\,\%$ at $\sqrt{s} = 2.76\,\text{TeV}$ and $2.4\,\%$ at $\sqrt{s} = 0.9\,\text{TeV}$. Above a transverse momentum $p_T = 2\,\text{GeV/c}$ all spectra exhibit a power-law behavior.

[1] For later comparisons the abbreviation *PCM* for Photon Conversion Method is used for the presented analysis.

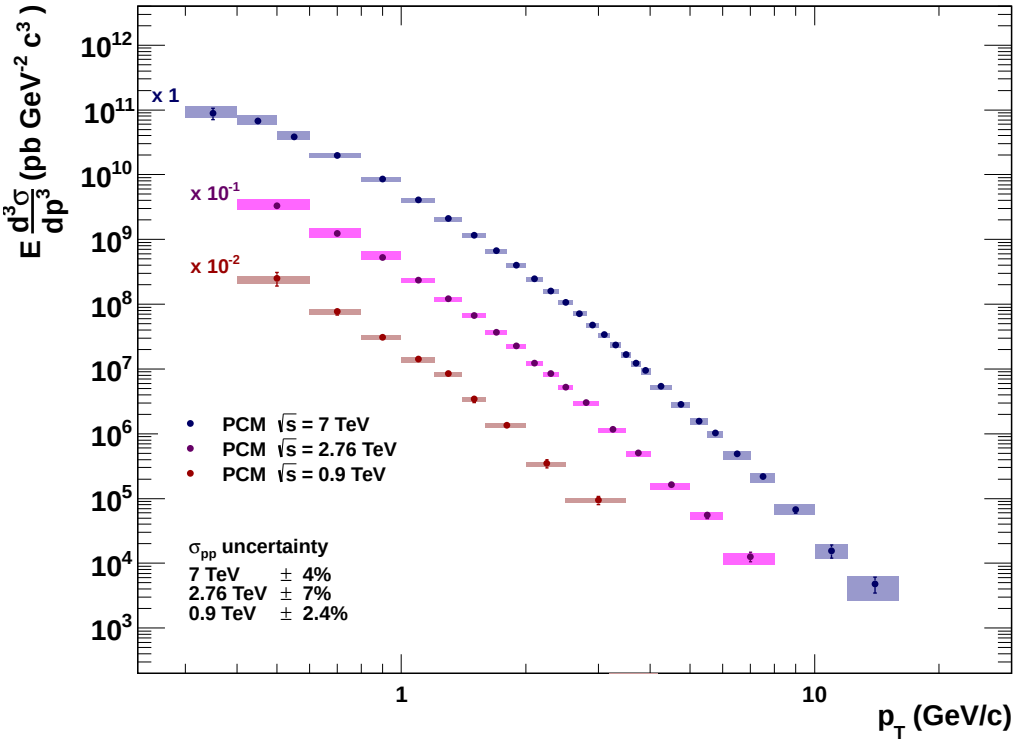

Figure 7.1.: π^0 differential invariant cross sections at $\sqrt{s} = 0.9$ (brown), 2.76 (purple) and 7 TeV (blue) as a function of the transverse momentum. The measured spectra at $\sqrt{s} = 0.9$ and 2.76 TeV are scaled for clarity. The statistical errors are shown as bars, the systematic uncertainties as boxes. The systematic uncertainties of the interaction cross section σ_{pp} are not included.

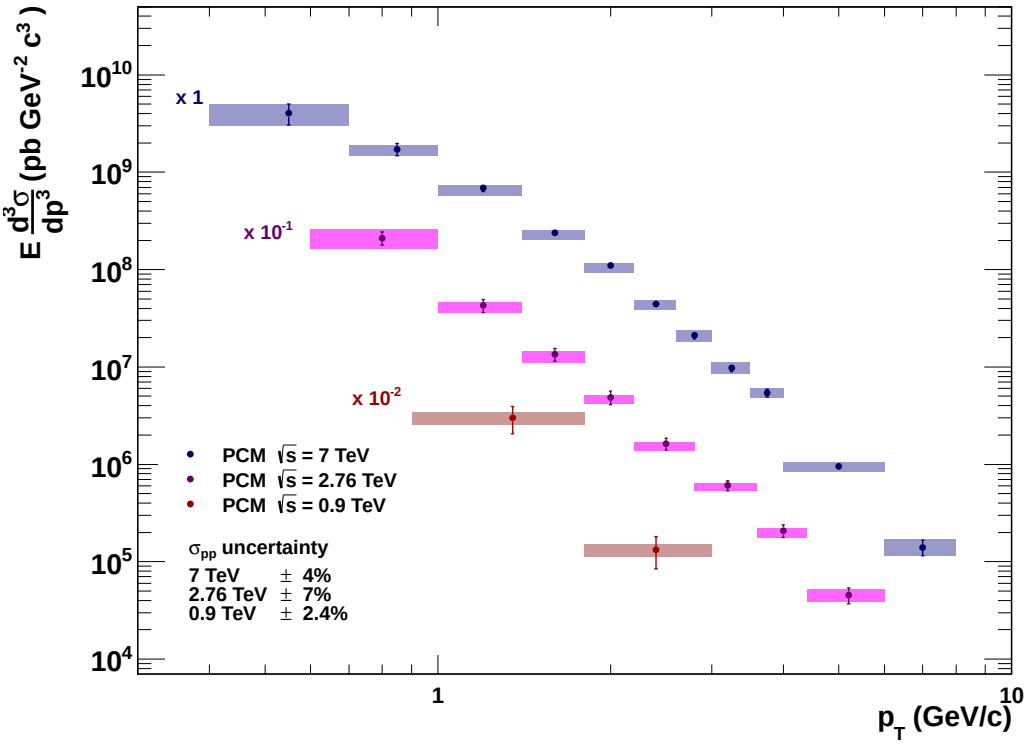

Figure 7.2.: η differential invariant cross sections at $\sqrt{s} = 0.9$ (brown), 2.76 (purple) and 7 TeV (blue) as a function of the transverse momentum. The measured spectra at $\sqrt{s} = 0.9$ and 2.76 TeV are scaled for clarity. The statistical errors are shown as bars, the systematic uncertainties as boxes. The systematic uncertainties of the interaction cross section σ_{pp} are not included.

The differential invariant cross sections have been fitted with the Tsallis function $\mathcal{T}$, eq. 6.4. The fit parameters $\mathrm{d}N/\mathrm{d}y$, $T$and n are shown in table 7.1, where the uncertainties are the quadratic sum of statistical and systematic uncertainties. The particle rapidity densities $\mathrm{d}N/\mathrm{d}y$ have been obtained using inelastic cross section σ_{INEL}, see section 4.3. At $\sqrt{s} = 0.9\,\mathrm{TeV}$ it has not been possible to extract reasonable fit parameters for the η meson.

Meson	$\sqrt{s}$ (TeV)	$\mathrm{d}N/\mathrm{d}y$	T (MeV/c^2)	n
π^0	7	2.29 ± 0.19	143 ± 7	6.89 ± 0.18
	2.76	1.74 ± 0.23	140 ± 12	7.31 ± 0.34
	0.9	1.65 ± 0.54	123 ± 30	7.44 ± 1.36
η	7	0.20 ± 0.03	238 ± 28	7.08 ± 0.69
	2.76	0.14 ± 0.04	229 ± 26	7.31 fixed as for π^0

Table 7.1.: Fit parameters of the Tsallis function for the π^0 and η differential invariant cross section at the different LHC energies. The given $\mathrm{d}N/\mathrm{d}y$ values correspond to the yield per inelastic collision. It has not been possible to extract reasonable parameters for the η meson at $\sqrt{s} = 0.9\,\mathrm{TeV}$. The uncertainties are the quadratic sum of statistical and systematic uncertainties. The systematic uncertainties of the interaction cross section σ_{pp} are not included.

For both mesons the particle rapidity densities $\mathrm{d}N/\mathrm{d}y$ show a dependence on the collision energy. In figure 7.3 the parameters $\mathrm{d}N/\mathrm{d}y$ for π^0 (black) and η (red) are shown as a function of collision energy $\sqrt{s}$. The figure includes the results of a logarithmic fit for both mesons [Gro2010]. For neutral pions the extracted curve is given by $\mathrm{d}N^{\pi^0}/\mathrm{d}y = 0.21\,\log(s/TeV) + 1.42$, for η mesons by $\mathrm{d}N^{\eta}/\mathrm{d}y = 0.03\,\log(s/TeV) + 0.07$, see table 7.2. The fit function for π^0 has been evaluated at the RHIC energy of $\sqrt{s} = 200\,\mathrm{GeV}$ and compared to measurement of the PHENIX experiment. For neutral pions $\mathrm{d}N/\mathrm{d}y$ has been found to be 1.13 ± 0.40 . The value measured by PHENIX is 1.065 ± 0.11 for π^0 [Ada2011a]. Both values agree within the errors. Neither for the parameter T nor for n a significant trend with $\sqrt{s}$ can be seen.

Meson	a	b
π^0	0.21±0.12	1.42±0.36
η	0.03±0.03	0.07±0.09

Table 7.2.: Fit parameters of the logarithmic fit of the particle rapidity density $\mathrm{d}N/\mathrm{d}y = a\,\log(s/TeV) + b$ for π^0 and η mesons. The uncertainties include statistical and systematic uncertainties.

Using the Tsallis function $\mathcal{T}$, which describes $\mathrm{d}^2N/\mathrm{d}p_T\mathrm{d}y$, the mean transverse momentum $<p_T>$ can be numerically calculated:

$$<p_T> = \frac{\int_0^{p_{T,max}} \mathcal{T} \cdot p_T \mathrm{d}p_T}{\int_0^{p_{T,max}} \mathcal{T} \cdot \mathrm{d}p_T} \tag{7.3}$$

The extracted mean transverse momenta $<p_T>$ are summarized in table 7.3 and depicted in figure 7.4 as a function of $\sqrt{s}$. For the estimation of the uncertainties of $<p_T>$, the extracted parameters of $\mathcal{T}$ have been set to their upper and lower limits, respectively, and the calculation has been repeated. The largest deviation has been taken as uncertainty. These calculations have been performed twice, once including only statistical error, once including the quadratic sum of statistical and systematic error. The systematic uncertainty is then

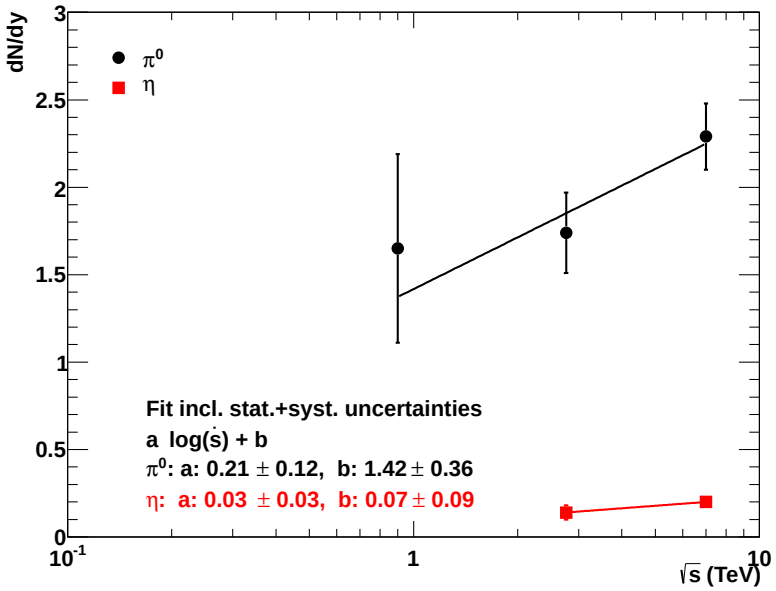

Figure 7.3.: Parameter dN/dy extracted from Tsallis fit function $\mathcal{T}$ for π^0 and η at the different LHC energies. The parameters show a logarithmic dependence (solid line) from the collision energy for both mesons.

given by $\sigma_{sys.} = \sqrt{\sigma^2_{tot.} - \sigma^2_{stat.}}$. The extracted $<p_T>$ at $\sqrt{s} = 0.9\,\text{TeV}$ for π^0 has been compared to the observed $<p_T> = (0.404 \pm 0.001_{stat.} \pm 0.02_{sys.})\,\text{GeV/c}$ of positive and negative charged pions at $\sqrt{s} = 0.9\,\text{TeV}$ in ALICE [Aam2011e][2]. Both are in good agreement. For the inclusive charged-hadron spectrum at $\sqrt{s} = 7\,\text{TeV}$ the mean transverse momentum $<p_T> = (0.545 \pm 0.005_{stat.} \pm 0.015_{sys.})\,\text{GeV/c}$ has been measured by the CMS collaboration [CMS2010]. This is barely consistent in the limit of the uncertainties with the measured $<p_{T,\pi^0}>$ for neutral pions at $\sqrt{s} = 7\,\text{TeV}$. However, the result for the inclusive charged-hadron spectrum is expected to be higher since it contains contributions from kaons and protons. The energy dependence of $<p_T>$ for charged hadrons measured by different experiments is given in figure 7.5. The data can be fitted by $<p_T> = 0.413 - 0.0171 \ln s + 0.00143 \ln^2 s\,\text{GeV/c}$ [CMS2010]. For neutral pions a difference of about 20 % in $<p_T>$ has been found between $\sqrt{s} = 0.9\,\text{TeV}$ and $\sqrt{s} = 7\,\text{TeV}$. This is consistent with the ratio of $<p^{7TeV}_{T,h^+ + h^-}>/<p^{0.9TeV}_{T,h^+ + h^-}> \approx 20\,\%$ measured by the CMS collaboration, see figure 7.5. For the η meson the obtained increase between $\sqrt{s} = 2.76\,\text{TeV}$ and $\sqrt{s} = 7\,\text{TeV}$ is much higher, about 60 %. Since only 3 (2) data points have been measured for π^0 (η), they have been fitted for both mesons by a linear function. For the π^0 a dependence of $<p_{T,\pi^0}> = 0.01\sqrt{s} + 0.44$ GeV/c has been found, for the η of $<p_{T,\eta}> 0.07\sqrt{s} + 0.28$ GeV/c, see table 7.4.

$\sqrt{s}$ (TeV)	$<p_{T,\pi^0}>$ (GeV/c)	$<p_{T,\eta}>$ (GeV/c)
7	$0.490 \pm 0.007 \pm 0.025$	$0.751 \pm 0.069 \pm 0.070$
2.76	$0.466 \pm 0.017 \pm 0.036$	$0.463 \pm 0.198 \pm 0.080$
0.9	$0.411 \pm 0.089 \pm 0.066$	

Table 7.3.: Mean transverse momenta $<p_T>$ for the π^0 and η measured at $\sqrt{s} = 0.9, 2.76$ and $7\,\text{TeV}$. The first error corresponds to the statistical uncertainty, the second to the systematic uncertainty.

[2]The method used for charged pions is slightly different. The measured spectra themselves are used for the estimation. Only in regions without data points the fit function is taken.

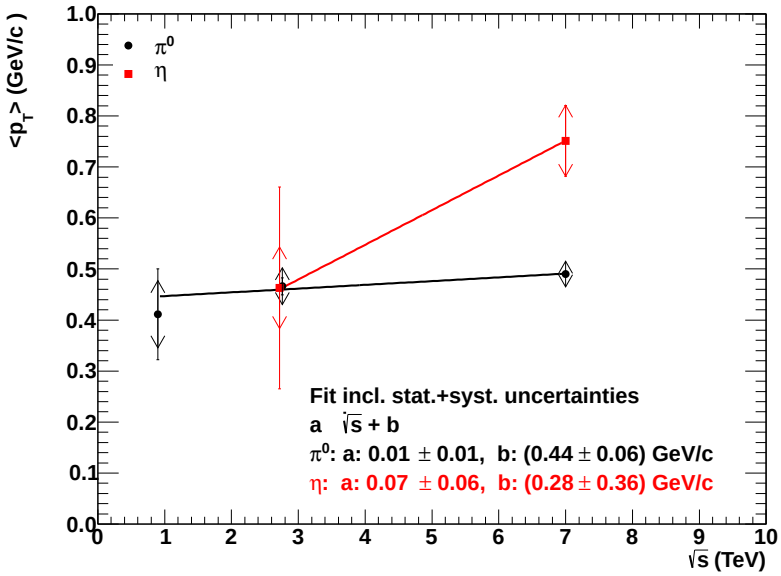

Figure 7.4.: Mean transverse momenta $<p_T>$ for π^0 (black) and η (red) as a function of collision energy. The statistical uncertainties are shown as bars, the systematic uncertainties are drawn as arrows. The solid lines correspond to the linear fits.

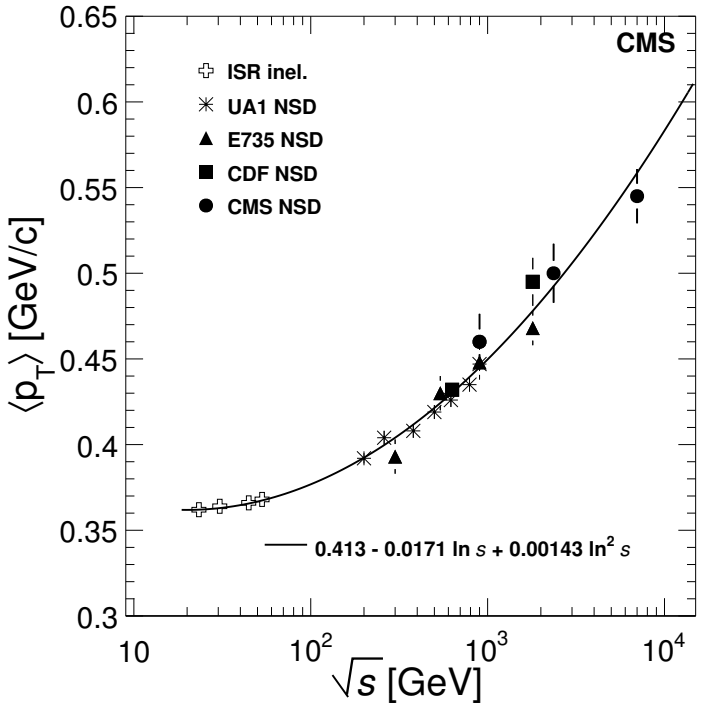

Figure 7.5.: Energy dependence of $<p_T>$ of charged particles measured by the ISR, UA1, E375, CDF and CMS collaborations. The solid line corresponds to a fit of the form $<p_T> = (0.413 - 0.0171 \ln s + 0.00143 \ln^2 s)$ GeV/c. At $\sqrt{s} = 7$ TeV $<p_T> = 0.545 \pm 0.005_{stat.} \pm 0.015_{sys.}$ GeV/c has been measured by CMS collaboration [CMS2010].

Meson	a	b (GeV/c)
π^0	0.01±0.01	0.44±0.06
η	0.07±0.06	0.28±0.36

Table 7.4.: Fit parameters of the linear fit of the mean transverse momentum $<p_T> = a\sqrt{s} + b$ for π^0 and η mesons. The uncertainties include statistical and systematic uncertainties.

7.2. η/π^0 ratio

The η/π^0 ratio is an important quantity to understand the particle production mechanism. In the ratio the systematic errors of material budget and the global normalization cancel. The η/π^0 ratios at the three collision energies are shown in figure 7.6. At $\sqrt{s} = 7\,\text{TeV}$ the ratio increases with transverse momentum and flattens above $p_T \approx 3.5\,\text{GeV/c}$ at a value around 0.45 . The same behavior has been obtained at $\sqrt{s} = 2.76\,\text{TeV}$, the ratio shows the same rise and flattens approximately at 0.65 . The systematic uncertainties above $p_T = 3.5\,\text{GeV/c}$ are about 15 -20 %. Within these uncertainties the ratio agrees with the measurement at $\sqrt{s} = 7\,\text{TeV}$. At $\sqrt{s} = 0.9\,\text{TeV}$ it was only possible to extract the η meson yield in two p_T bins, nevertheless the ratio could be calculated. It has large errors, but it is in agreement with the ratios at the two other energies.

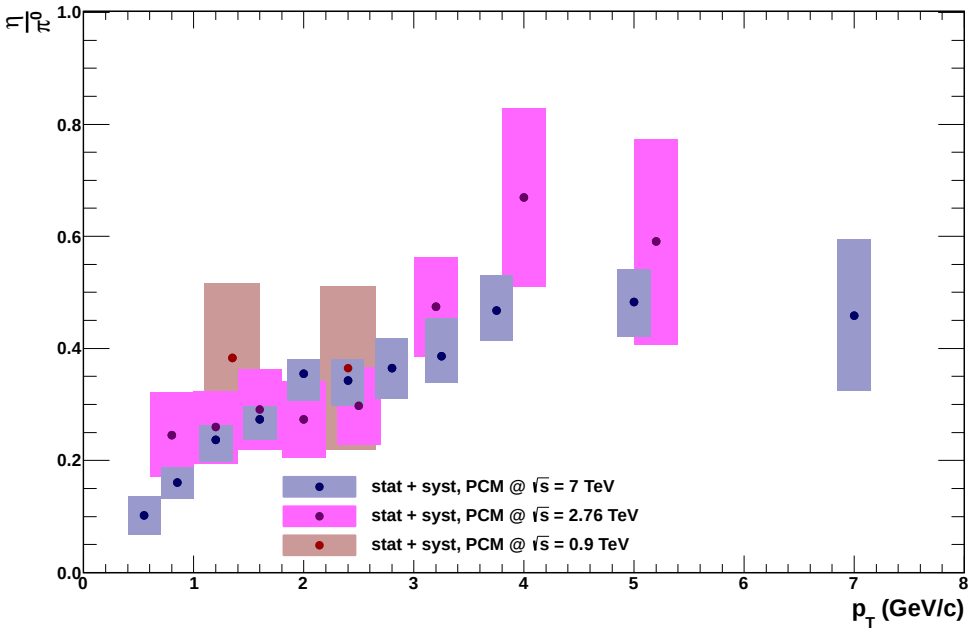

Figure 7.6.: Measured η/π^0 ratio at $\sqrt{s} = 0.9$ (brown), 2.76 (purple) and 7 TeV (blue) as a function of transverse momentum.

In figure 7.7 a comparison of the η/π^0 ratio to world data [Adl2007] is shown. The displayed world data have been measured in proton-proton collisions at different center-of-mass energies in the range of $\sqrt{s} = 13.8 - 200\,\text{GeV}$. The measured η/π^0 ratios at the different LHC energies agree with measurements at lower energies. The data at $\sqrt{s} = 30.6,\ 52.7,\ 53,\ 62.4$ and 200 GeV (green symbols) have been collected in collider experiments. The minimum transverse momentum for those experiments is about 2.5 GeV/c. In contrast, the measured η/π^0 ratio at $\sqrt{s} = 2.76$ and $\sqrt{s} = 7\,\text{TeV}$ from the presented analysis starts at $p_T = 0.6\,\text{GeV/c}$ and $0.4\,\text{GeV/c}$,

respectively. The low transverse momentum reach is the main feature of the π^0 and η meson reconstruction using photon conversions in the detector material. It results from the powerful tracking capabilities of ITS and TPC together with the excellent particle identification in the TPC.

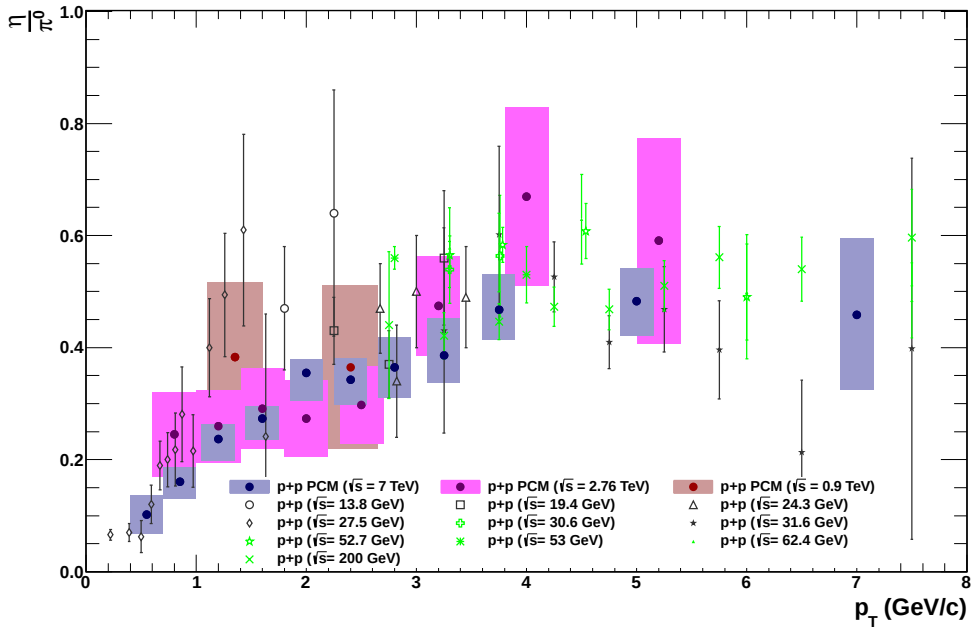

Figure 7.7.: η/π^0 ratio as a function of the transverse momentum measured at $\sqrt{s} = 0.9, 2.76$ and 7 TeV compared to world data [Adl2007].

7.3. Comparison to preliminary results presented at Hard Probes 2010

The measurement of the differential invariant yield of the π^0 meson up to 7 GeV/c as well as the η/π^0 ratio (up to 6 GeV/c) have been already presented at the Hard Probes conference 2010 [Koc2011].

Figure 7.8 (left) shows a comparison between the spectrum shown there and the measurement presented in this thesis. For the latter the statistics increased by a factor of more than 3. Therefore, it has been possible to extend the p_T reach for both mesons and to use a smaller binning in p_T. For the new measurement a correction for the finite bin width has been applied. As has been shown in section 6.3 the effect of the correction is negligible at low p_T, where the bin width is small. The obtained η/π^0 ratios agree as shown in figure 7.8 (right). For the measurement presented at the conference the systematic uncertainties were estimated to be $\pm 20\,\%$. In the present analysis the systematic uncertainties have been studied in detail, see section 5.4.4. The present measurement of the η meson at $\sqrt{s} = 7$ TeV with larger statistics also allows an extension of the η/π^0 ratio to higher p_T.

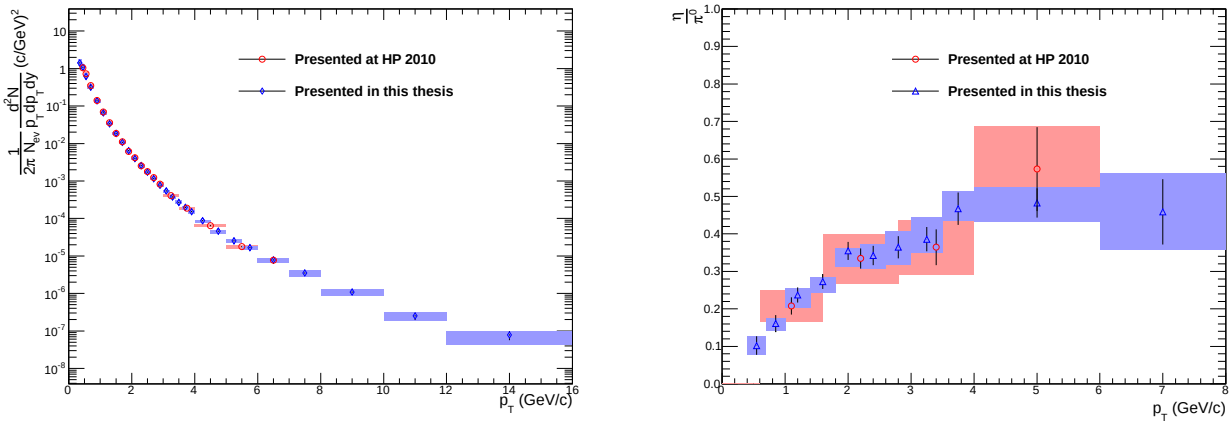

Figure 7.8.: Comparison of the present π^0 spectrum and the η/π^0 ratio (both in blue) to the data shown at the Hard Probes conference 2010 (red) [Koc2011].

7.4. m_T scaling

It has also been checked wether m_T scaling, where $m_T = \sqrt{m^2 + p_T^2}$ is the transverse mass of the particle, is still valid at LHC energies. If m_T scaling is fulfilled the differential invariant cross sections of different particle species plotted as a function of transverse mass have the same shape [Bou1976] [Adl2007].

In figure 7.9 the measured differential invariant cross sections for different particle types, namely pions (black), η (red circle), kaons (red rhomb), ω (triangle) and J/Ψ (turned triangle), in pp collisions at $\sqrt{s} = 200\,\text{GeV}$ at RHIC are shown as a function of transverse momentum [Ada2011a]. The measured spectra have been compared to the parametrization of m_T scaling. For all spectra a good agreement has been found.

In figure 7.10 the ratio of the η differential invariant yield to the fit of the π^0 differential invariant yield is shown as a function of the transverse mass for $\sqrt{s} = 2.76$ and $7\,\text{TeV}$. At $\sqrt{s} = 7\,\text{TeV}$ a decrease of the ratio towards low transverse mass is clearly visible, above $m_T = 2\,\text{GeV/c}$ the ratio at $\sqrt{s} = 7\,\text{TeV}$ flattens. This is an indication that m_T scaling is violated at low transverse mass for high collision energies, where the particle production is driven by soft processes. In case of $\sqrt{s} = 2.76\,\text{TeV}$ no clear conclusions can be drawn. The ratio also seems to rise as m_T increases and seems to flatten at higher m_T. However, within the statistical and systematical uncertainties the ratio could also be constant.

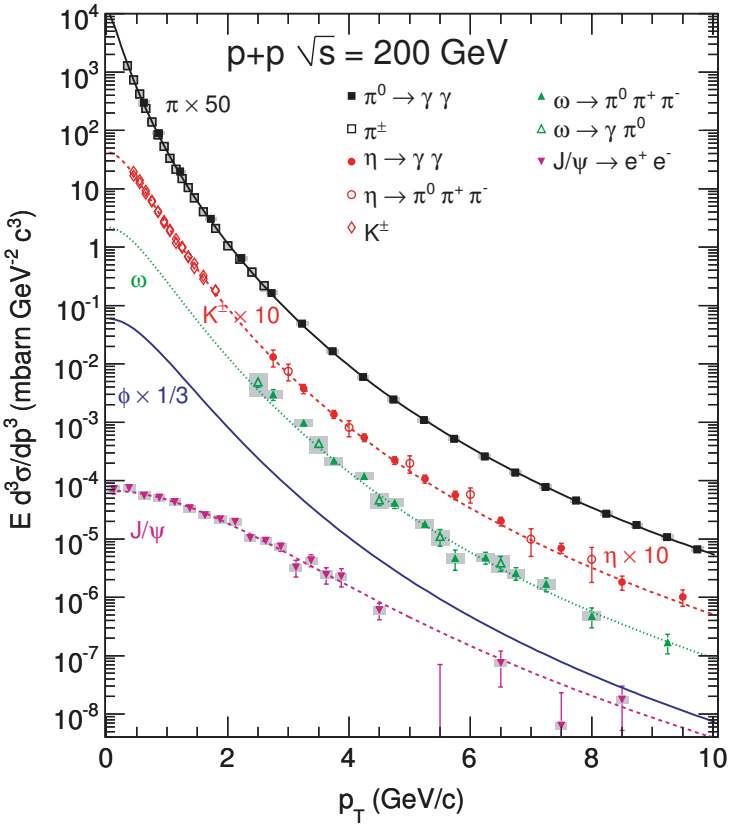

Figure 7.9.: Compilation of meson production cross sections for pions (black), η (red circle), kaons (red rhomb), ω (triangle) and J/Ψ (turned triangle) in pp collisions at $\sqrt{s} = 200\,\text{GeV}$ at RHIC as functions of transverse momentum. The data are compared to the parametrization of m_T scaling, drawn as lines [Ada2011a].

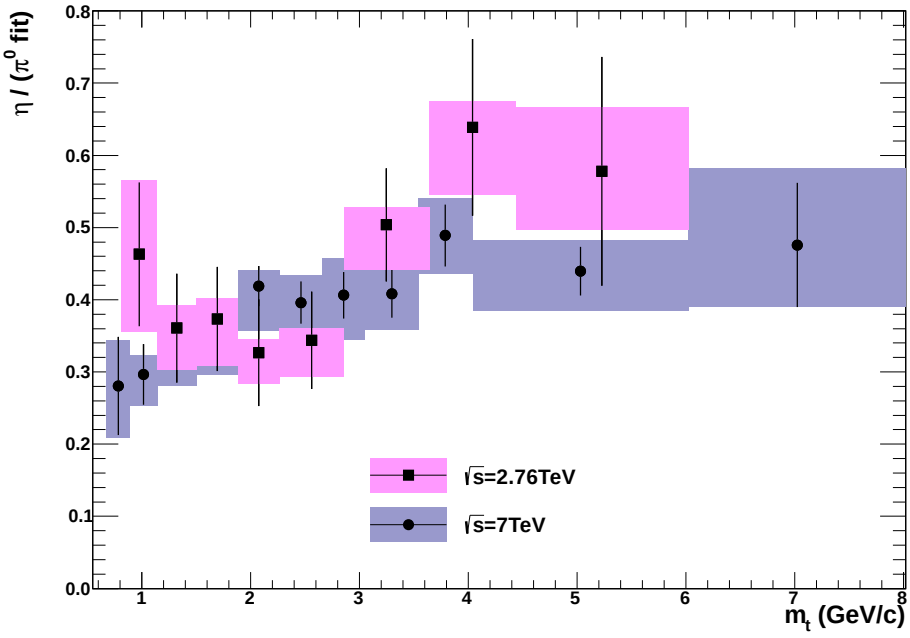

Figure 7.10.: Ratio η yield/π^0 fit as a function of m_T at $\sqrt{s} = 2.76$ (purple) and 7 TeV (blue).

7.5. Comparison to charged pions

The differential invariant π^0 yields measured with the photon conversion method have been compared to the charged pion spectra at the different energies. Due to isospin symmetry the yields are expected to be $\pi^0 \approx \frac{1}{2}(\pi^+ + \pi^-)$. For each comparison the sum of the measured charged pion yields $(\pi^+ + \pi^-)$ has been divided in each common bin by twice the measured π^0 yield. In the case of charged pions no correction for finite bin width has been applied. Therefore, the invariant differential yields of neutral pions without this correction have been used for the comparison. Furthermore, in case of charged pions, differential invariant yields have been normalized to the number of inelastic events N_{INEL} while the spectra for neutral pions have been normalized to the number of triggered events $N_{MB_{OR}}$. Thus, a correction factor $N_{MB_{OR}}/\ N_{INEL}$ given by the ratio of the trigger efficiencies for both conditions has been applied to the neutral pion spectra. All calculated ratios are shown as a function of transverse momentum. The uncertainties include the statistical and systematic uncertainties. For each bin the positive and negative error have been compared. The larger one is used for the comparison to the charged-pion spectra. For a better overview a line is drawn at $(\pi^+ + \pi^-)/(2\pi^0) = 1$.

In figure 7.11 the ratio of both yields is shown for $\sqrt{s} = 0.9\,\text{TeV}$. The charged-pion spectrum has been extracted in the rapidity range of $|y| < 0.5$ by various methods. The analysis is described in [Aam2011e]. The points of the ratio are mainly located at 0.9 but within the uncertainties both spectra agree. At a transverse momentum $p_T \approx 1.3\,\text{GeV/c}$ the neutral pion spectrum exhibits a small jump. This is reflected in the ratio.

The comparison at $\sqrt{s} = 2.76\,\text{TeV}$ is given in figure 7.12. Charged pions are obtained from the measured $h^+ + h^-$ spectrum [Kni2011] and the measured fraction of charged pions to charged hadrons [Chr2011]. Both are measured within a rapidity range $|y| < 0.8$. These two measurements are described in [Otw2011] and [Dob2010]. At this collision energy only three common p_T bins exist in the range of $4 - 8\,\text{GeV/c}$. In these bins the ratio is close to 1.

At $\sqrt{s} = 7\,\text{TeV}$, figure 7.13, the differential invariant yields of charged pions have been measured in ALICE at low p_T with the same method as used at $\sqrt{s} = 0.9\,\text{TeV}$ and at high p_T with the same method as used at $\sqrt{s} = 2.76\,\text{TeV}$. This opens a wide transverse-momentum range. The measurement at low transverse momentum $p_T < 1.5\,\text{GeV/c}$ (blue) is described in [Cho2011]. In this p_T range the first three data points within $p_T = 0.3 - 0.6\,\text{GeV/c}$ agree, mainly due to their large uncertainties. Above $0.4\,\text{GeV/c}$ the ratio is about $0.85 - 0.9$. The reason for this deviation is not yet understood. It is not clear yet whether the deviation is due to the measurement of neutral or of charged pions. At high transverse momentum common bins exist in the range of $3 - 16\,\text{GeV/c}$. In this transverse-momentum range the differential invariant yields of neutral and charged pions agree marginally within the uncertainties of $10 - 20\,\%$.

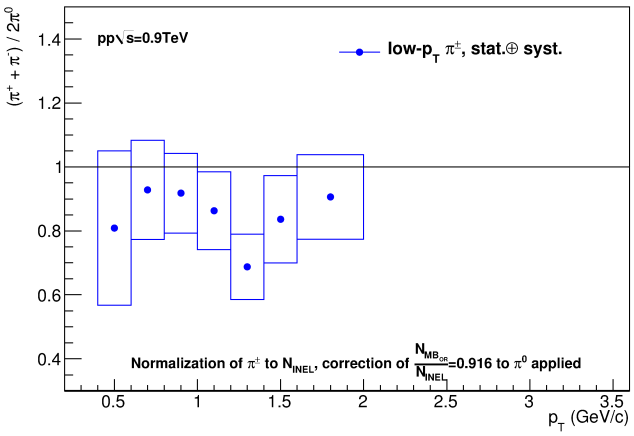

Figure 7.11.: Ratio of the differential invariant yields for $\pi^+ + \pi^-$ to $2 \cdot \pi^0$ as function of transverse momentum at $\sqrt{s} = 0.9\,\text{TeV}$. The given uncertainties include statistical and systematic uncertainties.

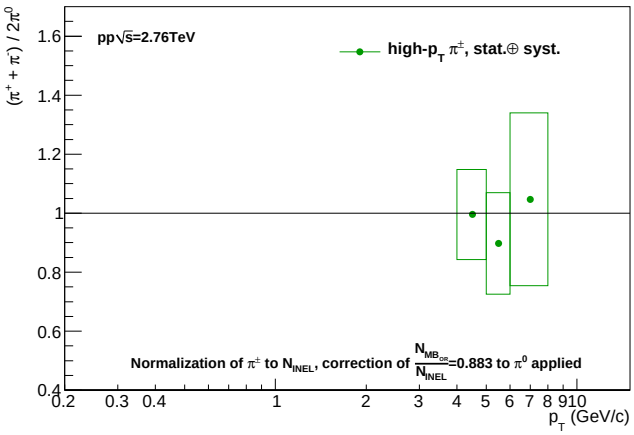

Figure 7.12.: Ratio of the differential invariant yields for $\pi^+ + \pi^-$ to $2 \cdot \pi^0$ as function of transverse momentum at $\sqrt{s} = 2.76\,\text{TeV}$. The given uncertainties include statistical and systematic uncertainties.

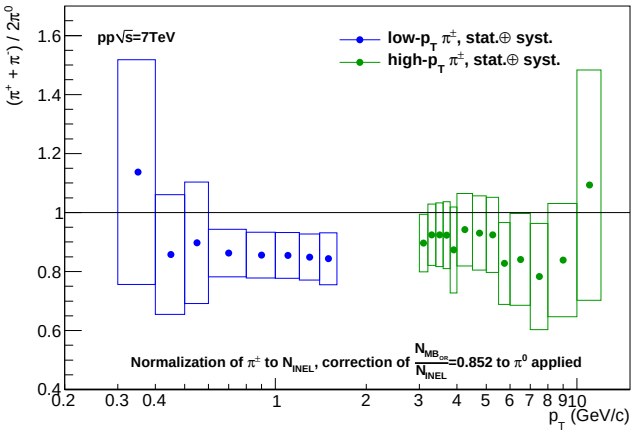

Figure 7.13.: Ratio of the differential invariant yields for $\pi^+ + \pi^-$ to $2 \cdot \pi^0$ as function of transverse momentum at $\sqrt{s} = 7\,\text{TeV}$. The given uncertainties include statistical and systematic uncertainties.

7.6. Comparison to π^0 and η measurements with PHOS

Within the ALICE experiment the π^0 spectra at all energies and the η spectrum at $\sqrt{s} = 7\,\text{TeV}$ have also been extracted with the PHOton Spectrometer PHOS [Ale2011], see section 4.2.5. The present transverse-momentum ranges for the meson detection in PHOS are given in table 7.5.

The number of mesons is estimated after combinatorial background subtraction by the integration of the peak. The combinatorial background has been calculated using a mixed-event technique. The reconstruction efficiency including geometrical acceptance for π^0 increases with transverse momentum and saturates at about $2 \cdot 10^{-2}$ above 15 GeV/c [Ale2011]. Above a transverse momentum of about 25 GeV/c the efficiency decreases again due to merging of photon clusters coming from the same π^0. The normalization window for the combinatorial background and the integration window for the yield have been varied for the estimation of systematic uncertainties. The largest contributions to the systematic errors come from yield extraction, reconstruction efficiency including acceptance, non-linearity of the energy response of the PHOS detector, conversions and vertex offset.

$\sqrt{s}$ (TeV)	$p_T^{\pi^0}$ (GeV/c)	p_T^{η} (GeV/c)
0.9	0.6 - 7.0	
2.76	0.6 - 15.0	
7	0.6 - 25.0	1.0 - 15.0

Table 7.5.: Present transverse-momentum range for π^0 and η meson reconstructed at the different LHC pp collision energies with PHOS.

7.6.1. Mass resolution

In figure 7.14 a comparison of the reconstructed peak position (bottom) and the mass resolution (top) for the π^0 at $\sqrt{s} = 7\,\text{TeV}$ of PHOS (red) to the reconstruction method via photon conversions (PCM) (black) is shown. In PHOS the absolute energy scale has been calibrated using the π^0 peak position. The final energy resolution together with the slope of the neutral pion spectrum leads to a deviation in the observed position from the PDG reference value at low transverse momentum. Above $p_T > 3\,\text{GeV/c}$ the non-linearity effects are already very small and the reconstructed peak positions get very close to the reference. The reconstruction of the neutral pion via conversions depends on the momentum of the reconstructed tracks, therefore the peak position is much closer to the reference at lower p_T and gets slightly worse above 3 GeV/c.

The differences between both methods are also reflected in the mass resolution. The energy resolution of PHOS measured in nominal test beams amounts to $\sigma_E/E = 1.12\% \oplus (3.6\%)/(\sqrt{E/GeV})$ [Ale2006]. The resolution in the measured transverse-momentum range is about $7\,\text{MeV/c}^2$ while for the conversion method it is about $3 - 4\,\text{MeV/c}^2$ at low p_T and worse for increasing transverse momentum. Up to $p_T = 8\,\text{GeV/c}$ the resolution for the conversion method is better than for PHOS, in the p_T range $8 - 16\,\text{GeV/c}$ it is similar.

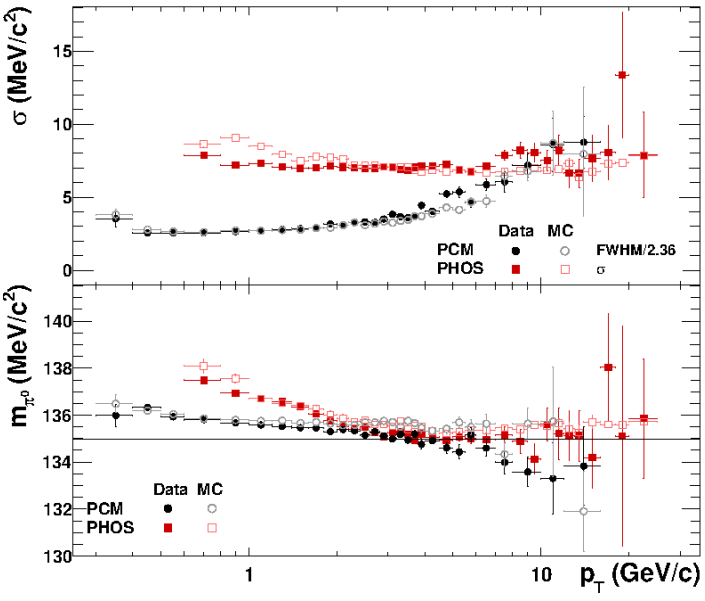

Figure 7.14.: Reconstructed π^0 mass resolution (top) and peak positions (bottom) as functions of transverse momentum compared to Monte Carlo simulations for PHOS (red) and PCM (black).

7.6.2. Differential invariant cross sections

The differential invariant cross sections in PHOS have been calculated following eq. 7.2. Afterwards the obtained cross sections from both methods have been combined, following eq. 6.1, here x_i corresponds to the different analysis methods PHOS and PCM and δx_i to their quadratic sum of statistical and systematic uncertainties. The data points have been combined in case of the same binning. Above $p_T = 12\,\mathrm{GeV/c}$ only data points from PHOS have been taken, below $p_T = 0.8\,\mathrm{GeV/c}$ only data points from PCM. The resulting average differential invariant cross sections are presented in figure 7.15 for π^0 and in figure 7.16 for η mesons. The combined transverse-momentum range is for π^0 $0.4 - 25\,\mathrm{GeV/c}$ at $\sqrt{s} = 7\,\mathrm{TeV}$, $0.4 - 15\,\mathrm{GeV/c}$ at $\sqrt{s} = 2.76\,\mathrm{TeV}$ and $0.4 - 7\,\mathrm{GeV/c}$ at $\sqrt{s} = 0.9\,\mathrm{TeV}$, for η mesons the range is $0.4 - 15\,\mathrm{GeV/c}$ at $\sqrt{s} = 7\,\mathrm{TeV}$.

The spectra have been fitted by the Tsallis fit function $\mathcal{T}$, eq. 6.4. The extracted fit parameters for the combined spectra are given in table 7.6. The values are in agreement with those from PCM, table 7.1. Also for the combined spectra a dependence on the collision energy is visible only for the parameter $\mathrm{d}N/\mathrm{d}y$. The two other parameters do not show a significant trend.

Meson	$\sqrt{s}$ (TeV)	$\mathrm{d}N/\mathrm{d}y$	T (MeV/c^2)	n
π^0	7	2.41 ± 0.13	141 ± 4	6.96 ± 0.07
	2.76	1.99 ± 0.26	130 ± 8	7.05 ± 0.18
	0.9	1.48 ± 0.31	136 ± 15	7.99 ± 0.56
η	7	0.21 ± 0.02	234 ± 21	7.08 ± 0.49

Table 7.6.: Parameters of the Tsallis fit to the combined π^0 and η differential invariant cross section. The given $\mathrm{d}N/\mathrm{d}y$ values correspond to the yield per inelastic collision. The errors include statistical and systematic uncertainties. The systematic uncertainty of the interaction cross section σ_{pp} is not included.

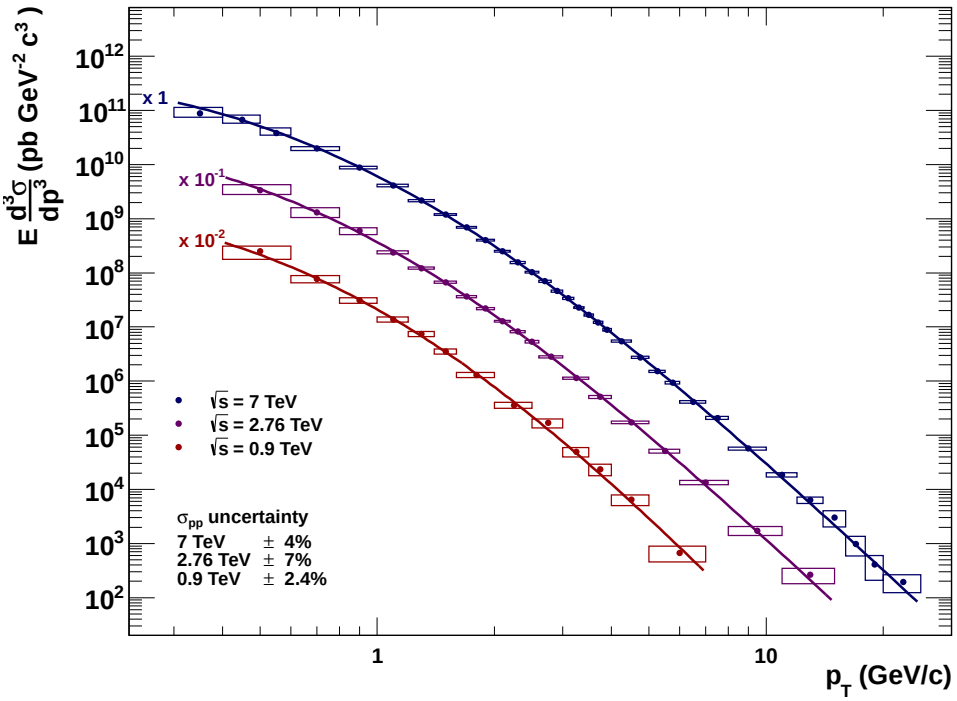

Figure 7.15.: Combined π^0 differential invariant cross sections at $\sqrt{s} = 0.9$ (brown), 2.76 (purple) and 7 TeV (blue) as a function of the transverse momentum. The measured spectra at $\sqrt{s} = 0.9$ and 2.76 TeV are scaled for a better overview. The errors include statistical and systematic uncertainties. The systematic uncertainty of the interaction cross section σ_{pp} is not included. The lines represent the Tsallis fit.

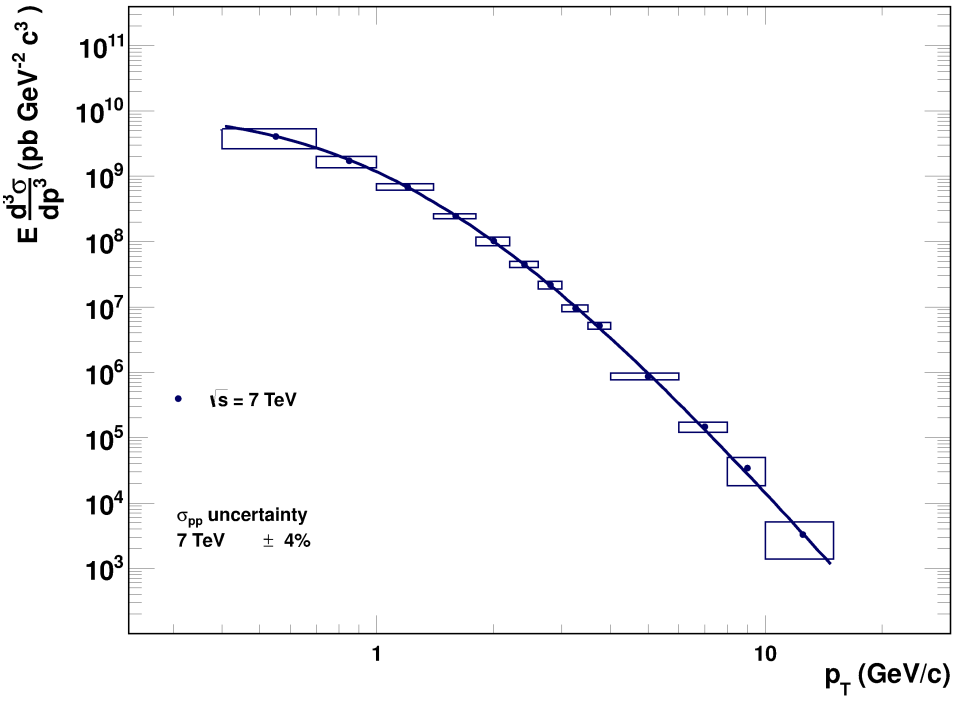

Figure 7.16.: Combined η differential invariant cross section at $\sqrt{s} = 7$ TeV as a function of the transverse momentum. The errors include statistical and systematic uncertainties. The systematic uncertainty of the interaction cross section σ_{pp} is not included. The line represent the Tsallis fit.

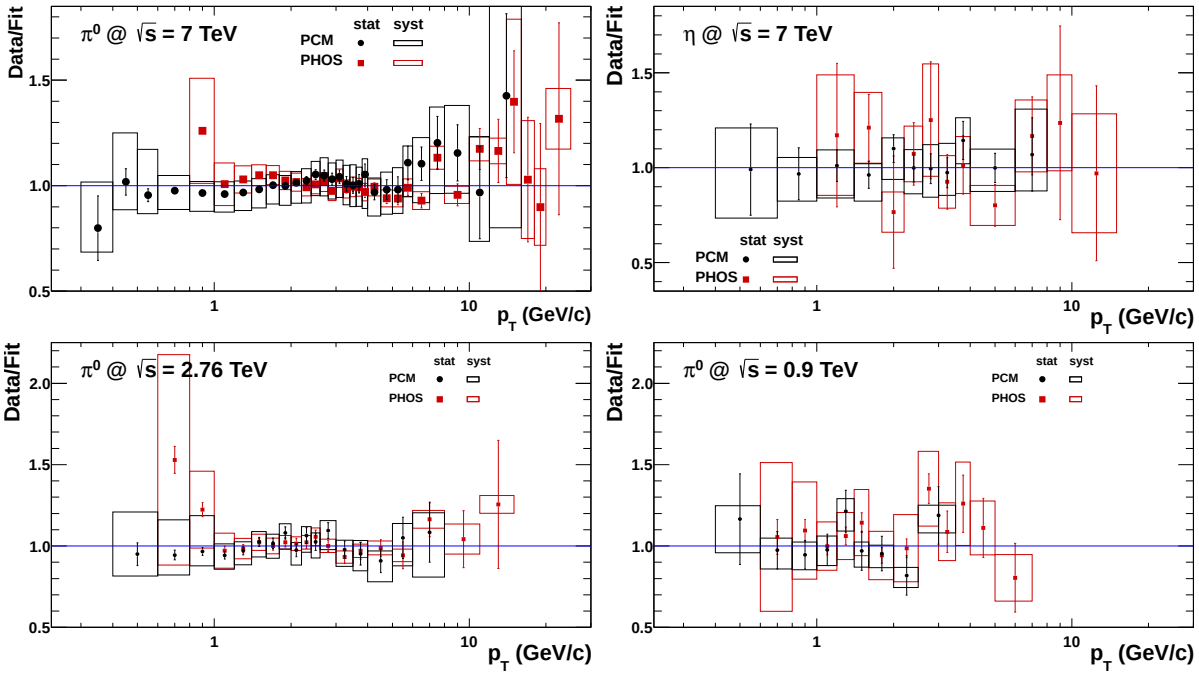

Figure 7.17.: Ratios of the two independent results (PCM and PHOS) to the fit of the combined invariant cross section. On top left for π^0 and top right for η, both at $\sqrt{s} = 7\,\text{TeV}$. Bottom left for π^0 at $\sqrt{s} = 2.76\,\text{TeV}$ and bottom right for π^0 at $\sqrt{s} = 0.9\,\text{TeV}$. All distributions are shown as a function of transverse momentum.

The ratios of the individual data sets of PHOS (red) and PCM (black) to the fit to the combined result are shown in figure 7.17. In the top panel the comparison of π^0 (left) and η (right) at $\sqrt{s} = 7\,\text{TeV}$, in the bottom π^0 at $\sqrt{s} = 2.76$ (left) and $\sqrt{s} = 0.9\,\text{TeV}$ (right) are shown. For all compared spectra a good agreement has been found.

7.7. Comparison to NLO calculations

The combined π^0 differential invariant cross sections of PHOS and PCM at $\sqrt{s} = 0.9, 2.76$ and 7 TeV as well as the combined η cross sections at $\sqrt{s} = 7$ TeV and the η cross sections of PCM at $\sqrt{s} = 0.9$ and 2.76 TeV have been compared to NLO pQCD calculations. The calculations use CTEQ6M5 PDF's and DSS FF's [DSS2007] for π^0 and CTEQ6M5 PDF's and AESSS' FF [Aid2010] for η mesons. The uncertainties of the theoretical predictions are taken into account by varying the factorization and renormalization scale $\mu = p_T/2$, $\mu = p_T$ and $\mu = 2p_T$. For neutral pions also the theoretical predictions of CTEQ5M PDF's and BKK' FF [BKK1995], calculated with INCNLO [Aur2000], at $\mu = 2p_T$ are shown for $\sqrt{s} = 0.9$ and 7 TeV.

For the comparison of the measured spectra and theoretical predictions the measured spectra have been fitted by the Tsallis fit function $\mathcal{T}$. The theoretical predictions have been divided by the result of the fit. In figure 7.18 and 7.19 the calculated ratios are shown for neutral pions and η mesons as well as the ratios of the combined spectra of PCM + and PHOS to the fit. The given uncertainties include statistical and systematic errors. At $\sqrt{s} = 0.9$ TeV (bottom) the predictions for both mesons agree well with NLO pQCD calculations. For neutral pions as well as for η mesons the measured spectra lie between $\mu = 1\,p_T$ and $\mu = 2\,p_T$. For $\sqrt{s} = 2.76$ TeV (middle) a discrepancy appears between the measurement and the prediction for neutral pions. The measured spectrum touches the line from predictions only in few points. For η mesons the spectrum above $p_T = 3$ GeV/c is in agreement with NLO pQCD calculations at $\mu = 2\,p_T$. At the highest collision energy $\sqrt{s} = 7$ TeV both meson spectra do not agree with the calculations. In both cases the theoretical predictions have a harder slope than the measured spectra. The NLO calculations overestimate the meson yields by a factor up to 3. Only calculations with BKK FF for $\mu = 2p_T$ are in agreement with the measured π^0 spectrum below a transverse momentum $p_T = 8$ GeV/c. It needs to be checked whether NLO pQCD calculations at higher μ like $\mu = 4\,p_T$ still fail to reproduce the measured spectra. A trend towards higher μ for increasing collision energies has already been seen in the range of $\sqrt{s} = 62.4 - 500$ GeV [SZS2010].

Although the theoretical predictions cannot reproduce the π^0 and η spectra they are able to describe the η/π^0 ratios. The comparison of the measured η/π^0 ratios to NLO pQCD calculations are shown in figure 7.20 as a function of transverse momentum. In the top the η/π^0 ratio of the combined measurement at $\sqrt{s} = 7$ TeV is compared, in the bottom the measured ratio with PCM at $\sqrt{s} = 2.76$ TeV is used for comparison. The given uncertainties include systematic and statistical errors. The overestimation of the particle productions are similar for π^0 and η mesons, less convincing for $\sqrt{s} = 2.76$ TeV. In the η/π^0 ratio the influence of the PDF's and the unphysical scale μ are reduced.

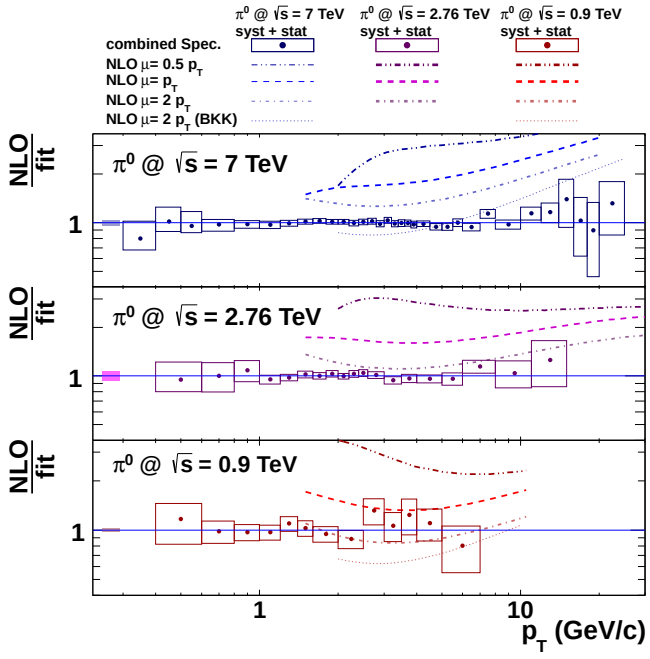

Figure 7.18.: Ratios of the combined π^0 differential invariant cross sections to NLO predictions from [DSS2007] and [BKK1995] for $\sqrt{s} = 7\,\mathrm{TeV}$ (top), $\sqrt{s} = 2.76\,\mathrm{TeV}$ (middle) and $\sqrt{s} = 0.9\,\mathrm{TeV}$ (bottom). The lines are drawn as $[-\cdot\cdot-]$ for $\mu = 0.5\,\mathrm{p_T}$, $[--]$ for $\mu = 2\,\mathrm{p_T}$, $[-\cdot-]$ for $\mu = 0.5\,\mathrm{p_T}$ and $[\cdots]$ for [BKK1995]. The systematic uncertainty of the measured interaction cross section σ_{pp} is not included, but drawn as boxes on the left.

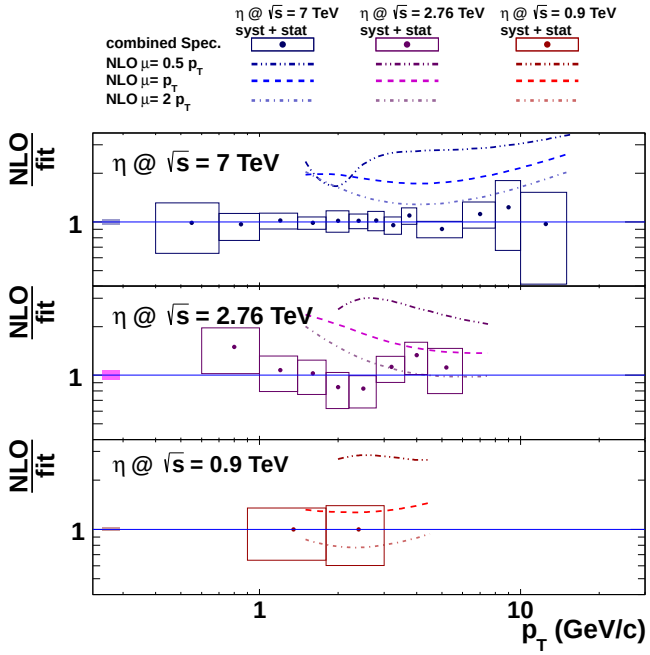

Figure 7.19.: Ratios of the η differential invariant cross sections to NLO predictions from [DSS2007] and [BKK1995] for $\sqrt{s} = 7\,\mathrm{TeV}$ (top), $\sqrt{s} = 2.76\,\mathrm{TeV}$ (middle) and $\sqrt{s} = 0.9\,\mathrm{TeV}$ (bottom). For $\sqrt{s} = 7\,\mathrm{TeV}$ the combined measured spectra has been used. The lines are drawn in $[-\cdot\cdot-]$ for $\mu = 0.5\,\mathrm{p_T}$, $[--]$ for $\mu = 2\,\mathrm{p_T}$ and $[-\cdot-]$ for $\mu = 0.5\,\mathrm{p_T}$. The systematic uncertainty of the measured interaction cross section σ_{pp} are not included, but drawn as boxes on the left.

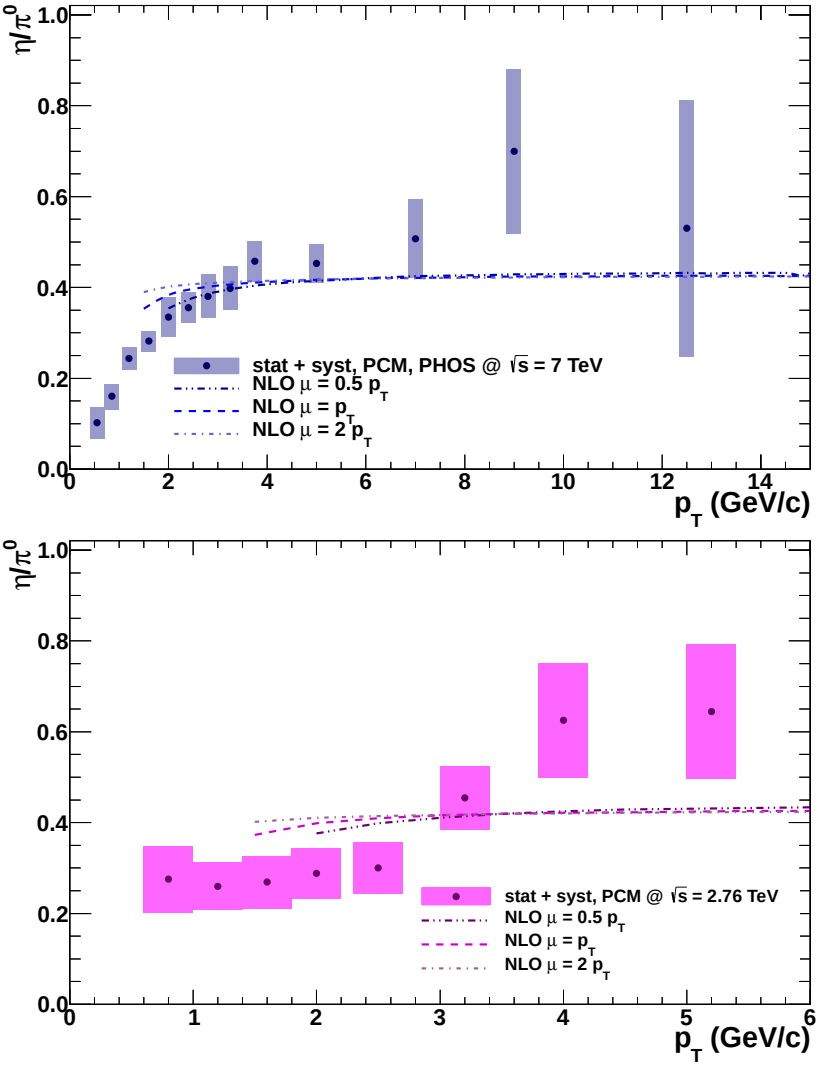

Figure 7.20.: Comparison of the measured η/π^0 ratios at $\sqrt{s} = 2.76$ (bottom) and 7 TeV (top) to NLO pQCD predictions as functions of transverse momentum. The theoretical predictions are drawn as $[-\cdot\cdot-]$ for $\mu = 0.5\,\mathrm{p_T}$, $[--]$ for $\mu = 2\,\mathrm{p_T}$ and $[-\cdot-]$ for $\mu = 0.5\,\mathrm{p_T}$. At $\sqrt{s} = 7$ TeV the combined ratio is compared, at $\sqrt{s} = 2.76$ TeV the measured ratio from PCM is used.

7.8. Dependence of the π^0 production on charged-particle multiplicity

Recent publications emphasize that „proton-proton collisions are not trivial, especially in the regime of high multiplicity events“ [Por2011]. It is believed that high multiplicity events result from three effects: „high underlying multiplicity for collisions at small impact parameters, upward fluctuations of the gluon density in the colliding protons, and production of hadrons in the fragmentation of dijets” [Str2011]. Figure 7.21 shows the mean transverse momentum $<p_T>$ as a function of measured charged-particle multiplicity n_{ch} at $\sqrt{s} = 0.9$ TeV, obtained in the ALICE experiment [Aam2010a]. A rise of $<p_T>$ with respect to n_{ch} is clearly visible. However, the underlying physics is not fully understood. Therefore, the study of identified particle productions in different charged-particle multiplicity classes can help to get more insights on this topic.

In the presented analysis the charged-particle multiplicity n_{ch} is based on tracks coming from the primary vertex and measured in the Inner Tracking System and the Time Projection Chamber

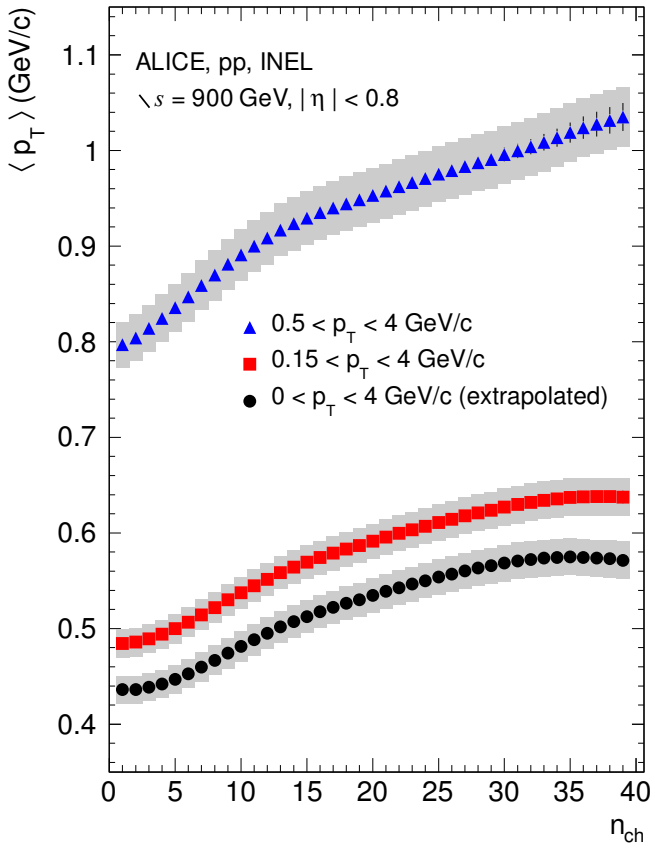

Figure 7.21.: Mean transverse momentum as function of the charged-particle multiplicity for proton-proton collisions at $\sqrt{s} = 0.9\,\text{TeV}$ [Aam2010a].

of ALICE. Only tracks with a transverse momentum of least 150 MeV/c and within $|\eta| < 0.8$ have been taken into account. Due to detector effects, e.g. dead regions and pedestal noise, the measured charged-particle multiplicity does not correspond to the real one. The correlation between measured and true charged-particle multiplicity is shown in figure 7.22. The entries at high n_{true} but $n_{meas.} = 0$ are not fully understood yet and thus, the measured charged-particle multiplicity is used for the analysis.

The analyzed events have been divided into five multiplicity classes. The first class has been defined below the typical charged-particle multiplicity of proton-proton events, while the second and third class roughly correspond to this number. In the two last bins the limits are defined such that the number of charged tracks is about a factor 3 and 5, respectively, enhanced. The lines in figure 7.23 indicate the defined multiplicity classes. Their limits and the extracted mean multiplicity $<n_{ch}>$ are summarized in table 7.7.

For each multiplicity class the raw yield has been extracted and the yield evaluated following eq. 7.1 has been applied. To exclude a possible bias the π^0 reconstruction efficiencies in each multiplicity class $\epsilon_{MultClass}$ have been compared to the reconstruction efficiency of minimum-bias events $\epsilon_{MinBias}$. The ratios $\epsilon_{MultClass}/\epsilon_{MinBias}$ are given in figure 7.24 as a function of transverse momentum. For the first multiplicity class a flat deviation of $-5\,\%$ is seen in the entire transverse-momentum range. Nevertheless, the observed deviation of the corrected yield with respect to miminum-bias events is larger than 5 % and the given uncertainties do not include systematic errors, therefore this efficiency has been used to correct the spectra.

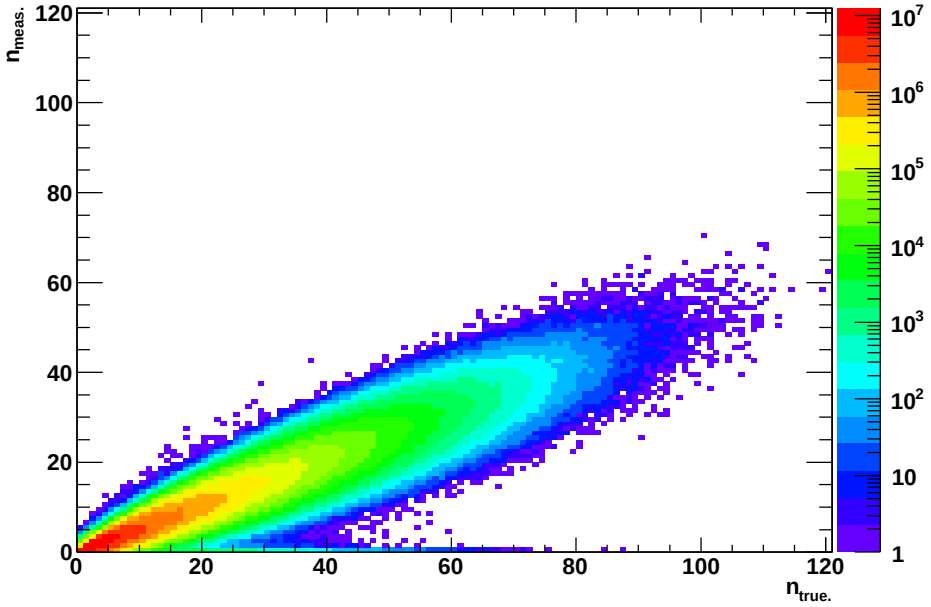

Figure 7.22.: Correlation matrix of measured charged-particle multiplicity $n_{meas.}$ versus true charged-particle multiplicity n_{true} at $\sqrt{s} = 7$ TeV. The measure multiplicity has been obtained with tracks traversing both ITS and TPC within $|\eta| < 0.8$ and $p_T > 150 MeV/c$. For the true multiplicity no least transverse momentum has been applied. The correlation matrix is obtained by simulations. The entries at high n_{true} but $n_{meas.} = 0$ are not understood yet.

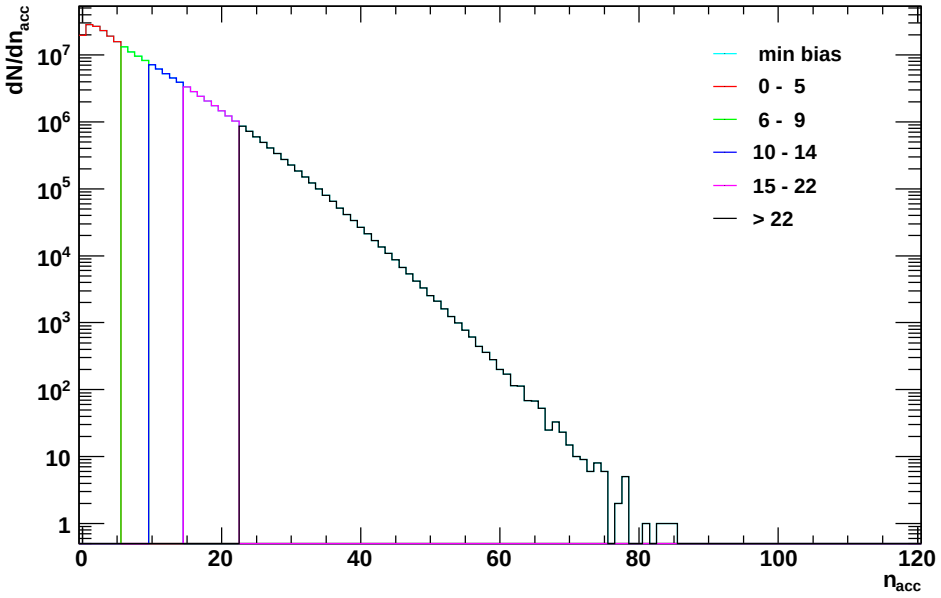

Figure 7.23.: Distribution of measured charged-particle multiplicity in data at $\sqrt{s} = 7$ TeV. The lines indicate the different multiplicity classes defined for this analysis.

The π^0 differential invariant yields in the different multiplicity bins are presented as a function of transverse momentum in figure 7.25. For each multiplicity bin the π^0 differential invariant yield has been measured over about 5 orders of magnitude in the transverse-momentum range $p_T = 0.4 - 8.0\,\mathrm{GeV/c}$. The errors bars are statistical only. The enhancement of the π^0 differential invariant yield with increasing charged-particle multiplicity is clearly visible.

$n_{meas.}$	$<n_{ch}>$
0-5	2.31 ± 1.59
6-9	7.31 ± 1.12
10-14	11.70 ± 1.39
15-22	17.65 ± 2.19
> 22	27.40 ± 4.66
minimum bias	6.06 ± 5.92

Table 7.7.: Defined multiplicity bins for measured charged-particle multiplicity $n_{meas.}$ and corresponding mean charged-particle multiplicity $<n_{ch}>$. The error corresponds to the standard deviation.

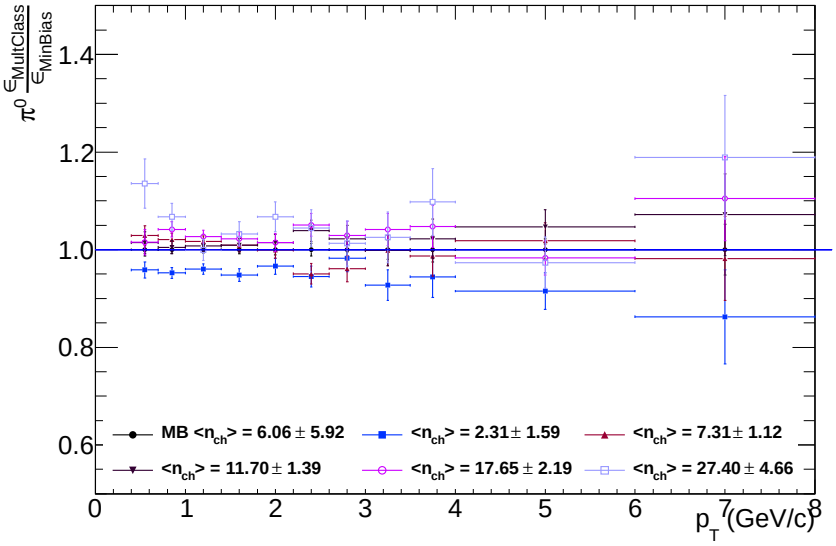

Figure 7.24.: Ratios $\epsilon_{Mult}/\epsilon_{MinBias}$ of the π^0 reconstruction efficiencies as function of transverse momentum. The error bars only include statistical errors.

The ratios of the particular spectra to the minimum-bias spectrum

$$R_{mult} = \frac{E\frac{d^3N}{dp^3} \text{ MultClass}}{E\frac{d^3N}{dp^3} \text{ Minimum Bias}} \tag{7.4}$$

are shown as a function of transverse momentum in figure 7.26. For the first bin (blue squares), where the mean charged multiplicity $<n_{ch}> = 2.31 \pm 1.59$ is below the measured mean charged multiplicity in minimum bias events $<n_{ch}> = 6.06 \pm 5.92$, the ratio R_{Mult} decreases significantly. Above $p_T \approx 4\,\text{GeV/c}$ it levels out at about $R_{Mult} \approx 0.15$. The second multiplicity bin $<n_{ch}> = 7.31 \pm 1.12$ (red triangles) corresponds to the typical multiplicity of proton-proton collisions. The same applies to the third multiplicity bin with $<n_{ch}> = 11.70 \pm 1.39$ (purple triangles), where the ratio is flat, too. This behavior changes in the two highest multiplicity classes. In both the ratios increase with increasing transverse momentum and flatten above $p_T \approx 4\,\text{GeV/c}$. For $<n_{ch}> = 17.65 \pm 2.19$ (purple circles) the limit is about 4, in case of the highest bin $<n_{ch}> = 27.40 \pm 4.66$ (blue open squares) the amount of π^0's is about 10 times higher with respect to minimum bias at high p_T.

To get an idea about the nature of the production mechanism in the different classes the distibutions R_{Mult} have been scaled by the ratio of the mean multiplicity in minimum bias events to

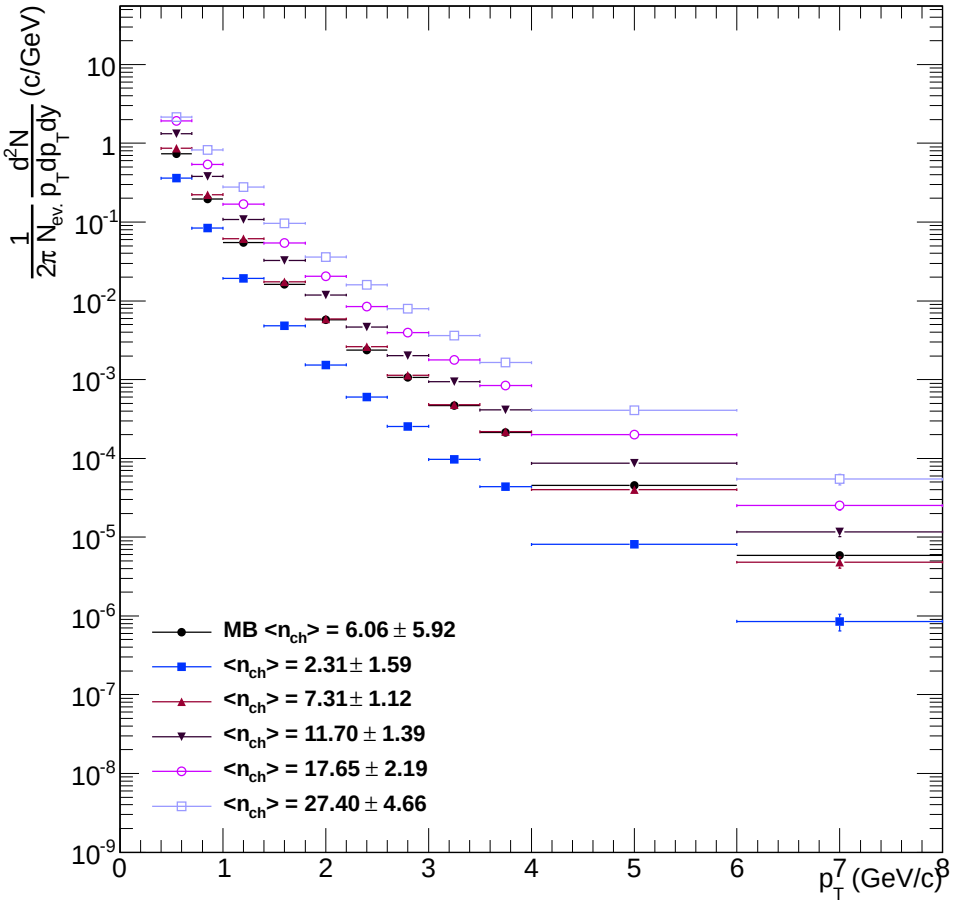

Figure 7.25.: Corrected π^0 differential invariant yield as function of transverse momentum for each multiplicity bin. The error bars include statistical errors only.

the mean multiplicity in the different classes $<n_{ch}^{MinBias}>/<n_{ch}^{MultClass}>$, shown in figure 7.27. The negative slope towards high transverse momentum in the first class is an indication that at low charged-particle multiplicity events soft processes are preferred. A similar trend, although much less pronounced is visible in the second multiplicity class. The scaled spectrum in the third class describes exactly the minimum bias distribution. In the two last classes the scaled differential invariant yield is about a factor 2 higher compared to minimum bias events in the transverse-momentum range above $p_T = 4\,\mathrm{GeV/c}$. This indicates an enhancement of hard production processes.

The hardening of the differential invariant spectra with increasing charged-particle multiplicity is also reflected in the mean transverse momentum. The obtained $< p_T >$ as a function of $<n_{ch}>$ are summarized in table 7.8 and plotted in figure 7.28. From the lowest to the highest multiplicity class $<p_T>$ increases about 65 %. From a linear fit a slope of $(0.011 \pm 0.002)\,\mathrm{GeV/c}$ and an intercept $< p_T >$ for π^0 of $(0.374 \pm 0.019)\,\mathrm{GeV/c}$ have been extracted, see table 7.9.

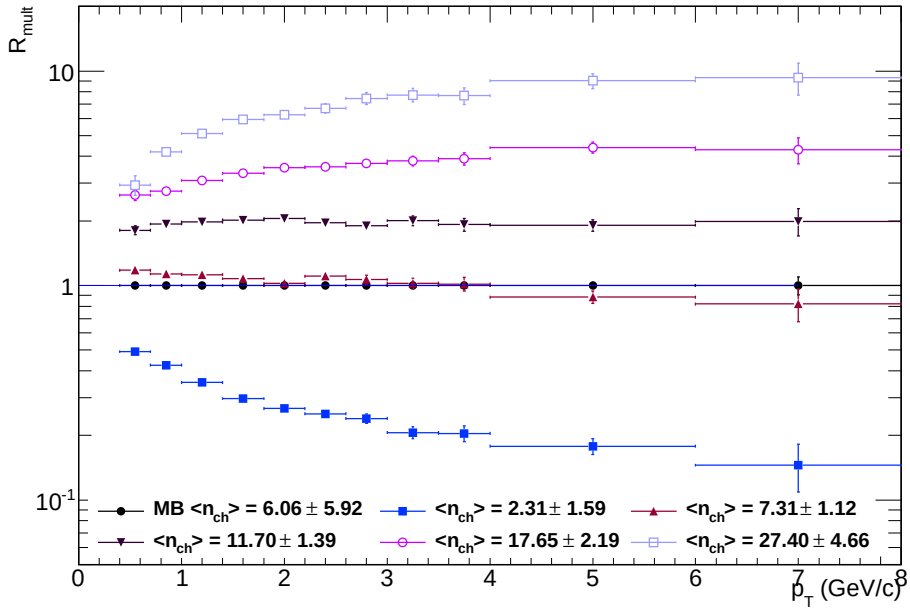

Figure 7.26.: Ratio of the π^0 spectrum to the minimum bias distribution R_{mult} for each charged particle multiplicity bin as a function of the transverse momentum at $\sqrt{s} = 7\,\text{TeV}$. The given uncertainties are statistical only.

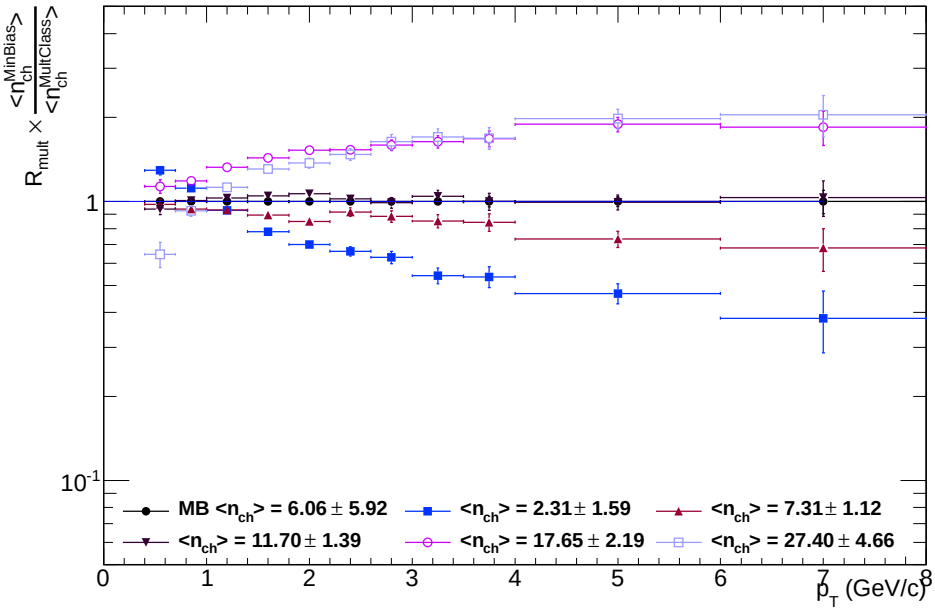

Figure 7.27.: Ratio of the π^0 spectrum to the minimum bias distribution R_{mult} for each charged particle multiplicity bin as a function of the transverse momentum at $\sqrt{s} = 7\,\text{TeV}$, scaled by the ratio of $<n_{ch}^{MinBias}>/<n_{ch}^{MultBin}>$. The given uncertainties are statistical only.

$<n_{ch}>$	$< p_T >$ π^0 (GeV/c)
2.31 ± 1.59	0.384 ± 0.011
7.31 ± 1.12	0.468 ± 0.015
11.70 ± 1.39	0.503 ± 0.017
17.65 ± 2.19	0.545 ± 0.021
27.40 ± 4.66	0.638 ± 0.036

Table 7.8.: Mean transverse momentum of the π^0 differential invariant yields for different mean charged-particle multiplicities at $\sqrt{s} = 7$ TeV. The given errors are statistical only.

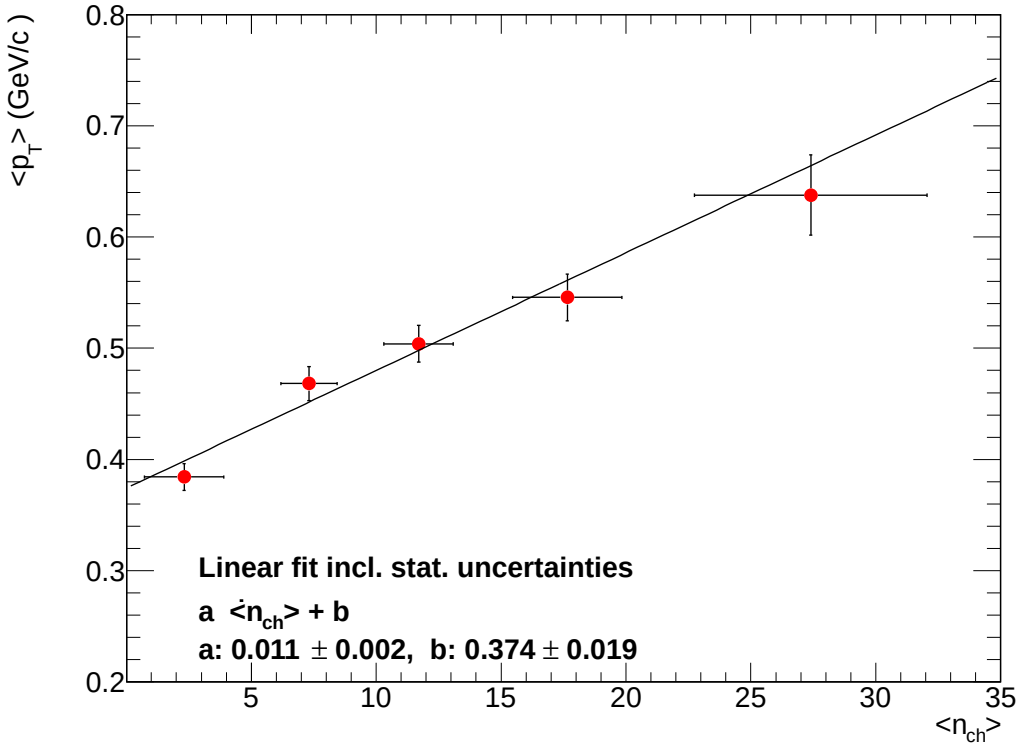

Figure 7.28.: Mean π^0 transverse momentum as a function of mean charged-particle multiplicity at $\sqrt{s} = 7$ TeV. The given errors are statistical only. The linear fit is drawn as a solid line.

Meson	a	b (GeV/c)
π^0	0.011±0.002	0.374±0.019

Table 7.9.: Fit parameters of the linear fit of the mean transverse momentum $<p_T> = a < n_{ch} > +b$ for π^0 as a function of the charged-particle multiplicity. The uncertainties include statistical uncertainties.

8. Summary

In this thesis the first measurements of the π^0 and η meson production at the LHC proton-proton collision energies $\sqrt{s} = 0.9, 2.76$ and $7\,\text{TeV}$ are presented. The data samples were collected by the ALICE experiment in 2010 for the energies $\sqrt{s} = 0.9\,\text{TeV}$ and $\sqrt{s} = 7\,\text{TeV}$ and in 2011 for the collision energy $\sqrt{s} = 2.76\,\text{TeV}$.

Both mesons are measured via the reconstruction of their decay photons. Photons can convert into electron-positron pairs in the detector material which are then reconstructed with the Inner Tracking System and the Time Projection Chamber of ALICE. The detected photon candidates are combined to pairs. The estimation of the combinatorial background is based on a mixed-event technique where events with the same photon candidate multiplicity and in the same z collision vertex class are mixed. After the background subtraction the invariant mass spectra have been fitted around the expected meson mass position with a Gaussian modified with an exponential part to account for electron bremsstrahlung and a linear part to account for remaining background.

The achieved mass resolution for the π^0 meson is about $3-4\,\text{MeV/c}^2$ up to a transverse momentum of about $4\,\text{GeV/c}$, up to a transverse momentum of $10\,\text{GeV/c}$ the mass resolution of the photon conversion method is better than the resolution achieved by the PHOton Spectrometer in ALICE. For the η meson the achieved mass resolution ranges between $5-10\,\text{MeV/c}^2$. The peak position of the π^0 is within $\pm1\,\text{MeV/c}^2$ of the PDG value of $135\,\text{MeV/c}^2$, for the η meson it is within $\pm3\,\text{MeV/c}^2$ of the PDG value of $548\,\text{MeV/c}^2$.

To ensure the correctness of the obtained spectra a detailed estimation of the systematic uncertainties has been done. The main contributions come from yield extraction, electron selection and pion rejection, constraints on mass and origin of the photons and, especially for the η meson, from the background estimation. An overall contribution to the uncertainty comes from the uncertainty in the knowledge of the material budget. At present this is the main contribution in the intermediate transverse momentum range.

The π^0 meson has been detected in a transverse-momentum range from $0.3\,\text{GeV/c}$ to $16.0\,\text{GeV/c}$ at $\sqrt{s} = 7\,\text{TeV}$, from $0.4\,\text{GeV/c}$ to $8.0\,\text{GeV/c}$ at $\sqrt{s} = 2.76\,\text{TeV}$ and $0.4\,\text{GeV/c}$ to $3.5\,\text{GeV/c}$ at $\sqrt{s} = 0.9\,\text{TeV}$. The η meson has been measured in the range of $0.4\,\text{GeV/c}$ to $8.0\,\text{GeV/c}$ at $\sqrt{s} = 7\,\text{TeV}$ and $0.6\,\text{GeV/c}$ to $6.0\,\text{GeV/c}$ at $\sqrt{s} = 2.76\,\text{TeV}$. It has also been possible to observe the η meson at $\sqrt{s} = 0.9\,\text{TeV}$ in the range $0.9\,\text{GeV/c}$ to $3.0\,\text{GeV/c}$, albeit only in two transverse momentum bins. Due to the steeply falling spectra the transverse momentum at the bin center does not represent the true value. Therefore, the differential invariant yields include an additional correction for the finite bin width. With the measured interaction cross sections σ_{pp} the π^0 and η differential invariant cross sections have been obtained.

With the given invariant differential yields the η/π^0 ratios have been obtained at the three collision energies and found to be in agreement with world data from proton-proton collisions. Additionally, m_T scaling has been tested at $\sqrt{s} = 2.76$ and $7\,\text{TeV}$. For $\sqrt{s} = 7\,\text{TeV}$ an indication of m_T scaling violation at low transverse momentum has been found while for $\sqrt{s} = 2.76\,\text{TeV}$ no clear statement can be given. At this energy the ratio seems to decrease toward low p_T, but

it could also be constant within the systematical and statistical errors.

The obtained spectra of neutral pions have been compared to the measurements of charged pions at the three energies. The measurements agree, only in the low transverse momentum range up to 1.5 GeV/c at $\sqrt{s} = 7$ TeV a deviation of 10 % has been found. It is not understood yet, whether the difference result due to the measurement of neutral or charged pions.

In the ALICE experiment neutral pions and η mesons have been measured by the ALICE PHOS calorimeter, too. At $\sqrt{s} = 7$ TeV both mesons have been obtained, at $\sqrt{s} = 0.9$ and 2.76 TeV only π^0 has been detected. The obtained spectra of the photon conversion method and PHOS show a very good agreement and, thus, they can be combined to enlarge the measured transverse momentum range. The combined spectra have been used for comparison to NLO pQCD calculations. The present calculations using CTEQ6M5 PDF and DSS FF reproduce the data at $\sqrt{s} = 0.9$ TeV, but overestimate the measurement at $\sqrt{s} = 7$ TeV. Therefore, these measurements provide very important constraints on the pluon-to-pion and gluon-to-η fragmentation functions used in these calculations.

Furthermore, the production of neutral pions has been investigated as a function of charged-particle multiplicity. A strong correlation has been observed. For charged-particle multiplicities below the typical multiplicity in proton-proton collisions the production of neutral pions is reduced, above an enhancement has been found. Furthermore, the mean transverse momenta have been calculated and found to be linearly increasing with charged-particle multiplicity.

The measurement of the π^0 and η differential invariant yields are crucial for the calculation of the nuclear modification function R_{AA} which describes the suppression of the particle production in heavy ion collisions compared to proton-proton collisions. At $\sqrt{s_{NN}} = 2.76$ TeV the measured R_{AA} has already been presented [Rus2011]. Last, but not least, the measured spectra allow to extract the direct photon spectrum from the background of decay photons. In heavy-ion collisions the direct-photon spectrum contains information about the temperature of the quark-gluon plasma.

The high p_T TRD trigger at trigger level L1 for electrons and positrons can improve the measurements at high transverse momentum. Following this, precise measurements of π^0 and η mesons via conversions can be done up to high transverse regions. As a consequence these results are able to compete with calorimeter measurements.

A. List of runs

118506	118507	118512	118518	118556
118558	118560	118561	121039	121040

Table A.1.: List of runs for $\sqrt{s} = 0.9\,\text{TeV}$, pass 3.

146746	146747	146748	146801	146802
146803	146804	146805	146806	146807
146817	146824	146856	146858	146859
146860				

Table A.2.: List of runs for $\sqrt{s} = 2.76\,\text{TeV}$, pass 2.

114931	115186	115193	115310	115318
115322	115328	115393	115401	115414
116102	116288	116402	116403	116562
116571	116574	116643	116645	117048
117050	117052	117053	117054	117059
117060	117063	117065	117077	117086
117092	117099	117109	117112	117116
117220	117222			

Table A.3.: List of runs for $\sqrt{s} = 7\,\text{TeV}$, period b, pass 2.

119159	119161	119163	119841	119842
119844	119845	119846	119849	119853
119856	119859	119862	120067	120069
120072	120073	120076	120079	120244
120503	120504	120505	120616	120617
120671	120741	120750	120758	120820
120821	120822	120823	120824	120825
120829				

Table A.4.: List of runs for $\sqrt{s} = 7\,\text{TeV}$, period c, pass 2.

122374	122375	124751	125023	125085
125097	125100	125101	125134	125296
125630	125632	125633	125842	125843
125844	125847	125848	125849	125850
125851	125855	126004	126007	126008
126073	126078	126081	126082	126088
126090	126097	126158	126160	126167
126168	126283	126284	126285	126351
126352	126359	126403	126404	126405
126406	126407	126408	126409	126422
126424	126425	126432	126437	

Table A.5.: List of runs for $\sqrt{s} = 7\,\text{TeV}$, period d, pass 2.

127822	127932	127933	127935	127936
127937	127940	127941	127942	128185
128186	128189	128191	128192	128260
128366	128452	128483	128486	128494
128495	128503	128504	128507	128582
128605	128609	128611	128615	128677
128678	128777	128778	128820	128823
128824	128835	128836	128843	128853
128855	128913	129512	129513	129514
129523	129527	129528	129540	129586
129587	129599	129639	129641	129647
129650	129652	129653	129654	129659
129666	129667	129723	129725	129726
129729	129735	129736	129738	129742
129744	129959	129960	129961	129983
130149	130157	130158	130172	130178
130179	130342	130343	130354	130356
130358	130480	130517	130519	130696
130704	130793	130795	130798	130799
130834	130840			

Table A.6.: List of runs for $\sqrt{s} = 7\,\text{TeV}$, period e, pass 2.

B. Tables to data points

$\sqrt{s} = 7\,\mathrm{TeV}$

π^0

p_T (GeV/c)	Yield (c/GeV)	stat. err. (%)	neg. sys. err. (%)	pos. sys. err. (%)
0.35	1.42E+00	19.21	-14.19	27.41
0.45	1.08E+00	6.18	-13.00	22.86
0.55	6.20E-01	3.18	-9.12	22.71
0.70	3.20E-01	1.35	-9.17	7.40
0.90	1.39E-01	1.09	-8.96	5.68
1.10	6.57E-02	1.06	-8.88	6.14
1.30	3.39E-02	1.11	-8.88	5.62
1.50	1.86E-02	1.20	-8.92	5.22
1.70	1.08E-02	1.35	-8.94	4.93
1.90	6.40E-03	1.49	-9.17	5.05
2.10	4.00E-03	1.67	-9.43	5.28
2.30	2.57E-03	1.90	-10.30	5.55
2.50	1.73E-03	2.14	-9.45	5.91
2.70	1.15E-03	2.44	-9.16	8.04
2.90	7.74E-04	2.75	-9.08	7.43
3.10	5.46E-04	3.08	-9.46	7.62
3.30	3.75E-04	3.44	-9.74	8.79
3.50	2.69E-04	3.79	-10.13	9.74
3.70	1.99E-04	4.38	-10.55	7.87
3.90	1.54E-04	4.76	-15.35	7.08
4.25	8.66E-05	3.73	-11.70	6.45
4.75	4.59E-05	4.76	-11.86	8.40
5.25	2.54E-05	6.13	-11.51	10.67
5.75	1.66E-05	7.10	-14.50	7.13
6.50	7.84E-06	7.16	-16.72	11.24
7.50	3.53E-06	10.49	-19.97	14.16
9.00	1.08E-06	11.52	-16.59	19.42
11.00	2.51E-07	22.57	-23.95	27.43
14.00	7.75E-08	27.23	-43.85	30.87

Table B.1.: Data points for π^0 differential invariant yield at $\sqrt{s}$ =7 TeV

π^0 in η binning

p_T (GeV/c)	Yield (c/GeV)	stat. err. (%)	neg. sys. err. (%)	pos. sys. err. (%)
0.55	6.10E-01	1.72	-8.99	9.38
0.85	1.68E-01	0.92	-8.99	5.42
1.20	4.55E-02	0.77	-8.90	5.25
1.60	1.38E-02	0.90	-8.93	4.99
2.00	4.96E-03	1.11	-8.93	4.97
2.40	2.07E-03	1.42	-9.15	5.18
2.80	9.30E-04	1.83	-9.14	5.61
3.25	4.07E-04	2.12	-9.26	5.51
3.75	1.86E-04	2.82	-9.35	5.43
5.00	3.15E-05	2.51	-10.10	5.28
7.00	4.92E-06	5.99	-17.99	7.62

Table B.2.: Data points for π^0 differential invariant yield in η binning at $\sqrt{s}$ =7 TeV

η

p_T (GeV/c)	Yield (c/GeV)	stat. err. (%)	neg. sys. err. (%)	pos. sys. err. (%)
0.55	6.51E-02	24.24	-25.77	22.20
0.85	2.77E-02	14.14	-14.79	8.94
1.20	1.11E-02	8.30	-16.89	8.11
1.60	3.85E-03	7.34	-14.35	6.11
2.00	1.78E-03	6.60	-14.72	5.16
2.40	7.15E-04	7.38	-13.56	9.70
2.80	3.41E-04	7.92	-15.08	12.73
3.25	1.58E-04	8.10	-12.22	15.89
3.75	8.72E-05	8.80	-10.79	10.45
5.00	1.54E-05	7.70	-12.35	9.97
7.00	2.25E-06	18.06	-17.93	22.34

Table B.3.: Data points for η differential invariant yield at $\sqrt{s}$ =7 TeV

$\sqrt{s} = 2.76\,\mathrm{TeV}$

π^0

p_T (GeV/c)	Yield (c/GeV)	stat. err. (%)	neg. sys. err. (%)	pos. sys. err. (%)
0.50	6.05E-01	7.43	-14.10	27.37
0.70	2.25E-01	3.17	-13.04	22.86
0.90	9.62E-02	2.50	-9.14	22.71
1.10	4.30E-02	2.45	-9.01	7.40
1.30	2.19E-02	2.55	-8.93	5.68
1.50	1.22E-02	2.72	-8.97	6.14
1.70	6.71E-03	3.16	-8.99	5.62
1.90	4.14E-03	3.43	-9.19	5.22
2.10	2.25E-03	4.10	-9.33	4.93
2.30	1.54E-03	4.54	-9.67	5.05
2.50	9.53E-04	5.20	-9.72	5.28
2.80	5.50E-04	4.43	-10.75	5.55
3.25	2.14E-04	5.43	-10.46	5.91
3.75	9.15E-05	7.41	-10.96	8.48
4.50	2.97E-05	7.98	-14.08	6.69
5.50	1.01E-05	12.15	-16.32	8.44
7.00	2.31E-06	16.82	-25.32	11.15

Table B.4.: Data points for π^0 differential invariant yield at $\sqrt{s}$ =2.76 TeV

π^0 in η binning

p_T (GeV/c)	Yield (c/GeV)	stat. err. (%)	neg. sys. err. (%)	pos. sys. err. (%)
0.80	1.40E-01	1.98	-8.95	9.38
1.20	2.95E-02	1.77	-8.87	5.42
1.60	8.80E-03	2.07	-8.98	5.25
2.00	3.01E-03	2.65	-9.20	4.99
2.50	9.54E-04	2.97	-9.33	5.29
3.20	2.33E-04	4.13	-9.32	4.91
4.00	5.90E-05	7.25	-9.29	6.67
5.20	1.21E-05	8.76	-9.29	6.74

Table B.5.: Data points for π^0 differential invariant yield in η binning at $\sqrt{s}$ =2.76 TeV

η

p_T (GeV/c)	Yield (c/GeV)	stat. err. (%)	neg. sys. err. (%)	pos. sys. err. (%)
0.80	3.40E-02	21.52	-23.18	22.20
1.20	7.70E-03	20.91	-15.96	8.73
1.60	2.58E-03	19.31	-17.28	7.80
2.00	8.29E-04	22.59	-13.46	5.60
2.50	2.89E-04	19.58	-14.50	5.02
3.20	1.13E-04	15.56	-12.42	4.81
4.00	4.03E-05	19.14	-14.68	5.62
5.20	7.54E-06	27.45	-14.13	15.32

Table B.6.: Data points for η differential invariant yield at $\sqrt{s}$ =2.76 TeV

$\sqrt{s} = 0.9\,\mathrm{TeV}$

π^0

p_T (GeV/c)	Yield (c/GeV)	stat. err. (%)	neg. sys. err. (%)	pos. sys. err. (%)
0.50	5.45E-01	23.94	-17.76	7.03
0.70	1.68E-01	11.75	-11.80	7.64
0.90	6.69E-02	9.29	-9.77	8.18
1.10	3.08E-02	9.90	-9.82	8.77
1.30	1.83E-02	10.58	-10.07	6.32
1.50	7.47E-03	12.32	-10.40	5.61
1.80	2.93E-03	11.12	-9.08	5.29
2.25	7.55E-04	14.74	-9.19	6.03
3.00	2.04E-04	14.91	-8.99	5.32

Table B.7.: Data points for π^0 differential invariant yield at $\sqrt{s}$ =0.9 TeV

π^0 **in** η **binning**

p_T (GeV/c)	Yield (c/GeV)	stat. err. (%)	neg. sys. err. (%)	pos. sys. err. (%)
1.35	1.06E-02	5.38	-9.14	5.45
2.40	5.53E-04	9.22	-9.14	5.45

Table B.8.: Data points for π^0 differential invariant yield in η binning at $\sqrt{s}$ =0.9 TeV

η

p_T (GeV/c)	Yield (c/GeV)	stat. err. (%)	neg. sys. err. (%)	pos. sys. err. (%)
1.35	6.52E-03	31.38	-15.73	13.88
2.40	2.84E-04	36.41	-15.73	13.88

Table B.9.: Data points for η differential invariant yield at $\sqrt{s}$ =0.9 TeV

C. Tables to systematic uncertainties

$\sqrt{s} = 7\,\text{TeV}$

π^0

Negative error

p_t	Cluster	p_t $e^{\pm}$	dE/dx	χ^2_γ	α	Yield extr.	BG	Σ w mat	Σ w/o mat
0.35	-2.83	0.00	-0.69	-10.12	-1.50	-1.64	-2.96	-14.19	-11.16
0.45	-2.83	0.00	-0.69	-8.36	-1.50	-1.64	-2.96	-13.00	-9.59
0.55	-1.52	0.00	-0.53	-0.49	-0.75	-1.64	-0.54	-9.12	-2.52
0.70	-0.87	0.00	-0.37	-0.70	-0.48	-2.29	-0.55	-9.17	-2.68
0.90	-0.21	-0.11	-0.26	-0.75	-0.34	-1.52	-0.48	-8.96	-1.83
1.10	-0.31	-0.16	-0.15	-0.59	-0.21	-1.07	-0.49	-8.88	-1.39
1.30	-0.37	-0.21	-0.12	-0.76	-0.28	-0.97	-0.51	-8.88	-1.43
1.50	-0.28	-0.42	-0.54	-0.42	-0.25	-1.33	-0.37	-8.92	-1.64
1.70	-0.49	-0.82	-0.44	-0.67	-0.23	-1.08	-0.57	-8.94	-1.76
1.90	-0.41	-1.56	-0.39	-0.65	-0.88	-1.20	-1.36	-9.17	-2.69
2.10	-1.42	-1.93	-0.34	-0.62	-1.21	-1.15	-1.76	-9.43	-3.48
2.30	-2.43	-2.30	-1.36	-2.58	-1.53	-1.61	-2.16	-10.30	-5.41
2.50	-1.46	-1.58	-0.25	-1.80	-0.77	-1.65	-1.08	-9.45	-3.52
2.70	-0.97	-1.22	-0.36	-1.41	-0.38	-1.09	-1.06	-9.16	-2.65
2.90	-0.49	-0.86	-0.30	-1.02	-0.58	-1.44	-1.04	-9.08	-2.37
3.10	-1.55	-0.43	-1.60	-1.50	-0.68	-1.92	-1.03	-9.46	-3.55
3.30	-1.74	-1.80	-1.83	-1.34	-0.78	-2.02	-1.37	-9.74	-4.24
3.50	-1.83	-2.49	-2.07	-1.26	-0.87	-2.65	-1.61	-10.13	-5.08
3.70	-1.93	-3.17	-1.46	-1.18	-0.96	-3.57	-1.84	-10.55	-5.86
3.90	-5.73	-1.46	-6.07	-4.43	-3.16	-4.24	-6.27	-15.35	-12.60
4.25	-0.94	-1.76	-1.74	-3.60	-2.65	-4.12	-4.01	-11.70	-7.74
4.75	-2.18	-2.05	-2.45	-2.76	-2.14	-5.79	-1.74	-11.86	-7.98
5.25	-1.66	-3.91	-2.94	-2.64	-4.11	-1.86	-1.26	-11.51	-7.46
5.75	-1.15	-4.85	-3.43	-2.52	-5.09	-7.99	-0.78	-14.50	-11.55
6.50	-4.67	-5.78	-8.08	-5.42	-6.08	-2.93	-2.74	-16.72	-14.24
7.50	-5.66	-7.40	-8.95	-7.69	-3.04	-1.46	-9.19	-19.97	-17.94
9.00	-5.66	-7.40	-5.23	0.00	0.00	0.00	-9.19	-16.59	-14.09
11.00	-6.56	-7.81	-16.31	0.00	0.00	-6.08	-9.48	-23.95	-22.29
14.00	-21.27	-7.81	-17.90	0.00	0.00	-30.38	-9.48	-43.85	-42.97

Table C.1.: Final estimation of the systematic error in % (with each divided by $\sqrt{2}$) for the π^0 at $\sqrt{s} = 7\,\text{TeV}$, negative error.

Positive error

p_t	Cluster	p_t $e^{\pm}$	dE/dx	χ^2_γ	α	Yield extr.	BG	Σ w mat	Σ w/o mat
0.35	0.00	22.13	5.26	8.05	0.00	1.57	11.99	27.41	26.99
0.45	0.00	22.13	1.21	1.61	0.00	0.31	2.40	22.86	22.35
0.55	0.00	22.13	0.65	0.81	0.00	0.16	1.40	22.71	22.19
0.70	0.00	5.50	0.63	0.40	0.00	0.08	0.90	7.40	5.62
0.90	0.00	2.92	0.62	0.20	0.00	0.04	0.40	5.68	3.02
1.10	0.00	3.80	0.10	0.10	0.00	0.02	0.20	6.14	3.81
1.30	0.00	2.90	0.16	0.05	0.00	0.01	0.10	5.62	2.90
1.50	0.00	1.99	0.17	0.03	0.00	0.00	0.36	5.22	2.03
1.70	0.25	0.87	0.17	0.29	0.00	0.00	0.50	4.93	1.09
1.90	0.38	1.26	0.29	0.42	0.00	0.00	0.63	5.05	1.54
2.10	0.51	1.64	0.28	0.55	0.25	0.00	1.18	5.28	2.18
2.30	0.71	1.83	0.71	1.06	0.38	0.00	1.45	5.55	2.78
2.50	0.91	2.02	1.13	1.56	0.50	0.00	1.73	5.91	3.44
2.70	1.10	4.17	1.34	3.48	2.66	0.00	1.40	8.04	6.45
2.90	1.20	3.34	2.11	2.04	2.29	0.00	2.35	7.43	5.66
3.10	1.29	2.52	2.76	0.61	1.92	0.00	3.90	7.62	5.91
3.30	1.09	3.74	3.42	2.11	0.96	0.00	4.67	8.79	7.35
3.50	0.78	4.97	3.51	2.06	0.48	0.00	5.44	9.74	8.47
3.70	1.04	3.26	2.97	2.11	0.24	0.00	3.70	7.87	6.23
3.90	1.16	2.40	2.70	2.14	0.12	0.00	2.83	7.08	5.20
4.25	1.29	1.55	2.43	2.16	0.06	0.00	1.97	6.45	4.30
4.75	2.28	3.18	3.27	3.44	0.03	0.00	3.09	8.40	6.88
5.25	3.27	4.81	4.12	4.72	0.02	0.00	4.21	10.67	9.52
5.75	1.63	3.84	1.74	0.64	0.01	1.57	2.10	7.13	5.27
6.50	0.82	6.46	1.74	2.69	0.00	2.36	6.72	11.24	10.16
7.50	0.41	7.76	1.75	4.73	0.00	3.15	9.03	14.16	13.31
9.00	0.00	9.07	5.94	9.67	0.00	3.80	11.33	19.42	18.81
11.00	0.00	4.54	2.97	4.83	0.00	22.59	12.90	27.43	27.01
14.00	0.00	4.54	2.97	4.83	0.00	22.59	19.15	30.87	30.49

Table C.2.: Final estimation of the systematic error in % (with each divided by $\sqrt{2}$) for the π^0 at $\sqrt{s} = 7\,\text{TeV}$, positive error.

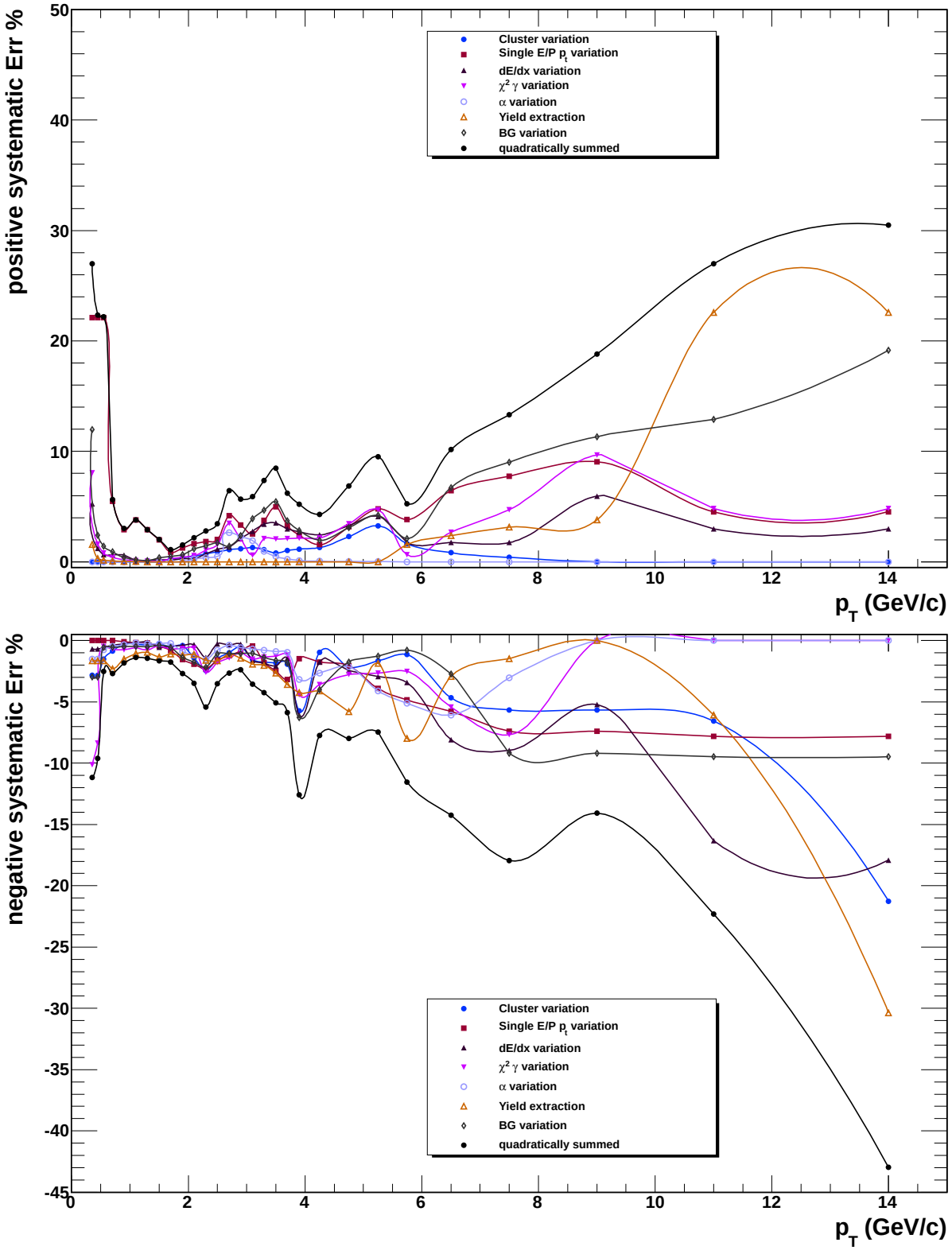

Figure C.1.: Positive (top) and negative (bottom) systematic uncertainties for π^0 at $\sqrt{s} = 7\,\mathrm{TeV}$.

π^0 in η binning

Negative error

p_t	Cluster	p_t $e^{\pm}$	dE/dx	χ^2_γ	α	Yield extr.	BG	Σ w mat	Σ w/o mat
0.55	-0.19	0.00	-0.04	-0.79	-0.10	-1.77	-0.23	-8.99	-1.96
0.85	-0.19	-0.50	-0.04	-0.74	-0.10	-1.74	-0.23	-8.99	-1.98
1.20	-0.29	-0.57	-0.13	-0.76	-0.16	-1.05	-0.51	-8.90	-1.55
1.60	-0.34	-0.63	-0.25	-0.54	-0.48	-1.26	-0.47	-8.93	-1.71
2.00	-0.66	-0.60	-0.33	-0.33	-0.64	-1.15	-0.23	-8.93	-1.67
2.40	-0.99	-0.57	-0.40	-1.14	-0.80	-1.71	-0.66	-9.15	-2.60
2.80	-1.44	-0.71	-0.61	-0.88	-0.75	-1.24	-0.92	-9.14	-2.59
3.25	-1.89	-0.86	-0.82	-0.63	-0.70	-1.30	-1.18	-9.26	-2.99
3.25	-0.58	-0.86	-0.89	-0.57	-1.19	-2.62	-0.33	-9.35	-3.25
5.00	-1.10	-2.24	-1.33	-0.95	-1.20	-3.54	-1.51	-10.10	-5.01
7.00	-5.42	-7.76	-5.36	-7.25	-4.96	-3.54	-6.24	-17.99	-15.71

Table C.3.: Final estimation of the systematic error in % (with each divided by $\sqrt{2}$) for the π^0 in η binning at $\sqrt{s} = 7\,\text{TeV}$, negative error.

Positive error

p_t	Cluster	p_t $e^{\pm}$	dE/dx	χ^2_γ	α	Yield extr.	BG	Σ w mat	Σ w/o mat
0.55	0.00	8.05	0.21	0.00	0.00	0.00	0.22	9.38	8.06
0.85	0.00	2.45	0.45	0.00	0.00	0.00	0.22	5.42	2.50
1.20	0.00	2.07	0.36	0.00	0.00	0.00	0.25	5.25	2.12
1.60	0.00	1.27	0.31	0.00	0.00	0.00	0.27	4.99	1.33
2.00	0.25	0.74	0.27	0.73	0.52	0.12	0.28	4.97	1.26
2.40	0.38	0.91	0.54	1.09	0.78	0.18	0.74	5.18	1.92
2.80	0.51	1.64	0.82	1.46	1.05	0.24	1.20	5.61	2.89
3.25	0.25	1.66	1.35	1.06	0.52	0.12	1.07	5.51	2.69
3.25	0.00	1.68	1.89	0.00	0.00	0.00	0.00	5.43	2.53
5.00	0.00	0.74	1.29	0.66	0.00	1.12	0.94	5.28	2.19
7.00	0.00	0.74	1.29	0.66	0.00	5.61	0.94	7.62	5.91

Table C.4.: Final estimation of the systematic error in % (with each divided by $\sqrt{2}$) for the π^0 in η binning at $\sqrt{s} = 7\,\text{TeV}$, positive error.

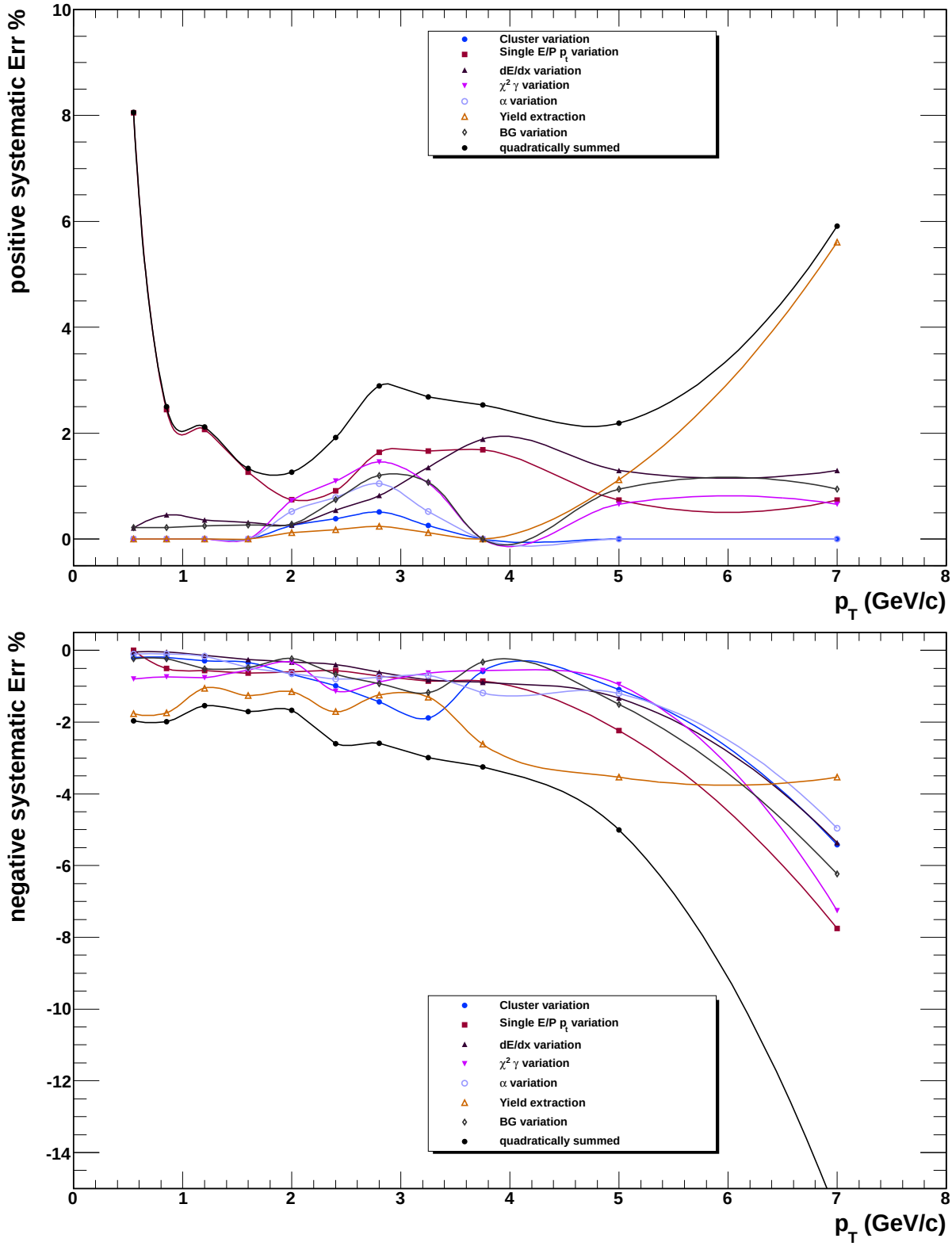

Figure C.2.: Positive (top) and negative (bottom) systematic uncertainties for π^0 in η binning at $\sqrt{s} = 7\,\text{TeV}$.

η

Negative error

p_t	Cluster	p_t $e^{\pm}$	dE/dx	χ^2_γ	α	Yield extr.	BG	Σ w mat	Σ w/o mat
0.55	-10.76	0.00	-1.75	-9.62	-10.39	-11.41	-11.73	-25.77	-24.23
0.85	-4.23	-2.89	-1.75	-5.94	-4.54	-5.96	-4.59	-14.79	-11.91
1.20	-3.42	-3.25	-4.24	-5.48	-3.81	-10.60	-3.37	-16.89	-14.44
1.60	-2.60	-3.61	-2.06	-5.02	-3.08	-5.49	-6.34	-14.35	-11.36
2.00	-3.48	-3.27	-2.79	-7.56	-6.07	-2.17	-3.25	-14.72	-11.82
2.40	-3.97	-4.53	-2.11	-3.51	-5.66	-4.12	-2.25	-13.56	-10.35
2.80	-4.47	-5.52	-1.85	-6.32	-5.25	-1.39	-5.22	-15.08	-12.27
3.35	-2.23	-4.25	-0.92	-3.16	-5.09	-0.91	-3.45	-12.22	-8.52
3.75	0.00	0.00	0.00	0.00	-4.93	-3.53	-1.68	-10.79	-6.29
5.00	0.00	-2.98	0.00	0.00	-6.46	-4.54	-2.12	-12.35	-8.70
7.00	0.00	-2.98	0.00	0.00	-12.57	-8.57	-2.12	-17.93	-15.64

Table C.5.: Final estimation of the systematic error in % (with each divided by $\sqrt{2}$) for the η at $\sqrt{s} = 7\,\text{TeV}$, negative error.

Positive error

p_t	Cluster	p_t $e^{\pm}$	dE/dx	χ^2_γ	α	Yield extr.	BG	Σ w mat	Σ w/o mat
0.55	2.30	4.12	5.73	3.34	0.00	0.00	20.09	22.20	21.67
0.85	2.30	4.12	1.15	3.34	0.00	1.96	4.28	8.94	7.54
1.20	2.30	4.12	0.57	3.15	0.00	2.20	2.30	8.11	6.53
1.60	1.15	2.06	0.29	1.58	0.00	2.45	0.33	6.11	3.77
2.00	0.57	1.03	0.14	0.79	0.00	1.22	0.16	5.16	1.89
2.40	2.71	5.34	0.07	4.85	0.00	2.72	2.07	9.70	8.43
2.80	3.78	7.49	0.04	6.87	0.00	3.46	3.03	12.73	11.78
3.35	4.85	9.64	0.02	8.90	0.00	4.21	3.98	15.89	15.14
3.75	0.00	3.84	0.00	2.55	0.00	6.99	3.98	10.45	9.27
5.00	0.00	6.17	0.00	2.40	0.00	3.50	4.50	9.97	8.74
7.00	0.00	15.51	0.00	13.41	0.00	3.50	6.55	22.34	21.81

Table C.6.: Final estimation of the systematic error in % (with each divided by $\sqrt{2}$) for the η at $\sqrt{s} = 7\,\text{TeV}$, positive error.

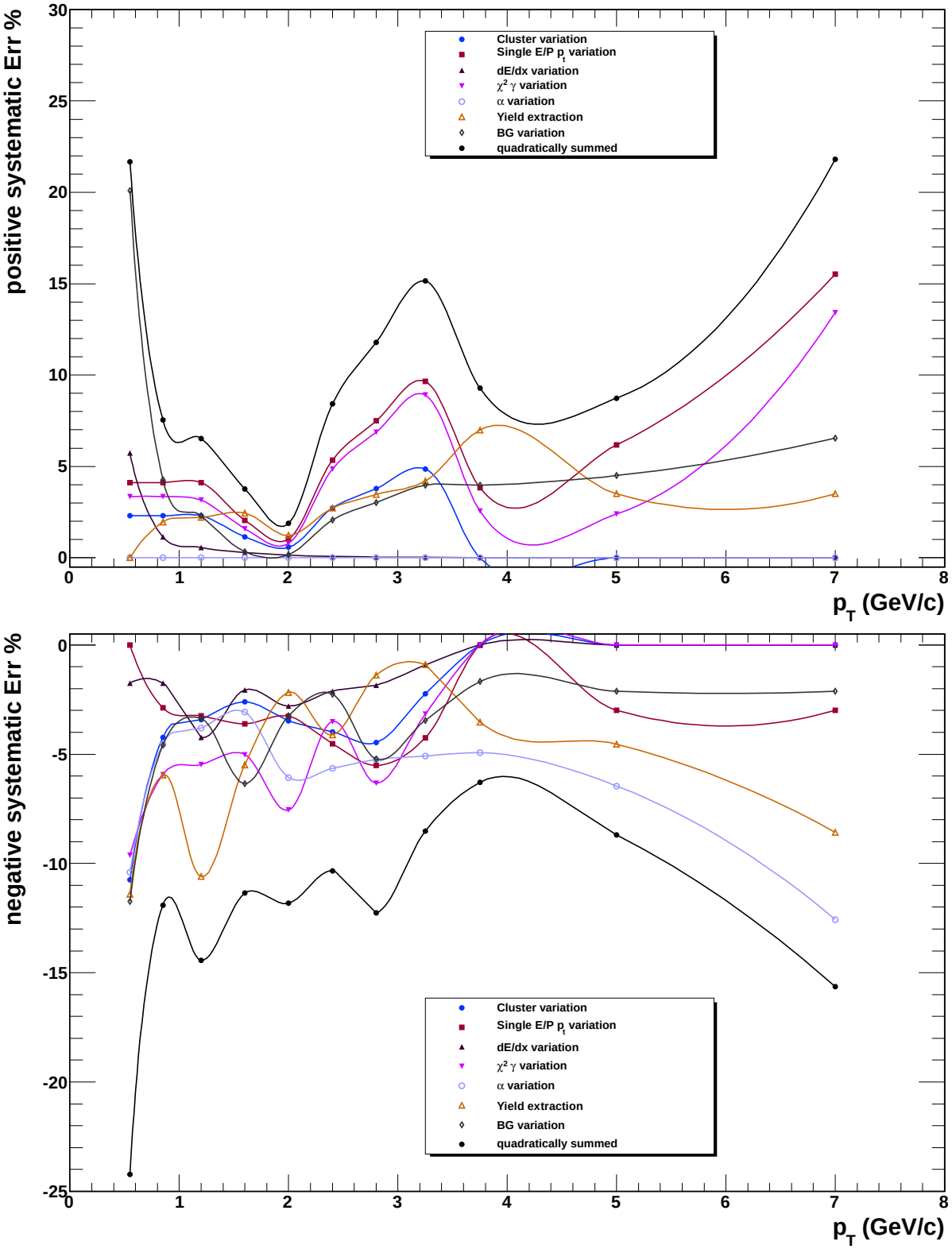

Figure C.3.: Positive (top) and negative (bottom) systematic uncertainties for η at $\sqrt{s} = 7\,\mathrm{TeV}$.

$\sqrt{s} = 2.76\,\mathrm{TeV}$

π^0

Negative Error

p_t	Cluster	p_t $e^{\pm}$	$\mathrm{d}E/\mathrm{d}x$	χ^2_γ	α	Yield extr.	BG	Σ w mat	Σ w/o mat
0.50	-2.83	0.00	-0.69	-10.12	-1.50	-0.18	-2.96	-14.10	-11.04
0.70	-2.83	0.00	-0.69	-8.36	-1.50	-1.94	-2.96	-13.04	-9.65
0.90	-1.52	0.00	-0.53	-0.49	-0.75	-1.73	-0.53	-9.14	-2.58
1.10	-0.87	0.00	-0.37	-0.70	-0.48	-1.53	-0.55	-9.01	-2.06
1.30	-0.21	-0.11	-0.26	-0.75	-0.34	-1.33	-0.48	-8.93	-1.67
1.50	-0.31	-0.16	-0.15	-0.59	-0.21	-1.68	-0.49	-8.97	-1.89
1.70	-0.37	-0.21	-0.12	-0.76	-0.28	-1.69	-0.51	-8.99	-1.99
1.90	-0.28	-0.42	-0.54	-0.42	-0.25	-2.57	-0.37	-9.19	-2.74
2.10	-0.49	-0.82	-0.44	-0.67	-0.23	-2.86	-0.57	-9.33	-3.18
2.30	-0.41	-1.56	-0.39	-0.65	-0.88	-3.30	-1.36	-9.67	-4.09
2.50	-1.42	-1.93	-0.34	-0.62	-1.21	-2.62	-1.76	-9.72	-4.20
2.80	-2.43	-2.30	-1.36	-2.58	-1.53	-3.46	-2.16	-10.75	-6.22
3.25	-1.46	-1.58	-0.25	-1.80	-0.77	-4.78	-1.08	-10.46	-5.71
3.75	-0.97	-1.22	-0.36	-1.41	-0.38	-6.11	-1.06	-10.96	-6.57
4.50	-0.49	-0.86	-0.30	-1.02	0.00	-10.92	0.00	-14.08	-11.02
5.50	-1.55	-0.43	-1.60	-1.50	-0.16	-13.45	-1.03	-16.32	-13.76
7.00	-1.55	-0.43	-1.60	-1.50	-0.78	-23.54	-1.37	-25.32	-23.75

Table C.7.: Final estimation of the systematic error in % (with each divided by $\sqrt{2}$) for the π^0 at $\sqrt{s} = 2.76\,\mathrm{TeV}$, negative error.

Positive Error

p_t	Cluster	p_t $e^{\pm}$	dE/dx	χ^2_γ	α	Yield extr.	BG	Σ w mat	Σ w/o mat
0.50	0.00	22.13	5.26	8.05	0.00	0.00	11.99	27.37	26.94
0.70	0.00	22.13	1.21	1.61	0.00	0.00	2.40	22.86	22.35
0.90	0.00	22.13	0.65	0.81	0.00	0.00	1.40	22.71	22.19
1.10	0.00	5.50	0.63	0.40	0.00	0.00	0.90	7.40	5.62
1.30	0.00	2.92	0.61	0.20	0.00	0.00	0.40	5.68	3.02
1.50	0.00	3.80	0.10	0.10	0.00	0.00	0.20	6.14	3.81
1.70	0.00	2.90	0.16	0.05	0.00	0.00	0.10	5.62	2.90
1.90	0.00	1.99	0.17	0.03	0.00	0.00	0.36	5.22	2.03
2.10	0.25	0.87	0.17	0.29	0.00	0.00	0.50	4.93	1.09
2.30	0.38	1.26	0.29	0.42	0.00	0.00	0.63	5.05	1.54
2.50	0.51	1.64	0.29	0.55	0.25	0.00	1.18	5.28	2.19
2.80	0.71	1.83	0.71	1.06	0.38	0.00	1.45	5.55	2.78
3.25	0.91	2.02	1.13	1.56	0.50	0.00	1.73	5.91	3.44
3.75	1.10	4.17	1.34	3.48	2.66	2.70	1.40	8.48	6.99
4.50	1.10	2.52	2.11	0.61	1.92	0.00	2.36	6.69	4.65
5.50	1.29	2.52	2.37	0.61	1.92	5.40	1.18	8.44	6.94
7.00	1.09	2.52	3.42	2.11	1.92	8.51	1.18	11.15	10.06

Table C.8.: Final estimation of the systematic error in % (with each divided by $\sqrt{2}$) for the π^0 at $\sqrt{s} = 2.76\,\text{TeV}$, positive error.

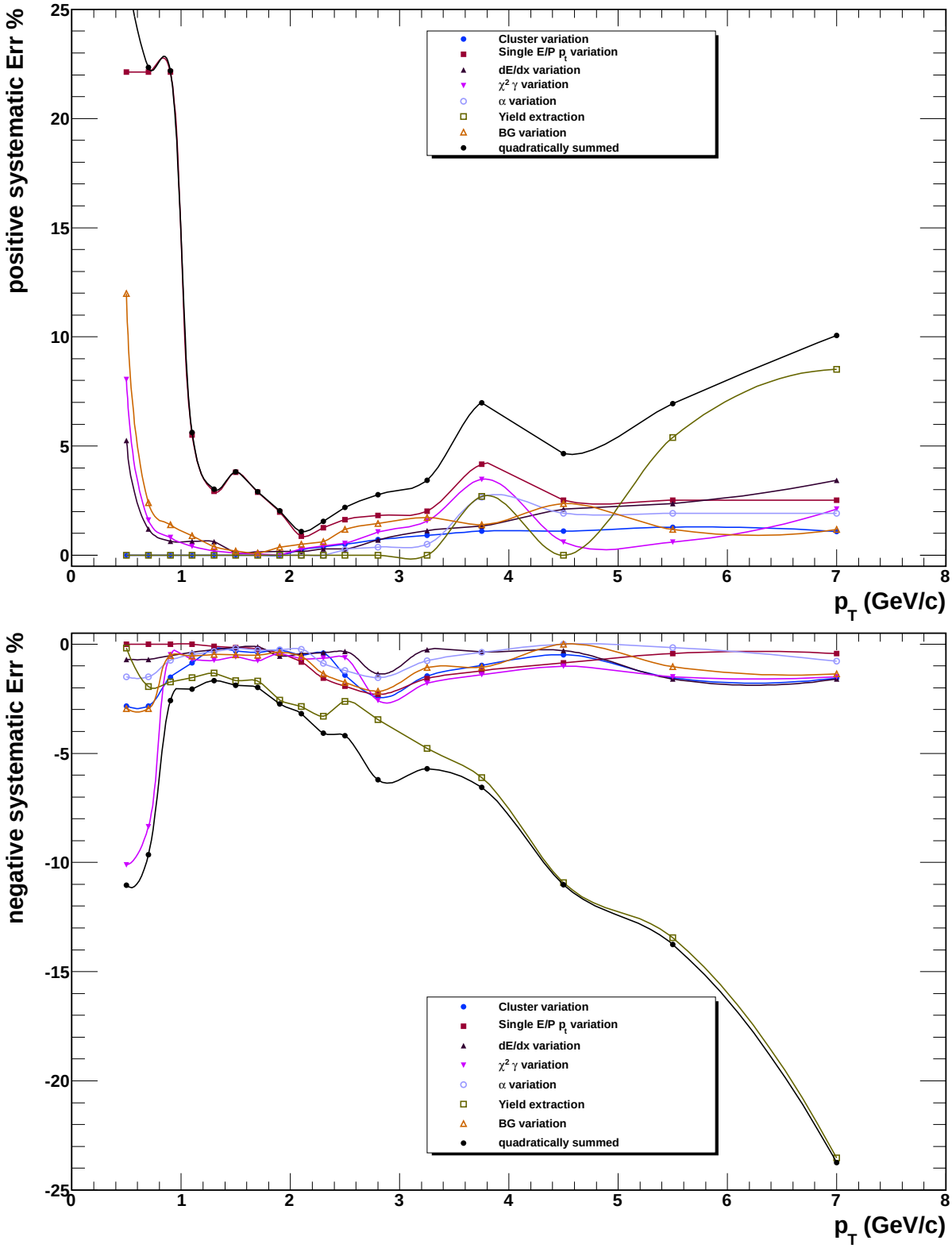

Figure C.4.: Positive (top) and negative (bottom) systematic uncertainties for π^0 at $\sqrt{s} = 2.76\,\text{TeV}$.

π^0 in η binning

Negative error

p_t	Cluster	p_t $e^{\pm}$	dE/dx	χ^2_γ	α	Yield extr.	BG	Σ w mat	Σ w/o mat
0.80	-0.19	0.00	-0.04	-0.79	-0.10	-1.57	-0.24	-8.95	-1.79
1.20	-0.19	-0.50	-0.04	-0.74	-0.10	-0.95	-0.24	-8.87	-1.35
1.60	-0.29	-0.56	-0.13	-0.76	-0.16	-1.59	-0.51	-8.98	-1.95
2.00	-0.34	-0.63	-0.26	-0.55	-0.48	-2.52	-0.48	-9.20	-2.77
2.50	-0.67	-0.60	-0.33	-0.34	-0.64	-2.95	-0.22	-9.33	-3.19
3.20	-0.99	-0.57	-0.40	-1.14	-0.80	-2.47	-0.66	-9.32	-3.15
4.00	-1.17	-0.63	-0.48	-1.04	-0.78	-2.27	-0.77	-9.29	-3.07
5.20	-1.89	-0.86	-0.82	-0.63	-0.70	-1.47	-1.18	-9.29	-3.07

Table C.9.: Final estimation of the systematic error in % (with each divided by $\sqrt{2}$) for the π^0 in η binning at $\sqrt{s} = 2.76\,\text{TeV}$, negative error.

Positive error

p_t	Cluster	p_t $e^{\pm}$	dE/dx	χ^2_γ	α	Yield extr.	BG	Σ w mat	Σ w/o mat
0.80	0.00	8.05	0.20	0.00	0.00	0.00	0.22	9.38	8.06
1.20	0.00	2.45	0.45	0.00	0.00	0.00	0.22	5.42	2.50
1.60	0.00	2.07	0.36	0.00	0.00	0.00	0.25	5.25	2.12
2.00	0.00	1.26	0.31	0.00	0.00	0.00	0.26	4.99	1.33
2.50	0.25	0.74	0.27	0.73	0.52	1.81	0.28	5.29	2.20
3.20	0.00	0.91	0.27	0.00	0.00	0.00	0.28	4.91	0.99
4.00	0.51	1.64	0.82	1.46	1.04	3.62	1.20	6.67	4.63
5.20	0.51	1.64	0.82	1.46	1.04	3.74	1.20	6.74	4.72

Table C.10.: Final estimation of the systematic error in % (with each divided by $\sqrt{2}$) for the π^0 in η binning at $\sqrt{s} = 2.76\,\text{TeV}$, positive error.

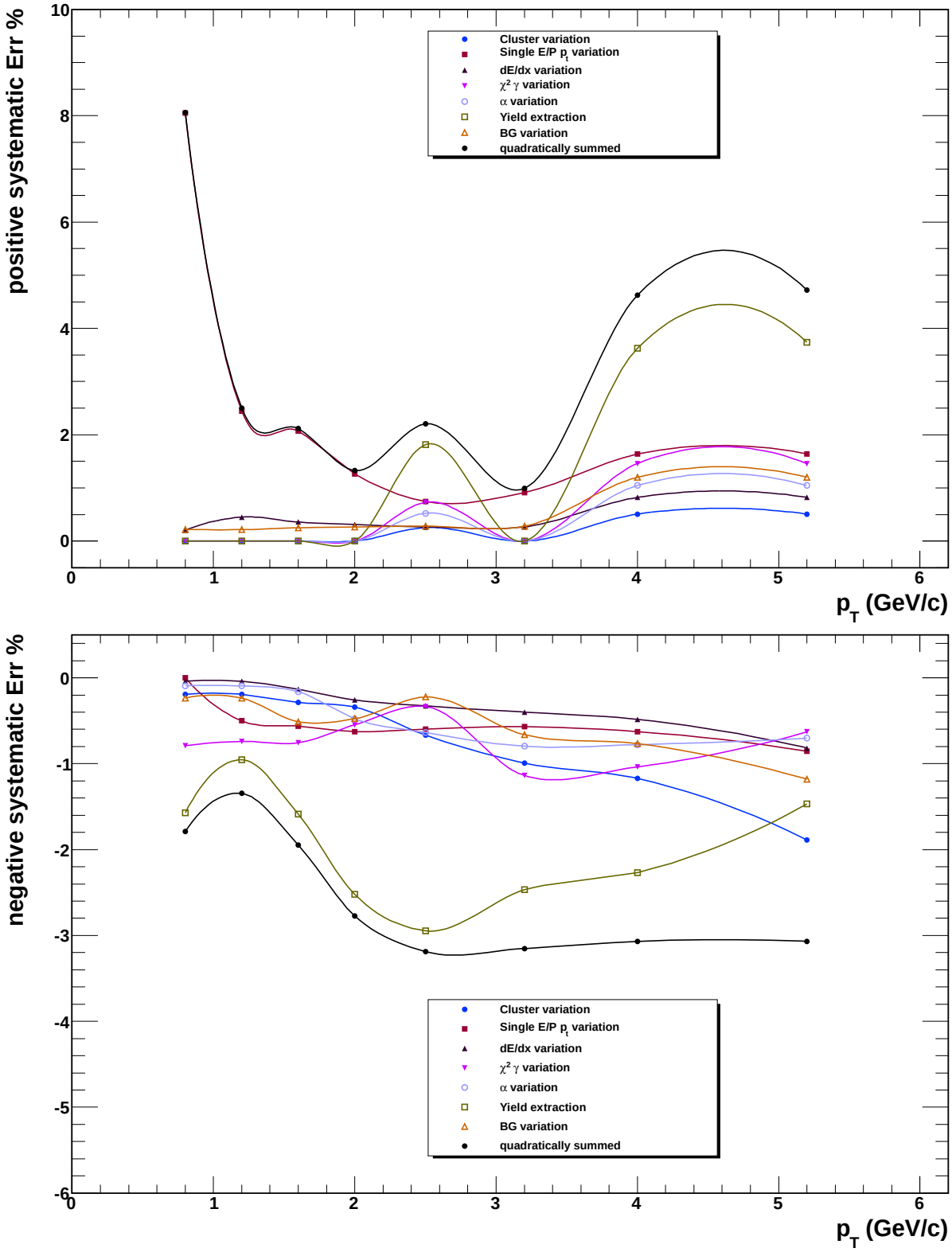

Figure C.5.: Positive (top) and negative (bottom) systematic uncertainties for π^0 in η binning at $\sqrt{s} = 2.76\,\mathrm{TeV}$.

η

Negative error

p_t	Cluster	p_t $e^{\pm}$	dE/dx	χ^2_γ	α	Yield extr.	BG	Σ w mat	Σ w/o mat
0.80	-10.76	0.00	-1.74	-9.62	-10.39	-5.10	-10.74	-23.18	-21.46
1.20	-4.23	-2.89	-1.74	-5.94	-4.54	-8.49	-4.54	-15.96	-13.33
1.60	-3.42	-3.25	-4.24	-5.48	-3.81	-11.62	-1.44	-17.28	-14.89
2.00	-2.60	-3.61	-2.06	-5.02	-3.08	-5.81	-3.45	-13.46	-10.21
2.50	-3.48	-3.27	-2.79	-7.56	-6.07	-2.90	-0.75	-14.50	-11.55
3.20	-3.48	-4.53	-2.11	-3.51	-5.25	0.00	-0.75	-12.42	-8.80
4.00	-4.47	-5.52	-1.85	-6.32	-5.25	0.00	-4.15	-14.68	-11.77
5.20	-4.47	-5.52	-1.85	-6.32	-5.25	0.00	-1.26	-14.13	-11.08

Table C.11.: Final estimation of the systematic error in % (with each divided by $\sqrt{2}$) for the η at $\sqrt{s} = 2.76\,\text{TeV}$, negative error.

Positive error

p_t	Cluster	p_t $e^{\pm}$	dE/dx	χ^2_γ	α	Yield extr.	BG	Σ w mat	Σ w/o mat
0.80	2.30	4.12	5.73	3.34	0.00	0.00	20.09	22.20	21.68
1.20	2.30	4.12	1.15	3.34	0.00	0.00	4.28	8.73	7.28
1.60	2.30	4.12	0.57	3.15	0.00	0.00	2.30	7.80	6.15
2.00	1.15	2.06	0.29	1.58	0.00	0.00	0.33	5.60	2.87
2.50	0.57	1.03	0.14	0.79	0.00	0.00	0.16	5.02	1.43
3.20	0.00	0.00	0.00	0.00	0.00	0.00	0.00	4.81	0.00
4.00	0.97	1.93	0.00	1.78	0.00	0.00	0.80	5.62	2.91
5.20	4.85	9.64	0.00	8.90	0.00	0.00	3.98	15.32	14.55

Table C.12.: Final estimation of the systematic error in % (with each divided by $\sqrt{2}$) for the η at $\sqrt{s} = 2.76\,\text{TeV}$, positive error.

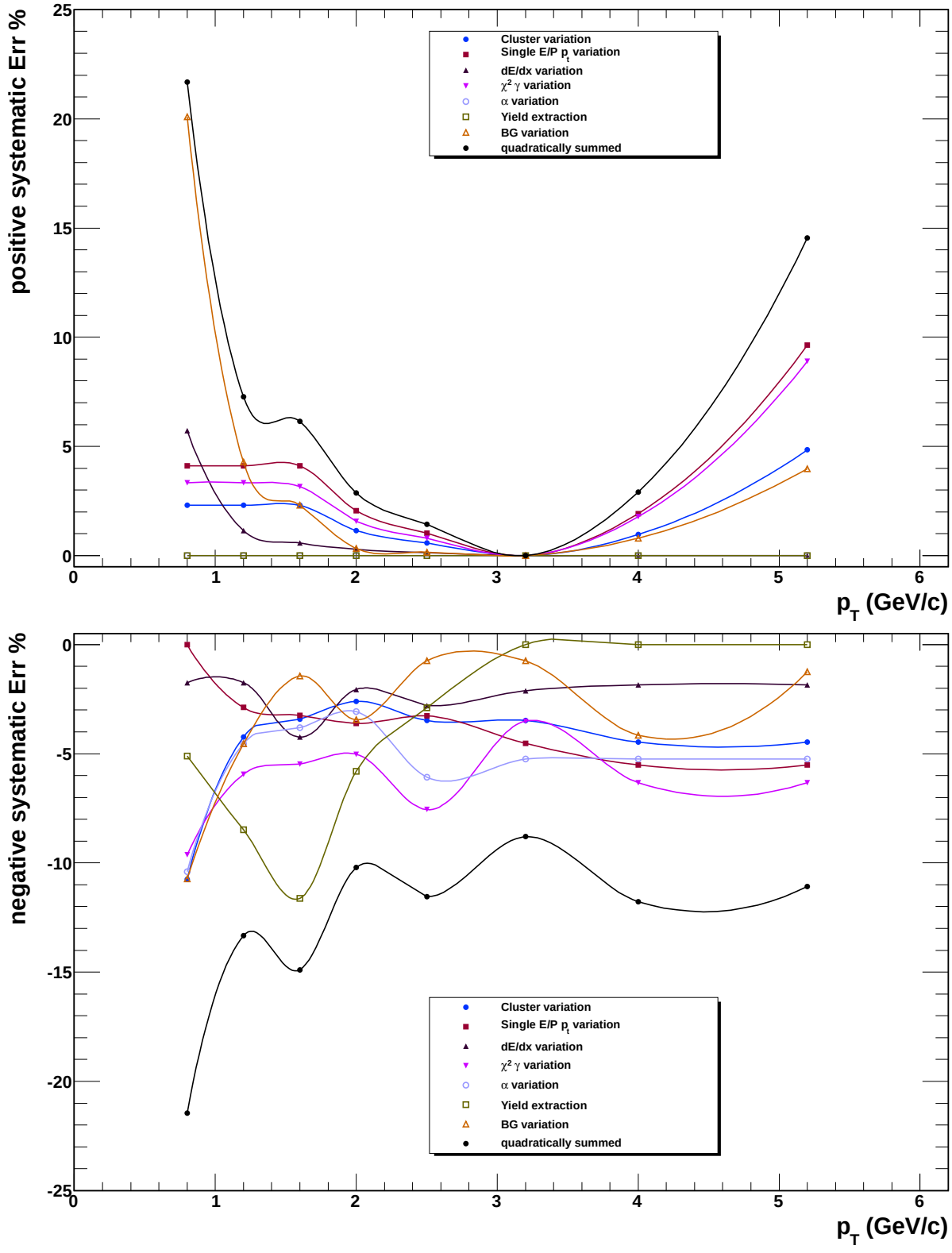

Figure C.6.: Positive (top) and negative (bottom) systematic uncertainties for η at $\sqrt{s} = 2.76\,\mathrm{TeV}$.

$\sqrt{s} = 0.9\,\text{TeV}$

π^0

Negative Error

p_t	Cluster	p_t $e^{\pm}$	dE/dx	χ^2_γ	α	Yield extr.	BG	Σ w mat	Σ w/o mat
0.50	-0.54	-4.26	-0.40	-1.26	-0.28	-14.32	-3.64	-17.76	-15.44
0.70	-0.54	-4.26	-0.40	-1.05	-0.28	-5.98	-2.65	-11.80	-7.90
0.90	-0.27	-2.13	-0.20	-0.88	-0.28	-2.99	-2.06	-9.77	-4.32
1.10	-0.13	-1.06	-0.10	-0.77	-0.30	-4.19	-0.45	-9.82	-4.43
1.30	-0.07	-0.53	-0.05	-0.72	-0.32	-4.79	-0.80	-10.07	-4.95
1.50	-0.03	-0.27	-0.02	-0.66	-0.95	-5.39	-0.94	-10.40	-5.60
1.80	0.00	0.00	0.00	-1.39	0.00	-1.65	-0.94	-9.08	-2.36
2.25	0.00	0.00	0.00	-2.02	0.00	-0.83	-1.65	-9.19	-2.74
3.25	0.00	0.00	0.00	-0.95	0.00	-0.83	-1.56	-8.99	-2.01

Table C.13.: Final estimation of the systematic error in % (with each divided by $\sqrt{2}$) for the π^0 at $\sqrt{s} = 0.9\,\text{TeV}$, negative error.

Positive Error

p_t	Cluster	p_t $e^{\pm}$	dE/dx	χ^2_γ	α	Yield extr.	BG	Σ w mat	Σ w/o mat
0.50	0.00	0.00	0.24	5.13	0.00	0.00	0.00	7.03	5.13
0.70	0.57	5.16	0.24	1.03	0.00	2.59	0.69	7.64	5.94
0.90	0.64	5.81	0.12	0.74	0.00	2.91	0.77	8.18	6.62
1.10	0.71	6.46	0.06	0.60	0.00	3.24	0.86	8.77	7.33
1.30	0.36	3.59	0.40	0.45	0.90	1.49	0.62	6.32	4.10
1.50	0.18	0.71	0.57	1.62	1.35	1.67	0.51	5.61	2.89
1.80	0.00	0.95	0.74	0.00	1.80	0.00	0.39	5.29	2.20
2.25	0.00	0.47	2.95	0.00	0.90	1.85	0.20	6.03	3.63
3.25	0.00	0.47	0.80	0.00	0.90	1.85	0.20	5.32	2.27

Table C.14.: Final estimation of the systematic error in % (with each divided by $\sqrt{2}$) for the π^0 at $\sqrt{s} = 0.9\,\text{TeV}$, positive error.

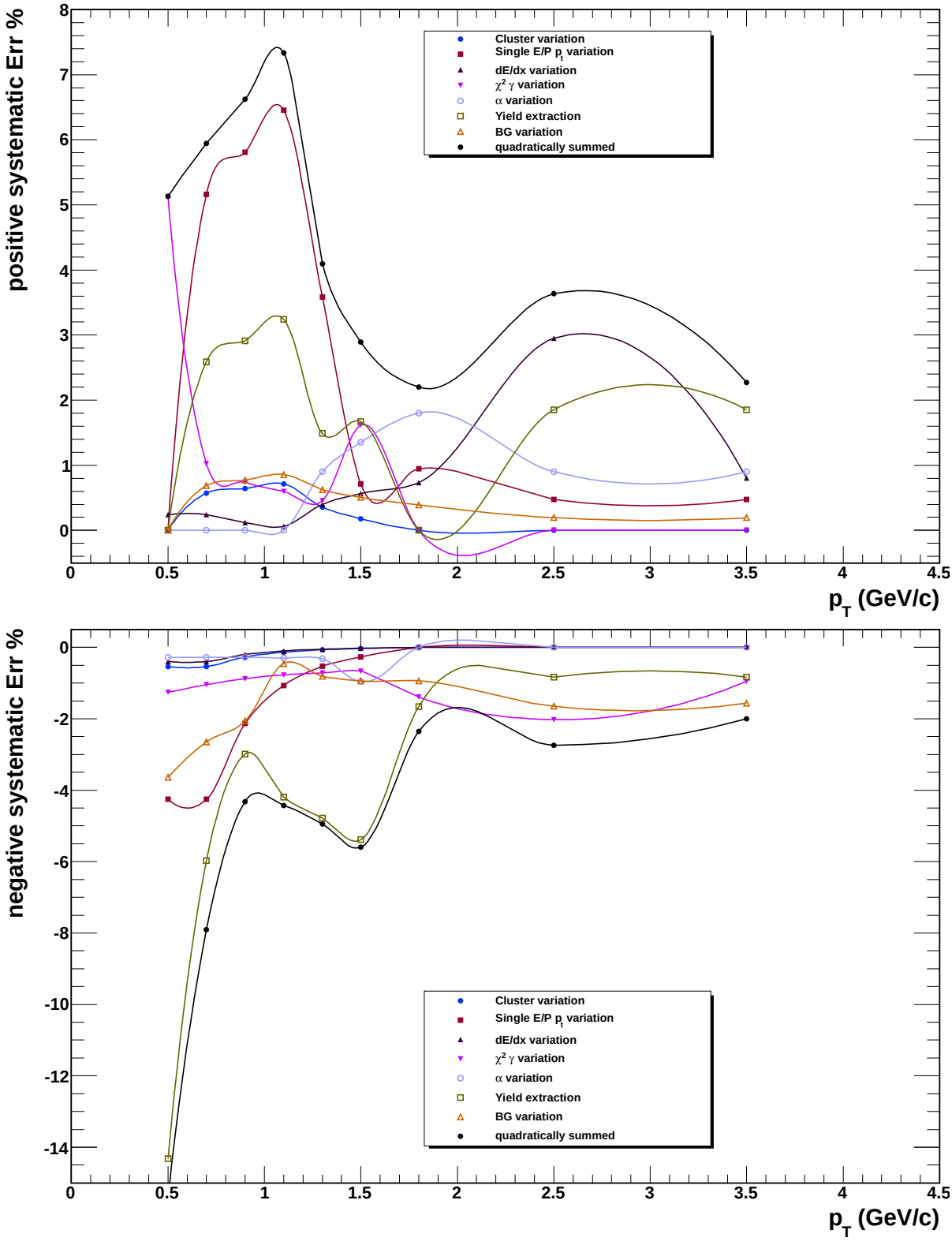

Figure C.7.: Positive (top) and negative (bottom) systematic uncertainties for π^0 at $\sqrt{s} = 0.9\,\mathrm{TeV}$.

π^0 in η binning

Negative Error

p_t	Cluster	p_t $e^{\pm}$	dE/dx	χ^2_γ	α	Yield extr.	BG	Σ w mat	Σ w/o mat
1.35	0.00	-1.92	-0.14	-1.61	0.00	0.00	-0.54	-9.14	-2.56
2.40	0.00	-1.92	-0.14	-1.61	0.00	0.00	-0.54	-9.14	-2.56

Table C.15.: Final estimation of the systematic error in % (with each divided by $\sqrt{2}$) for the π^0 in *eta* binning at $\sqrt{s} = 0.9\,\text{TeV}$, negative error.

Positive Error

p_t	Cluster	p_t $e^{\pm}$	dE/dx	χ^2_γ	α	Yield extr.	BG	Σ w mat	Σ w/o mat
1.35	0.00	0.00	0.66	0.00	0.00	2.47	0.12	5.45	2.56
2.40	0.00	0.00	0.66	0.00	0.00	2.47	0.12	5.45	2.56

Table C.16.: Final estimation of the systematic error in % (with each divided by $\sqrt{2}$) for the π^0 in η binning at $\sqrt{s} = 0.9\,\text{TeV}$, positive error.

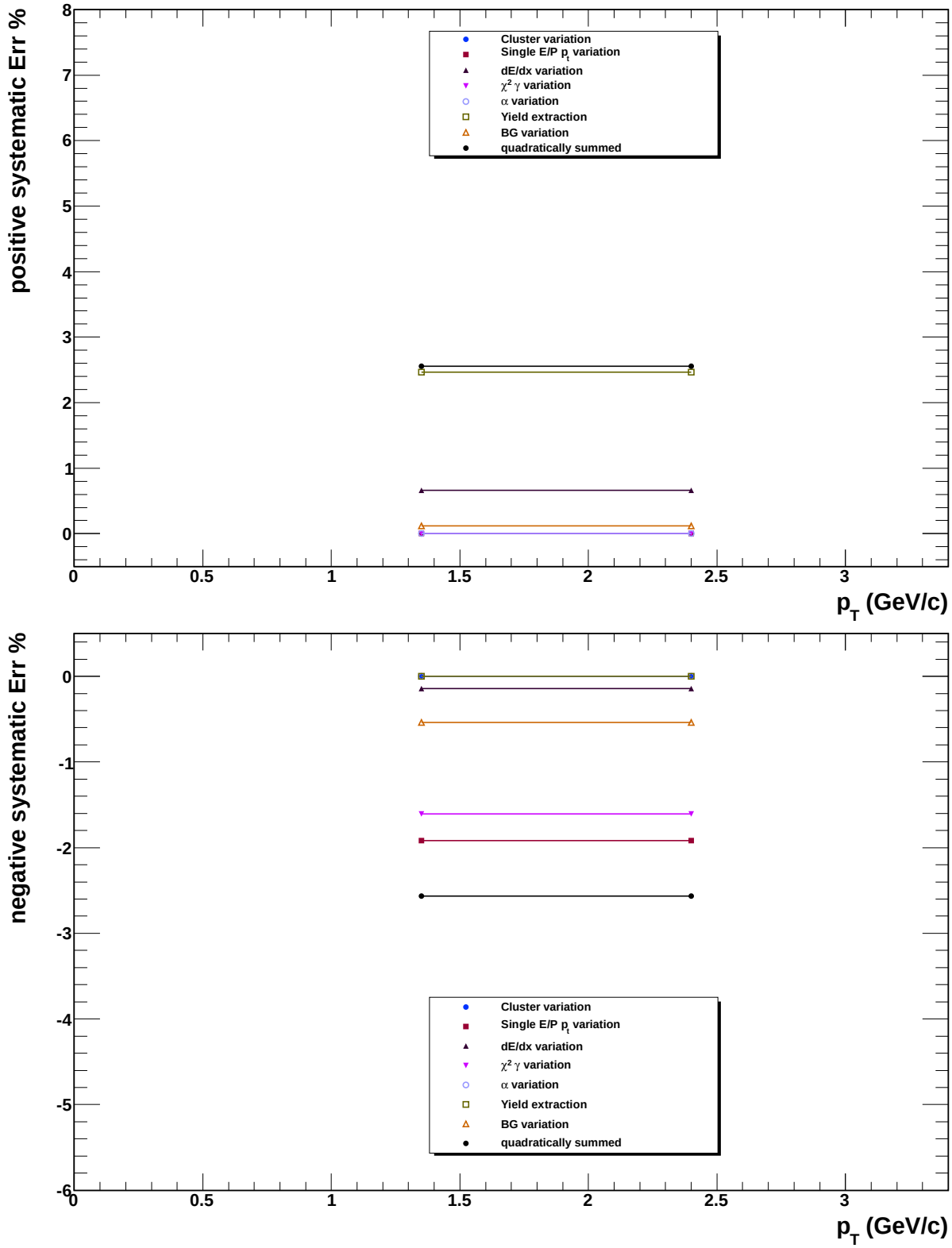

Figure C.8.: Positive (top) and negative (bottom) systematic uncertainties for π^0 in η binning at $\sqrt{s} = 0.9\,\text{TeV}$.

η

Negative Error

p_t	Cluster	p_t $e^{\pm}$	dE/dx	χ^2_γ	α	Yield extr.	BG	Σ w mat	Σ w/o mat
1.35	0.00	-1.92	-2.71	-3.20	-1.90	-12.07	0.00	-15.73	-13.06
2.40	0.00	-1.92	-2.71	-3.20	-1.90	-12.07	0.00	-15.73	-13.06

Table C.17.: Final estimation of the systematic error in % (with each divided by $\sqrt{2}$) for the η at $\sqrt{s} = 0.9\,\text{TeV}$, negative error.

Positive Error

p_t	Cluster	p_t $e^{\pm}$	dE/dx	χ^2_γ	α	Yield extr.	BG	Σ w mat	Σ w/o mat
1.35	0.00	8.95	0.00	7.39	0.00	0.00	5.89	13.88	13.02
2.40	0.00	8.95	0.00	7.39	0.00	0.00	5.89	13.88	13.02

Table C.18.: Final estimation of the systematic error in % (with each divided by $\sqrt{2}$) for the η at $\sqrt{s} = 0.9\,\text{TeV}$, positive error.

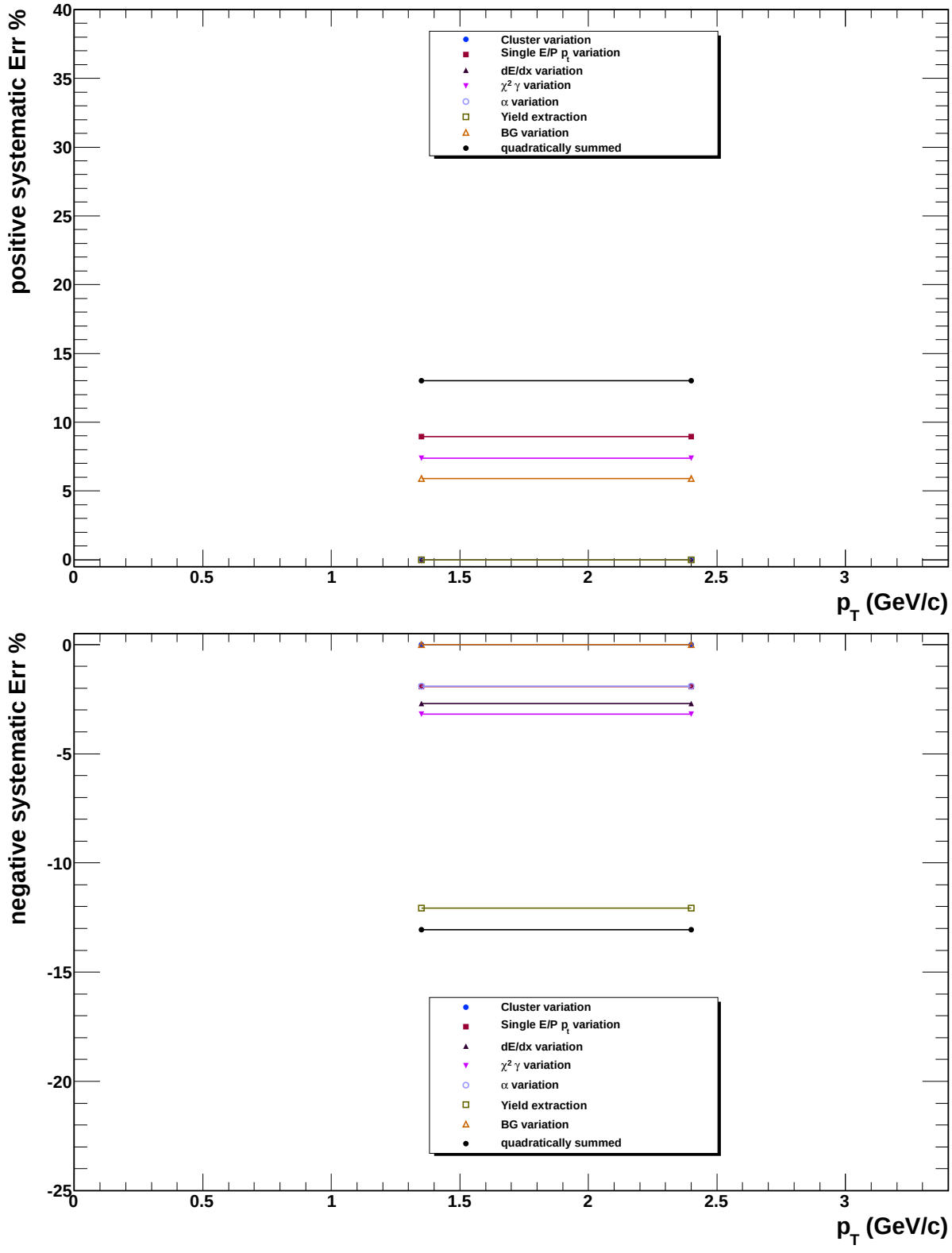

Figure C.9.: Positive (top) and negative (bottom) systematic uncertainties for η at $\sqrt{s} = 0.9\,\mathrm{TeV}$.

D. Reconstructed meson peak positions and widths

$\sqrt{s} = 7\,\mathrm{TeV}$

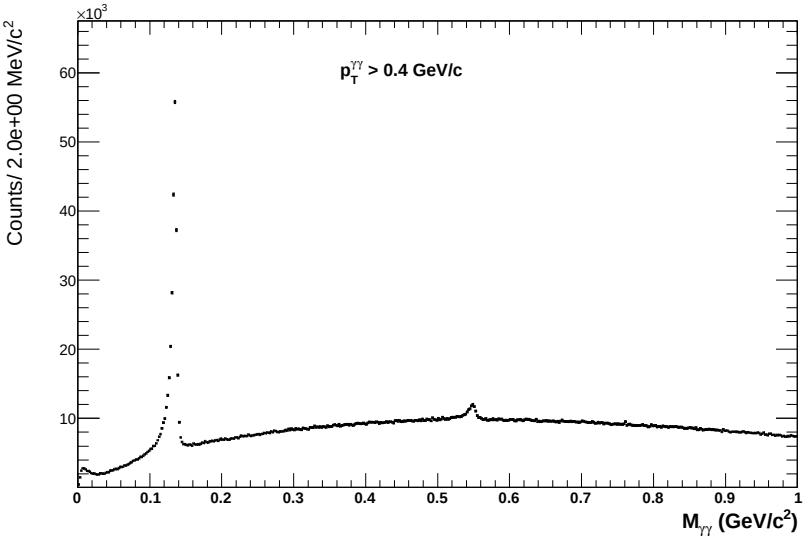

Figure D.1.: Invariant mass distribution of reconstructed photon pairs $M_{\gamma\gamma}$ with $p_T > 0.4\,\mathrm{GeV/c}$ at $\sqrt{s} = 7\,\mathrm{TeV}$.

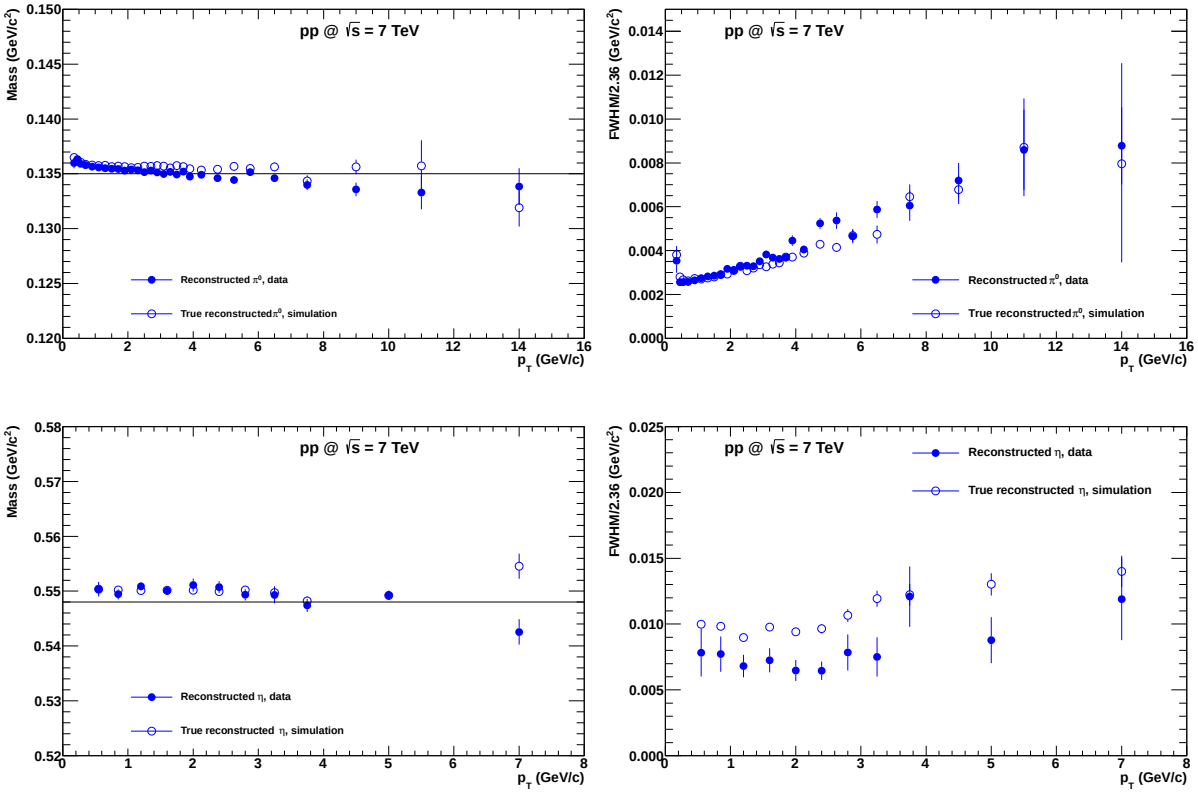

Figure D.2.: Reconstructed mass (left) and resolution (right) for π^0 (top) and η meson (bottom) as functions for transverse momentum at $\sqrt{s} = 7\,\mathrm{TeV}$. The full symbols correspond to the measured data and open symbols to simulations.

$\sqrt{s} = 2.76\,\mathrm{TeV}$

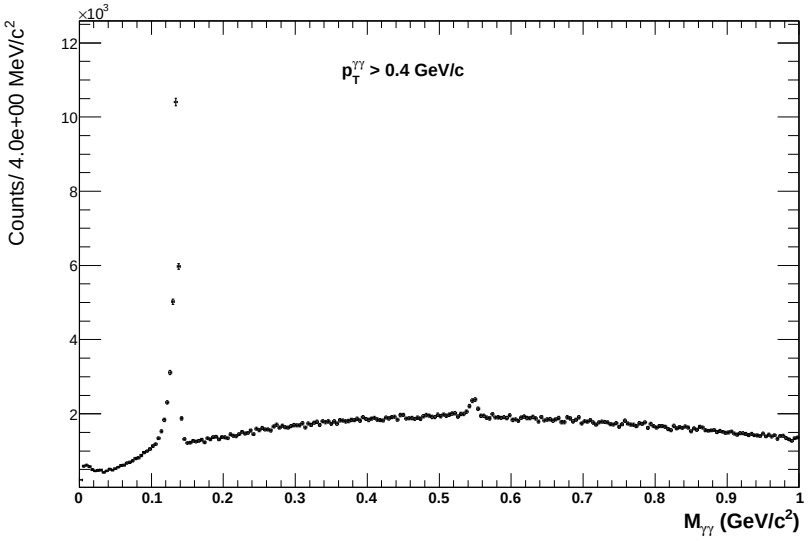

Figure D.3.: Invariant mass distribution of reconstructed photon pairs $M_{\gamma\gamma}$ with $p_T > 0.4\,\mathrm{GeV/c}$ at $\sqrt{s} = 2.76\,\mathrm{TeV}$.

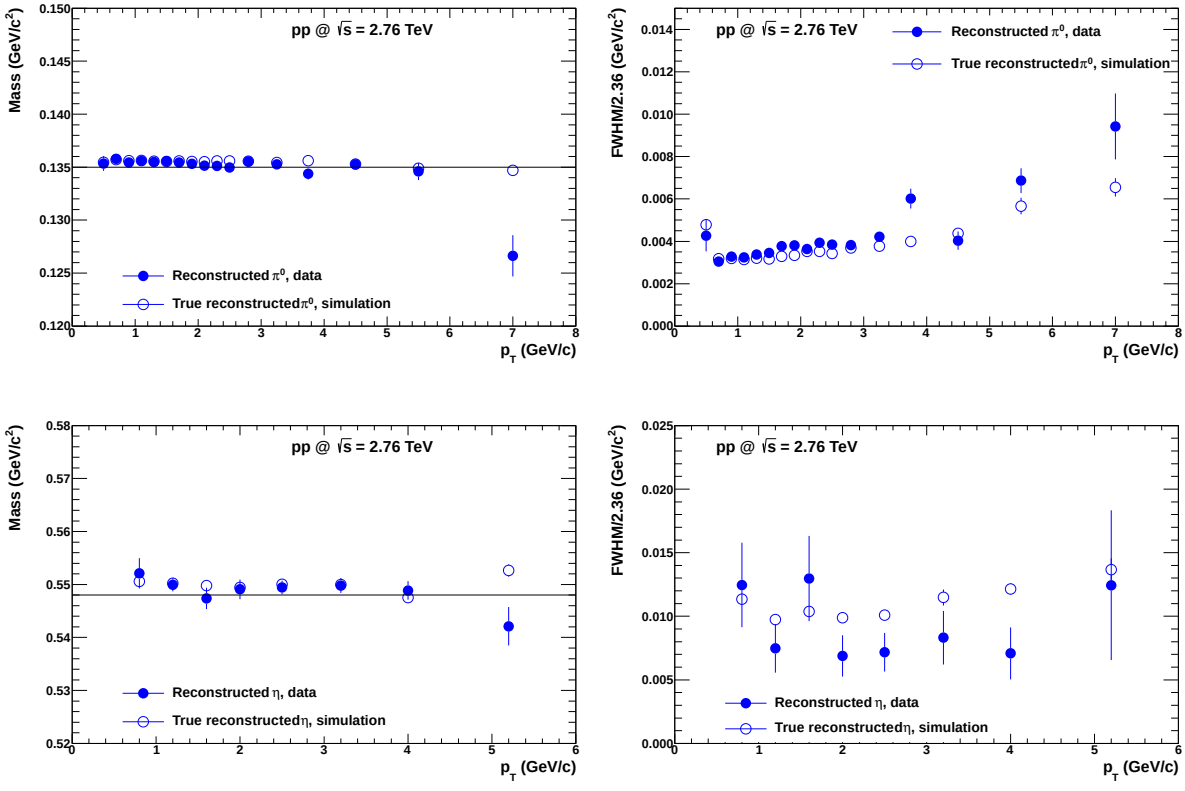

Figure D.4.: Reconstructed mass (left) and resolution (right) for π^0 (top) and η meson (bottom) as functions for transverse momentum at $\sqrt{s} = 2.76\,\mathrm{TeV}$. The full symbols correspond to the measured data and open symbols to simulations.

$\sqrt{s} = 0.9\,\mathrm{TeV}$

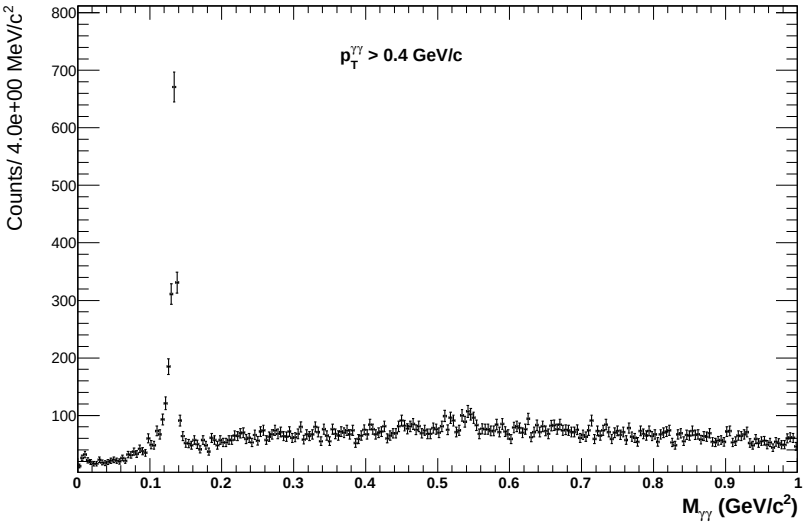

Figure D.5.: Invariant mass distribution of reconstructed photon pairs $M_{\gamma\gamma}$ with $p_T > 0.4\,\mathrm{GeV/c}$ at $\sqrt{s} = 0.9\,\mathrm{TeV}$.

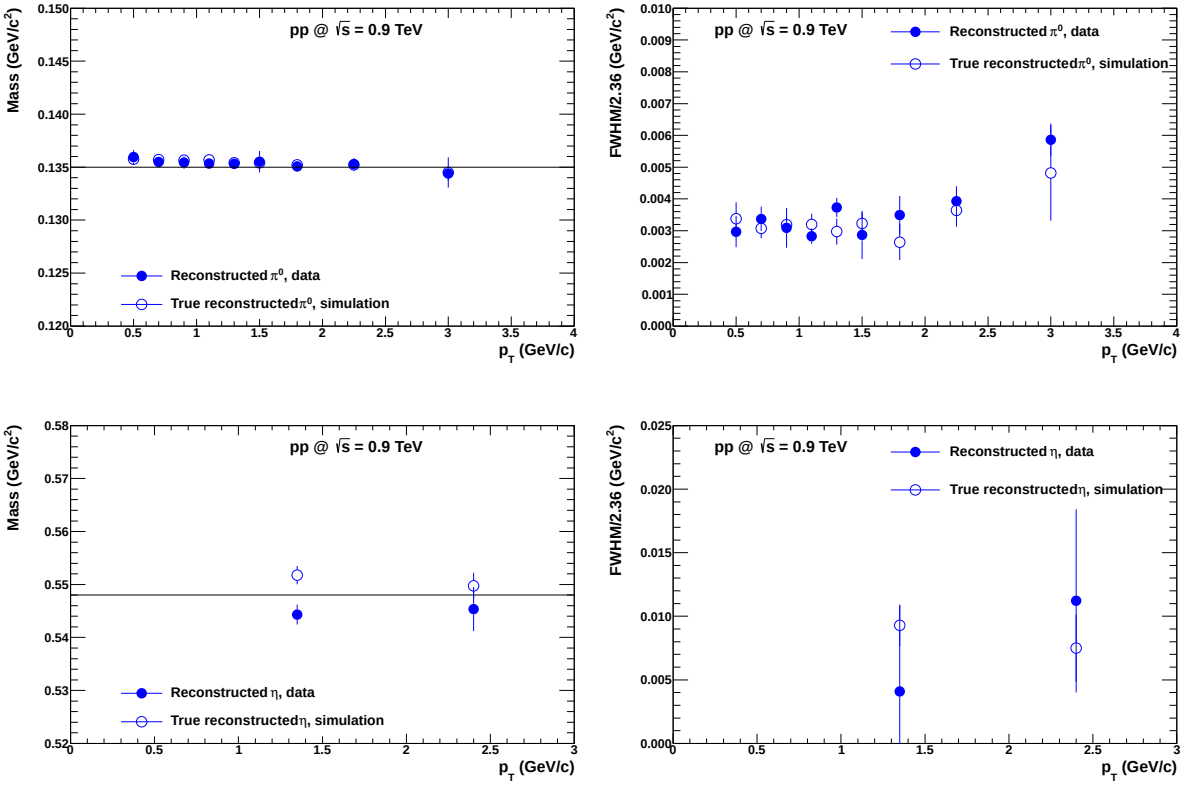

Figure D.6.: Reconstructed mass (left) and resolution (right) for π^0 (top) and η meson (bottom) as functions for transverse momentum at $\sqrt{s} = 0.9\,\mathrm{TeV}$. The full symbols correspond to the measured data and open symbols to simulations.

E. Invariant mass distributions before and after background subtraction

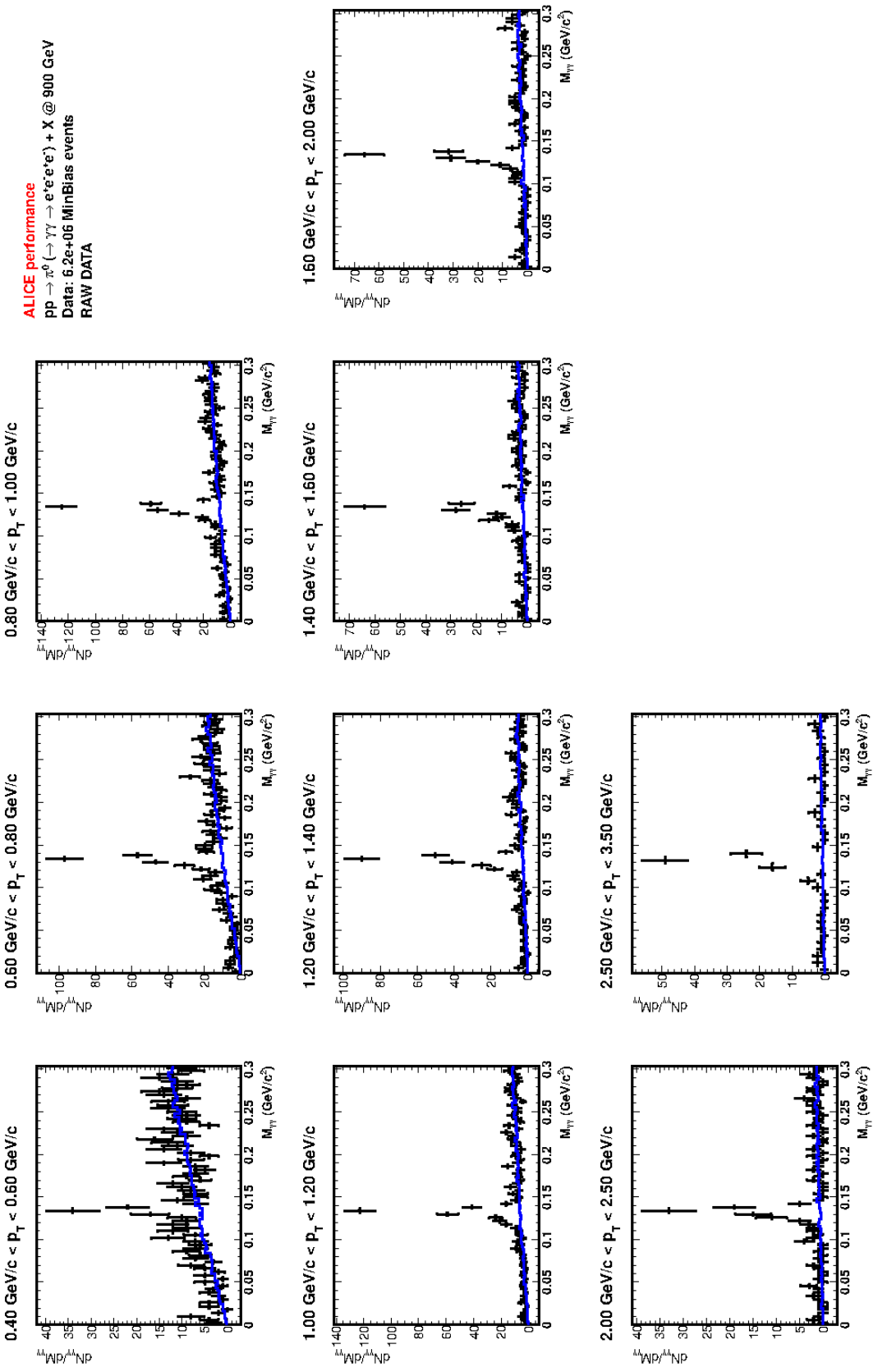

Figure E.1.: Reconstructed signal before background subtraction for π^0 at $\sqrt{s} = 0.9\,\text{TeV}$ for each transverse momentum bin.

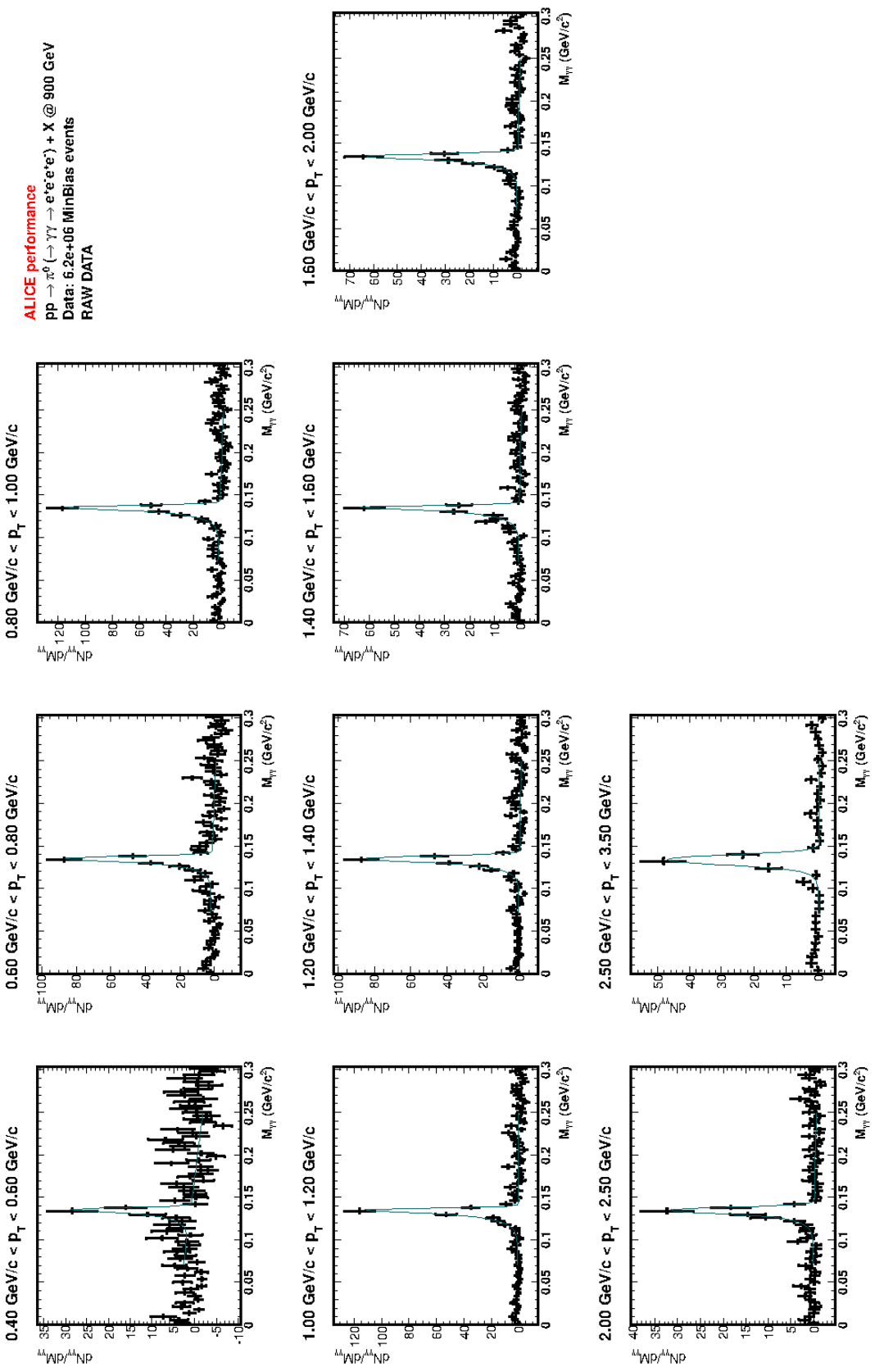

Figure E.2.: Reconstructed signal after background subtraction for π^0 at $\sqrt{s} = 0.9\,\text{TeV}$ for each transverse momentum bin.

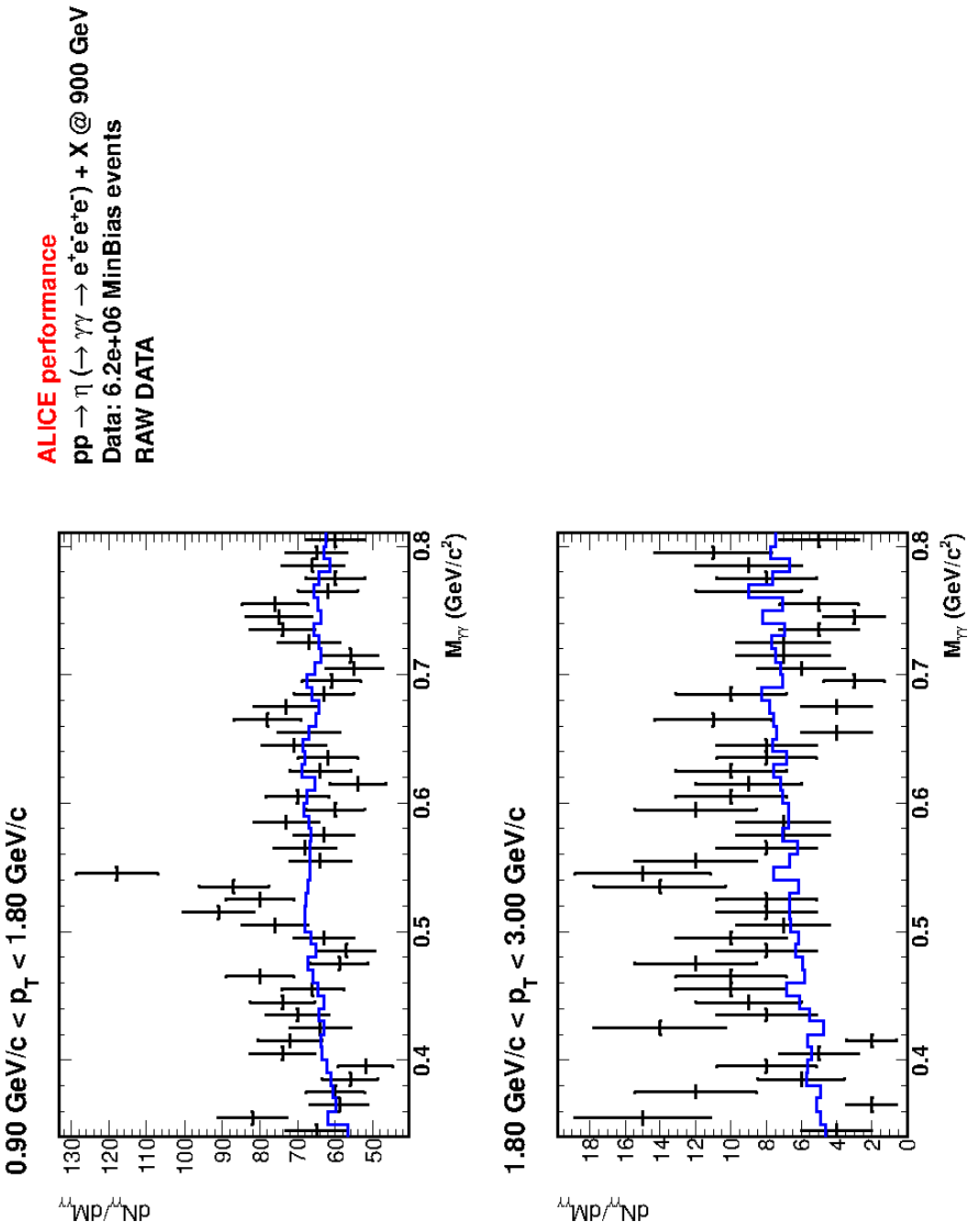

Figure E.3.: Reconstructed signal before background subtraction for π^0 at $\sqrt{s} = 0.9\,\text{TeV}$ for each transverse momentum bin.

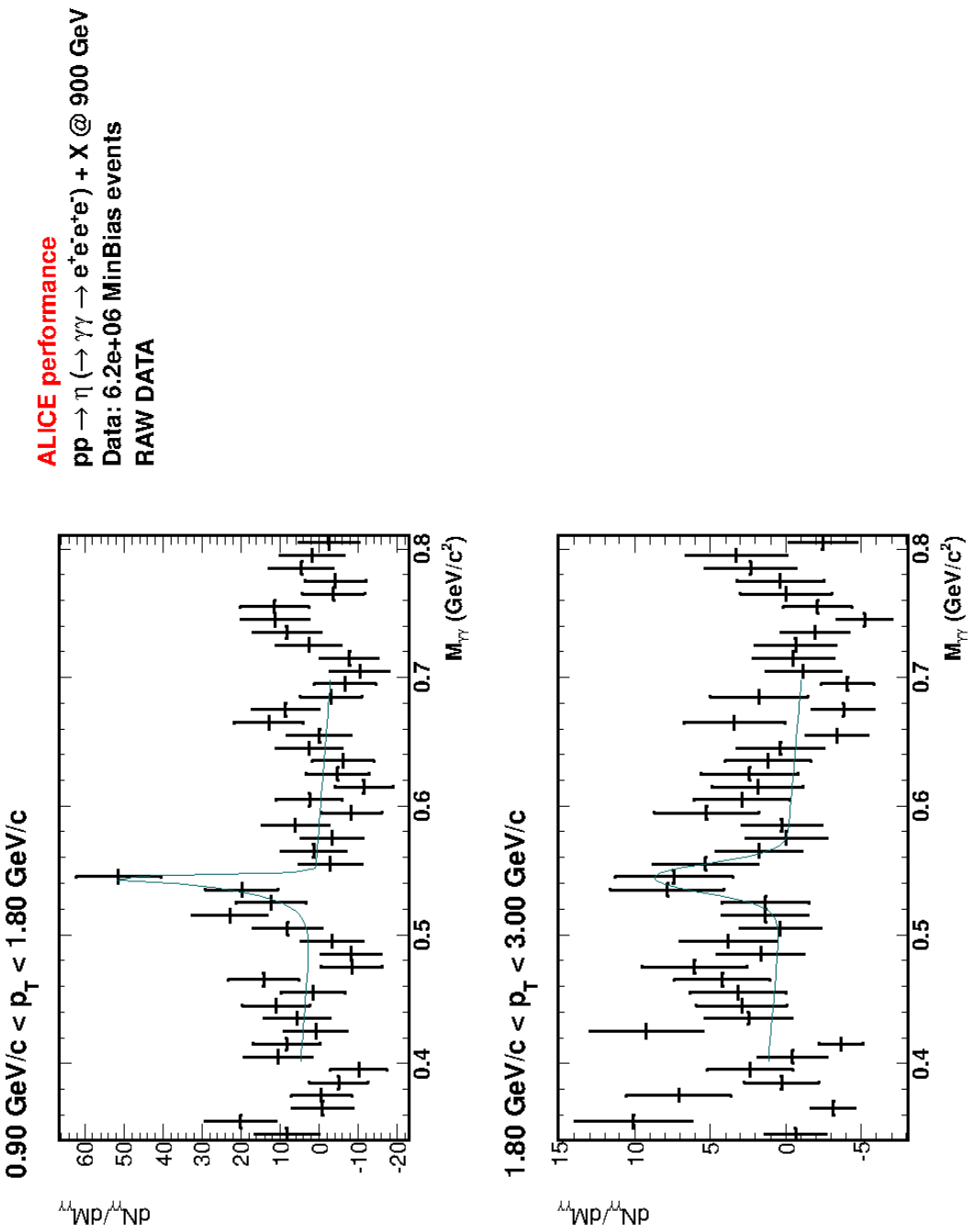

Figure E.4.: Reconstructed signal after background subtraction for π^0 at $\sqrt{s} = 0.9\,\text{TeV}$ for each transverse momentum bin.

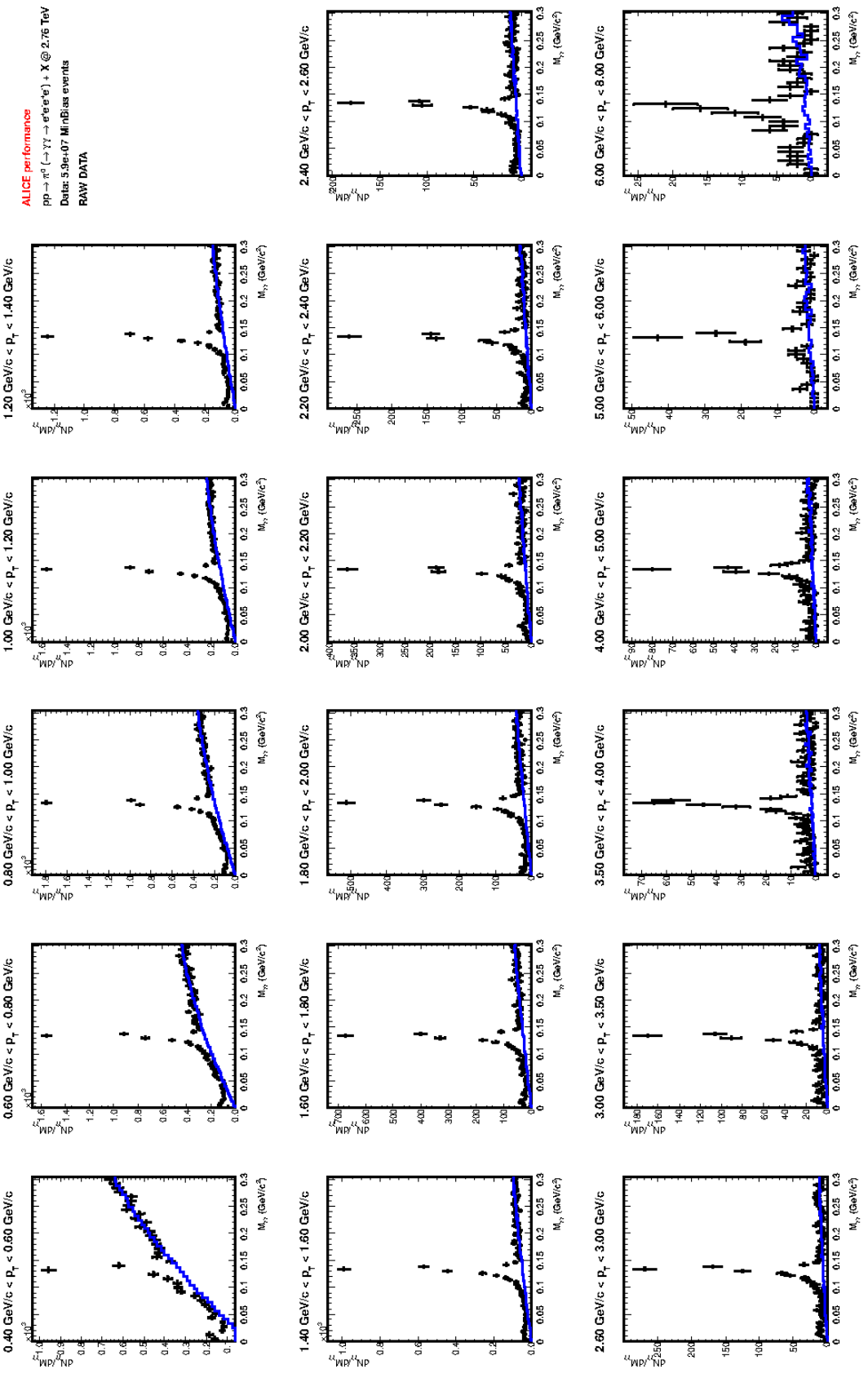

Figure E.5.: Reconstructed signal before background subtraction for π^0 at $\sqrt{s} = 2.76\,\text{TeV}$ for each transverse momentum bin.

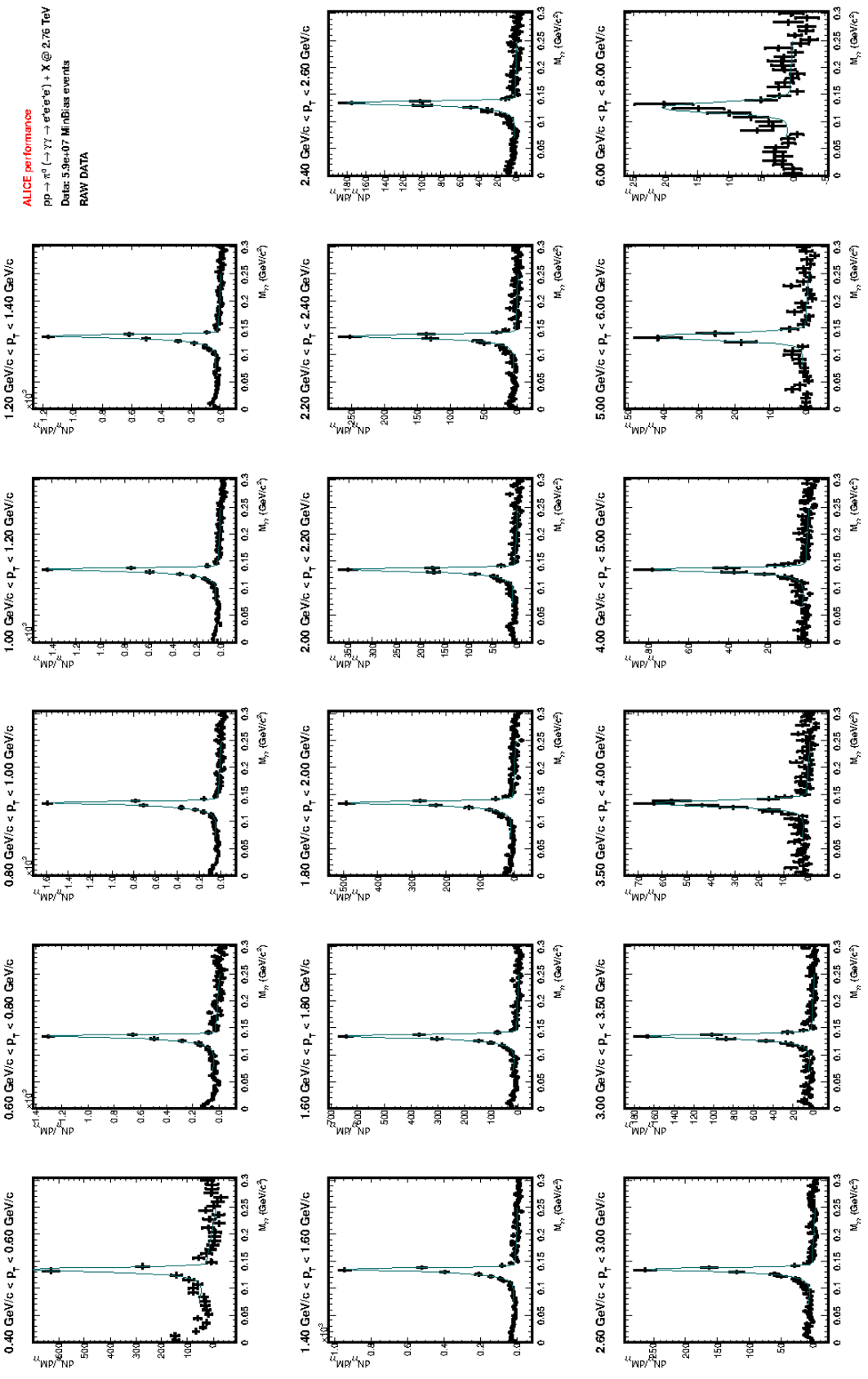

Figure E.6.: Reconstructed signal after background subtraction for π^0 at $\sqrt{s} = 2.76\,\text{TeV}$ for each transverse momentum bin.

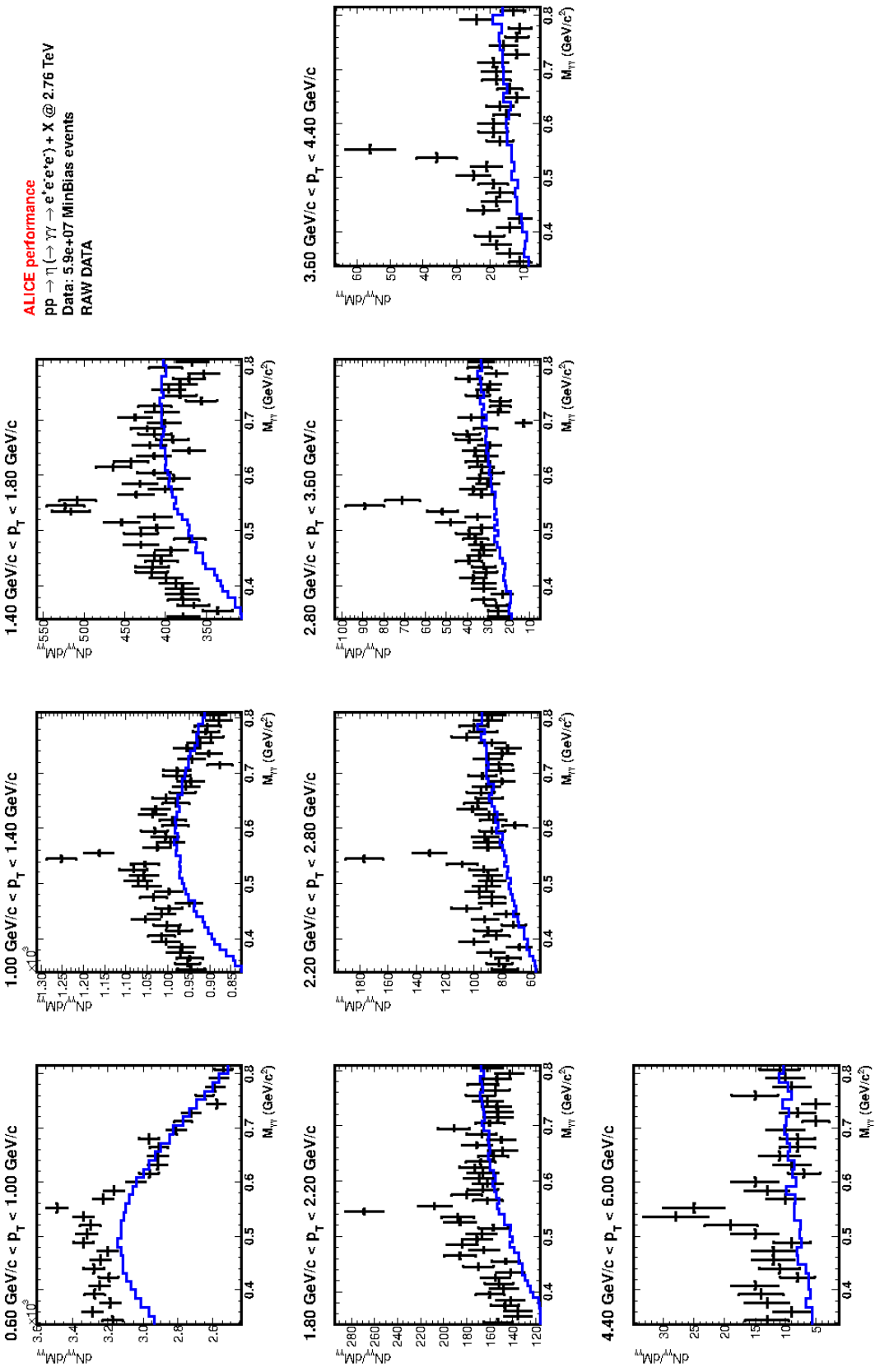

Figure E.7.: Reconstructed signal before background subtraction for π^0 at $\sqrt{s} = 2.76\,\text{TeV}$ for each transverse momentum bin.

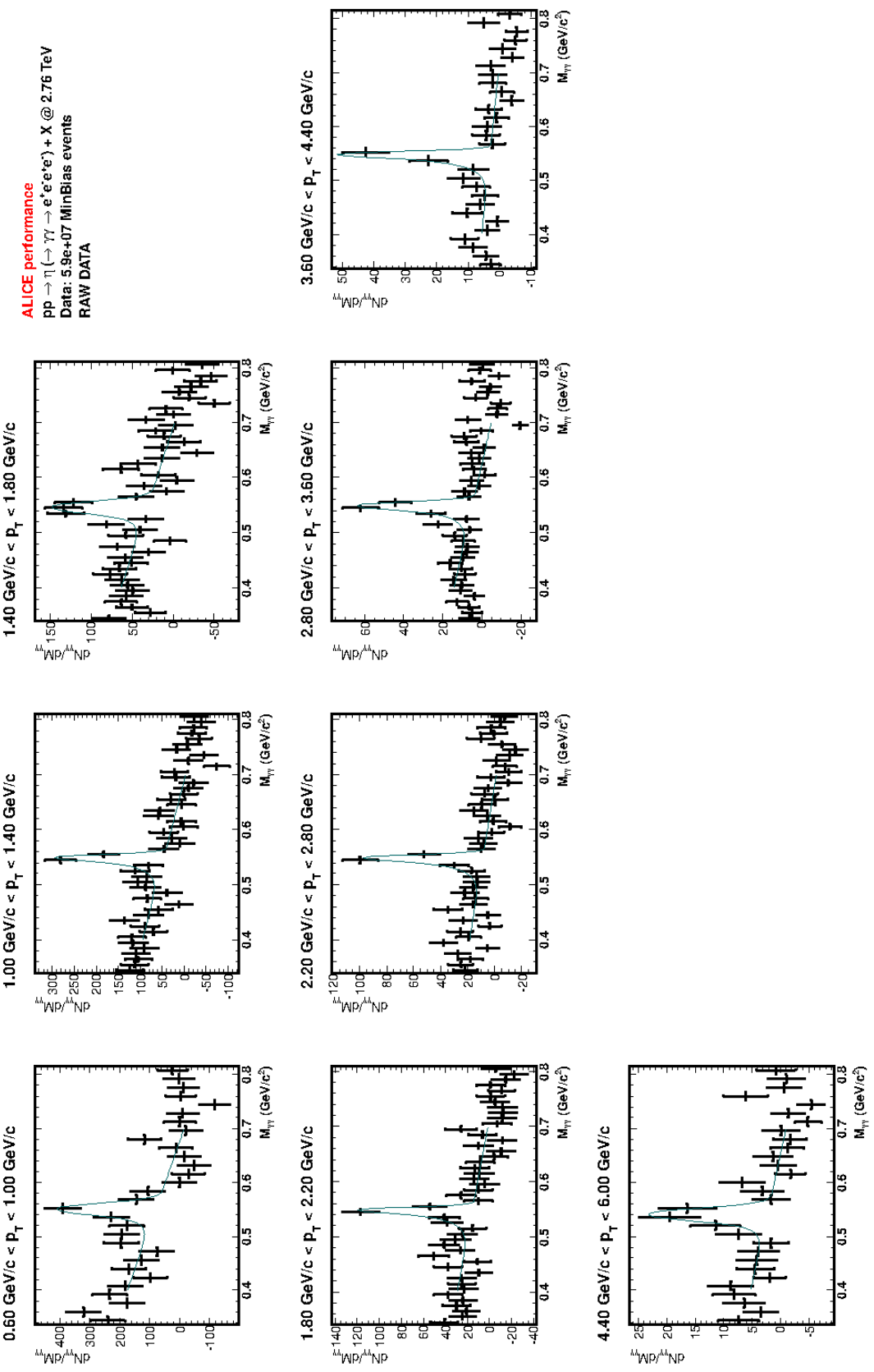

Figure E.8.: Reconstructed signal after background subtraction for π^0 at $\sqrt{s} = 2.76\,\text{TeV}$ for each transverse momentum bin.

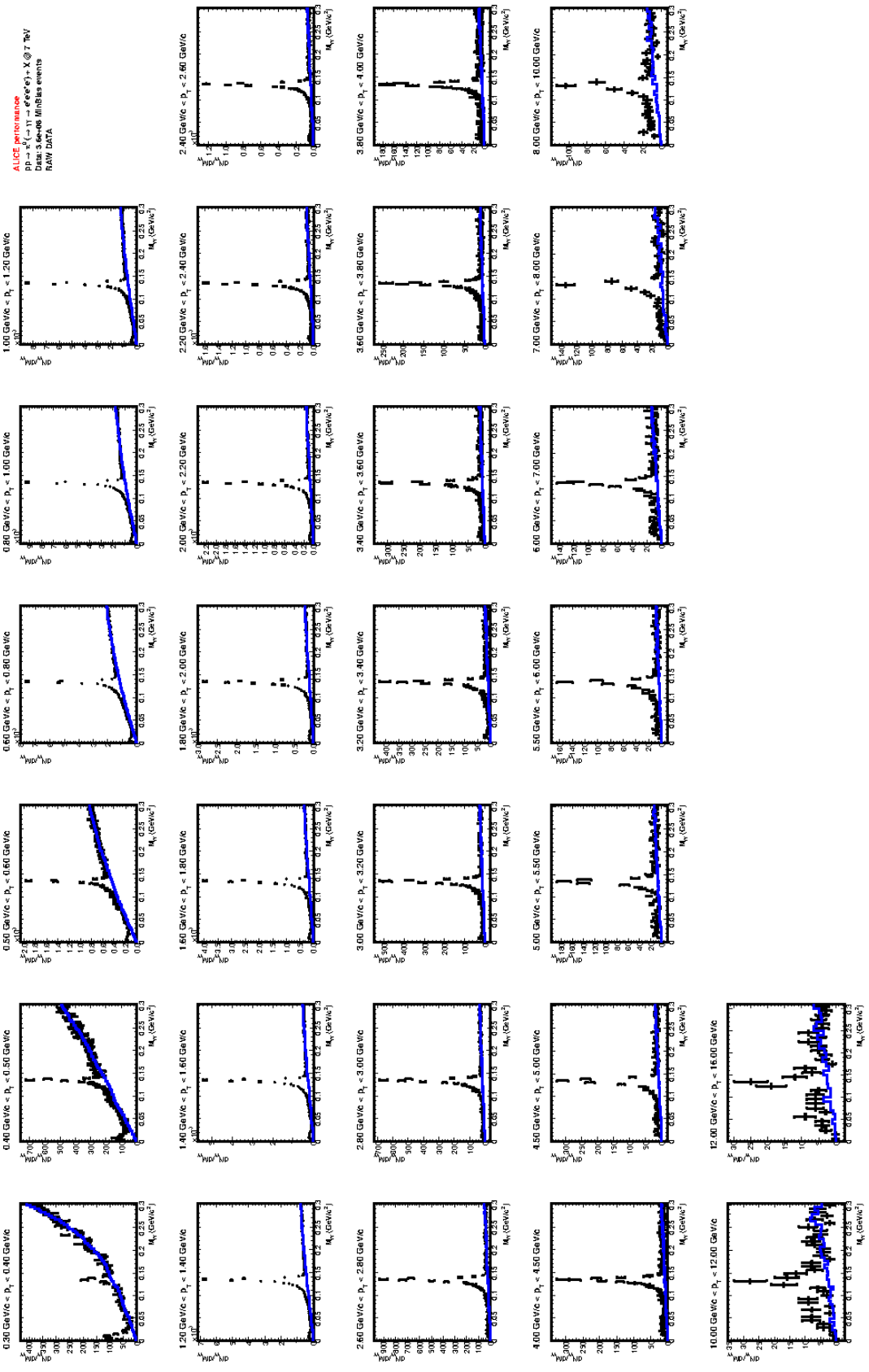

Figure E.9.: Reconstructed signal before background subtraction for π^0 at $\sqrt{s} = 7\,\text{TeV}$ for each transverse momentum bin.

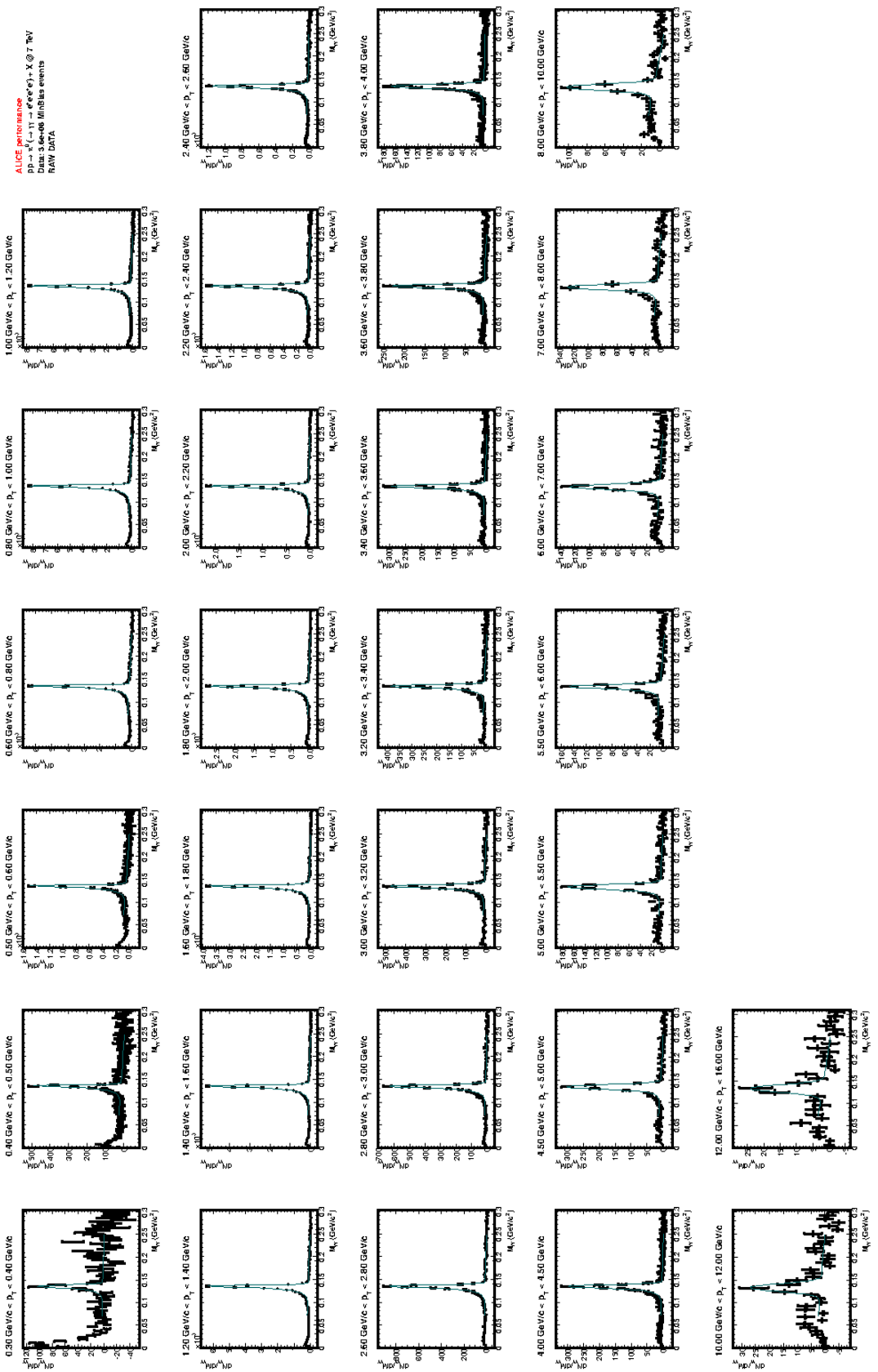

Figure E.10.: Reconstructed signal after background subtraction for π^0 at $\sqrt{s} = 7\,\mathrm{TeV}$ for each transverse momentum bin.

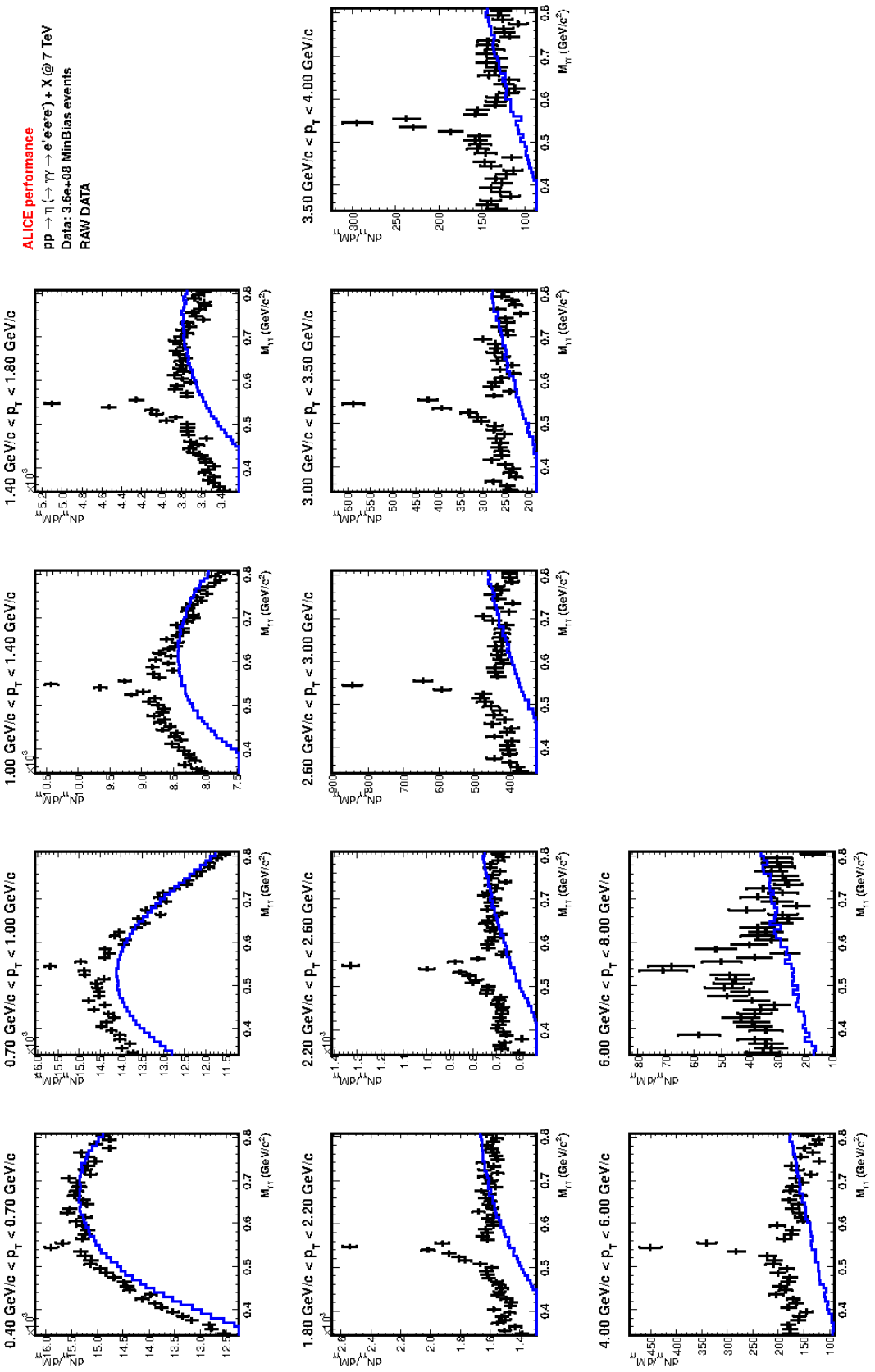

Figure E.11.: Reconstructed signal before background subtraction for π^0 at $\sqrt{s} = 7\,\text{TeV}$ for each transverse momentum bin.

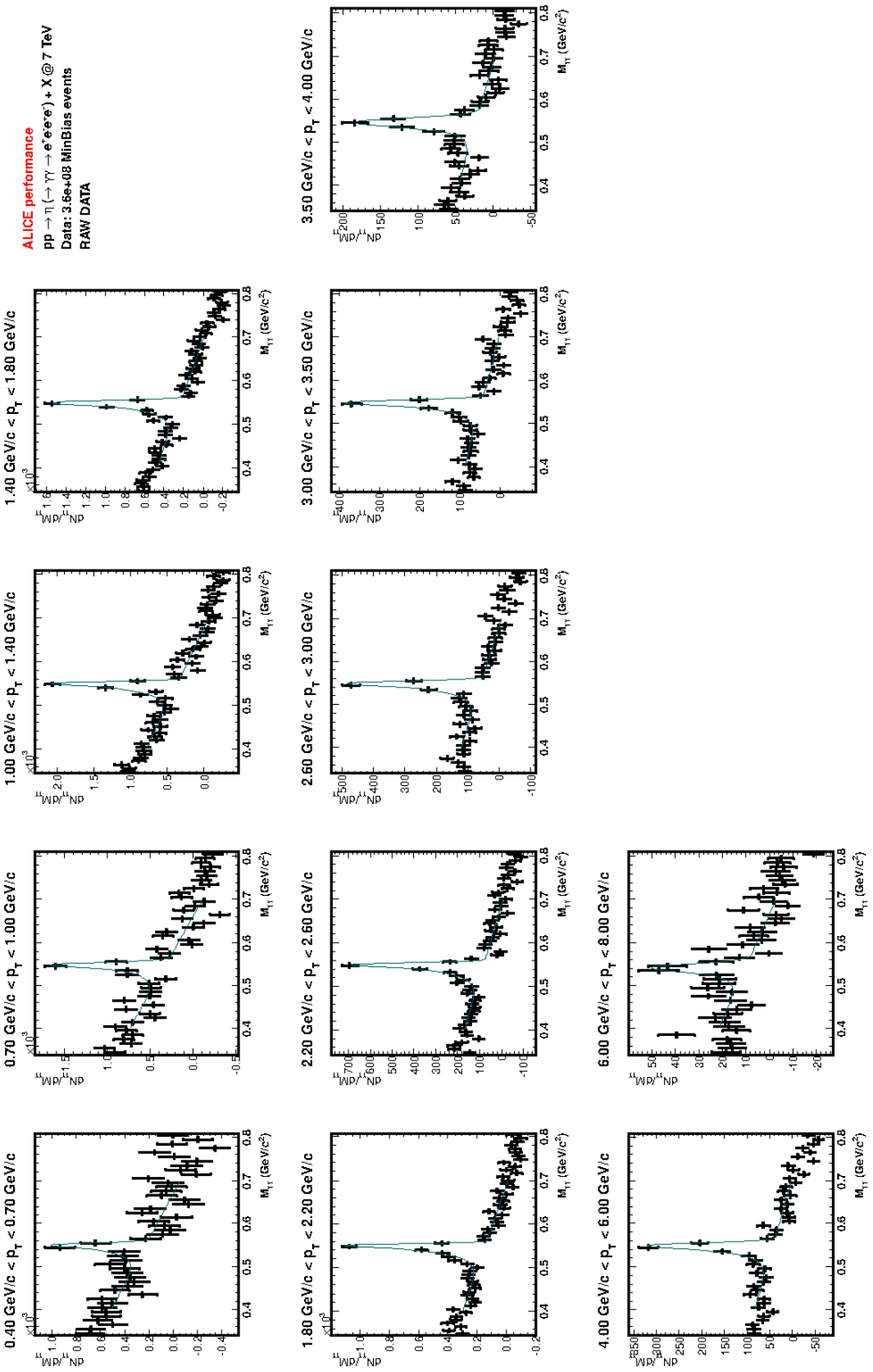

Figure E.12.: Reconstructed signal after background subtraction for π^0 at $\sqrt{s} = 7\,\mathrm{TeV}$ for each transverse momentum bin.

F. Background shape

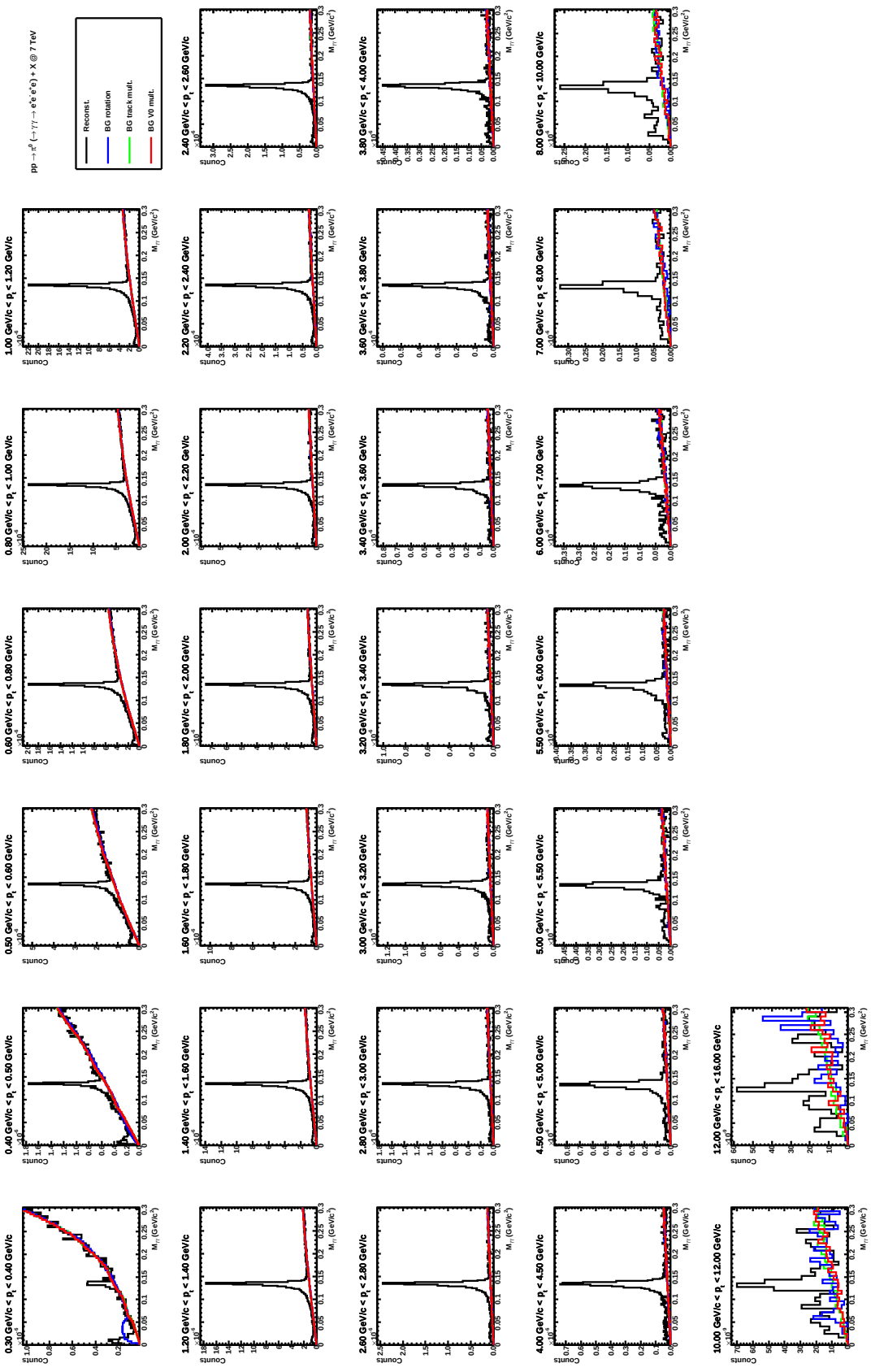

Figure F.1.: Background description for π^0 at $\sqrt{s} = 7\,\text{TeV}$ in the $M_{\gamma\gamma}$ distribution for each transverse momentum bin.

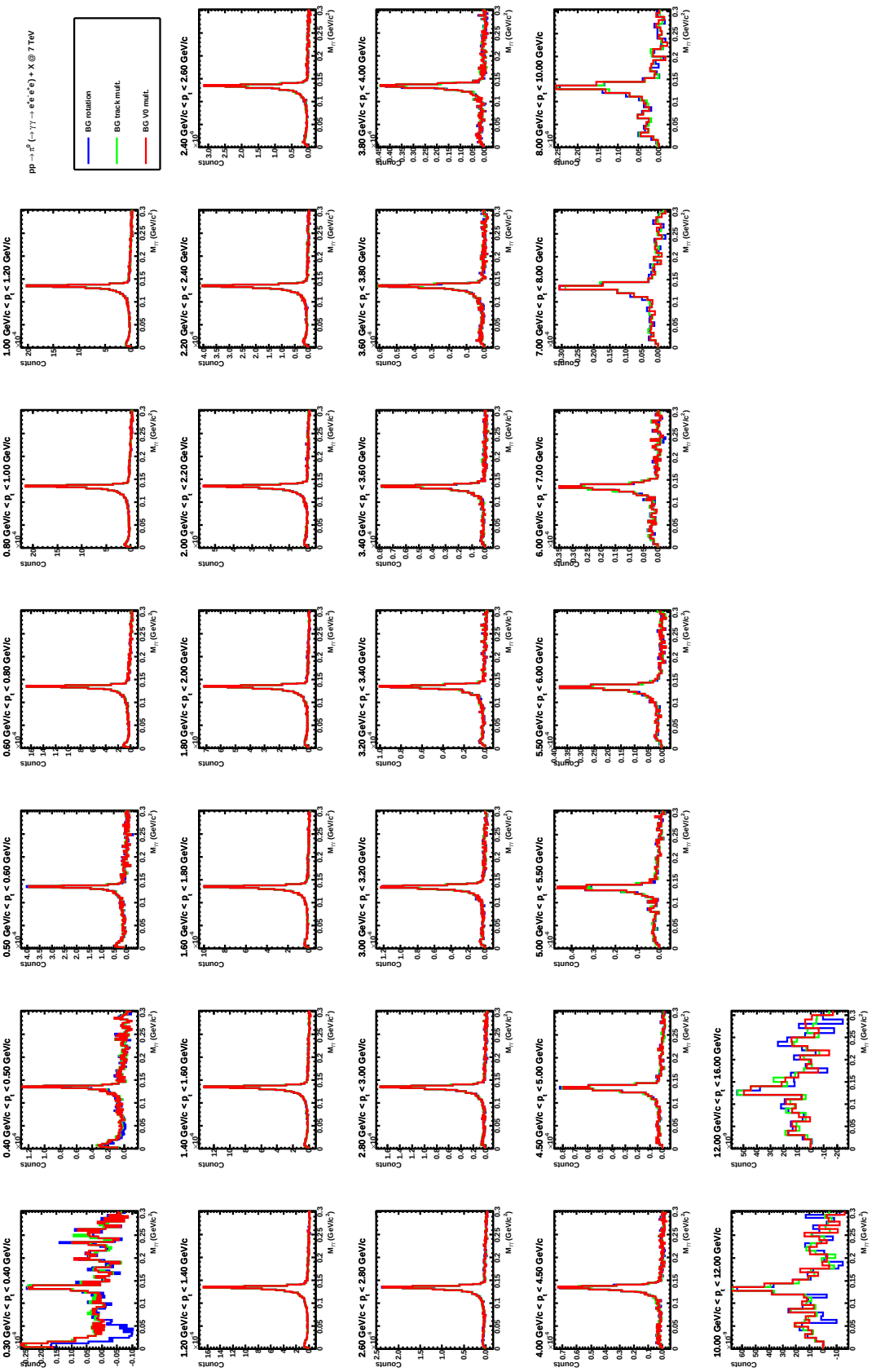

Figure F.2.: Signal after background subtraction for π^0 at $\sqrt{s} = 7\,\text{TeV}$ in the $M_{\gamma\gamma}$ distribution for each transverse momentum bin.

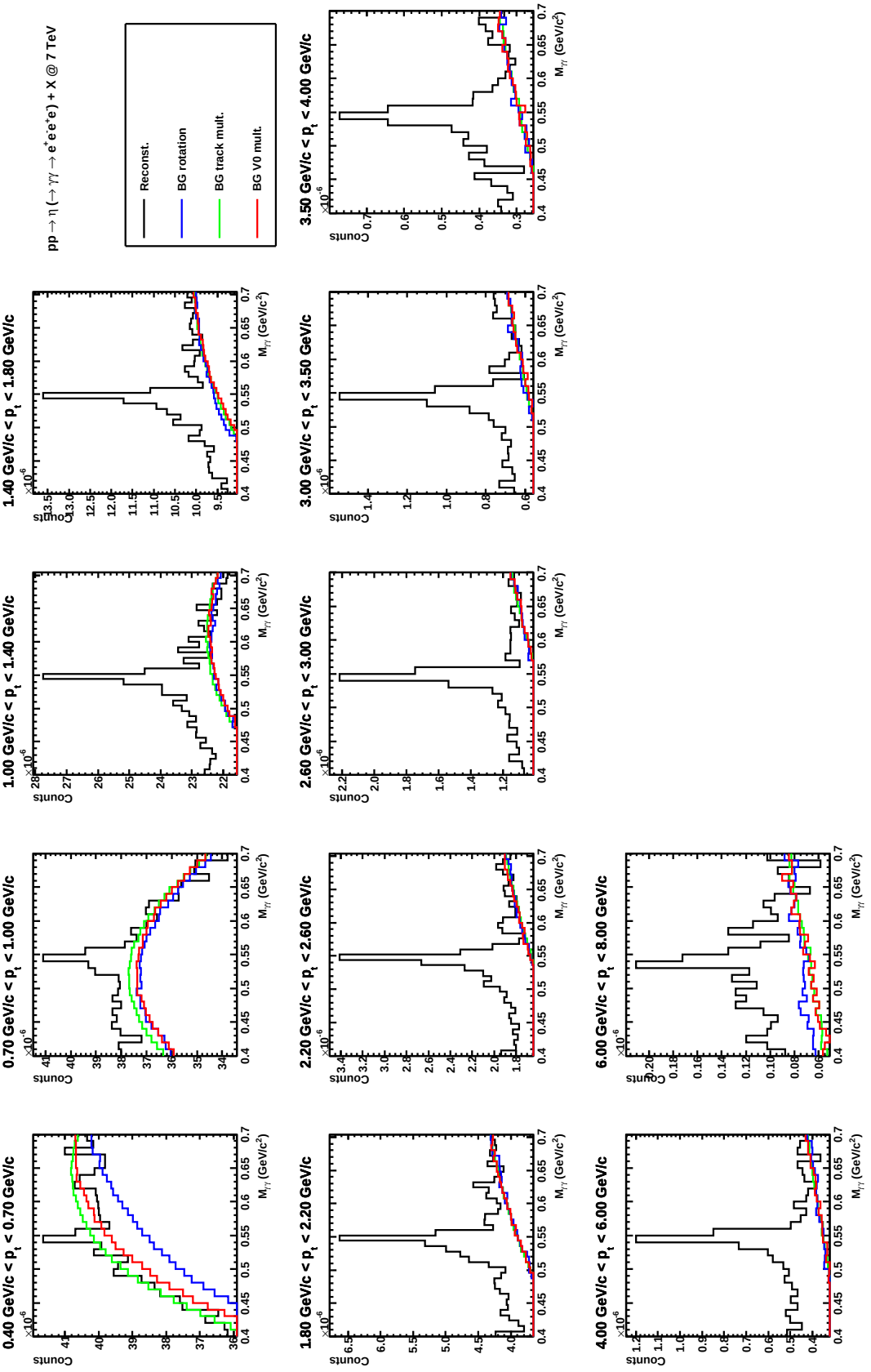

Figure F.3.: Background discription for η at $\sqrt{s} = 7\,\mathrm{TeV}$ in the $M_{\gamma\gamma}$ distribution for each transverse momentum bin.

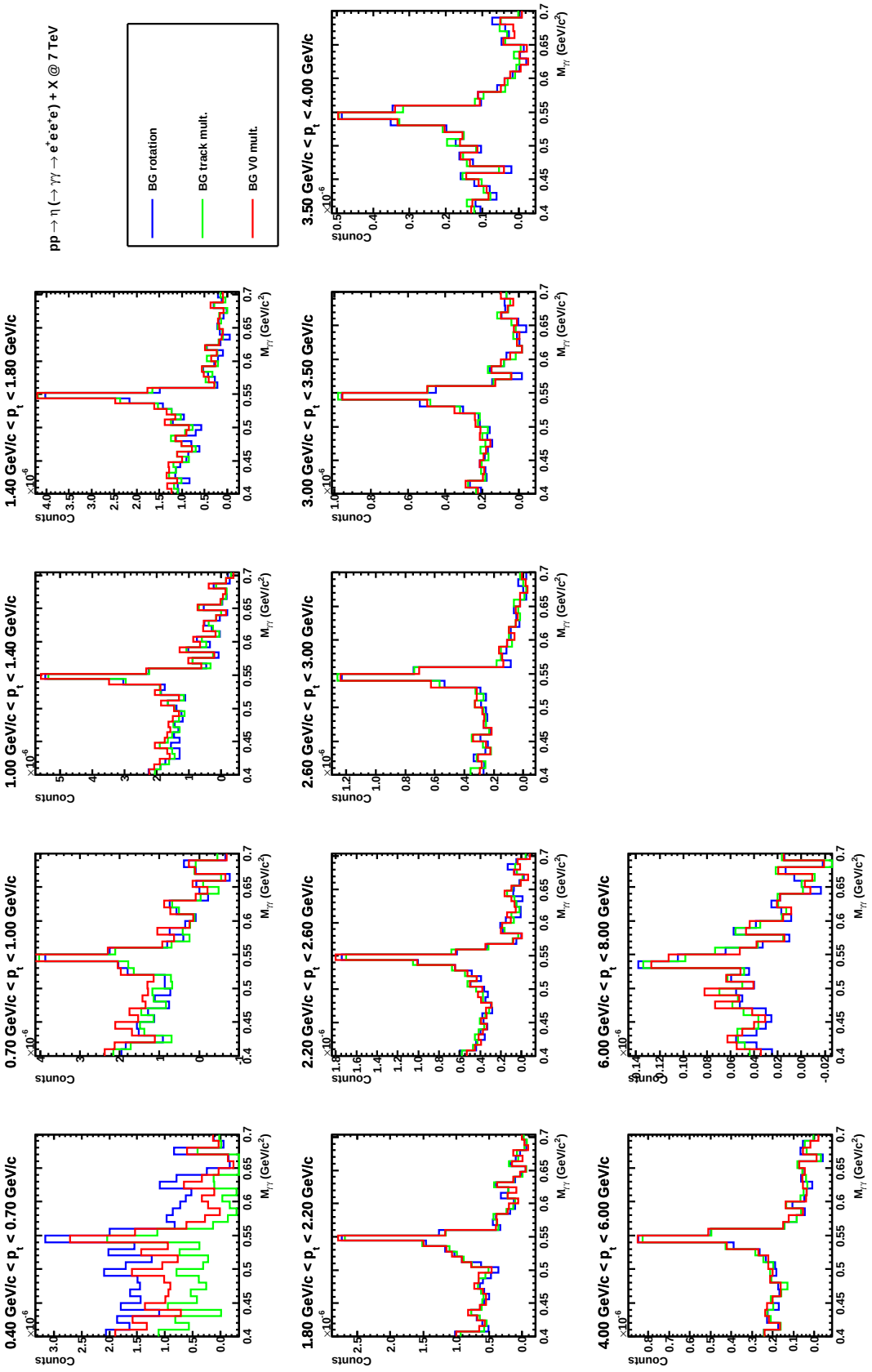

Figure F.4.: Signal after background subtraction for η at $\sqrt{s} = 7\,\text{TeV}$ in the $M_{\gamma\gamma}$ distribution for each transverse momentum bin.

Bibliography

[Aam2008] K. Aamodt et al. (ALICE Collaboration),
The ALICE experiment at the CERN LHC,
JINST 3 S08002 (2008).

[Aam2010] K. Aamodt et al. (ALICE Collaboration),
Alignment of the ALICE Inner Tracking System with cosmic-ray tracks,
JINST 5 P03003 (2010).

[Aam2010a] K. Aamodt et al. (ALICE Collaboration),
Transverse momentum spectra of charged particles in proton–proton collisions at $\sqrt{s}$=900 GeV with ALICE at the LHC,
Physics Letters B 693, 53-69 (2010).

[Aam2011] K. Aamodt et al. (ALICE Collaboration),
Centrality dependence of the charged-particle multiplicity density at mid-rapidity in Pb-Pb collisions at $\sqrt{s_{NN}} = 2.76\,\text{TeV}$,
Phys. Rev. Lett. 106, 032301 (2011).

[Aam2011a] K. Aamodt et al.,
π^0 and η meson measurement with conversions in ALICE in proton-proton collisions at $\sqrt{s} = 0.9\,\text{TeV}$, $\sqrt{s} = 2.76\,\text{TeV}$ and $\sqrt{s} = 900\,\text{GeV}$ at the CERN LHC,
ALICE Internal Note (2011).

[Aam2011b] K. Aamodt,
Photon, π^0 and η measurements in proton-proton collisions at $\sqrt{s} = 7\,\text{TeV}$ with the ALICE TPC at the LHC,
PhD thesis, University of Oslo, to be published (2011).

[Aam2011c] K. Aamodt et al.,
Material determination with conversions in ALICE in proton-proton collisions at $\sqrt{s} = 7\,\text{TeV}$ at the CERN LHC,
ALICE Internal Note (2011).

[Aam2011d] K. Aamodt et al. (ALICE Collaboration),
Strange particle production in proton–proton collisions at $\sqrt{s} = 7\,\text{TeV}$ with ALICE at the LHC,
Eur. Phys. J. C 71 (3), 1594 (2011).

[Aam2011e] K. Aamodt et el. ALICE Collaboration,
Production of pion, kaons and protons in pp collisions at $\sqrt{s} = 900\,\text{GeV}$ with ALICE at the LHC,
Eur. Phys. J. C 71 (6), 1655 (2011).

[Abe1988] F. Abe et al. (CDF collaboration),
Transverse-Momentum Distributions of Charged Particles Produced in $\overline{p}p$ Interactions at $\sqrt{s} = 630$ and $1800\,\text{GeV}$,
Phys. Rev. Lett. 61, 1819 (1988).

[Ada2007] A. Adare et al. (PHENIX collaboration),
Inclusive cross section and double helicity asymmetry for π^0 production in $p + p$ collisions at $\sqrt{s} = 200\,\text{GeV}$: Implications for the polarized gluon distribution in the proton,
Physics Review D, 76:051106 (2007).

[Ada2011] A. Adare et al. (PHENIX collaboration),
Inclusive cross section and double helicity asymmetry for η mesons and their comparison to π^0 production in $p+p$ collisions at $\sqrt{s} = 200\,\mathrm{GeV}$,
Physics Review D, 83:032001 (2011).

[Ada2011a] A. Adare et al. (PHENIX collaboration),
Detailled measurement of the e^+e^- pair continuum in $p+p$ and $AuAu$ collisions at $\sqrt{s} = 200\,\mathrm{GeV}$ and implications for direct photon production,
Physics Review D, 81:034911 (2011).

[Adl2007] S.S. Adler et al. (PHENIX collaboration),
High transverse momentum η meson production in p+p, d+Au, and Au+Au collisions at $\sqrt{s_{NN}} = 200\,\mathrm{GeV}$,
Physics Review C, 75: 024909 (2007).

[Aid2010] C.A. Aidala et al.,
Global Analysis of Fragmentation Functions for Eta Mesons,
Physics Review D, 83: 034002 (2010), arXiv:hep-ph/1009.6145v2.

[Ago2003] S. Agostinelli et al.,
Geant4, a simulation toolkit,
Nucl. Instr. Meth. A 506, 250 (2003).

[Ale2006] B. Alessandro, F. Antinori, J.A. Belikov, C. Blume, A. Dainese, P. Foka, P. Giubellino, B. Hippolyte, C. Kuhn, G. Martínez, M. Monteno, A. Morsch, T.K. Nayak, J. Nystrand, M. López Noriega, G. Paic, J. Pluta, L. Ramello, J.-P. Revol, K. Safarik, J. Schukraft, Y. Schutz, E. Scomparin, R. Snellings, O. Villalobos Baillie and E. Vercellin (editors) (ALICE Collaboration),
ALICE Physics Performance Report, Volume II,
J. Phys. G: Nucl. Part. Phys. 32, 1295–2040 (2006).

[Ale2005] D.V. Aleksandrov et al,
A high resolution electromagnetic calorimeter based on lead-tungstate crystals,
Nucl. Instr. Meth. A 550, 169–184 (2005).

[Ale2011] D. Aleksandrov et. al,
Analysis of inclusive π^0 production in pp collisions at $\sqrt{s} = 900\,\mathrm{GeV}$ and $7\,\mathrm{TeV}$ measured with ALICE PHOS,
ALICE Internal Note (2011).

[ALI2011] ALICE twiki web page,
https://twiki.cern.ch/twiki/ bin/viewauth/ALICE/PublishedAndPreliminaryPictures, 2011.

[ALI2011doc] AliRoot Documentation,
http://aliweb.cern.ch/Offline/AliRoot/Manual.html#tutorial.

[Alm2010] J. Alme et al.
The ALICE TPC, a large 3-dimensional tracking device with fast readout for ultra-high multiplicity events,
Nucl. Instr. Meth. A 622, 316-367 (2010).

[And2002] B. Andersson, S. Mohanty and F. Söderberg,
Recent Developments in the Lund Model,
LU TP 02-45 (2002), arXiv:[hep-ph]0212122v1.

[Ans1986] R.E. Ansorge et al. (UA5 Collaboration)
Diffraction dissociation at the CERN pulsed collider at energies of $900\,\mathrm{GeV}$ and $200\,\mathrm{GeV}$.
Zeitschrift für Physik C 33: 175 (1986).

[Aur2000] P. Aurenche et al.,
Large-p_T Inclusive π^0 Cross Sections and Next-to-Leading-Order QCD Predictions,
Eur. Phys. J. C 13, 347 (2000), http://lapth.in2p3.fr/PHOX_FAMILY.

[Bar1987] D. S. Barton,
Heavy Ion Acceleration in the BNL AGS,
Part. Accel. 22, pp.179-181 (1987).

[Bar1996] R. M. Barlett et al.,
Review of Particle Physics,
Physics Review D 54, 1-708 (1996).

[Bel2010] R. Bellwied for the ALICE EMCal collaboration,
ALICE EMCAL Physics Performance Report,
arXiv:[physics.ins-det]1008.0413v1 (2010).

[Bet2009] S. Bethke,
The 2009 world average of α_s,
Eur. Phys. J. C 64, 689–703 (2009).

[Bil1984] P. Billoir,
Track fitting with multiple scattering: a new method,
Nucl. Instr. Meth. A 225, 352 (1984).
P. Billoir et al.,
Track element merging strategy an vertex fitting in complex modular detectors,
Nucl. Instr. Meth. A 241, 115 (1985).

[Boc1998] R.K. Bock and A. Vasilescu,
The Particle Detector BriefBook,
Springer-Verlag Berlin Heidelberg New York, ISBN 3-540-64120-3 (1998).

[Boc2010] F. Bock,
ALICE Capabilities for Studying Photon Physics with the Conversion Method at LHC Energies,
Bachelor Thesis, University of Heidelberg (2010).

[Bou1976] M. Bourquin and J. M. Gaillard,
A simple phenomenological description of hadron production,
Nucl. Phys. B 114, 334 (1976).

[Bra2001] P. Braun-Munzinger,
Chemical Equilibration and the Hadron-QGP Phase Transition,
Nucl. Phys. A 681, 119-123 (2001).

[Bra2007] P. Braun-Muntzinger & J. Stachel,
The quest for the quark-gluon plasma,
Nature Vol. 488: 19 July 2008, doi:10.1038/nature06080 (2007).

[Bru1985] R. Brun, F. Bruyant, M. Maire, A.C. McPherson and P. Zanarini,
GEANT3 user guide,
CERN data handling division DD/EE/84-1 (1985),
http://wwwinfo.cern.ch/asdoc/geantold/GEANTMAIN.html;
M. Goossens et al.,
GEANT detector description and simulation tool,
CERN program library long write-up W5013 (1994), http://cdsweb.cern.ch/record/1073159.

[Bru1997] R. Brun, F. Rademakers,
ROOT - An Object Oriented Data Analysis Framework,
Nucl. Instr. Meth A, 389 (1997).

[BKK1995] J. Binnewies, B.A.Kniehl and G. Kramer,
Next-to-Leading Order Fragmentation Functions for Pions and Kaons,
Zeitschrift für Physik C 65: 471 (1995), arXiv:hep-ph/9407347.

[Cap1994] A. Capella, U. Sukhatme, C.I.Tang and J. Tran Thanh Vane,
DUAL PARTON MODEL,
PHYSICS REPORTS (Review Section of Physics Letters) 236, Nos. 4 & 5, 225—329 (1994).

[Car2004] F. Carminati, P. Foka, P. Giubellino, A. Morsch, G. Paic, J.-P. Revol, K. Safarik, Y. Schutz and U. A.Wiedemann (editors) (ALICE Collaboration),
ALICE Physics Performance Report, Volume I,
J. Phys. G: Nucl. Part. Phys. 30, 1517–1763 (2004).

[Cas1998] C. Caso et al.,
Eur. Phys. J. C 3, 1-794 (1998).

[Cho2011] M. Chojnacki for the ALICE collaboration,
Measurement of π, K, p transverse momentum spectra with ALICE in proton-proton collisions at $\sqrt{s} = 0.9$ and 7 TeV.;
Proceedings to Quark Matter 2011, to be published in J. Phys. G , arXiv:[hep-ex]1109.6744v1 (2011).

[Cho1974] A. Chodos, R. L. Jaffe, K. Johnson, C. B. Thorn, and V. F. Weisskopf,
A new extended model of hadrons,
Physics Review D 9, 3471–3495 (1974).

[Chr2011] P. Christiansen,
Private communication, 2011.

[CMS2010] CMS collaboration,
Transverse-momentum and pseudorapidity distributions of charged hadrons in pp collisions at $\sqrt{s} = 7$ TeV,
Phys. Rev. Lett. 105.022002 (2010).

[Col1975] J. C. Collins and M. J. Perry,
Superdense matter: neutrons or asymptotically free quarks?,
Phys. Rev. Lett. 34, 1353-1356 (1975).

[Col1977] P.D.B. Collins,
An Introduction to Regge Theory and High-Energy Physics, Cambridge University Press (1977).

[CTE2011] The Coordinated Theoretical-Experimental Project on QCD,
http://www.phys.psu.edu/ cteq/ (2011).

[Dag1995] G. D'Agonstini,
A multidimensional unfolding method based on Bayes theorem,
Nucl. Inst. Meth. A 362, 487-498 (1995).

[Dem2005] W. Demtröder
Experimentalphysik 4 – Kern-, Teilchen- und Astrophysik,
2. Auflage, Springer-Verlag Berlin Heidelberg New York, ISBN 3-540-21451-8 (2005).

[Dis2008] G. Dissertori, I. Knowles, M. Schmelling,
Quantum Chromodynamics - High Energy Experiments and Theory,
Oxford University Press Inc., ISBN 978-019-850572-3, (Reprint 2008).

[Dob2010] A. Dobrin,
R-hadron Searches and Charged Pion Spectra at High Transverse Momentum in Proton-Proton Collisions at the LHC using the ALICE Detector,
CERN-THESIS-2010-129 (2010).

[DSS2007] D. De Florian, R. Sassot and M. Stratmann,
Global analysis of fragmentation functions for pions and kaons and their uncertainties,
Physics Review D 75, 114010 (2007), arXiv:[hep-ph]0703242.

[Eng1995] R. Engel, J. Ranft, S. Roesler,
Hard diffraction in hadron–hadron interactions and in photoproduction,
Physics Review D 52, 1459-1468 (1995), arXiv:[hep-ph]9502319v1.

[Ell1996] R.K. Ellis, W.J. Sterling and B.R. Webber,
QCD and Collider Physics,
Cambridge University Press, ISBN 0 521 58189 7 (1996).

[Eva2008] L. Evans and P. Bryant (editors),
LHC Machine,
JINST 3 S08001 (2008).

[Fas1993] A. Fasso, A. Ferrari, J. Ranft, and P. R. Sala,
FLUKA: present status and future developments,
Proceedings of the IV Int. Conf. on Calorimetry in High Energy Physics (1993).

[Fuk2003] M. Fukugita, T. Yanagida
Physics of Neutrinos and Applications to Astrophysics,
Springer-Verlag Berlin Heidelberg New York, ISBN 3-540-43800-9 (2003).

[Gag2011] M. Gagliardi
Measurement of reference cross sections in pp and Pb-Pb collisions at the LHC in van der Meer scans with the ALICE detector,
Proceedings to EPIC@LHC, to be published in AIP proceedings (2011), arXiv:[hep-ex]1109.5369v1.

[Gar2011] K. Garrett, G. Duda,
Dark Matter: A Primer,
Adv. Astron. 2011, 968283 (2011).

[Gel1964] M. Gell-Mann,
A Schematic Model of Baryons and Mesons.,
Physics Letters 8 (3), 214-215 (1964).

[Gla1962] S.L. Glashow,
Symmetries of Weak Interactions,
Nucl. Phys. 22, 579–588 (1962).

[Gor2007] S. Gorbunov and I. Kisel,
Reconstruction of decay particles based on the Kalman filter,
CBM-SOFT-note-2007-003 (2007).

[Gro2010] J.F. Grosse-Oetringhaus and K. Reygers,
Charged-Particle Multiplicity in Proton–Proton Collisions,
J. Phys. G 37, 083001 (2010).

[Gru1996] C. Grupen,
Particle Detectors,
Cambridge University Press, ISBN 0 521 55216 8 (1996).

[GSI2011] GSI Helmholtzzentrum für Schwerionenforschung GmbH,
http://www.gsi.de/forschung/fair_experiments/CBM/Phasendiagram.jpg (2011).

[Hei2008] U. Heinz,
From SPS to RHIC: Maurice and the CERN heavy-ion program,
Part. Accel. 22, 179-181 (1987).

[Hig1964] P.W. Higgs,
Broken symmetries, massless particles and gauge fields.,
Phys. Letters 12, 132 (1964).
Broken symmetries and the masses of gauge bosons.,
Phys. Rev. Lett. 13, 508–509 (1964).

[Hub1931] E. Hubble, M.L. Humason,
The Velocity-Distance Relation among Extra-Galactic Nebulae,
Astrophysical Journal Vol. 74, 43 (1931).

[JoP2006] Particle Data Group,
Review of particle physics,
J. Phys. G: Nucl. Part. Phys. 33 (2006).

[Kal2011] A. Kalweit for the ALICE Collaboration,
Particle identification in the ALICE experiment,
Proceedings to Quark Matter 2011, to be published in J. Phys. G (2011), arXiv:[hep-ex]1107.1514v1

[Kni2011] M.L. Knichel,
Private communication, 2011.

[Kar2002] F. Karsch,
Lattice Results on QCD Thermodynamics,
Nucl. Phys. A 698, 199-208 (2002).

[Kha2002] D. E. Kharzeev, J. Raufeisen,
High energy nuclear interactions and QCD: an introduction,
BNL-NT-02/15, LA-UR-02-3956 (2002), arcXiv:nucl-th/0206073.

[Kle1987] K. Kleinknecht,
Detektoren für Teilchenstrahlung,
2. Auflage, B.G. Teubner Stuttgart, ISBN 3-519-13058-0 (1987).

[Koc2011] K. Koch for the ALICE collaboration,
π^0 and η measurements with photon conversions in ALICE in proton-proton collisions at $\sqrt{s} = 7\,\mathrm{TeV}$,
Nucl. Phys. A 855: 281 (2011).

[Kra2011] F. Krauss,
Private communications.

[Laf1995] G. D. Lafferty and T. R. Wyatt,
Where to stick your data points: The treatment of measurements within wide bins,
Nucl. Instr. Meth. A 355, 541 (1995).

[Lem1927] G. Lemaître,
Expansion of the universe, A homogeneous universe of constant mass and increasing radius accounting for the radial velocity of extra-galactic nebulae,
Monthly Notices of the Royal Astronomical Society Vol. 91, 483-490 (1927).

[Lem1931] G. Lemaître,
The Beginning of the World from the Point of View of Quantum Theory.
Nature, Volume 127 (3210), 706 (1931).

[LHC2011] CERN Press release,
LHC experiments present latest results at Mumbai conference 22. August 2011,
http://press.web.cern.ch/press/PressReleases/Releases2011/PR14.11E.html

[Nak2010] K. Nakamura et al.,
Review of Particle Physics,
J. Phys. G 37, 075021 (2010).

[Oya2011] K. Oyama for the ALICE collaboration,
Cross section normalization in proton-proton collisions at $\sqrt{s} = 2.76\,\text{TeV}$ and $7\,\text{TeV}$, with ALICE at LHC,
Proceedings to Quark Matter 2011, to be published in J. Phys. G (2011), arXiv:[physics.ins-det]1107.0692v1.

[Otw2011] J. Otwinowski for the ALICE collaboration,
Charged Particle Production at Large Transverse Momentum in Pb−Pb Collisions at $\sqrt{s} = 2.76\,\text{TeV}$ Measured with ALICE at the LHC.
Proceedings to Quark Matter 2011, to be published in J. Phys. G (2011), arXiv:1110.2985v1[hep-ex]13Oct2011.

[Pen1965] A.A. Penzias, R.W. Wilson,
A Measurement of Excess Antenna Temperature at 4080 Mc/s.,
Astrophysical Journal 142, 419-421 (1965).

[PHE2011] PHENIX collaboration,
http://www.phenix.bnl.gov/WWW/plots/show_plot.php?editkey=p0820 (2011).

[Pod1954] J. Podolanski and R. Armenteros,
Analysis of v-events,
Phil. Mag. 45, 13–30 (1954).

[Por2011] S. Porteboeuf, R. Granier de Cassagnac,
$J\Psi$ yield vs. multiplicity in proton-proton collisions at the LHC,
Nucl. Phys. B Proceedings Supplements 214, Issue 1, 181-184 (2011).

[Rus2011] R. Rusanov,
Measurement of neutral-pion production suppression in Pb–Pb collisions at $\sqrt{s_{NN}} = 2.76\,\text{TeV}$ with ALICE at the CERN LHC,
Diploma Thesis, University of Heidelberg, 2011.

[Sal1969] A. Salam,
Fundamental Theory of Matter: A Survey of Results and Methods.,
In Contemporary physics: Trieste Symposium: Proceedings of the International Symposium on Contemporary Physics 19, 3 (1969).

[Sal1970] A. Salam and others,
Weak and Electromagnetic Interactions in Elementary Particle Theory,
Physics Review D 2, 1285 (1970).

[SZS2010] R. Sassot P. Zurita and M. Stratmann,
Inclusive Hadron Production in the CERN-LHC Era,
Physics Review D 82: 329 074011 (2010), arXiv:[hep-ph]1008.0540v1.

[Sch1995] P. Schmüser
Feynman-Graphen und Eichtheorien für Experimentalphysiker,
2. Auflage, Springer-Verlag Berlin Heidelberg New York, ISBN 3-540-58486-2 (1995).

[Sjo1987] Torbjörn Sjöstrand and Maria van Zijl,
A multiple-interaction model for the event structure in hadron collisions,
Physics Review D 36, 2019 (1987).

[Sjo2006] T. Sjöstrand, S. Mrenna and P. Skands,
PYTHIA 6.4: Physics and Manual,
HEP 0605:026 (2006), arXiv:[hep-ex]0603175v2.

[Ska2010] P. Skands
Tuning Monte Carlo Generators: The Perugia Tunes,
Physics Review D 82: 074018 (2010), arXiv:[hep-ph]1005.3457v4.

[Str2011] M.Strikman
Remarks on the observation of high multiplicity events at the LHC,
Physics Review D 84: 011501 (R) (2011).

[Tsa1988] C. Tsallis
Possible Generalization of Boltzmann-Gibbs Statistics,
J. Stat. Phys. 52, 479 (1988).

[Vit2006] Ivan Vitev,
Testing the theory of QGP-induced energy loss at RHIC and the LHC,
Phys. Lett. B 639, 38-45 (2006).

[Vog2010] W. Vogelsang,
Private communication.

[Vog2011] W. Vogelsang,
Private communication.

[Wik2011] http://en.wikipedia.org/wiki/Standard_Model .

[Wil1974] K.G. Wilson,
Confinement of Quarks.,
Physics Review D 10, 2445-2459 (1974).

[Wei1967] S. Weinberg,
A Model of Leptons.
Phys. Rev. Lett. 19(21), 1264–1266 (1967).

[Wil1997] W.S.C. Williams,
Nuclear and Particle Physics,
Oxford University Press Inc., ISBN 0 19 852046 8 (1997).

[Zwe1964] G. Zweig,
An SU(3) Model for Strong Interaction Symmetry and its Breaking. Part II.,
CERN-TH-412, published in: Developments in the Quark Theory of Hadrons, 22-101 (1964).

Acknowledgements

I would not have been able to write this thesis without the help of many people that I want to thank here for encouraging, motivating, advertising and teaching me or giving my their friendships and love. They all have contributed to the outcome of this work and I am deeply thankful.

Firstly, I would like to thank Prof. Dr. Johanna Stachel to give me the opportunity to join the ALICE collaboration and to write this thesis, for all helping comments and discussions. Thank you!

The members of our *photon conversion group* also deserve special thanks. They are great physicists and it is a pleasure to work with. Thank you for fruitful discussions during our meetings and beside of them and for your support. Many thanks to PD Dr. Klaus Reygers, Friederike Bock, Kenneth Aamodt, Martin Wilde, Radoslav Rusanov and Daniel Lohner and the other members of the group. My special thanks I would like to give to Dr. Ana Marin for her great guiding and support within the last four years, for her positive and focused approach to our work, for motivation and inspiration. Thank you, Ana!

Thanks to my day-to-day colleagues of the third corridor for sharing coffee, chocolate and many things to laugh about. I have found new friends during my PhD and old friends have stayed with me, although I was far away and too often too busy even for an extended chat on the phone. Thank you very much for your support and distractions that you offer from a sometimes overwhelming amount of work. Thank you very much, Anne P., Anne R., Ben, David, Friederike, Gela, Jochen, Katrin, Karlin, Karsten, Korinna, Kristian, Maren, MinJung, Rachik, Rebecca, Sara, Torben, Tom and Yvonne!

Many thanks go to my parents, my brother and his girlfriend for believing in me. Thank you!

Finally, and most important, I want to thank my boyfriend Olaf and our daughter Marlene. Thank you so much for your love, support and patience. You are my sunshine!